

**An Improved Framework for the  
Inverse Analysis of Skeletal  
Muscle Tissue *In-Vivo***

**Kevin Mattheus Moerman**

**A thesis submitted to the University of Dublin, Trinity College, in partial fulfilment  
of the requirements for the degree of**

**Doctor in Philosophy**

**The University of Dublin, Trinity College**

**April 2012**



# An Improved Framework for the Inverse Analysis of Skeletal Muscle Tissue *In-Vivo*

**Kevin Mattheus Moerman, M.Sc. B.Eng.**

A thesis submitted to the University of Dublin Trinity College, in partial fulfilment of the  
requirements for the degree of

**Doctor in Philosophy**

Trinity College Dublin

April 2012

Supervisor:

**Dr. Ciaran K. Simms<sup>1</sup>**

Internal Examiner:

**Prof. Daniel J. Kelly<sup>1</sup>**

External Examiner:

**Prof. Cees W.J. Oomens<sup>2</sup>**

<sup>1</sup>Trinity Centre for Bioengineering, University of Dublin, Trinity College, Dublin, Ireland

<sup>2</sup>Mechanical Engineering, Eindhoven University of Technology, Eindhoven, The Netherlands













# Declaration

I declare that this thesis has not been submitted as an exercise for a degree at this or any other university and it is, unless otherwise referenced, entirely my own work.

I agree to deposit this thesis in the University's open access institutional repository or allow the library to do so on my behalf, subject to Irish Copyright Legislation and Trinity College Library conditions of use and acknowledgement.

Kevin Mattheus Moerman

*Naarden, The Netherlands, the 30<sup>th</sup> of April 2012*

# Summary

This thesis focusses on the development of an experimental and computational framework for the non-invasive analysis of the passive mechanical properties of living human skeletal muscle tissue. This is relevant to many areas of research including impact biomechanics and rehabilitation engineering.

Although constitutive models have been proposed for muscle tissue these have been insufficiently validated for human tissue which requires non-invasive methods. Non-invasive analysis of the mechanical properties of soft tissue requires non-invasive mechanical exciting and inverse analysis of non-invasively measured experimental boundary conditions such as tissue deformation and applied load.

Magnetic Resonance Imaging (MRI) provides excellent soft tissue contrast without ionizing radiation. In addition it allows for the measurement of soft tissue anatomy, architecture and deformation boundary conditions. Hence for mechanical excitation a novel MRI compatible and computer controllable soft tissue indentation device was developed and implemented with an accurate high acquisition rate (100Hz) optical force sensor capable of viscoelastic force registration.

In order to measure the resultant deformation SPATial Modulation of the Magnetisation (SPAMM) tagged MRI was used. Traditional SPAMM tagging methods require large numbers of repetitions of motion cycles causing repeatability difficulties and volunteer discomfort. However for this thesis a unique set of high speed SPAMM tagged MRI techniques, and fully automatic post-processing methods based on Gabor wavelet filtering, were developed allowing for the measurement of complex dynamic 3D deformation following the combination of just 3 motion cycles. The SPAMM tagged MRI techniques were validated using marker tracking in a silicone gel phantom and underwent *in-vivo* evaluation whereby sub-voxel accuracy and precision levels were reported.

Constitutive models for passive skeletal muscle tissue were evaluated using inverse Finite Element (FE) Analysis (FEA) based fitting to experimental data from the literature. It was shown that current models do not allow appropriate modelling of anisotropy. A new constitutive law was proposed which formed a close match to the data and was based on Gaussian weighting of transverse and longitudinal direction contributions of a spherical fibre distribution model.

Finally an FE modelling framework was presented whereby detailed anatomically accurate 3D FE models can be generated from anatomical MRI and where diffusion tensor MRI based fibre directions could be incorporated as well.

A bank of experimental data was created for MRI based volunteer upper arm indentation for use in future biomechanical studies consisting of anatomical and diffusion tensor MRI data, 3D displacement vector fields and indentation force data.

Future work will focus on the application of the experimental and computational methods presented to the analysis of skeletal muscle tissue mechanical properties.



~ *For Elizabeth & Isaac* ~



# Acknowledgements

First of all I would like to thank Dr. Ciaran Simms (Trinity College Dublin) for his fantastic role as my supervisor! I don't think I could imagine a better supervisor, always there, always positive, always motivating. Thanks for being so incredibly patient with me and for trusting me and allowing me to explore tangents sometimes and for steering me back into the right direction other times. Thanks Ciaran, and also my Principal Investigator Dr Caitríona Lally (Dublin City University) for this fantastic opportunity!

Thanks also to my colleague Vittoria Flamini at Dublin City University for our collaboration early on in the project. I would also like to thank my colleagues at the Trinity Centre for Bioengineering for the nice working atmosphere. Thanks especially to Thomas Nagel for coffees and walks around campus while discussing continuum mechanics when I was in Dublin and later over Skype when I was in Amsterdam. Thanks also to Michael Takaza and Dr. Melanie van Looke for sharing their experimental data with me.

I am also grateful to Dr. Aart Nederveen and Drs. Andre Sprengers at the Academic Medical Centre, Amsterdam. Thanks for the very fruitful collaboration in relation to MRI. Also, Aart thank you for effectively co-supervising me on the MRI side of things and for financially adopting me after my third year and allowing me to work at the AMC! I would like to thank all colleagues at the AMC. Especially Andre Sprengers for advice on SPAMM tagged MRI and for joining me even on Sundays or in the middle of the night if required for some more MRI scanning! Thanks also for advice on the implementation of scale-space methods for SPAMM tagged MRI analysis. I'm also grateful to Dr. Matthan Caan (Matlab advice), Martijn Froeling (assistance for diffusion tensor MRI) and Paul Groot (advice on the TTL triggering system and help compiling the customized FEBio source codes).

Thanks to Prof. Sam Evans and Dr. Cathy Holt (Cardiff University Wales) for the collaboration in relation to DIC and Sam for introducing me to FEBio.

I would also like to thank Prof. Gerard Ateshian and Dr. Steve Maas for their often extensive replies to my FEBio queries posted on the FEBio forum.

Thanks to Karel van den Berg and Lucien Voogd at Lely Technologies N.V. for donating the electric motor for the MRI compatible loading device and for providing advice on its implementation.

Thanks also to my dear friends and former housemates while in Dublin Dr. Brendan Holland and Dr. Daniel Iseemann. Thanks for always being there to discuss difficulties with my project or for pure procrastination and the many hours spend on Trinity's croquet lawn.

I also thank my parents and family for always supporting me.

Lastly I am eternally grateful to my dearest wife Elizabeth! Thanks for the never ending support and your enormous patience! Thanks for listening whenever I went on and on about bubble membranes, Gabor wavelets and Bucky-balls. Isaac thanks also to you also for giving me something amazing to look forward to and thank you for granting me a reasonable amount of sleep during your first weeks on this world so that I felt fit enough to get this thesis finished.

I would also like to acknowledge the funding for this project: Research Frontiers Grant (06/RF/ENM076) awarded by Science Foundation Ireland.



# Table of Contents

<b>DECLARATION</b> .....	<b>I</b>
<b>SUMMARY</b> .....	<b>II</b>
<b>ACKNOWLEDGEMENTS</b> .....	<b>VII</b>
<b>LIST OF PUBLICATION RESULTING FROM THIS STUDY</b> .....	<b>XIV</b>
<b>Journal papers</b>	<b>XIV</b>
<b>Co-authored journal papers</b>	<b>XIV</b>
<b>Conference proceedings</b>	<b>XV</b>
<b>NOMENCLATURE</b> .....	<b>XVII</b>
<b>Mathematical notation</b>	<b>XVII</b>
<b>Symbols</b>	<b>XVII</b>
<b>Abbreviations</b>	<b>XX</b>
<b>1 INTRODUCTION</b> .....	<b>1</b>
<b>1.1 RATIONALE OF THE STUDY</b> .....	<b>1</b>
<b>1.2 OBJECTIVES OF THE STUDY</b> .....	<b>3</b>
<b>1.3 OUTLINE OF THE THESIS</b> .....	<b>4</b>
<b>2 THEORETICAL FRAMEWORK</b> .....	<b>7</b>
<b>2.1 INTRODUCTION</b> .....	<b>8</b>
<b>2.2 BASICS OF CONTINUUM MECHANICS</b> .....	<b>8</b>
<b>2.2.1 Introduction</b>	<b>8</b>
<b>2.2.2 Vector and tensor algebra</b>	<b>8</b>
<b>2.2.3 The continuum hypothesis</b>	<b>14</b>
<b>2.2.4 Motion</b>	<b>14</b>
<b>2.2.5 Deformation</b>	<b>15</b>
<b>2.2.6 Stretch and rotation</b>	<b>16</b>
<b>2.2.7 Strain</b>	<b>18</b>
<b>2.2.8 Stress</b>	<b>19</b>
<b>2.2.9 Strain energy</b>	<b>21</b>
<b>2.2.10 Constitutive equations</b>	<b>22</b>
<b>2.2.11 Modelling anisotropy</b>	<b>26</b>
<b>2.2.12 Viscoelasticity</b>	<b>29</b>
<b>2.3 BASICS OF MAGNETIC RESONANCE IMAGING</b> .....	<b>34</b>
<b>2.3.1 Introduction</b>	<b>34</b>
<b>2.3.2 Angular momenta and magnetic moments</b>	<b>34</b>
<b>2.3.3 Equilibrium alignment of spin</b>	<b>36</b>
<b>2.3.4 Dynamic equilibrium</b>	<b>37</b>
<b>2.3.5 Alteration of dynamic equilibrium</b>	<b>39</b>
<b>2.3.6 Relaxation to dynamic equilibrium</b>	<b>39</b>
<b>2.3.7 Detecting the magnetization of the system</b>	<b>41</b>

2.3.8	Position encoding	42
2.3.9	Anatomical magnetic resonance imaging	44
2.3.10	MRI techniques based on motion induced phase shifts	45
2.3.11	Tagged Magnetic Resonance Imaging	49
2.4	BASICS OF IMAGE PROCESSING.....	52
2.4.1	Introduction	52
2.4.2	Background on image data	52
2.4.3	Segmentation and filtering	54
2.4.4	Spatial transformations	56
2.4.5	Image correlation and registration	57
<b>3</b>	<b>LITERATURE REVIEW.....</b>	<b>60</b>
3.1	INTRODUCTION.....	60
3.2	SKELETAL MUSCLE ANATOMY AND PHYSIOLOGY.....	61
3.2.1	Introduction	61
3.2.2	Skeletal muscle tissue architecture	61
3.2.3	Muscle tone and passive stiffness enhancement	64
3.2.4	Muscle fibre type, distribution and orientation	65
3.2.5	Conclusions	66
3.3	SKELETAL MUSCLE TISSUE MECHANICAL BEHAVIOUR.....	67
3.3.1	Introduction	67
3.3.2	Invasive mechanical property assessment and analysis of excised tissue samples	67
3.3.3	Non-invasive mechanical property assessment	77
3.3.4	Comments on constitutive modelling of skeletal muscle tissue	83
3.3.5	Conclusions	85
3.4	NON-INVASIVE IMAGING MODALITIES.....	87
3.5	MRI COMPATIBLE ACTUATOR AND SENSOR DEVICES.....	87
3.6	MRI BASED MEASUREMENT OF SOFT TISSUE DEFORMATION.....	90
3.7	VALIDATION OF MRI DERIVED MOTION AND DEFORMATION.....	91
3.8	SUMMARY AND PROPOSED APPROACH.....	92
<b>4</b>	<b>STUDY I A NOVEL MRI COMPATIBLE SOFT TISSUE INDENTOR AND OPTICAL FIBRE BRAGG GRATING FORCE SENSOR.....</b>	<b>97</b>
4.1	INTRODUCTION.....	98
4.2	METHODS.....	98
4.2.1	Fibre Bragg Grating Based optical force sensing	99
4.2.2	The soft tissue indenter system	100
4.2.2.1	THE MRI COMPATIBLE SOFT TISSUE INDENTOR ASSEMBLY.....	100
4.2.2.2	THE MRI ACTUATOR ASSEMBLY.....	101
4.2.2.3	THE INDENTOR HEAD AND FORCE SENSOR ASSEMBLY.....	102
4.2.2.4	ACTUATOR MOTION CONTROL AND DATA ACQUISITION.....	103
4.2.3	Optical force sensor calibration	104
4.2.4	Evaluation of the indenter system performance	105
4.2.4.3	EVALUATION OF THE SYSTEM MRI COMPATIBILITY.....	108
4.3	RESULTS.....	109
4.3.1	Optical force sensor performance	109
4.3.2	Repeatability of indenter motion	113
4.3.3	MRI compatibility of indenter system	115

4.4	DISCUSSION .....	115
4.5	CONCLUSIONS .....	120
<b>5</b>	<b>STUDY II DIC AND INVERSE FEA FOR THE DETERMINATION OF THE MECHANICAL PROPERTIES OF SOFT TISSUE.....</b>	<b>122</b>
5.1	INTRODUCTION .....	123
5.2	METHODS .....	123
5.3	RESULTS .....	125
5.4	DISCUSSION AND CONCLUSIONS .....	128
<b>6</b>	<b>STUDY III A VALIDATION FRAMEWORK FOR MRI BASED DEFORMATION MEASUREMENT.....</b>	<b>130</b>
6.1	INTRODUCTION .....	131
6.1.1	The tissue phantom	131
6.1.2	MR Imaging	132
6.1.3	Marker tracking method	132
6.1.4	Evaluation of marker tracking method using simulated magnitude MR image data	135
6.1.5	Simulation of a noiseless image and analysis of geometric bias	136
6.1.6	Simulation of noisy magnitude MR data and analysis of the noise effects	140
6.2	RESULTS .....	141
6.2.1	Evaluation of the geometric bias in the marker tracking method	142
6.2.2	Evaluation of the performance on the marker tracking method in the presence of noise.	143
6.3	DISCUSSION .....	144
6.4	CONCLUSIONS .....	144
<b>7</b>	<b>STUDY IV THE MRI BASED MEASUREMENT OF STATIC 3D SOFT TISSUE DEFORMATION .....</b>	<b>146</b>
7.1	INTRODUCTION .....	147
7.2	METHODS .....	148
7.2.1	MRI sequence design	148
7.2.2	The validation set-up: indenter and soft tissue phantom	152
7.2.3	Deriving tissue deformation from the SPAMM tagged MRI data	153
7.2.4	Analysis of precision and accuracy	158
7.3	RESULTS .....	159
7.3.1	Precision of tag point location	159
7.3.2	Precision of displacement magnitude	160
7.3.3	Accuracy of displacement measurement in the phantom	162
7.4	DISCUSSION .....	163
7.5	CONCLUSIONS .....	166
<b>8</b>	<b>STUDY V THE MRI BASED MEASUREMENT OF DYNAMIC 3D SOFT TISSUE DEFORMATION.....</b>	<b>168</b>
8.1	INTRODUCTION .....	169
8.2	METHODS .....	170
8.2.1	The experimental set-up: indenter and soft tissue phantom	170
8.2.2	MRI sequence	171
8.2.3	Spatial characteristics of SPAMM tags	174
8.2.4	Deriving tissue deformation from the SPAMM tagged MRI data	176
8.2.5	Analysis of precision and accuracy	186
8.3	RESULTS .....	187
8.3.1	Precision of tag point location	187

8.3.2	Precision of individual dynamic displacement	189
8.3.3	Accuracy of cumulative dynamic displacement	190
8.3.4	Accuracy of displacement in the phantom	192
8.4	DISCUSSION .....	193
8.5	CONCLUSIONS.....	196
<b>STUDY VI CONSTITUTIVE MODELLING OF SKELETAL MUSCLE TISSUE .....198</b>		
8.6	INTRODUCTION.....	199
8.7	METHODS.....	200
8.7.1	The anisotropic and non-linear elastic properties of muscle tissue	200
8.7.2	Constitutive modelling of non-linear elasticity	204
8.7.3	Modelling of volumetric tension compression non-linearity	213
8.7.4	Inverse FEA based constitutive model evaluation	213
8.8	RESULTS.....	216
8.8.1	Isotropic Ogden hyperelastic (ISO)	216
8.8.2	Fibre reinforced transversely isotropic Ogden hyperelastic (TISO)	217
8.8.3	Orthotropic fibre family reinforced Ogden (TCNL) model for compression	219
8.8.4	Ellipsoidal fibre distribution (EFD) models for tension and compression	220
8.8.5	Gaussian Modulated Spherical Fibre Distribution Ogden hyperelastic (GMSFD) model for tension and compression	223
8.8.6	Modelling of volumetric tension compression non-linearity	226
8.9	DISCUSSION .....	226
8.10	CONCLUSIONS.....	228
<b>9 STUDY VII MRI BASED DERIVATION OF DETAILED FINITE ELEMENT MODELS INCORPORATING FIBRE ARCHITECTURE .....229</b>		
9.1	INTRODUCTION.....	230
9.2	METHODS.....	230
9.2.1	MRI based indentation experiments	230
9.2.2	FE model construction	231
9.2.3	Iterative inverse FEA based optimisation	235
9.3	RESULTS.....	235
9.4	DISCUSSION .....	236
9.5	CONCLUSIONS.....	236
10	DISCUSSION, CONCLUSIONS AND FUTURE WORK.....	237
11	REFERENCES .....	243



# List of publication resulting from this study

## *Journal papers*

- Moerman, K.M., Holt, C.A., Evans, S.L. and Simms, C.K., "Digital image correlation and finite element modelling as a method to determine mechanical properties of human soft tissue in vivo", *Journal of Biomechanics* 42, 1150-1153 (2009).
- Moerman, K.M., Kerskens, C.M., Lally, C., Flamini, V. and Simms, C.K., "Evaluation of a Validation Method for MR Imaging-Based Motion Tracking Using Image Simulation", *EURASIP Journal on Advances in Signal Processing* 2010, 11 pages (2010).
- Moerman, K.M., Sprengers, A.M., Simms, C.K., Lamerichs, R.M., Stoker, J. and Nederveen, A.J., "Validation of SPAMM tagged MRI based measurement of 3D soft tissue deformation", *Medical Physics* 38, 13 (2011).
- Moerman, K.M., Sprengers, A.M., Simms, C.K., Lamerichs, R.M., Stoker, J. and Nederveen, A.J., "Validation of Continuously Tagged MRI for the Measurement of Dynamic 3D Soft Tissue Deformation", *Medical Physics* 39, 1793-1810, (2012).
- Moerman, K.M., Sprengers, A.M.J., Nederveen, A.J. and Simms, C.K., "A Novel MRI Compatible Soft Tissue Indentor and Fibre Bragg Grating Force Sensor", *Medical Engineering & Physics* Article in review (2012).

## *Co-authored journal papers*

- Flamini, V., Kerskens, C.M., Moerman, K.M., Simms, C.K. and Lally, C., "*Imaging Arterial Fibres Using Diffusion Tensor Imaging—Feasibility Study and Preliminary Results*", *EURASIP Journal on Advances in Signal Processing* 2010, 13 (2010).
- Takaza, M., Moerman, K.M., Gindre, J., Lyons, C.G. and Simms, C.K., "*The anisotropic mechanical behaviour of passive skeletal muscle tissue subjected to large tensile strain*", *Journal of the Mechanical Behavior of Biomedical Materials* (in review).

## Conference proceedings

- K.M. Moerman and C.K. Simms, “Non-invasive determination of soft tissue deformation using tagged MRI: application to a silicone phantom”, *Bioengineering in Ireland*, 2008.
- K.M. Moerman and C.K. Simms, “A Validation Method for Motion Tracking Techniques Based on Tagged MRI”, *Bioengineering in Ireland*, 2009.
- K.M. Moerman, C. Lally, C.K. Simms, “A 3D Image Object tracking Algorithm Based on Sparse Masking and Adjacency Analysis”, *The 10<sup>th</sup> United States National Congress of Computational Mechanics*, (Columbus, OHIO, 2009)
- K.M. Moerman, A. M. Sprengers, A. J. Nederveen, C.K. Simms, “Towards the Non-Invasive Determination of the Mechanical Properties of Living Human Soft Tissue”, *Bioengineering in Ireland*, 2010.
- K. M. Moerman, A. M. Sprengers, A. J. Nederveen, C. A. Holt, S. L. Evans, C. Lally and C. K. Simms, "Non-Invasive Imaging and Inverse Finite Element Analysis for the Determination of the Mechanical Properties of Soft Tissue," in *Computational Methods in Biomechanics Biomedical Engineering*, (Valencia, Spain, 2010).
- K. M. Moerman, C. K. Simms, A. M. Sprengers and A. J. Nederveen, "Experimental Validation of SPAMM Tagged Magnetic Resonance Imaging Based Measurement of Non-uniform 3D Soft Tissue Deformation," in *ISMRM ESMRMB Joint Annual Meeting*, (Stockholm, Sweden, 2010).
- K. M. Moerman, A. M. Sprengers, A. J. Nederveen and C. K. Simms, "Non-invasive Measurement of 3D Soft Tissue Deformation and Force: Application to Indentation Tests on the Human Upper Arm," in *17th Congress of the European Society of Biomechanics*, (Edinburgh, 2010).
- K. M. Moerman and C. K. Simms, "A novel MRI compatible Soft Tissue Indentor and Fibre Bragg Grating Force Sensor " in *Fourth European Workshop on Optical Fibre Sensors, Vol. 7653*, edited by J. L. Santos, B. Culshaw, J. M. López-Higuera and W. N. MacPherson (SPIE, Porto, Portugal, 2010).
- K. M. Moerman, A. M. Sprengers, A. J. Nederveen and C. K. Simms, "Passive Human Muscle Properties for Finite Element Human Body Models for Safety," in *IRCOBI 2010*, (Hanover, 2010).

- K. M. Moerman, A. M. Sprengers, C. K. Simms, A. E. Bohte, R. Lamerichs, R. Sinkus and A. J. Nederveen, "Combined MRE and SPAMM tagged MRI for the analysis of large strain soft tissue mechanical properties " in *ISMRRM ESMRMB Joint Annual Meeting*, (Montreal, 2011).
- K. M. Moerman, A. M. Sprengers, C. K. Simms, R. Lamerichs, J. Stoker and A. J. Nederveen, "Validation of Fast Dynamic SPAMM Tagged MRI Based Measurement of Non-linear 3D Soft Tissue Deformation," in *ISMRRM ESMRMB Joint Annual Meeting*, (Montreal, 2011).



# Nomenclature

## *Mathematical notation*

Notation	Description
$a, \alpha, b, \beta$	Scalars
$\mathbf{a}$	Vector
$ \mathbf{a} $	Magnitude of vector $\mathbf{a}$
$\mathbf{a} \cdot \mathbf{b}$	The dot (or scalar or inner) product of the vectors $\mathbf{a}$ and $\mathbf{b}$
$\mathbf{a} \times \mathbf{b}$	The cross (or vector or outer) product of the vectors $\mathbf{a}$ and $\mathbf{b}$
$\mathbf{a} \otimes \mathbf{b}$	The dyad (or tensor) product of the vectors $\mathbf{a}$ and $\mathbf{b}$
$\mathbf{A}$	A (second-order unless otherwise stated) tensor or matrix
$A_{ij}$	Element $i, j$ of tensor $\mathbf{A}$
$\mathbf{A} : \mathbf{B}$	The double-dot contraction of tensors $\mathbf{A}$ and $\mathbf{B}$
$\mathbf{A}^{-1}$	The inverse of tensor $\mathbf{A}$
$\mathbf{A}^T$	The transpose of tensor $\mathbf{A}$
$\text{tr}(\mathbf{A})$	The trace of tensor $\mathbf{A}$
$\det(\mathbf{A})$	The determinant of tensor $\mathbf{A}$
$\text{dev}(\mathbf{A})$	The deviatoric of tensor $\mathbf{A}$
$\Delta \mathbf{a}$	The gradient of $\mathbf{a}$
$\nabla_x \mathbf{a}$	The gradient of $\mathbf{a}$ , defined as $\frac{\partial a_i}{\partial x_i}$
$\tilde{\lambda}$	Modified variable $\lambda$
$\mathbf{I}$	The identity tensor
$\mathbf{0}$	The zero tensor
$\mathbf{M} * \mathbf{F}$	Convolution of $\mathbf{M}$ and $\mathbf{F}$
$\mathcal{F}\{\mathbf{M}\}$	The Fourier transform of $\mathbf{M}$
$\mathcal{F}\{\mathbf{M}\}^{-1}$	The inverse Fourier transform of $\mathbf{M}$

## *Symbols*

Below is a list of commonly used symbols. Symbols which are only locally used and clearly elaborated in the text are not included in this list.

<b>Symbol</b>	<b>Description</b>
$\mathbb{E}^3$	3D Euclidian space
$\mathcal{E}$	Right-handed orthonormal Cartesian basis in $\mathbb{E}^3$
$\mathbf{e}_i$	Orthonormal basis vectors
$\delta$	The Kronecker Delta
$\Omega$	A continuum body
$P$	A material point in $\Omega$
$t$	Time
$\mathbf{x}$	Position vector in Eulerian configuration
$\mathbf{X}$	Position vector in Lagrangian configuration
$\chi$	Motion of material point
$\mathbf{u}$	Displacement vector
$\mathbf{F}$	Deformation gradient tensor
$\mathbf{D}$	Inverse of the deformation gradient tensor $\mathbf{F}$
$v, V$	Volume in the in Eulerian, Lagrangian configuration
$J$	The Jacobian of the deformation gradient tensor (continuum mechanics) or angular momentum (MRI physics)
$\lambda, \lambda_i$	Stretch, a Lamé modulus (continuum mechanics), may also represent diffusion tensor Eigenvalue (MRI physics) or the reflected Bragg wavelength (physics of FBG sensors)
$\mathbf{Q}$	The rotation tensor
$\mathbf{U}$	The left stretch tensor
$\mathbf{V}$	The right stretch tensor
$\mathbf{C}$	The right Cauchy-Green tensor
$\mathbf{B}$	The left Cauchy-Green or Finger tensor (continuum mechanics), External magnetic field (MRI physics)
$I_i$	Deformation invariants
$\boldsymbol{\varepsilon}$	The linear (Cauchy, Biot, small or infinitesimal) strain tensor
$\mathbf{E}$	The Green-Lagrange strain tensor
$\mathbf{H}$	The Logarithmic (or Hencky) strain tensor
$f, F$	Force, $f$ may also refer to a function
$s, S$	Surface element in Eulerian, Lagrangian configuration

$\mathbf{n}, \mathbf{N}$	Surface normal vector in Eulerian, Lagrangian configuration
$\mathbf{t}, \mathbf{T}$	Traction vectors, in Eulerian, Lagrangian configuration (continuum mechanics), $\mathbf{T}$ may also represent a spatial transformation tensor (image processing)
$\boldsymbol{\sigma}$	The Cauchy or true stress tensor (continuum mechanics), standard deviation of Gaussian function (statistics, image processing)
$\mathbf{P}$	Piola-Kirchoff or Lagrangian stress tensor
$\mathbf{S}$	Second Piola-Kirchoff stress tensor (continuum mechanics), may also represent a deformation transformation tensor (image processing)
$\boldsymbol{\tau}$	Kirchoff stress tensor
$\mathcal{P}_{ext}$	External mechanical power
$\mathcal{K}$	Kinetic energy
$\Pi_{int}$	Internal mechanical work
$\Psi$	Strain-energy density (Helmholtz free-energy) function
$\lambda$	A Lamé (material) parameter, or spring constant in rheological model
$\mu, \mu_i$	A Lamé material parameter, the shear modulus, a spring constant in rheological model, constant in (e.g. Ogden) hyperelastic constitutive law
$E$	The Young's modulus
$\nu$	The Poisson's ratio
$\kappa$	The bulk modulus
$c_{ij}$	Material constants in constitutive law
$\alpha_i$	Material constant in (e.g. Ogden) hyperelastic constitutive law
$n, N$	Population size or number of summation iterations, or number of spins in a voxel (MRI physics)
$\mathbf{A}$	Texture or structure tensor
$\mathbf{a}$	Fibre or texture direction vector
$\xi_i, \xi$	Fibre material parameter for tension-compression non-linear orthotropic and ellipsoidal/spherical fibre distribution models
$\beta_i, \beta$	(Fibre) material parameter for tension-compression non-linear

	orthotropic and ellipsoidal/spherical fibre distribution models. Alternatively this may refer to Criscione invariations
$\eta$	Viscosity constant in rheological model
$G$	Relaxation modulus (continuum mechanics). Magnetic field gradient (MRI physics).
$\tau_i$	Viscoelastic material constant for discrete relaxation function
$\gamma_i$	Viscoelastic material constant for discrete relaxation function
$M$	An image matrix (image processing)
$T_1$	Spin-lattice relaxation time
$T_2$	Spin-spin relaxation time

## ***Abbreviations***

<b>Abbreviation</b>	<b>Description</b>
MR	Magnetic Resonance
MRI	Magnetic Resonance Imaging
MRE	Magnetic Resonance Elastography
SPAMM	SPAtial Modulation of the Magnetisation
CSPAMM	Complementary SPAMM
PCMRI	Phase Contrast MRI
HARP	Harmonice Phase
DENSE	Displacement Encoding with Stimulated Echoes
DTI	Diffusion Tensor Imaging
DICOM	Digital Imaging and Communication in Medicine
FE	Finite Element
FEA	Finite Element Analysis
FBG	Fibre Bragg Grating
ACG	Adjacency Coordinate Group
OCV	Object Central Voxel
PDF	Probability Density Function
SNR	Signal to Noise Ratio
tSNR	Temporal SNR

TTL	Transistor-Transistor Logic
SSDM	Sum of Squared Differences Matrix
ECG	Electrocardiogram
POM	polyoxymethylene
RMS	Root Mean Square
SSQD	Sum of Squared Differences
ISO	Isotropic Ogden hyperelastic
TISO	Transversely Isotropic Ogden hyperelastic
TCNL	Tension Compression Non-Linear Orthotropic Ogden hyperelastic
EFD	Ellipsoidal Fibre Distribution
GMSFD	Gaussian Modulation Spherical Fibre Distribution Ogden Hyperelastic
TLA	Three Letter Acronym/Abbreviation



# 1 INTRODUCTION

## 1.1 Rationale of the study

This thesis focusses on the development of an experimental and computational framework for the non-invasive analysis of the passive mechanical properties of skeletal muscle tissue. Of interest here is the development of methods to non-invasively analyse the non-linear and anisotropic elastic and viscoelastic properties of passive living skeletal muscle tissue.

The analysis of passive skeletal muscle soft tissue mechanical properties is relevant to many fields of research including the well-known applications to: impact biomechanics<sup>1-3</sup>, rehabilitation engineering<sup>4-7</sup>, tissue engineering<sup>8, 9</sup>, skeletal muscle behaviour simulation during gait<sup>10</sup> and surgical simulation<sup>11-14</sup>. Less well-known are the applications to the study of: soft tissue drug transport<sup>15, 16</sup>, extra-ocular muscle disorders<sup>17</sup>, oro-facial movements<sup>18</sup>, and in zoology, caterpillar locomotion<sup>19</sup> and the simulation of squid tentacle strike to catch prey<sup>20</sup>.

Experimental work on the mechanical properties of muscle tissue have largely focussed on excised tissue samples (e.g. for compression<sup>21</sup> and tension<sup>22</sup>) demonstrating skeletal muscle tissue to be non-linear, viscoelastic and anisotropic. Constitutive models have also been proposed (e.g.<sup>23, 24</sup>) however the anisotropic properties of such models have not been evaluated for multiple load directions. In addition, current constitutive modelling approaches model muscle tissue as reinforced in the fibre direction while recent experimental data<sup>21, 22</sup> demonstrates that the transverse direction is most dominant. Hence appropriately validated models for anisotropy have not been presented to date.

Translation of constitutive property analysis to living human tissue presents with significant challenges and requires non-invasive methods. Apart from validation of constitutive models for living human tissue, non-invasive mechanical property analysis has many medical applications such as: lesion detection<sup>25</sup>, pressure ulcer research<sup>26, 27</sup>, to distinguish healthy and pathologic muscle<sup>28</sup>, or for the assessment of limb immobilisation and contracture<sup>29</sup>. However the non-invasive evaluation of detailed constitutive models describing the complex mechanical (anisotropic, non-linear and viscoelastic) properties of soft tissues require: non-invasive mechanical tissue excitation

and inverse analysis of detailed non-invasively measured experimental boundary conditions (including 3D tissue deformation and fibre architecture). Some authors have used indentation tests on skeletal muscle<sup>30, 31</sup>, but the tissue was then assumed to be isotropic and linear in elastic and viscoelastic properties. In addition elastography methods have been employed (using image based analysis of small strain wave propagations) for soft tissue. However elastography has only been applied to small strain measures and often linear elasticity is assumed (see review article<sup>32</sup>). In contrast, non-invasive imaging methods that allow detailed measurement of human soft tissue motion and deformation (due to known loading conditions), combined with inverse FEA allow for the evaluation of more complex and large strain constitutive models.

Magnetic resonance imaging (MRI) is an ideal modality for the non-invasive analysis of soft tissue biomechanics as it provides excellent soft tissue contrast without exposing subjects to ionizing radiation. In addition it allows for the measurement of various biomechanical boundary conditions required for inverse analysis of tissue properties, such as 3D tissue geometry (segmentable from anatomical MRI), 3D architecture (based on diffusion tensor MRI e.g.<sup>33</sup>) and accurate 3D soft tissue deformation measurement (e.g. based on tagged MRI, see review article<sup>34</sup>).

Non-invasive mechanical excitation of tissue (e.g. indentation) for mechanical property analysis inside an MRI scanner requires accurate computer controllable and MRI compatible actuators and force sensors. Ensuring safety and compatibility of such systems is not trivial. Although MRI compatible actuators and force sensors have been developed for other applications such as MRI robotics (e.g.<sup>35, 36</sup>), MRI guided surgical interventions (e.g.<sup>37-39</sup>), MRI based catheterisation (e.g.<sup>40</sup>), functional MRI (e.g.<sup>41, 42</sup>) and the study of pressure ulcer development (e.g.<sup>43</sup>), to date no computer controlled MRI based actuator system suitable for human skeletal muscle tissue mechanical property investigation has been proposed.

Once mechanical excitation has been applied, MRI can be employed for the non-invasive measurement of 3D soft tissue deformation. MRI based methods to study soft tissue deformation of human soft tissue *in-vivo* is also relevant to many research areas; for instance, the analysis of organ and bowel motility<sup>44</sup>, the assessment of tumor motion<sup>45</sup>, the study of cardiac biomechanics<sup>46</sup> and preoperative planning<sup>47</sup>. However current MRI based techniques for the measurement of soft tissue deformation, such as SPAtial Modulation of the Magnitisation (SPAMM) tagged MRI, employ segmented



acquisitions requiring the combination of large numbers of motion cycles. This has confined the application of SPAMM tagged MRI to the analysis of highly repeatable and periodic movements and has mainly been applied to the heart<sup>46, 48, 49</sup>. Recently other tissue types have also been analysed for repeatedly induced motions of the tongue<sup>50</sup> (16 volunteer speech repetitions per slice), brain<sup>51</sup> (144 volunteer rotational head accelerations) and eyes<sup>52</sup> (>135 repeated left to right eye movements). For the purpose of mechanical indentation based mechanical property investigation these methods thus result in repeatability constraints and possible discomfort, highlighting the need to develop faster SPAMM techniques requiring a minimum of repeated motion cycles.

## 1.2 Objectives of the study

This thesis focusses on the development of a framework of computational and experimental methods for the non-invasive analysis of skeletal muscle tissue mechanical properties. Since MRI is the most suitable non-invasive modality and large strain is of interest, indentations will be applied during which force measurements are required, hence our first objective is:

- 1) *To design and validate an MRI compatible soft tissue indentation system and force sensor*

Since MRI based deformation measurement was challenging at the start of this thesis and required validation the second objective evaluates an alternative imaging method for deformation measurement combined with indentation and inverse FEA, namely digital image correlation (DIC), the second objective is thus:

- 2) *To evaluate the indentation and inverse FEA based derivation of constitutive parameters based on DIC based deformation measurement.*

The third objective for this thesis relates to the fact that MRI based motion measurement methods require validation:

- 3) *To develop and evaluate methods to validate MRI derived soft tissue deformation.*

The fourth objective concerns the MRI based measurement of deformation during the indentation:

- 4) *To develop MRI based techniques and post-processing methods to measure 3D soft tissue deformation in-vivo using a minimum of motion cycles.*

The inverse FEA based constitutive parameter identification framework requires an appropriate starting constitutive model with initial parameters based on excised animal tissue data. This model needs to capture anisotropy for the transverse, longitudinal and intermediate direction responses. Hence the fifth objective was:

- 5) *To develop a constitutive modelling framework capturing the anisotropic, non-linear and viscoelastic mechanical properties of skeletal muscle tissue.*

Finally once an MRI compatible indenter has been used to apply indentation to a volunteer muscle site, force was measured using an MRI compatible force sensor and deformation was measured using SPAMM tagged MRI, one can start with the derivation of inverse FEA procedures for constitutive parameter identification. Thus the final objective was:

- 6) *To develop methods to derive detailed anatomical models from MRI data incorporating fibre architecture allowing for the evaluation of tissue anisotropy.*

## 1.3 Outline of the thesis

### *Theoretical framework*

This chapter highlights: the theory of continuum mechanics, basics of MRI, and the basics of image processing.

### *Literature review*

The following topics are discussed: the anatomy and physiology of skeletal muscle and its relation to the mechanical properties, experimental and computational modelling studies on the mechanical properties of skeletal muscle tissue, a brief discussion on non-invasive imaging modalities, MRI compatible actuators and sensor devices, MRI based measurement of soft tissue deformation and finally validation methods for MRI derived motion and deformation measurement.

### *Study I: A Novel MRI Compatible Soft Tissue Indentor and Fibre Bragg Grating Force Sensor*

In this study the computer controlled MRI compatible indenter and high sampling rate force sensor system are described and its validation and calibration results are discussed.

*Study II: Digital Image Correlation and Finite Element Modelling as a Method to Determine Mechanical Properties of Soft Tissue*

Since the development of MRI techniques was initially challenging study II evaluates the more straight-forward (but limited to surface measurements) alternative of DIC combined with inverse FEA for bulk material property assessment.

*Study III: A Validation Framework for MRI Based Deformation Measurement*

In order to validate MRI derived deformation measures study III describes a validation framework for MRI derived deformation measurement based on tracking of markers in a silicone gel phantom. A marker tracking algorithm is proposed and independently validated.

*Study IV: The MRI Based Measurement of Static 3D Soft Tissue Deformation*

This study introduces novel SPAMM tagged MRI techniques and semi-automatic post-processing methods for the derivation of 3D static deformation measurements following just 3 motion cycles.

*Study V: The MRI Based Measurement of Dynamic 3D Soft Tissue Deformation*

This study expands the SPAMM tagged MRI techniques for dynamic 3D deformation measurements following only 3 motion cycles. In addition a novel fully automatic methodology is presented.

*Study VI: Constitutive Modelling of Skeletal Muscle Tissue*

Using experimental data on uni-axial loading of muscle tissue for tension and compression at varying load angles, an array of common constitutive models is put to the test. It is demonstrated that current models do not accurately model anisotropy and tension compression non-linearity of muscle tissue and a novel constitutive model is proposed incorporating longitudinal and transverse fibrous contributions.

*Study VII: MRI Based Derivation of Detailed Finite Element Models Incorporating Fibre Architecture*

A semi-automatic methodology is presented allowing for the construction of detailed anatomically accurate FE models derived from anatomical and diffusion tensor MRI

incorporating skin, muscle and fat tissue and muscle fibre directions. Thus enabling the study of anisotropy.

*Discussion, conclusions and future work*

The last chapter summarises the results for this thesis and the implications and limitations of the work presented and mentions recommendations for future work.

## 2 THEORETICAL FRAMEWORK

## 2.1 Introduction

The current study involves constitutive modelling, finite element modelling and analysis, non-invasive imaging and digital image processing. In order to provide the reader with an understanding of the theory behind these areas, prior to presenting a review of the literature, this section discusses the basics of continuum mechanics, magnetic resonance imaging and digital image processing.

## 2.2 Basics of continuum mechanics

### 2.2.1 *Introduction*

This section describes the basics of vector and tensor algebra and continuum mechanics. For a more detailed discussion the reader is referred to specialised literature (e.g. on tensor algebra<sup>53</sup> and continuum mechanics<sup>54-59</sup>).

### 2.2.2 *Vector and tensor algebra*

Physical quantities definable by a single real number are known as scalars and exhibit only magnitude. Vectors however are physical quantities with both direction and magnitude (in 3D vectors can be graphically represented by arrows as shown Figure 2.1). The magnitude (or length or norm) of a vector  $\mathbf{a}$  is denoted  $|\mathbf{a}|$  and is defined by:

$$|\mathbf{a}| = \sqrt{\mathbf{a} \cdot \mathbf{a}} \quad 2-1$$

A vector with a magnitude of 1 is called a unit vector. The dot (or inner or scalar) product of two vectors produces a scalar defined by:

$$\mathbf{a} \cdot \mathbf{b} = |\mathbf{a}||\mathbf{b}| \cos \theta \quad 2-2$$

with  $\theta$  the angle between the two vectors. Two vectors are orthogonal if their dot product equals zero.

According to the parallelogram law when two vectors are added or subtracted a new vector is obtained (top left in Figure 2.1). A 3D Euclidean vector space can be defined, denoted by  $\mathbb{E}^3$ , where the following properties hold (see also Figure 2.1):

$$\begin{aligned} \mathbf{a} + \mathbf{b} &= \mathbf{b} + \mathbf{a} \\ (\mathbf{a} + \mathbf{b}) + \mathbf{c} &= \mathbf{a} + (\mathbf{b} + \mathbf{c}) \\ \mathbf{a} + \mathbf{0} &= \mathbf{a}, \text{ and } \mathbf{a} + (-\mathbf{a}) = \mathbf{0}, \text{ with } \mathbf{0} \text{ the zero vector} \\ \alpha(\beta\mathbf{a}) &= (\alpha\beta)\mathbf{a} \end{aligned} \quad 2-3$$

$$\alpha(\mathbf{a} + \mathbf{b}) = \alpha\mathbf{a} + \alpha\mathbf{b}, \text{ and } \mathbf{a}(\alpha + \beta) = \alpha\mathbf{a} + \beta\mathbf{a}$$

$$\mathbf{a} \cdot \mathbf{b} = \mathbf{b} \cdot \mathbf{a}$$

$$(\mathbf{a} \cdot \mathbf{b}) \cdot \mathbf{c} = \mathbf{a} \cdot (\mathbf{b} \cdot \mathbf{c})$$

$$\alpha(\mathbf{a} \cdot \mathbf{b}) = (\alpha\mathbf{a}) \cdot \mathbf{b} = \mathbf{a} \cdot (\alpha\mathbf{b})$$

$$\mathbf{a} \cdot \mathbf{a} \geq 0, \text{ and if } \mathbf{a} \cdot \mathbf{a} = 0 \text{ then } \mathbf{a} = \mathbf{0}$$

This is displayed graphically in Figure 2.1.

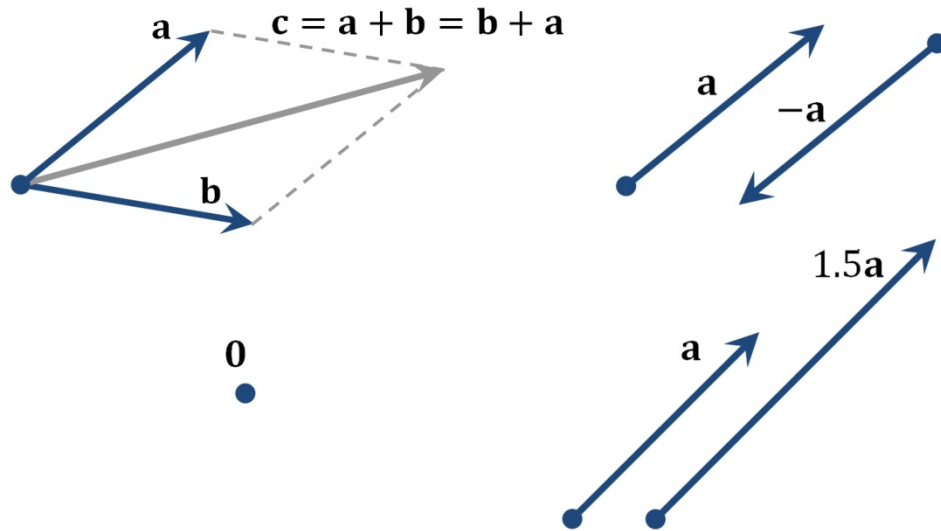


Figure 2.1 Geometric representation of vector addition (top left), the negative vector (top right), the zero vector (bottom left) and scalar vector multiplication

Due to equation 2-2 the projection of a vector  $\mathbf{a}$  along a unit vector  $\mathbf{e}$  is given by:

$$\mathbf{a} \cdot \mathbf{e} = |\mathbf{a}| \cos \theta \tag{2-4}$$

Hence unit vectors allow expression of vector components along the direction of the unit vector and allow formulation of what is known as a right-handed orthonormal Cartesian basis of  $\mathbb{E}^3$ :

$$\mathcal{E} = \{\mathbf{e}_1, \mathbf{e}_2, \mathbf{e}_3\} \tag{2-5}$$

where  $\mathbf{e}_i$  represent three mutually orthogonal unit vectors with the property:

$$\mathbf{e}_i \cdot \mathbf{e}_j = \delta_{ij}, \text{ with } i, j = 1, 2, 3 \tag{2-6}$$

Where  $\delta$  denotes the Kronecker delta

$$\delta_{ij} = \begin{cases} 1 & i = j \\ 0 & i \neq j \end{cases} \tag{2-7}$$

The orthonormal basis  $\mathcal{E}$  allows for the expression of any vector  $\mathbf{a}$  in terms of its three projected components (or coordinates)  $a_i$  (Figure 2.2) and can be uniquely represented by the linear combination:

$$\mathbf{a} = a_1 \mathbf{e}_1 + a_2 \mathbf{e}_2 + a_3 \mathbf{e}_3 = \sum_{i=1}^3 a_i \mathbf{e}_i \quad 2-8$$

which, employing Einstein's summation convention (unless otherwise stated, whenever an index is repeated in the same term a summation across this index is implied) can be written as:

$$\mathbf{a} = a_i \mathbf{e}_i \quad 2-9$$

The scalars  $a_i$  are termed the Cartesian (or rectangular) components of  $\mathbf{a}$ .

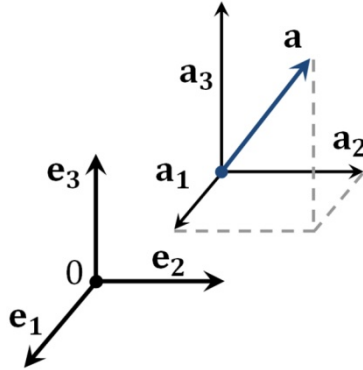


Figure 2.2 The projections of the vector  $\mathbf{a}$  in the orthonormal Cartesian basis  $\mathcal{E}$

This allows for the column or matrix notation of the vector  $\mathbf{a}$  expressed in  $\mathcal{E}$  as:

$$\mathbf{a} = \begin{bmatrix} a_1 \\ a_2 \\ a_3 \end{bmatrix} \quad 2-10$$

The gradient of a vector  $\mathbf{a}$  with respect to  $\mathbf{x}$  is denoted with the symbol  $\nabla$  and is defined:

$$\nabla_{\mathbf{x}} \mathbf{a} = \frac{\partial \mathbf{a}_i}{\partial x_j} \quad 2-11$$

The cross (or vector or outer) product of the vectors  $\mathbf{a}$  and  $\mathbf{b}$  is defined by:

$$\mathbf{a} \times \mathbf{b} = \begin{bmatrix} a_1 \\ a_2 \\ a_3 \end{bmatrix} \times \begin{bmatrix} b_1 \\ b_2 \\ b_3 \end{bmatrix} = \begin{bmatrix} a_2 b_3 - a_3 b_2 \\ a_3 b_1 - a_1 b_3 \\ a_1 b_2 - a_2 b_1 \end{bmatrix} \quad 2-12$$

and produces a new vector  $\mathbf{a} \times \mathbf{b}$  which is orthogonal to both  $\mathbf{a}$  and  $\mathbf{b}$  (Figure 2.3). The magnitude of the cross product, which equals the area of the parallelogram defined by the vectors  $\mathbf{a}$  and  $\mathbf{b}$ , is given by:

$$|\mathbf{a} \times \mathbf{b}| = |\mathbf{a}| |\mathbf{b}| \sin \theta \quad 2-13$$



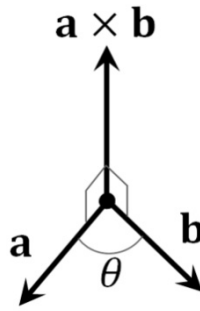


Figure 2.3 The cross product of two vectors produces a new orthogonal vector

The properties of the cross product can be summarised by:

$$\mathbf{a} \times \mathbf{b} = -(\mathbf{b} \times \mathbf{a})$$

$$\mathbf{a} \times \mathbf{b} = \mathbf{0}, \text{ then } \mathbf{a} \text{ and } \mathbf{b} \text{ are linearly dependent (parallel)}$$

$$(\alpha \mathbf{a}) \times \mathbf{b} = \mathbf{a} \times (\alpha \mathbf{b}) = \alpha(\mathbf{a} \times \mathbf{b})$$

$$\mathbf{a} \cdot (\mathbf{b} \times \mathbf{c}) = \mathbf{b} \cdot (\mathbf{c} \times \mathbf{a}) = \mathbf{c} \cdot (\mathbf{a} \times \mathbf{b}), \text{ (known as triple scalar product)} \quad 2-14$$

and equals volume of parallelepiped defined by  $\mathbf{a}$ ,  $\mathbf{b}$  and  $\mathbf{c}$ )

$$\mathbf{a} \times (\mathbf{b} + \mathbf{c}) = (\mathbf{a} \times \mathbf{b}) + (\mathbf{a} \times \mathbf{c}) = \mathbf{a} \times \mathbf{b} + \mathbf{a} \times \mathbf{c}$$

The so-called dyad of a vector pair e.g.  $\mathbf{a}$  and  $\mathbf{b}$  is given by their tensor product denoted by  $\mathbf{a} \otimes \mathbf{b}$  and produces a second-order tensor (vectors are first order tensors). The dyad can be illustrated in Cartesian component notation as:

$$\mathbf{a} \otimes \mathbf{b} = \begin{bmatrix} a_1 \\ a_2 \\ a_3 \end{bmatrix} \begin{bmatrix} b_1 & b_2 & b_3 \end{bmatrix} = \begin{bmatrix} a_1 b_1 & a_1 b_2 & a_1 b_3 \\ a_2 b_1 & a_2 b_2 & a_2 b_3 \\ a_3 b_1 & a_3 b_2 & a_3 b_3 \end{bmatrix} \quad 2-15$$

The tensor product has the following properties:

$$(\mathbf{a} \otimes \mathbf{b})\mathbf{c} = \mathbf{a}(\mathbf{b} \cdot \mathbf{c})$$

$$(\mathbf{a} \otimes \mathbf{b})(\mathbf{c} + \mathbf{d}) = \mathbf{a}(\mathbf{b} \cdot \mathbf{c} + \mathbf{b} \cdot \mathbf{d}) = (\mathbf{a} \otimes \mathbf{b})\mathbf{c} + (\mathbf{a} \otimes \mathbf{b})\mathbf{d}$$

$$(\mathbf{a} \otimes \mathbf{b})(\alpha \mathbf{c}) = \alpha(\mathbf{a} \otimes \mathbf{b})\mathbf{c} = \alpha(\mathbf{b} \cdot \mathbf{c})\mathbf{a} \quad 2-16$$

$$\mathbf{c} \otimes (\mathbf{a} + \mathbf{b}) = \mathbf{c} \otimes \mathbf{a} + \mathbf{c} \otimes \mathbf{b}, \text{ and } (\mathbf{a} + \mathbf{b}) \otimes \mathbf{c} = \mathbf{a} \otimes \mathbf{c} + \mathbf{b} \otimes \mathbf{c}$$

$$(\alpha \mathbf{a}) \otimes (\beta \mathbf{b}) = \alpha \beta (\mathbf{a} \otimes \mathbf{b})$$

Any second-order tensor may be expressed as a linear combination of dyads with respect to the orthonormal basis  $\mathcal{E}$ , e.g. for instance the second-order tensor  $\mathbf{A}$ :

$$\mathbf{A} = A_{ij} \mathbf{e}_i \otimes \mathbf{e}_j = \begin{bmatrix} A_{11} & A_{12} & A_{13} \\ A_{21} & A_{22} & A_{13} \\ A_{31} & A_{32} & A_{33} \end{bmatrix} \quad 2-17$$

Second-order tensors are geometric objects describing linear mappings between scalars, vectors or other tensors. For instance  $\mathbf{A}$  may act as a rotation tensor, rotating the vector

**a** at an angle  $\theta$  around an axis coinciding with  $\mathbf{e}_3$  to the new vector **b** (Figure 2.4). This type of linear mapping may be written as:

$$\mathbf{Aa} = \mathbf{b} \quad 2-18$$

where in this case the tensor **A** would have the form:

$$\mathbf{A} = \begin{bmatrix} \cos \theta & -\sin \theta & 0 \\ \sin \theta & \cos \theta & 0 \\ 0 & 0 & 1 \end{bmatrix} \quad 2-19$$

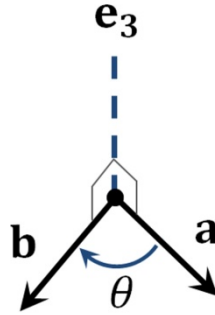


Figure 2.4 Vector rotation following rotation tensor multiplication

The so-called (second-order) identity tensor **I** can be expressed as:

$$\mathbf{I} = \mathbf{e}_i \otimes \mathbf{e}_i = \begin{bmatrix} 1 & 0 & 0 \\ 0 & 1 & 0 \\ 0 & 0 & 1 \end{bmatrix} \quad 2-20$$

The inverse of a tensor **A** is denoted  $\mathbf{A}^{-1}$  and is defined such that:

$$\mathbf{AA}^{-1} = \mathbf{A}^{-1}\mathbf{A} = \mathbf{I} \quad 2-21$$

The determinant of a tensor **A** is denoted:  $\det(\mathbf{A})$  and has the properties:

$$\det(\mathbf{AB}) = \det \mathbf{A} \det \mathbf{B}, \text{ and } \det \mathbf{A}^T = \det \mathbf{A} \quad 2-22$$

Properties of second-order tensors can be summarised as:

$$\mathbf{A} + \mathbf{B} = \mathbf{B} + \mathbf{A}$$

$$\mathbf{A} + (\mathbf{B} + \mathbf{C}) = (\mathbf{A} + \mathbf{B}) + \mathbf{C}$$

$$(-1)\mathbf{A} = -\mathbf{A}, \text{ the negative tensor}$$

$$\mathbf{0a} = \mathbf{o}, \text{ and } \mathbf{A} + (-1)\mathbf{A} = \mathbf{0}, \text{ with } \mathbf{0} \text{ the zero tensor}$$

$$1\mathbf{A} = \mathbf{IA} = \mathbf{0} + \mathbf{A} = \mathbf{A} \quad 2-23$$

$$\mathbf{A}(\mathbf{a} + \mathbf{b}) = \mathbf{Aa} + \mathbf{Ab}$$

$$\mathbf{A}(\alpha\mathbf{a}) = \alpha(\mathbf{Aa}) = (\alpha\mathbf{A})\mathbf{a} = \alpha(\mathbf{Aa})$$

$$(\mathbf{A} + \mathbf{B})\mathbf{a} = \mathbf{Aa} + \mathbf{Ba}$$

$$(\alpha + \beta)\mathbf{A} = \alpha\mathbf{A} + \beta\mathbf{A}$$

Another tensor operator is the double-dot (or double contraction) operator which yields a scalar quantity. For the two tensors **A** and **B** it can be written as:

$$\mathbf{A} : \mathbf{B} = \mathbf{B} : \mathbf{A} = \text{tr}(\mathbf{A}^T \mathbf{B}) = \text{tr}(\mathbf{B}^T \mathbf{A}) = \text{tr}(\mathbf{A} \mathbf{B}^T) = \text{tr}(\mathbf{B} \mathbf{A}^T) \quad 2-24$$

where  $\text{tr}(\mathbf{A})$  and  $\mathbf{A}^T$  (with  $\mathbf{A} = (\mathbf{A}^T)^T$ ) denote the trace and transpose of the tensor  $\mathbf{A}$  respectively. Properties of the double-dot operation include:

$$\begin{aligned} \mathbf{I} : \mathbf{A} &= \text{tr}(\mathbf{A}) \\ \mathbf{A} : (\mathbf{B}\mathbf{C}) &= (\mathbf{B}^T \mathbf{A}) : \mathbf{C} = (\mathbf{A}\mathbf{C}^T) : \mathbf{B} \\ \mathbf{A} : (\mathbf{a} \otimes \mathbf{b}) &= \mathbf{a} \cdot \mathbf{A}\mathbf{b} \end{aligned} \quad 2-25$$

An example use of the double dot operator is the mapping of tensor quantities along a certain direction, for instance the mapping of strain tensor  $\mathbf{E}$  along a texture (e.g. fibre) direction specified by the vector  $\mathbf{a}$  as  $\mathbf{E} : (\mathbf{a} \otimes \mathbf{a})$ . In the special case when the texture vector  $\mathbf{a}$  is aligned with one of the directions of  $\mathcal{E}$  then the double dot operator can be thought of as a “selector” of the tensor element in that direction since  $\mathbf{E} : (\mathbf{a} \otimes \mathbf{a}) = \mathbf{E} : (\mathbf{e}_i \otimes \mathbf{e}_i) = \mathbf{E}_{ii}$ .

Tensors can be subjected to eigenvalue decomposition. For a second-order tensor  $\mathbf{A}$  the eigenvalue problem is formulated as:

$$\mathbf{A}\mathbf{n}_i = \lambda_i \mathbf{n}_i, \text{ with } \mathbf{n}_i \neq \mathbf{0} \text{ and } i = 1, 2, 3 \text{ (no summation)} \quad 2-26$$

Here the scalars  $\lambda_i$  reflect the eigenvalues and  $\mathbf{n}_i$  the normalised eigenvectors of  $\mathbf{A}$ . The eigenvectors  $\mathbf{n}_i$  are mutually orthogonal and thus form an orthonormal basis  $\mathcal{N} = \{\mathbf{n}_1, \mathbf{n}_2, \mathbf{n}_3\}$ . Since  $\mathcal{N}$  forms an orthonormal basis, if a tensor is symmetric the following expression, known as the spectral decomposition can be obtained:

$$\mathbf{A} = \sum_{i=1}^3 \lambda_i \mathbf{n}_i \otimes \mathbf{n}_i \quad 2-27$$

If  $\mathcal{N}$  is assumed as the orthonormal basis then (using equation 2-9)  $\mathbf{A}$  can be reduced to the following diagonal matrix form:

$$\mathbf{A} = \begin{bmatrix} \lambda_1 & 0 & 0 \\ 0 & \lambda_2 & 0 \\ 0 & 0 & \lambda_3 \end{bmatrix} \quad 2-28$$

Since the eigenvalues  $\lambda_i$  describe a physical property of a tensor they are independent of the chosen coordinate system. This allows for the formulation of derived invariants such as the 3 so-called principal scalar invariants, e.g. for the tensor  $\mathbf{A}$ :

$$\begin{aligned} I_1 &= \lambda_1 + \lambda_2 + \lambda_3 = \text{tr}(\mathbf{A}) \\ I_2 &= \lambda_1 \lambda_2 + \lambda_1 \lambda_3 + \lambda_2 \lambda_3 = \frac{1}{2} \left[ (\text{tr}(\mathbf{A}))^2 - \text{tr}(\mathbf{A}^2) \right] = \text{tr}(\mathbf{A})^{-1} \det(\mathbf{A}) \\ I_3 &= \lambda_1 \lambda_2 \lambda_3 = \det(\mathbf{A}) \end{aligned} \quad 2-29$$

Another tensor decomposition is the representation of a tensor  $\mathbf{A}$  into the sum of its so-called spherical and deviatoric part:

$$\mathbf{A} = \frac{1}{3} \text{tr}(\mathbf{A})\mathbf{I} + \text{dev}(\mathbf{A}) \quad 2-30$$

where the deviatoric operator is defined as:

$$\text{dev}(\mathbf{A}) = \mathbf{A} - \frac{1}{3} \text{tr}(\mathbf{A})\mathbf{I} \quad 2-31$$

### 2.2.3 *The continuum hypothesis*

The main assumption underlying continuum mechanics is that the material body analysed is a continuum and is uniformly distributed throughout regions of space. In other words the material is regarded indefinitely divisible; it can be continually subdivided into infinitesimal small elements which still exhibit the same properties as the bulk material. For a uniform material this assumption is valid up to the so-called mesoscopic scale (i.e. a scale where the dimensions of the body analysed are large in comparison to the characteristic lengths (e.g. a grain of sand, inter-atomic space) of the body<sup>54</sup>).

### 2.2.4 *Motion*

Consider a body  $\Omega$  suspended in  $\mathbb{E}^3$  with orthonormal basis  $\mathcal{E} = \{\mathbf{e}_1, \mathbf{e}_2, \mathbf{e}_3\}$  and material point  $P$  at time  $t$  (Figure 2.5).

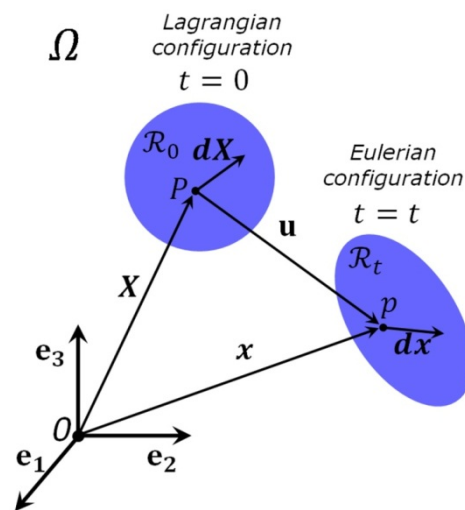


Figure 2.5 A continuum material body in the Lagrangian and Eulerian configuration

The body  $\Omega$  is in motion from its reference (Lagrangian) configuration  $\mathcal{R}_0$  at time  $t=0$  to the new or current (Eulerian) configuration  $\mathcal{R}_t$  at time  $t=t$ . The vectors  $\mathbf{X}$  and  $\mathbf{x}$  are the position vectors of any point  $P$  in  $\Omega$  with respect to the Lagrangian and Eulerian configuration respectively that undergo a displacement  $\mathbf{u}$ . The motion  $\chi$  of point  $P$  is defined by an equation of the form:

$$\mathbf{x} = \chi(\mathbf{X}, t) \quad \mathbf{X} = \chi^{-1}(\mathbf{x}, t) \quad 2-32$$

The displacement vector  $\mathbf{u}$  represents the displacement of the point  $P$  from its original to its final position  $p$  can be defined by:

$$\mathbf{u}(\mathbf{X}, t) = \mathbf{x}(\mathbf{X}, t) - \mathbf{X} \quad \mathbf{u}(\mathbf{x}, t) = \mathbf{x} - \mathbf{X}(\mathbf{x}, t) \quad 2-33$$

## 2.2.5 Deformation

Differentiating of equation 2-32 with respect to the Lagrangian coordinates leads to:

$$\partial \mathbf{x} = \mathbf{F} \partial \mathbf{X} \quad 2-34$$

where  $\mathbf{F}$  represents the deformation gradient tensor as:

$$\mathbf{F} = \frac{\partial \mathbf{x}}{\partial \mathbf{X}} = \nabla_{\mathbf{X}} \mathbf{u} + \mathbf{I} \quad 2-35$$

The deformation gradient tensor transforms any elementary segment  $\partial \mathbf{X}$  of  $\Omega$  in the Lagrangian configuration into a segment  $\partial \mathbf{x}$  in the Eulerian configuration. The inverse of  $\mathbf{F}$  is known as  $\mathbf{D}$  and is defined as:

$$\mathbf{D} = \mathbf{F}^{-1} = \frac{\partial \mathbf{X}}{\partial \mathbf{x}} \quad 2-36$$

and transforms any elementary segment  $\partial \mathbf{x}$  of  $\Omega$  in the Eulerian configuration into a segment  $\partial \mathbf{X}$  in the Lagrangian configuration. Now consider the deformation of a volume element (Figure 2.6).

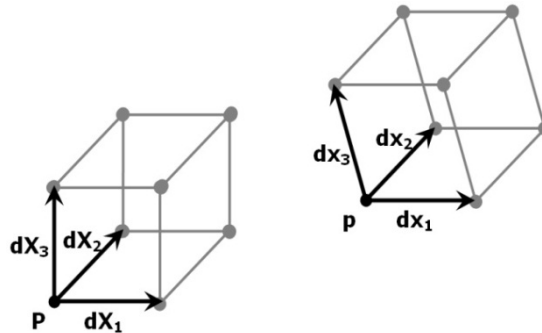


Figure 2.6 A volume element in the Lagrangian (left) and Eulerian (right) configuration

A volume element in the Lagrangian configuration  $dV$  with its sides aligned with the orthogonal basis vectors is defined by:

$$dV = (\partial X_1 \times \partial X_2) \cdot \partial X_3 \quad 2-37$$

and in the Eulerian configuration:

$$dv = (\partial x_1 \times \partial x_2) \cdot \partial x_3 \quad 2-38$$

The Lagrangian and Eulerian configurations are related according to:

$$dv = JdV \quad 2-39$$

The quantity  $J$  is referred to as the Jacobian of the deformation gradient tensor and is defined by:

$$J = \frac{dv}{dV} = \det\left(\frac{\partial \mathbf{x}}{\partial \mathbf{X}}\right) = \det(\mathbf{F}) \quad 2-40$$

In the Lagrangian configuration no deformation has occurred and therefore  $J$  equals 1. However  $J$  will also equal 1 during isochoric deformation (deformation without a change in volume). A material is incompressible if any deformation it undergoes is isochoric.

## 2.2.6 *Stretch and rotation*

In Figure 2.7 let  $\mathbf{a}$  and  $\mathbf{a}'$  be unit vectors along  $d\mathbf{X}$  and  $d\mathbf{x}$  respectively and let  $dS$  be the length of an arc element in the Lagrangian configuration and  $ds$  the length of an arc segment in the Eulerian configuration.

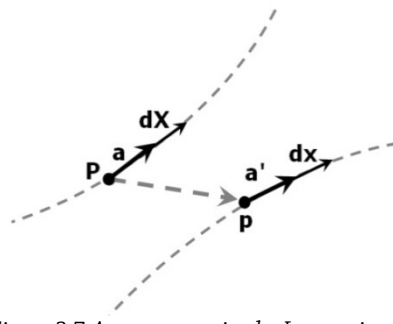


Figure 2.7 Arc segments in the Lagrangian (left) and Eulerian (right) configuration

The following relationships can then be defined:

$$d\mathbf{X} = dS\mathbf{a} \quad 2-41$$

$$d\mathbf{x} = ds\mathbf{a}'$$

Equation 2-34 can then be written as  $ds\mathbf{a}' = \mathbf{F}dS\mathbf{a}$  leading to:

$$\lambda\mathbf{a}' = \mathbf{F}\mathbf{a}, \text{ with } \lambda = \frac{ds}{dS} \quad 2-42$$

Where the  $\lambda$  is known as the stretch ratio, or simply stretch. In the special case where the vector  $\mathbf{a}$  is aligned with  $\mathbf{a}'$  the vector  $\mathbf{a}$  is actually an eigenvector of  $\mathbf{F}$  and  $\lambda$  an eigenvalue. However the vectors  $\mathbf{a}$  and  $\mathbf{a}'$  are generally not aligned and thus the vector  $\mathbf{a}$  is not always the eigenvector. This means that the deformation due to  $\mathbf{F}$  consists of two parts: a stretch

and a change in orientation. These parts can be separately expressed following what is known as polar decomposition:

$$\mathbf{F} = \mathbf{Q}\mathbf{U} = \mathbf{V}\mathbf{Q} \quad 2-43$$

Here  $\mathbf{Q}$  is an orthogonal tensor and  $\mathbf{U}$  and  $\mathbf{V}$  are (positive definite symmetric tensors) related to  $\mathbf{F}$  according to:

$$\begin{aligned} \mathbf{U}^2 &= \mathbf{F}^T\mathbf{F} \\ \mathbf{V}^2 &= \mathbf{F}\mathbf{F}^T \end{aligned} \quad 2-44$$

The tensor  $\mathbf{Q}$  is often referred to as the rotation tensor and  $\mathbf{U}$  and  $\mathbf{V}$  are known as the right and left stretch tensors.

Now equation 2-34 can then be rewritten:

$$d\mathbf{x} = (\mathbf{Q}\mathbf{U})d\mathbf{X} = \mathbf{Q}(\mathbf{U}d\mathbf{X}) \quad 2-45$$

The transformation from the Lagrangian to the Eulerian configuration due to  $\mathbf{F}$  can thus be seen as being composed of two operations: a tri-axial stretch due to the tensor  $\mathbf{U}$  and a rigid body transformation (rotation, translation) due to the tensor  $\mathbf{Q}$ . Since  $\mathbf{U}$  is positive definite and symmetric it has one set of mutually orthogonal eigenvectors and three corresponding eigenvalues. The eigenvectors describe the direction of the eigenvalues, which are often referred to as the principal stretches  $\lambda_1$ ,  $\lambda_2$  and  $\lambda_3$ . A similar analysis can be made using the tensor  $\mathbf{V}$ . However in this case the rigid body transformation due to  $\mathbf{Q}$  precedes the stretch transformations due to  $\mathbf{V}$ . The tensor  $\mathbf{V}$  has the same eigenvalues as  $\mathbf{U}$ . The tensors  $\mathbf{Q}$  (rotates, translates),  $\mathbf{U}$  (stretches) and  $\mathbf{V}$  (stretches) any elementary segment  $d\mathbf{X}$  of  $\Omega$  in the Lagrangian configuration into a segment  $d\mathbf{x}$  in the Eulerian configuration. Recall equation 2-42, squaring both sides gives:

$$\lambda^2 = \mathbf{a} \cdot (\mathbf{F}^T\mathbf{F})\mathbf{a} = \mathbf{a} \cdot \mathbf{U}^2\mathbf{a} = \mathbf{a} \cdot \mathbf{C}\mathbf{a} \quad 2-46$$

The tensor  $\mathbf{U}^2$  is better known as the tensor  $\mathbf{C}$  or the (right) Cauchy-Green tensor and can be used to calculate  $\lambda$  when the vector  $\mathbf{a}$  is known. Similarly the inverse relationship can be obtained for the square of the tensor  $\mathbf{V}^2$ :

$$\frac{1}{\lambda^2} = \mathbf{a}' \cdot (\mathbf{F}\mathbf{F}^T)^{-1}\mathbf{a} = \mathbf{a}' \cdot \mathbf{B}^{-1}\mathbf{a}' \quad 2-47$$

The tensor  $\mathbf{B}$  is often referred to as the Finger tensor and its inverse  $\mathbf{B}^{-1}$  is known as the Cauchy deformation tensor or Eulerian deformation tensor. Because of their relation with the left and right polar decompositions of the deformation gradient tensor  $\mathbf{F}$  the tensors  $\mathbf{B}$  and  $\mathbf{C}$  are also known as the left and right Cauchy-Green tensors respectively. Since the tensors  $\mathbf{U}$  and  $\mathbf{V}$  have the same eigenvalues (the principal stretches) the

eigenvalues of the tensors  $\mathbf{B}$  and  $\mathbf{C}$  are also the same; the square of the principal stretches:  $\lambda_i^2$ . The invariants  $I_i$  of  $\mathbf{B}$  and  $\mathbf{C}$  are defined by:

$$\begin{aligned} I_1 &= \text{tr}(\mathbf{C}) = \lambda_1^2 + \lambda_2^2 + \lambda_3^2 \\ I_2 &= \frac{1}{2}(\text{tr}(\mathbf{C})^2 - \text{tr}(\mathbf{C}^2)) = \text{tr}(\mathbf{C}^{-1}) \det(\mathbf{C}) = \lambda_1^{-2} \lambda_2^2 + \lambda_2^{-2} \lambda_3^2 + \lambda_1^{-2} \lambda_3^2 \quad 2-48 \\ I_3 &= \det(\mathbf{C}) = \det(\mathbf{F}^T \mathbf{F}) = \det(\mathbf{F})^2 = J^2 = \lambda_1^2 \lambda_2^2 \lambda_3^2 \end{aligned}$$

## 2.2.7 Strain

The before mentioned stretch measures and the deformation gradient tensor  $\mathbf{F}$  are fundamental finite deformation measures defining changes of material elements during motion. However it is often convenient to derive a measure of the change in length per unit of initial length. Such a quantity is known as a strain. A large variety of strain measures have been proposed but in general their Lagrangian (left) and Eulerian (right) expressions have the form:

$$\begin{cases} \frac{1}{n}(\mathbf{U}^n - \mathbf{I}) & n \neq 0 \\ \ln(\mathbf{U}) & n = 0 \end{cases} \quad \begin{cases} \frac{1}{n}(\mathbf{V}^n - \mathbf{I}) & n \neq 0 \\ \ln(\mathbf{V}) & n = 0 \end{cases} \quad 2-49$$

This section discusses the three most commonly used strain measures: Linear strain, Green-Lagrange strain and Logarithmic strain.

In classical engineering the linear strain tensor  $\boldsymbol{\varepsilon}$  is common (also referred to as the small, infinitesimal, engineering, Cauchy or Biot strain tensor) and is defined as ( $n = 1$  in equation 2-49):

$$\boldsymbol{\varepsilon} = \mathbf{U} - \mathbf{I} = \frac{1}{2}(\mathbf{F}^T + \mathbf{F}) - \mathbf{I} \quad 2-50$$

For a line segment undergoing a stretch  $\lambda$  the linear strain is thus:  $\varepsilon = \lambda - 1$ .

The Green-Lagrange strain  $\mathbf{E}$  is given by ( $n = 2$  in equation 2-49):

$$\mathbf{E} = \frac{1}{2}(\mathbf{U}^2 - \mathbf{I}) = \frac{1}{2}(\mathbf{C} - \mathbf{I}) = \frac{1}{2}(\mathbf{F}^T \mathbf{F} - \mathbf{I}) \quad 2-51$$

In this case the Green-Lagrange strain in a line segment subjected to a stretch  $\lambda$  is:  $E = \frac{1}{2}(\lambda^2 - 1)$ .

The logarithmic (or Hencky) strain tensor  $\mathbf{H}$  is defined as ( $n = 0$  in equation 2-49):

$$\mathbf{H} = \ln(\mathbf{U}) \quad 2-52$$

For a line segment subjected to a stretch  $\lambda$  the Logarithmic strain is therefore:  $H = \ln(\lambda)$ .



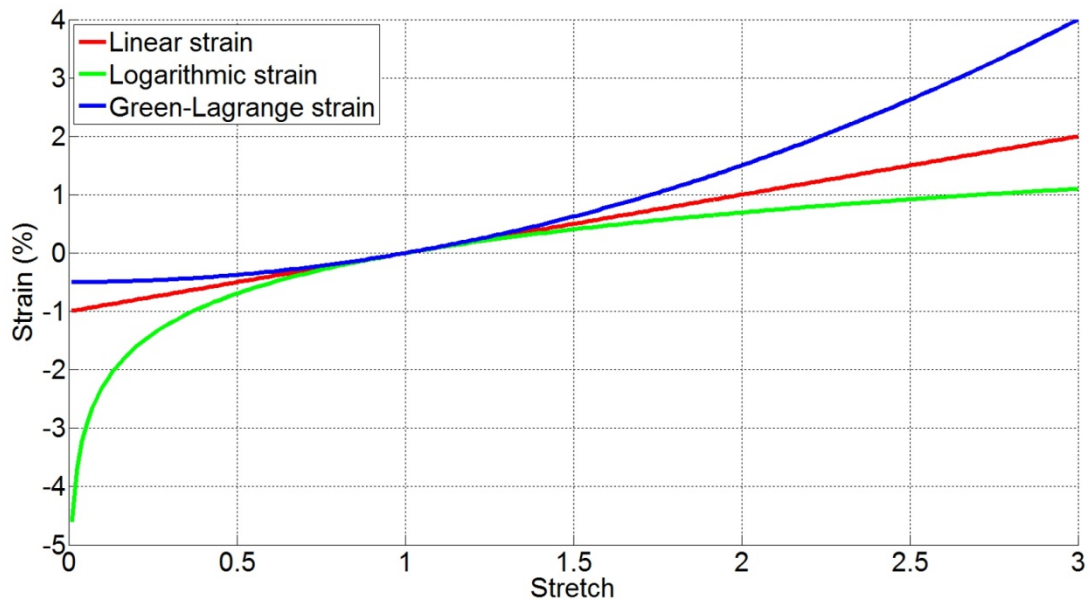


Figure 2.8 Linear, logarithmic and Green-Lagrange strain as a function of stretch

Figure 2.8 shows the three strain measures as a function of (1D) stretch. It is clear that in the small stretch domain the three measures converge. However at larger compressive and tensile stretches the graphs diverge.

As the graph for the linear strain indicates a linear relationship with stretch exists such that for uni-axial loading interpretation of linear strain is intuitive since a stretch of 1.02 simply corresponds to a tensile strain of 2%. However linear strain is only valid for infinitesimal strain levels and is therefore not commonly used for biological soft tissue. However the Green-Lagrange strain and logarithmic strain are suitable for large finite strains and are therefore more commonly used in finite strain and biological soft tissue applications.

### 2.2.8 Stress

In continuum mechanics stresses in a body are due to two types of forces, external and internal forces. External forces act on part or the whole of the boundary surface. When an external force acts on the whole volume of the body (e.g. gravity) it is referred to as a body force. Internal forces act on (imaginary) surfaces within the body. Figure 2.9 shows a surface element  $ds$  belonging to the continuum body  $\Omega$  in the Lagrangian and an Eulerian configuration.

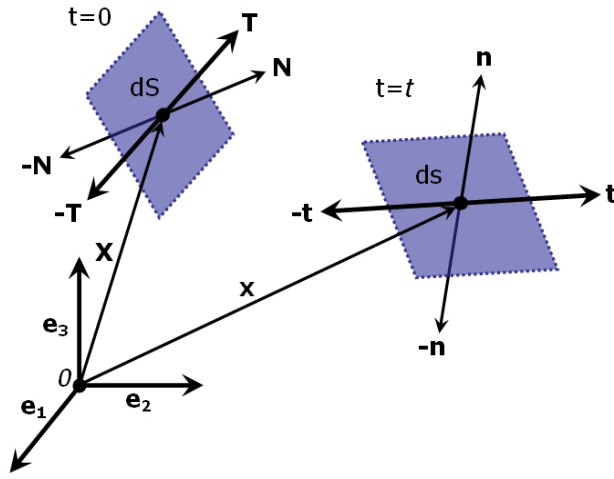


Figure 2.9 A surface element in the Lagrangian (left) and Eulerian (right) configuration

Since stress is force over unit area, the stress due to an infinitesimal force  $df$  acting on a surface element  $ds$  of  $\Omega$  can be defined as:

$$df = \mathbf{t}ds = \mathbf{T}dS \quad 2-53$$

Then due to Newton's law of action and reaction we obtain:

$$\mathbf{t}(\mathbf{x}, t, \mathbf{n}) = -\mathbf{t}(\mathbf{x}, t, -\mathbf{n}) \quad \mathbf{T}(\mathbf{X}, t, \mathbf{N}) = -\mathbf{T}(\mathbf{X}, t, -\mathbf{N}) \quad 2-54$$

Here  $\mathbf{t}$  represents the Cauchy traction vector acting on the surface element  $ds$  with surface normal  $\mathbf{n}$  at location  $\mathbf{x}$ . The Cauchy traction vector is the force per unit area of the current configuration. The traction vector  $\mathbf{T}$  is known as the first Piola-Kirchhoff traction vector and it is the force per unit area of the reference configuration.

According to Cauchy's stress theorem there exist two unique tensors  $\boldsymbol{\sigma}$  and  $\mathbf{P}$  such that:

$$\mathbf{t}(\mathbf{x}, t, \mathbf{n}) = \boldsymbol{\sigma}(\mathbf{x}, t)\mathbf{n} \quad \mathbf{T}(\mathbf{X}, t, \mathbf{N}) = \mathbf{P}(\mathbf{X}, t)\mathbf{N} \quad 2-55$$

The tensor  $\boldsymbol{\sigma}$  is known as the Cauchy (or true) stress tensor and the tensor  $\mathbf{P}$  is referred to as the first Piola-Kirchhoff or Lagrangian stress tensor. The two tensors are related to each other as:

$$\begin{aligned} \boldsymbol{\sigma} &= J^{-1}\mathbf{P}\mathbf{F}^T \\ \mathbf{P} &= J\boldsymbol{\sigma}\mathbf{F}^{-1} \end{aligned} \quad 2-56$$

In matrix notation  $\boldsymbol{\sigma}$  is:

$$\boldsymbol{\sigma} = \begin{bmatrix} \sigma_{11} & \sigma_{21} & \sigma_{31} \\ \sigma_{12} & \sigma_{22} & \sigma_{32} \\ \sigma_{13} & \sigma_{23} & \sigma_{33} \end{bmatrix} \quad 2-57$$

The columns of  $\boldsymbol{\sigma}$  are the components of the traction vectors acting on planes orthogonal to the basis  $\mathcal{E}$ . Figure 2.10 shows a graphical representation of the stress components acting on an infinitesimal cubic material element of  $\Omega$  aligned with  $\mathcal{E}$ . Because the Cauchy

stress tensor is symmetric it has six independent components ( $\sigma_{12} = \sigma_{21}, \sigma_{13} = \sigma_{31}, \sigma_{23} = \sigma_{32}$ ).

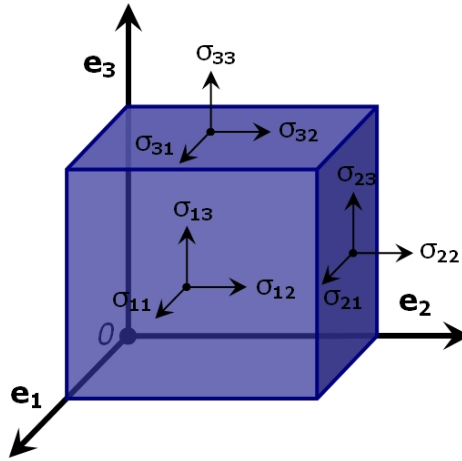


Figure 2.10 Schematic representation of stress tensor components acting on a material element

The Piola-Kirchhoff stress tensor is asymmetric and often symmetric stress formulations are preferred. However the Piola-Kirchhoff stress tensor can be decomposed as:

$$\mathbf{P} = \mathbf{F}\mathbf{S} \quad 2-58$$

Here the tensor  $\mathbf{S}$  is symmetric and is known as the second Piola-Kirchhoff stress tensor and can be related to  $\boldsymbol{\sigma}$  and  $\mathbf{P}$  via:

$$\begin{aligned} \mathbf{S} &= J\mathbf{F}^{-1}\boldsymbol{\sigma}\mathbf{F}^{-T} = \mathbf{F}^{-1}\mathbf{P} = \mathbf{S}^T \\ \boldsymbol{\sigma} &= J^{-1}\mathbf{F}\mathbf{S}\mathbf{F}^T \end{aligned} \quad 2-59$$

It is often convenient to work with the so-called Kirchoff stress tensor  $\boldsymbol{\tau}$  which differs from the Cauchy stress tensor by the Jacobian  $J$ :

$$\boldsymbol{\tau} = J\boldsymbol{\sigma} \quad 2-60$$

## 2.2.9 Strain energy

In a (thermodynamic) continuum the first law of thermodynamics states there must be a balance of both thermal and mechanical energy. Under isothermal conditions however (or when thermal effects are ignored) this reduces to balance of mechanical energy:

$$\mathcal{P}_{ext}(t) = \frac{d\mathcal{K}(t)}{dt} + \frac{d\Pi_{int}(t)}{dt} \quad 2-61$$

which states that the external mechanical power  $\mathcal{P}_{ext}$  equals the rate of change of the kinetic energy  $\mathcal{K}$  of the mechanical system plus the rate of change of the internal mechanical work  $\Pi_{int}$ . The internal mechanical work  $\Pi_{int}$  is due to internal stresses and can be written as:

$$\Pi_{int}(t) = \int_{\Omega} \Psi dV = \int_{\Omega} \Psi J^{-1} dv \quad 2-62$$

The symbol  $\Psi$  denotes a scalar function known as the Helmholtz free-energy function which, under the isothermal conditions mentioned, coincides with the internal strain energy and can therefore be considered solely a function of a deformation or strain tensor. For an isotropic material we may thus express the Helmholtz free-energy function purely in terms of deformation measures such the tensors  $\mathbf{F}$ ,  $\mathbf{C}$ , the invariants  $I_i$  or the principal stretches  $\lambda_i$ :

$$\Psi(\mathbf{F}) = \Psi(\mathbf{C}) = \Psi(I_1, I_2, I_3) = \Psi(\lambda_1, \lambda_2, \lambda_3) \quad 2-63$$

Because of this the Helmholtz free-energy function is often referred to as the strain-energy density function. Strain-energy density functions are important for the formulation of constitutive laws since derivatives of it with respect to deformation measures yield stress measures. For homogeneous hyperelastic materials for instance the following relations can be made between  $\Psi$  and selected stress tensors:

$$\begin{aligned} \mathbf{P} &= \frac{\partial \Psi(\mathbf{F})}{\partial \mathbf{F}} = 2\mathbf{F} \frac{\partial \Psi(\mathbf{C})}{\partial \mathbf{C}} \\ \mathbf{S} &= \mathbf{F}^{-1} \frac{\partial \Psi(\mathbf{F})}{\partial \mathbf{F}} = 2 \frac{\partial \Psi(\mathbf{C})}{\partial \mathbf{C}} = \frac{\partial \Psi(\mathbf{E})}{\partial \mathbf{E}} \\ \boldsymbol{\sigma} &= J^{-1} \mathbf{F} \left( \frac{\partial \Psi(\mathbf{F})}{\partial \mathbf{F}} \right)^T = 2J^{-1} \mathbf{F} \frac{\partial \Psi(\mathbf{C})}{\partial \mathbf{C}} \mathbf{F}^T \\ \boldsymbol{\tau} &= 2\mathbf{F} \frac{\partial \Psi(\mathbf{C})}{\partial \mathbf{C}} \mathbf{F}^T = 2\mathbf{B} \frac{\partial \Psi(\mathbf{B})}{\partial \mathbf{B}} = \frac{\partial \Psi(\boldsymbol{\varepsilon})}{\partial \boldsymbol{\varepsilon}} \end{aligned} \quad 2-64$$

## 2.2.10 Constitutive equations

### 2.2.10.1 Introduction

The continuum mechanics relations presented in the previous sections are not material specific and hold for any continuum. They do not describe a specific material response to loading conditions. In order to do that, constitutive equations need to be developed. Constitutive equations aim to relate parameters such as strain, strain-rate etc. to the state of stress at any point in a continuum body at any time. The current thesis and therefore this section focusses on solid mechanics and therefore only common constitutive theories for solid materials will be discussed. Figure 2.11 shows a typical stress strain curve for an engineering material such as steel. The deformation due to stress can be split up into elastic (recoverable) deformation and plastic (un-recoverable)

deformation. The term elasticity refers to a materials ability to recover from deformation once the stresses are removed and the term plasticity refers to a materials ability to undergo irreversible deformations. The current thesis focusses on elastic soft tissue behaviour and as such plasticity is not discussed here. Instead this section discusses the following constitutive theories: linear elasticity, non-linear elasticity and viscoelasticity.

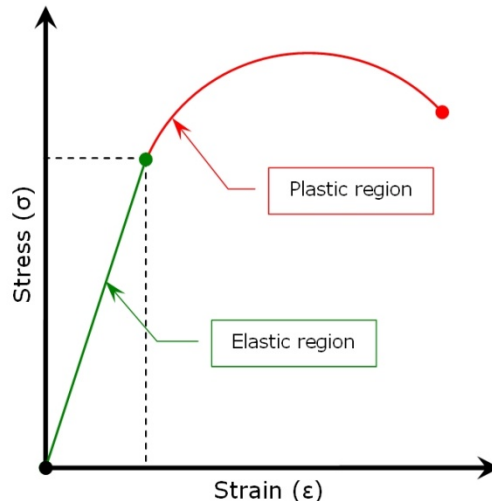


Figure 2.11 A typical stress strain curve for a linear elastic material

### 2.2.10.2 Linear elasticity

An elastic solid that undergoes an infinitesimal deformation and for which the governing material law is linear is called a linear elastic solid<sup>55</sup>. Figure 2.11 shows the shape of a typical stress strain curve for a uni-axial tensile test on such a linear elastic solid material. The theory of linear elasticity states that the stress at any time is directly proportional to the strain and is independent of strain history. Therefore for a certain deformed configuration there exists a single unique stress state. The stress ( $\sigma$ ) strain ( $\epsilon$ ) relationship in Figure 2.11 can be described by an equation of the form  $\sigma = E\epsilon$ . This constitutive equation is a special case of a material law known as Hooke's law. The constant  $E$  is known as the Young's Modulus and defines the slope of the curve and is effectively the stiffness of the material. The generalised form of Hooke's law for a homogeneous and isotropic linear elastic material relates the Cauchy stress  $\sigma$  to the linear strain tensor  $\epsilon$  as:

$$\sigma = \lambda \text{tr}(\epsilon) + 2\mu \epsilon$$

$$\epsilon = \frac{1}{2\mu} \left( \sigma - \frac{\lambda}{3\lambda + 2\mu} \text{tr}(\sigma) \mathbf{I} \right) \quad 2-65$$

These relationships introduce two elastic moduli  $\mu$  and  $\lambda$  referred to as the Lamé parameters. Alternatively this relationship can be written in matrix form:

$$\begin{bmatrix} \sigma_{11} \\ \sigma_{22} \\ \sigma_{33} \\ \sigma_{23} \\ \sigma_{31} \\ \sigma_{12} \end{bmatrix} = \begin{bmatrix} 2\mu + \lambda & \lambda & \lambda & 0 & 0 & 0 \\ \lambda & 2\mu + \lambda & \lambda & 0 & 0 & 0 \\ \lambda & \lambda & 2\mu + \lambda & 0 & 0 & 0 \\ 0 & 0 & 0 & \mu & 0 & 0 \\ 0 & 0 & 0 & 0 & \mu & 0 \\ 0 & 0 & 0 & 0 & 0 & \mu \end{bmatrix} \begin{bmatrix} \varepsilon_{11} \\ \varepsilon_{22} \\ \varepsilon_{33} \\ 2\varepsilon_{23} \\ 2\varepsilon_{31} \\ 2\varepsilon_{12} \end{bmatrix}$$

2-66

$$\begin{bmatrix} \varepsilon_{11} \\ \varepsilon_{22} \\ \varepsilon_{33} \\ 2\varepsilon_{23} \\ 2\varepsilon_{31} \\ 2\varepsilon_{12} \end{bmatrix} = \frac{1}{E} \begin{bmatrix} 1 & -\nu & -\nu & 0 & 0 & 0 \\ -\nu & 1 & -\nu & 0 & 0 & 0 \\ -\nu & -\nu & 1 & 0 & 0 & 0 \\ 0 & 0 & 0 & 2(1+\nu) & 0 & 0 \\ 0 & 0 & 0 & 0 & 2(1+\nu) & 0 \\ 0 & 0 & 0 & 0 & 0 & 2(1+\nu) \end{bmatrix} \begin{bmatrix} \sigma_{11} \\ \sigma_{22} \\ \sigma_{33} \\ \sigma_{23} \\ \sigma_{31} \\ \sigma_{12} \end{bmatrix}$$

where  $E$  and  $\nu$  represent the Young's modulus and Poisson's ratio respectively which can be related to the Lamé parameters using:

$$E = \frac{\mu(3\lambda + 2\mu)}{\lambda + \mu}$$

$$\nu = \frac{\lambda}{2(\lambda + \mu)}$$

$$\lambda = \frac{2\mu\nu}{1 - 2\nu} = \frac{E\nu}{(1 + \nu)(1 - 2\nu)}$$

2-67

$$\mu = \frac{\lambda(1 - 2\nu)}{2\nu} = \frac{E}{2(1 + \nu)}$$

$$\kappa = \lambda + \frac{2}{3}\mu = \frac{\mu E}{3(3\mu - E)} = \frac{2\mu(\nu + 1)}{3(1 - 2\nu)}$$

where  $\kappa$  represents the bulk modulus. The parameter  $\mu$  is also known as the shear modulus.

Many engineering materials can be successfully modelled using linear elasticity especially at infinitesimal strains. However for materials like polymers, rubbers and biological soft tissues which are non-linear and capable of undergoing large deformations the infinitesimal analysis and linearity assumptions are not valid.

### 2.2.10.3 Non-linear elasticity

In order to capture non-linear elasticity it is often convenient to work with the strain-energy density function  $\Psi$  for the derivation of stress formulations. Constitutive laws based on a strain-energy density function are referred to as Green elastic or hyperelastic laws. Various forms of  $\Psi$  have been proposed in the literature some are based on physical laws and some on experimental observations. A brief selection of common constitutive laws is presented here.

A general formulation is the so-called polynomial hyperelastic<sup>60</sup> given by the strain-energy density function:

$$\Psi(I_1, I_2) = \sum_{i,j=0}^N c_{ij} (I_1 - 3)^i (I_2 - 3)^j \quad 2-68$$

Here  $I_i$  are the strain invariants (equation 2-48) and  $c_{ij}$  are material constants (with  $c_{00} = 0$ ). Various strain energy formulations can be obtained by using different combinations of these constants. For instance for  $N = 1$  and  $c_{11} = 0$  the formulation reduces to the so called Mooney-Rivlin hyperelastic:

$$\Psi(I_1, I_2) = c_{01}(I_1 - 3) + c_{10}(I_2 - 3) \quad 2-69$$

If in addition  $c_{10} = 0$  the model reduces to the Neo-Hookean hyperelastic:

$$\Psi(I_1) = c_{01}(I_1 - 3) \quad 2-70$$

Another commonly used model is the Ogden hyperelastic model (see also <sup>56, 57, 61, 62</sup>). Its strain energy function for incompressible materials is defined by:

$$\Psi(\lambda_1, \lambda_2, \lambda_3) = \sum_{i=1}^N \frac{\mu_i}{\alpha_i} (\lambda_1^{\alpha_i} + \lambda_2^{\alpha_i} + \lambda_3^{\alpha_i} - 3) \quad 2-71$$

Here  $N$  is an integer ( $> 0$ ) dictating the model order and in practise often  $N < 4$  since  $N = 3$  is generally sufficient to achieve appropriate correlation<sup>56, 57, 61</sup>. The constants  $\mu_i$  are the shear moduli and  $\alpha_i$  are dimensionless constants. Again various strain energy formulations can be obtained by using different combinations of constants. When the following combination of constants is used:  $N = 2$ ,  $\alpha_1 = 2$ ,  $\alpha_2 = -2$ , the Ogden model reduces to the Mooney-Rivlin model (equivalent to equation 2-69):

$$\Psi(\lambda_1, \lambda_2, \lambda_3) = \frac{\mu_1}{2} (\lambda_1^2 + \lambda_2^2 + \lambda_3^2 - 3) - \frac{\mu_2}{2} (\lambda_1^{-2} + \lambda_2^{-2} + \lambda_3^{-2} - 3) \quad 2-72$$

When instead  $N = 1$  and  $\alpha_1 = 2$  then the Ogden model reduces to a Neo-Hookean model (equivalent to equation 2-70):

$$\Psi(\lambda_1, \lambda_2, \lambda_3) = \frac{\mu}{2} (\lambda_1^2 + \lambda_2^2 + \lambda_3^2 - 3) \quad 2-73$$

The above models are for incompressible materials ( $J = 1$ ). For compressible hyperelastic materials we can decompose the deformation gradient tensor  $\mathbf{F}$  and Cauchy strain tensor  $\mathbf{C}$  into a volumetric (volume changing, dilation) part, and an isochoric (volume preserving, distortional, deviatoric) part<sup>56</sup>:

$$\mathbf{F} = J^{\frac{1}{3}} \tilde{\mathbf{F}} \quad 2-74$$

$$\mathbf{C} = J^{\frac{2}{3}} \tilde{\mathbf{C}}$$

Here  $J^{1/3}$  and  $J^{2/3}$  are associated with volumetric deformation and the so called modified deformation gradient tensor  $\tilde{\mathbf{F}}$  and the modified strain tensor  $\tilde{\mathbf{C}}$  are associated with the isochoric deformation (thus  $\det(\tilde{\mathbf{F}}) = \det(\tilde{\mathbf{C}}) = 1$ ). Modified strain invariants and principal stretches may now be defined as:

$$\begin{aligned} \tilde{I}_1 &= J^{-\frac{2}{3}} I_1 \\ \tilde{I}_2 &= J^{-\frac{4}{3}} I_2 \\ \tilde{I}_3 &= 1 \\ \tilde{\lambda}_i &= J^{-\frac{1}{3}} \lambda_i \end{aligned} \tag{2-75}$$

The strain-energy functions can also be rewritten as the sum of an isochoric part  $\Psi_{\text{iso}}(\tilde{\mathbf{C}})$  and a volumetric part  $\Psi_{\text{vol}}(J)$  which is a function of the Jacobian:

$$\begin{aligned} \Psi(\tilde{\mathbf{C}}, J) &= \Psi_{\text{iso}}(\tilde{\mathbf{C}}) + \Psi_{\text{vol}}(J) \\ \Psi(\lambda_1, \lambda_2, \lambda_3) &= \Psi(\tilde{\lambda}_1, \tilde{\lambda}_2, \tilde{\lambda}_3, J) = \Psi_{\text{iso}}(\tilde{\lambda}_1, \tilde{\lambda}_2, \tilde{\lambda}_3) + \Psi_{\text{vol}}(J) \end{aligned} \tag{2-76}$$

Various forms of  $\Psi_{\text{vol}}(J)$  have been proposed including the following, which is common in finite element implementations, such as FEBio (FEBio, Musculoskeletal Research Laboratories, The University of Utah, USA):

$$\Psi_{\text{vol}}(J) = \frac{1}{2} \kappa (\ln(J))^2 \tag{2-77}$$

where  $\kappa$  is the bulk modulus. Compressible hyperelastic formulations of the before mentioned constitutive laws may thus be obtained by replacing the role of  $\lambda_i$  with  $\tilde{\lambda}_i$  and by adding  $\Psi_{\text{vol}}(J)$ .

### 2.2.11 *Modelling anisotropy*

So far the constitutive models discussed are for isotropic materials which exhibit equivalent mechanical properties in all directions. However many biological tissues present with anisotropy. This section summarises approaches to model anisotropy with focus on hyperelastic formulations commonly implemented in finite element software.

For isotropic materials the strain energy function can be represented in terms of the Right Cauchy-Green tensor  $\Psi(\mathbf{C})$ . However for anisotropic materials the strain energy takes the form  $\Psi(\mathbf{C}, \mathbf{A}_i)$  such that it is also a function of a so called texture or structure tensor (see Ehret et al. 2007<sup>63</sup> and Itskov 2009<sup>53</sup>):



$$\mathbf{A}_i = \mathbf{a}_i \otimes \mathbf{a}_i, \text{ and } i = 1, 2, \dots, n \quad 2-78$$

where  $\mathbf{a}_i$  represent unit vectors describing material texture (e.g. fibre) directions in the reference configuration. The simplest form of anisotropy is transverse isotropy. A material is transversely isotropic if one of the material directions, specified by the vector  $\mathbf{a}$ , presents with altered mechanical properties and if the material behaviour is axisymmetric around this altered direction. The alteration of the mechanical properties (generally a fibre reinforcement) can be modelled by also letting the strain-energy function depend on a unit vector field  $\mathbf{a}(\mathbf{X})$ , representing texture directions in the initial configuration. In this case the material behaviour may be fully characterised by:

$$\Psi(I_1(\mathbf{C}), I_2(\mathbf{C}), I_3(\mathbf{C}), I_4(\mathbf{C}, \mathbf{a}), I_5(\mathbf{C}, \mathbf{a})) \quad 2-79$$

where the invariants  $I_1, I_2, I_3$  are obtained as in equation 2-48 and the additional, so-called pseudo-invariants,  $I_4$  and  $I_5$  are defined as:

$$\begin{aligned} I_4 &= \mathbf{a} \cdot \mathbf{C} \mathbf{a} \\ I_5 &= \mathbf{a} \cdot \mathbf{C}^2 \mathbf{a} \end{aligned} \quad 2-80$$

The altered direction is often termed the fibre direction. The stretch along the fibre direction  $\lambda_f$  can be resolved via (analogous to equation 2-46):

$$\lambda_f = \sqrt{\mathbf{a} \cdot \mathbf{C} \mathbf{a}} = \sqrt{I_4} \quad 2-81$$

Similar to the relations 2-64 stress formulations can be derived using derivatives with respect to deformation measures. In this case summation across derivatives with respect to the invariants  $I_i$  is convenient, for instance the second Piola-Kirchhoff stress tensor can be derived using:

$$\mathbf{S} = 2 \sum_{i=1}^5 \frac{\partial \Psi}{\partial I_i} \frac{\partial I_i}{\partial \mathbf{C}} \quad 2-82$$

In addition transverse isotropic fibre reinforcement may be modelled by assuming that the material response, and thus the strain energy function, can be represented by the sum of an isotropic ground matrix response  $\Psi_{gm}(I_1(\mathbf{C}), I_2(\mathbf{C}), I_3(\mathbf{C}))$  (e.g. a Mooney-Rivlin model) and a fibre reinforcement response  $\Psi_f(I_4(\mathbf{C}, \mathbf{a}), I_5(\mathbf{C}, \mathbf{a}))$ . Such modelling approaches take the form:

$$\Psi_{total} = \Psi_{gm} + \Psi_f \quad 2-83$$

Any suitable formulation of  $\Psi_{gm}$  and  $\Psi_f$  may be combined whereby the former may be decomposed into an isochoric and deviatoric contribution (as in relations 2-76) to allow for compressibility. In addition multiple fibre families may be superimposed in  $\Psi_f$  to

achieve other types of anisotropy. A collection of multiple texture directions  $\mathbf{a}_i$  with  $i = 1, 2, \dots, n$  may then be formulated (e.g. ellipsoidal fibre distribution models<sup>64</sup>). For instance Ateshian *et al.*<sup>65</sup> formulated the tension compression non-linear orthotropic model to model cartilage tissue employing three mutually orthogonal fibre families. The ground matrix response  $\Psi_{gm}$  was represented by a compressible Mooney-Rivlin model while the orthotropic fibre response  $\Psi_f$  was modelled using the sum of the three fibre directions:

$$\Psi_f = \sum_{i=1}^3 \Psi_{f_i}(\tilde{\lambda}_i) \quad 2-84$$

with the individual fibre responses defined by:

$$\Psi_{f_i}(\tilde{\lambda}_i) = \begin{cases} \xi_i(\tilde{\lambda}_i - 1)^{\beta_i} & \tilde{\lambda}_i > 1 \\ 0 & \tilde{\lambda}_i \leq 1 \end{cases}, \text{ with } \xi_i \geq 0 \text{ and } \beta_i \geq 2 \quad 2-85$$

As equation 2-85 shows for this formulation the fibre families only act in tension when  $\tilde{\lambda}_i > 1$ . This allows modelling of slacking of fibres in compression and induces a basic form of tension compression non-linearity. Other types of fibre functions and conditions may be proposed here. For instance Blemker *et al.*<sup>23</sup> modelled muscle tissue and only let fibres contribute after a threshold stretch has been exceeded to model fibres that are initially slacked. In addition these authors defined both passive and active fibre contributions.

In many cases anisotropic constitutive models are formulated using  $\Psi(I_1, I_2, I_3, I_4, I_5)$ . However as was remarked by Criscione *et al.* 2001<sup>66</sup> experimental validation of models formulated with these invariants may be difficult since even a simple isochoric uni-axial fibre stretch tests perturbs  $I_1, I_2, I_4$  and  $I_5$  and pure dilatation perturbs all of them. Hence the experimental determination of individual contributions is challenging. Therefore Criscione *et al.* 2001<sup>66</sup> proposed an alternative set of invariants which have physical meaning and can be independently evaluated experimentally. These invariants  $\beta_1, \beta_2, \beta_3, \beta_4, \beta_5$  such that  $\Psi(I_1, I_2, I_3, I_4, I_5) = \Psi(\beta_1, \beta_2, \beta_3, \beta_4, \beta_5)$  take the following form in relation to the traditional invariants:

$$\begin{aligned} \beta_1 &= \frac{1}{2} \ln(I_3) \\ \beta_2 &= \frac{1}{4} (3 \ln(I_4) - \ln(I_3)) \end{aligned} \quad 2-86$$

$$\beta_3 = \ln \left( \left( \frac{I_1 I_4 - I_5}{2\sqrt{I_3 I_4}} \right) + \sqrt{\left( \frac{I_1 I_4 - I_5}{2\sqrt{I_3 I_4}} \right)^2 - 1} \right) = \cosh^{-1} \left( \frac{I_1 I_4 - I_5}{2\sqrt{I_3 I_4}} \right)$$

$$\beta_4 = \sqrt{\frac{I_5}{I_4^2} - 1}$$

$$\beta_5 = \frac{I_1 I_4 I_5 + I_1 I_4^3 + 2I_3 I_4 - I_5^2 - 2I_2 I_4^2 - I_5 I_4^2}{(I_5 - I_4^2) \sqrt{I_1^2 I_4^2 + I_5^2 - 2I_1 I_4 I_5 - 4I_3 I_4}}$$

These 5 invariants respectively relate to: 1) volumetric strain, 2) distortional fibre strain, 3) cross-fibre shear, 4) along-fibre shear and 5) the orientation of the along fibre shear plane relative to the cross-fibre shear diagonals.

### 2.2.12 Viscoelasticity

Elastic materials show a (non-)linear relationship between stress and strain, deform instantaneously due to stress and recover instantaneously once stress is removed. Viscous materials however (e.g. fluids) show a different behaviour. They demonstrate a strain rate dependency in part of the stress. Some materials demonstrate both elastic and viscous properties and are called viscoelastic<sup>58</sup>. In viscoelastic materials the stress depends not only on the current deformation but also on the history of the deformation, specifically its rate. A large variety of materials have viscoelastic properties, for instance various engineering materials (e.g. polymers) and biological materials<sup>67</sup>. When a viscoelastic material is suddenly strained and the strain is maintained constant afterwards, the corresponding stresses induced in the material decrease with time. This process is referred to as stress relaxation<sup>67</sup>. If the material is suddenly stressed, and then the stress is maintained constant afterward, a viscoelastic material continuous to deform. This phenomenon is called creep<sup>67</sup>. If a viscoelastic material is subjected to cyclic loading, the stress-strain relationship in the loading process is usually somewhat different from that in the unloading process, which is referred to as hysteresis<sup>67</sup>. Stress relaxation, creep and hysteresis are features of viscoelastic materials. This section briefly discusses common linear and non-linear viscoelasticity modelling approaches. For a more detailed discussion the reader is referred to<sup>59, 67</sup>.

### 2.2.12.1 Linear viscoelasticity

In order to simulate material properties it is often useful to use mechanical models such as springs and dashpots. The ideal spring (Figure 2.12a) can be used to represent the linear elastic solid.

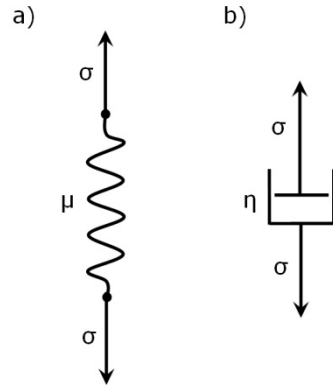


Figure 2.12 A spring (A) and dashpot model (B)

The stress in an ideal spring is elastic and can be expressed (in 3D) by the formula (equivalent to 2-65):

$$\boldsymbol{\sigma}_e = \lambda_S (\text{tr}(\boldsymbol{\epsilon})) \mathbf{I} + 2\mu \boldsymbol{\epsilon} \quad 2-87$$

Just like a linear elastic material an ideal spring allows instant deformation and the stress is dependent only on the strain and the spring (material) constants  $\lambda_S$  and  $\mu$ . Similarly for a viscous material a mechanism that simulates the velocity dependent response can be used, the dashpot (Figure 2.12b). The stress equivalent to an ideal dashpot can be expressed by:

$$\boldsymbol{\sigma}_v = \lambda_D \left( \text{tr} \left( \frac{\partial \boldsymbol{\epsilon}}{\partial t} \right) \right) \mathbf{I} + 2\eta \frac{\partial \boldsymbol{\epsilon}}{\partial t} \quad 2-88$$

For dashpots instant deformation is not allowed as the stress is dependent on the strain-rate  $\frac{\partial \boldsymbol{\epsilon}}{\partial t}$  and the material constants  $\lambda_D$  and  $\eta$  (dashpot viscosity).

As mentioned before viscoelastic materials have both elastic and viscous properties. This behaviour can be modelled by combining springs and dash-pots. For the so called Voigt model (Figure 2.13a) the equation for the total stress is simply the sum of the elastic stress  $\boldsymbol{\sigma}_e$  due to the spring and the viscous stress  $\boldsymbol{\sigma}_v$  due to the dashpot. However unlike most solid materials the Voigt model does not allow instantaneous elasticity due to the parallel dashpot. To allow instantaneous elasticity a spring can be added such as in the Kelvin model or standard linear solid model (Figure 2.13b).

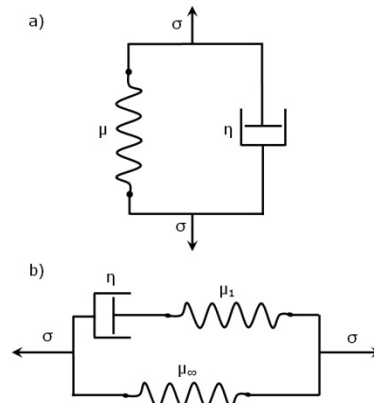


Figure 2.13 A Voigt (A) and Kelvin model (B)

However the internal strain components are unknown and the strain history may be complex. Therefore it is convenient to use the Boltzmann superposition principle which states that the total effect of applying several deformations is the sum of the effects of applying each one separately (see schematic representation in Figure 2.14). At time  $\tau$  an infinitesimal strain increment  $d\epsilon$  then results in an infinitesimal stress increment  $d\sigma$  at subsequent times  $t$ . The magnitude of this stress increment depends on the lapse of time since the strain increment was applied <sup>54</sup> and takes the form  $d\sigma(t) = G(t - \tau)d\epsilon(\tau)$ .

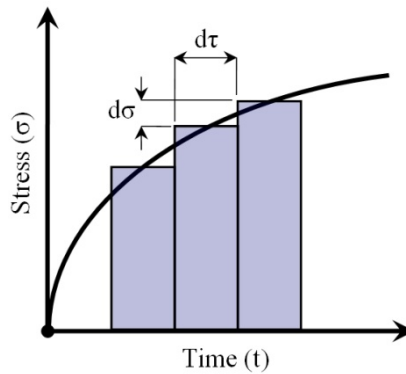


Figure 2.14 Schematic representation of the Boltzmann superposition principle for viscoelasticity

Using Boltzmann's superposition principle this leads to the following convolution integral for the total stress for the Kelvin model:

$$\sigma(t) = \int_{-\infty}^t G(t - \tau) \frac{d\epsilon}{d\tau} d\tau \quad 2-89$$

Here  $G$  is the relaxation function defined by:

$$G(t) = \mu_{\infty} + \mu_1 e^{-\frac{t}{\tau_{\epsilon}}} \quad 2-90$$

$$\tau_{\epsilon} = \frac{\eta_1}{\mu_1}$$

However the Kelvin model is rather limited due to the fact that only 1 dashpot and 2 springs are modelled. Hence it does not allow modelling of a continuous spectrum of

relaxation. A more advanced general model of a linear viscoelastic material can be developed from an assembly of multiple springs and dampers<sup>59</sup> for instance by repeating the parallel spring and dashpot array  $n$  times (Figure 2.15).

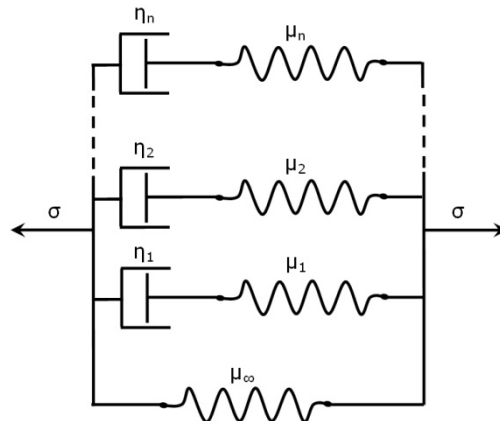


Figure 2.15 Generalised model

When  $n = \infty$  a continuous spectrum of relaxation can be achieved. The stress takes the same form however this time the relaxation function becomes:

$$G(t) = \mu_{\infty} + \sum_{i=1}^n \mu_i e^{-\frac{t}{\tau_{\varepsilon_i}}} \quad 2-91$$

$$\tau_{\varepsilon_i} = \frac{\eta_i}{\mu_i}$$

As is clear from these equations the relaxation function is composed of a series of negatively decaying exponentials. These series are known as Prony (or Dirichlet) series. The coefficients of the Prony series depend on the spring and dashpot constants which can be determined experimentally.

### 2.2.12.2 Non-linear viscoelasticity

Linear viscoelasticity discussed in the previous section has the same limitations as linear elasticity and is also an approximate theory only applicable to situations with infinitesimal strain and rotations<sup>54, 58</sup>. Many (non-Newtonian) fluids and solids are viscoelastic in that the stress depends on the deformation history, but this dependence is more complicated than a direct superposition of the form described in equation 2-89<sup>54</sup> especially at finite deformation and rotation. For finite deformation of such materials the non-linear stress-strain characteristics must be accounted for<sup>67</sup>. There are many different non-linear viscoelastic constitutive laws in the literature (see review<sup>68</sup>) however here we will focus on the discretised quasi-linear theory of viscoelasticity by introduced

Fung 1972<sup>67, 69</sup> since this is widely implemented in FEA software. For discretised quasi-linear viscoelasticity<sup>70</sup> the second Piola-Kirchhoff stress can be written in the following form:

$$\mathbf{S}(\mathbf{E}, t) = \int_{-\infty}^t G(t - \tau) \frac{\partial \mathbf{S}_e(\mathbf{E}, \tau)}{\partial \tau} \partial \tau \quad 2-92$$

with  $\mathbf{S}_e$  the pure elastic stress derivable from  $\frac{\partial \Psi(\mathbf{E})}{\partial \mathbf{E}}$  where  $\Psi$  may represent any suitable strain energy density function (e.g. a Mooney-Rivlin model<sup>70</sup>) including anisotropic material laws. The discrete relaxation function is defined by:

$$G(t) = \gamma_{\infty} + \sum_{i=1}^n \gamma_i e^{-\frac{t}{\tau_i}} \quad 2-93$$

with the parameters  $\gamma_i$  and  $\tau_i$  dictating the viscoelastic behaviour. The parameters  $\gamma_i$  are constrained such that (ensuring that eventually  $\mathbf{S}(\mathbf{E}, t) = \mathbf{S}_e$  following relaxation):

$$\gamma_{\infty} + \sum_{i=1}^n \gamma_i = 1 \quad 2-94$$

Alternatively the stress response may be written as:

$$\mathbf{S}(\mathbf{E}, t) = \gamma_{\infty} \mathbf{S}_e(\mathbf{E}, t) + \sum_{i=1}^n \int_{-\infty}^t \gamma_i e^{-\frac{t-\tau}{\tau_i}} \frac{\partial \mathbf{S}_e(\mathbf{E}, \tau)}{\partial \tau} \partial \tau \quad 2-95$$

As mentioned before, the elastic stress contribution  $\mathbf{S}_e$  may be due to an anisotropic constitutive formulation. However to the authors knowledge no constitutive formulations have been proposed whereby the viscoelastic constants (e.g.  $\gamma_i$  and  $\tau_i$ ) are orientation dependant.

## 2.3 Basics of magnetic resonance imaging

### 2.3.1 *Introduction*

Nuclear magnetic resonance imaging, better known as magnetic resonance (MR) imaging (MRI), is the application of nuclear magnetic resonance (NMR) to radiological imaging<sup>71</sup>. MRI is essentially based on measuring the response of matter to an externally applied electromagnetic field. In MRI tissue is exposed to an external magnetic field generated by a large coil. This external field causes all the tissue particles (e.g. protons) to align with this field in a certain way. This alignment is then modified by applying a series of radiofrequency pulses that match the frequency of the particles. During the time after these pulses the tissue particles will return (or relax) to their original orientation. This relaxation response can be measured and results in the MR signal. Gradient fields in all three dimensions result in a spatially varying signal thus enabling 3D imaging. In MRI the hydrogen nucleus (a proton) is the most dominant nucleus. It is found in water, lipids and other organic molecules. MRI provides excellent soft tissue contrast since soft tissues contain large quantities of water. Although the signal in MRI represents nuclear spin of hydrogen nuclei the signal can be interpreted in many different ways yielding many different types of tissue contrast.

This section provides a brief description of the basic principles of MRI. A detailed discussion requires the theory of quantum electrodynamics (a combination of special relativity theory and quantum mechanics). This however, is beyond the scope of this study and thus instead the basics will be explained using some quantum mechanical but also more classical mechanical analogies. For a detailed description of NMR and MRI the reader is referred to specialised literature<sup>71,72</sup>.

### 2.3.2 *Angular momenta and magnetic moments*

Nuclear magnetic resonance is one of a large range of phenomena associated with the interaction of electromagnetic radiation with matter or more precisely the interaction of atomic nuclear spin with an external magnetic field. In order to explain nuclear spin let's consider an example in classical mechanics. In classical mechanics angular momentum is a term used for the rotation of an object around an axis. In a simple view of the celestial mechanics of earth and the sun for example (Figure 2.16, adopted from<sup>73</sup>) we can



associate two angular momenta with the movement of the earth: one due to the rotation of the earth around the sun and one due to the earth's rotation around its own axis. The latter is referred to as spin. Although different in nature atomic particles and their building blocks, protons, neutrons and electrons also possess a property called spin.

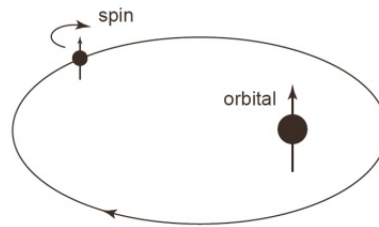


Figure 2.16 Angular momenta in celestial mechanics

In MRI the hydrogen proton ( ${}^1\text{H}$  present in water, lipids and other organic molecules) spins are the most relevant and dominant. Although strictly speaking incorrect the motions of the proton spin may be understood by imagining it as a spinning gyroscope that is also electrically charged. In MRI the external magnetic field results in a precession of the proton spin about the field direction and the actual imaging relies on the ability to manipulate the bulk precession of these hydrogen proton spins.

Particles that possess both charge and spin must also have an effective loop of electric current around the same axis about which it is spinning. Not only is this current loop capable of producing its own magnetic field it is also capable of interacting with external magnetic fields. Consider an atomic nucleus with angular momentum  $\mathbf{J}$  suspended in an external static magnetic field (see Figure 2.17, adopted from<sup>73</sup>) denoted by the vector  $\mathbf{B} = (0,0,B_z)$  and aligned with the Z-axis (the bore axis) of the MRI coordinate system.

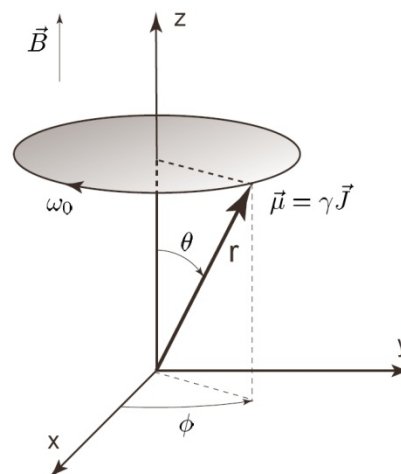


Figure 2.17 Angular momentum

Now let  $\boldsymbol{\mu}$  be the associated magnetic moment defined by:

$$\boldsymbol{\mu} = \gamma \mathbf{J}$$

Here  $\gamma$  is the so called gyromagnetic ratio which is a constant for a particular nucleus. The magnetic moment  $\mu$  can be thought of as a measure of both the ‘strength’ at which the current loop generates its own magnetic field and at which it interacts with external magnetic fields. The direction of  $\mu$  coincides with the spin axis which in turn will tend to align itself with the external static magnetic field vector  $\mathbf{B}$ . Similarly the precession of  $\mu$  tends to take place around the direction external field. The angular frequency of this precession is defined by:

$$\omega_0 = \gamma B_z \quad 2-97$$

A hydrogen proton in water has a gyromagnetic ratio  $\gamma$  of about  $2.68 \times 10^8$  rad/s/T, which means that at an external field of 3T the spin precession takes place at a (radio)frequency of 127.8 MHz ( $\gamma/(2\pi) = 42.6$  MHz/T)<sup>71</sup>. This precession frequency is known as the Larmor frequency.

### 2.3.3 Equilibrium alignment of spin

For hydrogen proton spins (which are most relevant to MRI), suspended in an external magnetic field, quantum mechanics dictates that there are only two possible quantum spin states (see Figure 2.18): The so called spin up state in which  $\mu$  is parallel to  $\mathbf{B}$  and the spin down state in which  $\mu$  is anti-parallel to  $\mathbf{B}$ .

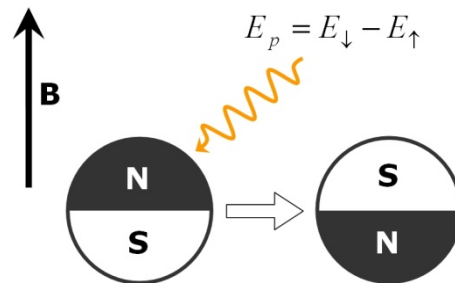


Figure 2.18 Quantum spin states, spin up (left) spin down (right)

Thus in a way the proton can be imaged as a subatomic magnet with its own local north and south pole. This ‘magnet’ can either align parallel or anti-parallel to the external magnetic field. The energy levels associated with these configurations spin up and spin down and are defined as  $E_{\uparrow}$  and  $E_{\downarrow}$  respectively:

$$E_{\uparrow} = -\frac{1}{2} \hbar \gamma B_z, \text{ and } E_{\downarrow} = \frac{1}{2} \hbar \gamma B_z \quad 2-98$$

$$\hbar = \frac{h}{2\pi}$$

Here  $h \approx 6.2607 \cdot 10^{-34}$  is Planck's constant. The  $E_{\uparrow}$  state is the lower energy configuration of the two and is therefore preferred. However as schematically illustrated in Figure 2.18 a hydrogen proton in the state  $E_{\uparrow}$  is able to switch to the state  $E_{\downarrow}$  by absorbing a photon with an energy equal to the quantum energy difference,  $E_p$ :

$$E_p = E_{\downarrow} - E_{\uparrow} = \hbar\gamma B_z = \hbar\omega_0 \quad 2-99$$

This equation is known as the resonance condition.

### 2.3.4 *Dynamic equilibrium*

Although the lower energy state (spin up) is preferred the actual distribution of spins in a given volume also depends on temperature. The ratio between the number of protons that are in the spin up state  $N_{\uparrow}$  with respect to the number in the spin down state  $N_{\downarrow}$  in a given volume is defined by:

$$\frac{N_{\uparrow}}{N_{\downarrow}} = e^{-\frac{\hbar\omega_0}{kT}} = e^{-\frac{E_p}{kT}} \quad 2-100$$

The fraction  $\frac{E_p}{kT}$  is the ratio between the quantum energy difference  $E_p$  and the average thermal energy,  $kT$ , with  $k \approx 1.3805 \cdot 10^{-23}$  Boltzmann's constant and  $T$  temperature. At room (or body) temperature the average thermal energy is millions of times larger than  $E_p$  resulting in an almost even distribution. There is however a slight excess of low energy state spins called the 'spin excess'  $\xi$ , which is then given by:

$$\xi = N \frac{E_p}{2kT} \quad 2-101$$

With  $N$  the total number of spins.

The spin of single protons is not detectable, instead the signal is averaged over macroscopic volumetric elements called voxels (volumetric 3D equivalents of pixels). These voxels contain large amounts of protons each with their own spin and magnetic moments. Figure 2.19a shows an atomic nucleus with spin and a magnetic moment  $\mu$ .

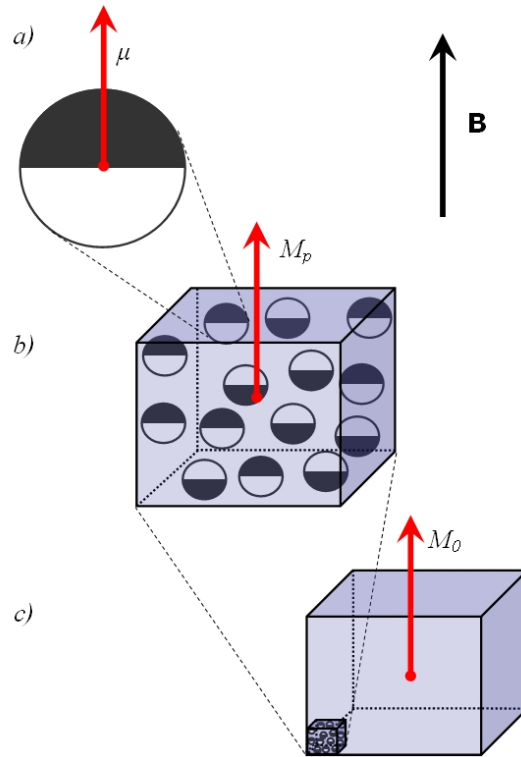


Figure 2.19 A particle with spin and magnetic moment  $\boldsymbol{\mu}$  (A), a spin packet (scale exaggerated) with a net magnetization  $\boldsymbol{M}_p$  (B) a voxel with a net magnetization  $\boldsymbol{M}_0$

The spin of this atomic nucleus is the vector sum of the spins of its subatomic particles (e.g. protons). Thus the magnitude of this spin depends on both the atomic number and the mass number. The net spin angular momentum (and the current loops) of an atomic particle results in a net magnetic moment  $\boldsymbol{\mu}$  of the atomic particle. Similarly it can be shown that the expected behaviour of a large number of spins is equivalent to the classical behaviour of a net magnetization vector representing the sum of all individual magnetic moments. For instance one could analyse a small volume (or spin packet) in which  $\boldsymbol{M}_p$ , represents the net magnetization vector (Figure 2.19b). On a larger, macroscopic scale the same applies to voxels. In dynamic equilibrium the macroscopic magnetization vector in each voxel  $\boldsymbol{M}_0$  (Figure 2.19c) is aligned with  $\boldsymbol{B}$  and does not have transverse components  $\boldsymbol{M}_0 = (M_{x0}, M_{y0}, M_{z0}) = (0, 0, M_{z0})$ , where:

$$M_{z0} = \frac{\rho_0 \gamma^2 \hbar^2}{4kT} |\boldsymbol{B}|$$

$$\rho_0 = \frac{V}{N}$$

2-102

with  $N$  the number of spins in the voxel,  $\rho_0$  the proton density and  $V$  the voxel volume. Just like each individual spins magnetic moment the net magnetization vector precesses

about the axis of the external magnetic field (and therefore with the  $Z$ -axis of the MRI coordinate system, see Figure 2.17).

### 2.3.5 *Alteration of dynamic equilibrium*

As discussed the spin states (and therefore the dynamic equilibrium) can be altered through ‘transmission’ of photons with the appropriate energy level. For hydrogen protons exposed to a 3T external field this can be achieved using an electromagnetic wave of a frequency of 127.71 MHz (42.57MHz/T). This wave is known as a RF (radiofrequency) wave and is generated through alternating currents in coils in the  $x$ - and  $y$ -axis of the MRI coordinate system. The magnetic component of the wave is denoted by  $B_1$ . The wave results in a change of orientation of the net magnetic moment in each voxel. The new net magnetization vector precesses about the field  $B_1$  with precession frequency:

$$\omega_1 = \gamma B_1 \quad 2-103$$

The new angle of the new net magnetization  $\mathbf{M}_1$  is defined by:

$$\alpha = \int_0^t \gamma B_1 d\tau = \gamma B_1 t = \omega_1 t \quad 2-104$$

This angle is called the flip angle. Through an appropriate choice of  $B_1$ . and  $t$  any desired flip angle can be obtained. There are two main flip angles relevant to MRI. The 90 degree pulse,  $\alpha = \frac{\pi}{2}$  where  $\mathbf{M}_1 = (0, M_{z1}, 0)$ , here there is no longitudinal magnetisation as an equal amount of spins are in the high and in the low energy configuration, and the 180 degree pulse,  $\alpha = \pi$  where  $\mathbf{M}_1 = (0, 0, -M_{z1})$ , here there the majority of spins is in the higher energy configuration. The RF field causes all spins rotate in phase. This important phenomenon is referred to as phase coherence. When the RF field is removed the system returns to its dynamic equilibrium and the net magnetization returns to  $\mathbf{M}_0 = (0, 0, M_{z0})$ . This returning to dynamic equilibrium is known as relaxation.

### 2.3.6 *Relaxation to dynamic equilibrium*

There are two types of relaxation processes distinguishable spin-lattice relaxation and spin-spin relaxation. Spin-lattice relaxation is the process of the longitudinal component of the net magnetization vector to grow from its modified state back to  $\mathbf{M}_0$ , see Figure 2.20 (adopted from<sup>73</sup>). This phenomenon is due to physical interactions of the spins with

the surrounding molecules or surrounding lattice. The time this process takes to complete is referred to as spin-lattice relaxation time or  $T_1$  and is related to  $M_z$  through:

$$M_z(t) = M_0 \cos(\alpha) e^{\frac{-t}{T_1}} + M_0(1 - e^{\frac{-t}{T_1}}) \quad 2-105$$

Spin-spin relaxation is a process through which the transverse component of the net magnetization vector vanishes. The hydrogen protons are found in different types of molecular environments (e.g. bonded as  $H_2O$ ,  $-OH$  or  $-CH_3$ ) which causes them to experience a slightly different magnetic field resulting in slightly different rotational frequencies. Therefore even though initially, after the RF pulse the spins are in phase they start to dephase and cancel each other out. This dephasing phenomenon occurs over a time known as the spin-spin relaxation time  $T_2$  and relates to the transverse magnetisation  $M_t$  through:

$$M_t(t) = M_{t0} e^{\frac{-t}{T_2}} \quad 2-106$$

Where subscript  $t$  denotes transverse and 0 values at time zero.

Both  $T_1$  and  $T_2$  are dependant magnetic field strength but most importantly they depend on tissue type and are thus useful for image contrast. For all materials  $T_1$  is larger than  $T_2$ . Table 2-1 shows a review of the literature of the  $T_1$  and  $T_2$  for tissue types at the field strength relevant to the current project (3 T).

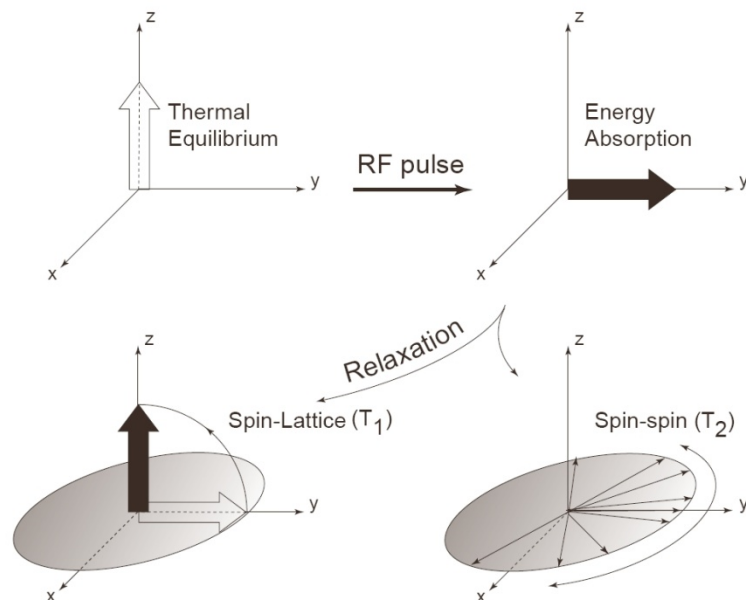


Figure 2.20: Schematic overview of MR experiment. The dynamic equilibrium state (top left) is altered using an RF pulse to achieve a desired flip angle (e.g.  $2/\pi$  shown in top right). After the RF pulse is stopped the system then relaxes. The relaxation can be split up into spin lattice relaxation (bottom left) and spin-spin relaxation (bottom right).

<b>Tissue type / Reference</b>	<b>T1 (ms)</b>	<b>T2 (ms)</b>
<b>Skeletal muscle</b>		
<i>In-vivo</i> human knee <sup>74</sup>	1420 ± 38.1	31.7 ± 1.90
<i>In-vivo</i> human paravertebral muscle <sup>75</sup>	898 ± 33	29 ± 4
<i>In-vitro</i> mouse skeletal muscle <sup>76</sup>	1412 ± 13	50 ± 4
<b>Cartilage</b>		
<i>In-vivo</i> human knee cartilage <sup>74</sup>	1240 ± 107	36.9 ± 3.81
<i>In-vivo</i> human knee cartilage <sup>77</sup> minimum and maximum		45.3 ± 2.5 74.1 ± 5.4
<i>In-vitro</i> bovine cartilage 0° <sup>76</sup>	1168 ± 18	27 ± 3
<i>In-vitro</i> bovine cartilage 55° <sup>76</sup>	1156 ± 10	43 ± 2
<b>Synovial fluid</b>		
<i>In-vivo</i> human knee joint synovial fluid <sup>74</sup>	3620 ± 320	767 ± 48.8
<b>Lipid and fatty tissue</b>		
<i>In-vivo</i> human knee joint subcutaneous fat <sup>74</sup>	371 ± 7.94	133 ± 4.43
<i>In-vivo</i> human knee joint marrow fat <sup>74</sup>	365 ± 9.0	133 ± 6.14
<i>In-vivo</i> human pelvic region subcutaneous fat <sup>75</sup>	382 ± 13	68 ± 4
<b>Bone marrow</b>		
<i>In-vivo</i> human bone marrow (L4 vertebra) <sup>75</sup>	586 ± 73	49 ± 4
<b>Myocardial tissue</b>		
<i>In-vitro</i> mouse heart <sup>76</sup>	1471 ± 31	47 ± 11

Table 2-1: Review of tissue T1 and T2 relaxation times at 3T

### 2.3.7 Detecting the magnetization of the system

As discussed above after an RF pulse the altered (flipped) net magnetization vector  $M$  precesses around  $B_1$ . This induces currents in a receiver coil array. The signal in the x and y-directions can be expressed by:

$$s_x(t) = Ae^{\frac{-t}{T_2}} \cos(-\omega_0 t)$$

$$s_y(t) = Ae^{\frac{-t}{T_2}} \sin(-\omega_0 t)$$

2-107

where  $A$  is a factor depending on number of excited spins.

### 2.3.8 Position encoding

The signal acquired using the receiver coils is dependent on the frequency  $\omega$ , which in turn depends on the magnetic field strength (external and due to RF pulses) which, in the examples above, is homogeneous. Therefore in the situation described no spatial information was available in the signal and the entire subject would produce the same signal frequency. Encoding position in the obtained signal is possible by superimposing a series of linear magnetic field gradients. Since the frequency  $\omega$  of the signal depends on the local field, this results in a spatially varying signal frequency. Thus in each voxel the net magnetization vector precesses about the field at a slightly different frequency. An example for a gradient in the z-direction for encoding slices will now be discussed and is illustrated in Figure 2.21 (Figure 2.21 is composed using images from <sup>73</sup> and <sup>78</sup>).

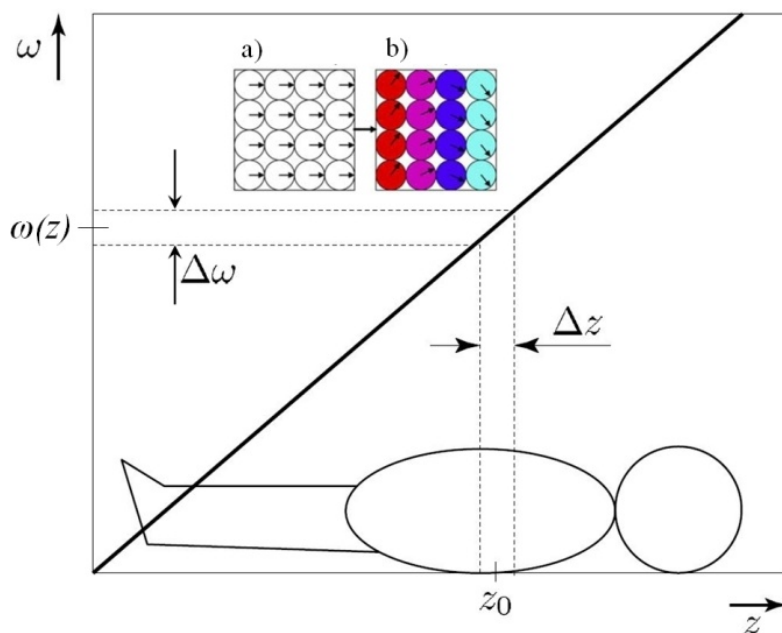


Figure 2.21: Applying magnetic field gradients.

Figure 2.21A shows a spin packet with all spins precessing in phase due to a homogeneous field. However, as shown in Figure 2.21B, by applying a field gradient in the z-direction the frequencies of the protons spins can be altered in the z-direction inducing signal frequency differences along this direction. These gradients fields (which are in the order of mT/m) thus serve to spatially encode slices and volumes. The addition of the spatially varying magnetic fields or gradient fields  $G = (G_x, G_y, G_z) = (0, 0, \frac{\partial B_z}{\partial z})$  produces a signal with a spatially varying Larmor frequency. In the example shown here in the z-direction:

$$\omega(z) = \gamma(B_0 + G_z z)$$

2-108



Consider the slice at  $z_0$ . In order to excite the spins in this slice an RF pulse with a bandwidth of  $\Delta\omega$  centred at  $\omega(z)$  is required.

$$\Delta\omega = \gamma G_z \Delta z \quad 2-109$$

The slice thickness can then be calculated using:

$$\Delta z = \frac{\Delta\omega}{\gamma G_z} \quad 2-110$$

This relationship shows that the slice thickness is proportional to bandwidth of the RF pulse and inversely proportional to the gradient. In the example discussed here the within slice position encoding can be performed using magnetic field gradients in the x- and y-directions. In the example discussed earlier the slice direction coincided with the z-direction, however in reality the RF coils are capable of producing gradients in any desired orientation not necessarily in the x-, y- and z-directions. Since the signal frequency varies spatially it is useful to use Fourier transform theory. The overall position encoding system in MRI is referred to as the  $k$ -theorem which states that the time signal is equivalent to the forward Fourier Transform of the desired image. After all data has been collected in the Fourier space ( $k$ -space) the inverse Fourier Transform yields the desired image, which represents the weighted spin density distribution in the selected slice or volume (see Figure 2.22, modified from <sup>73</sup>). A full discussion of the  $k$ -theorem is beyond the scope of the current study but can be found in specialised literature <sup>71,73</sup>.

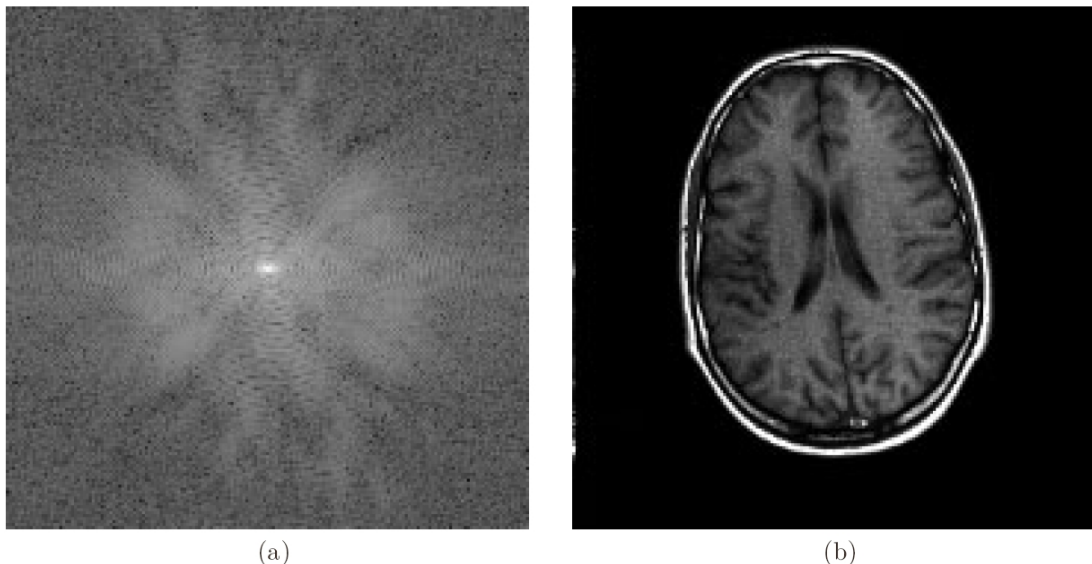


Figure 2.22: The  $k$ -theorem. MR data of the human brain in the  $k$ -space domain (A), the MR data in the image domain obtained via inverse Fourier transform of the  $k$ -space image (B)

### 2.3.9 *Anatomical magnetic resonance imaging*

In anatomical MRI the intensity of a voxel depends on its density of mobile hydrogen protons and on how these protons respond to the externally applied magnetic fields (both static and fluctuating). This response depends on the chemical and biophysical environment of the protons which is described concisely by the T1 and T2 relaxation times<sup>79</sup>. Depending on the tissue type and size of tissue structure of interest a large number of possible imaging sequences can be used. For the current study sequences useful for 3D musculoskeletal modelling are of interest e.g. the standard pulse sequences, such as T1-weighted spin-echo imaging, spoiled gradient echo imaging, and proton-density fast spin-echo imaging<sup>80</sup>. Imaging sequences of this type are implemented in the standard imaging sequence libraries of clinical MRI scanners<sup>79</sup>. Like many other MRI techniques anatomical MRI allows full 3D volume imaging of the anatomical structure and is thus a valuable tool for image based modelling<sup>80</sup>. Through post-processing of the 3D image data (e.g. thresholding and segmentation) it is possible to construct detailed 3D models (Figure 2.23, reproduced from<sup>80</sup>) e.g. for finite element modelling. For structures like bone automatic segmentation methods have been developed, however the boundaries between muscles are not as well defined and as such to date, there exists no robust, automatic routine for segmenting muscle boundaries<sup>80</sup>.

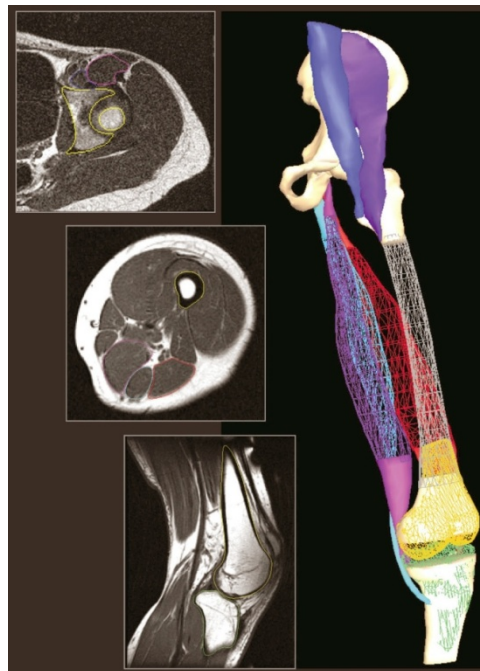


Figure 2.23: Musculoskeletal structures of the lower leg modelled from anatomical images.

## 2.3.10 MRI techniques based on motion induced phase shifts

### 2.3.10.1 Principle of motion induced phase shift

Section 2.3.8 discussed how hydrogen spins are in phase coherence when subjected to a homogeneous magnetic field and how the phase can be altered through the application of gradients. Figure 2.24 (modified from<sup>78</sup>) shows the phase coherence (left) and the phase difference after applying a first gradient (second from left). It is possible using a second gradient which is the exact inverse of the first gradient to return the proton spins to their original phase coherence. However phase coherence is only achieved when no movement occurred in between the application of the first and second gradient (top right). When movement occurs in the gradient direction phase coherence is not achieved (bottom right). After the two gradients stationary spins will be left with no net phase. Moving spins however will encounter different regions of the two gradients and will be left with a net phase proportional to the displacement in the time between the application of the first and second gradient, their velocity<sup>81, 82</sup>. This therefore yields a method to obtain images with a signal dependant on the amount of proton spin movement that occurred. In the example shown in Figure 2.24 the phase shift only occurs due to proton spin movement in the gradient (horizontal) direction. However multiple gradient directions can be combined following repeated acquisitions in order to analyse phase shift and motion in 3D.

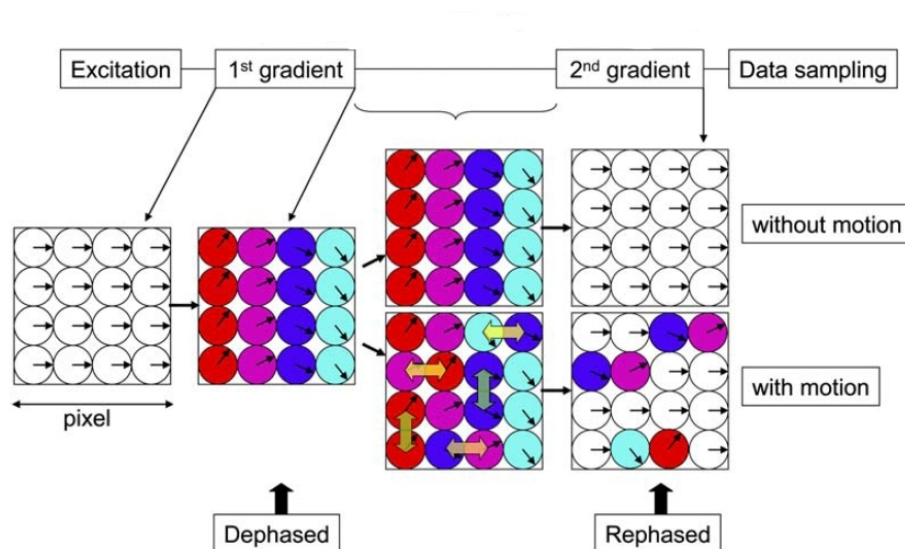


Figure 2.24: Phase shift

### 2.3.10.2 Diffusion tensor MRI

As mentioned before the phenomena of phase shift due to movement allows motion to be ‘encoded’ within the image. Diffusion Tensor MRI (DTI) is a phase shift based technique that analyses the diffusive movement of water molecules (hydrogen protons) in tissues (e.g. in the brain in order of 10  $\mu\text{m}$  in 50 milliseconds) movement water chooses the path of least resistance and will therefore diffuse along rather than through denser fibrous structures. By combining the information from diffusion sensitive images from multiple axes a diffusion tensor can be formulated (Figure 2.25, modified from<sup>78</sup>). The diffusion tensor eigenvalues ( $\lambda_i$ ) and eigenvectors allow derivation of the so called diffusion ellipsoid (Figure 2.25b). The per voxel principle eigenvector direction ( $v_1$  in Figure 2.25c) correlates with the average fibre direction within each voxel allowing mapping of average fibre orientations (e.g. for muscle tissue see Figure 2.26, reproduced from<sup>80</sup>). The technique has been extensively applied to imaging of the fibre architecture in the brain<sup>78, 83</sup>, but also in the heart<sup>84-86</sup> and muscle<sup>33, 87-96</sup> and other musculoskeletal tissues such as cartilage<sup>97</sup>. For more information on the theory of DTI the reader is referred to: <sup>78, 83, 98-100</sup>.

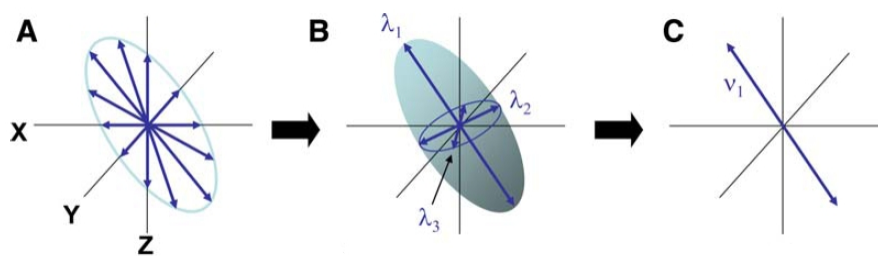


Figure 2.25: Schematic illustration of Diffusion Tensor Eigenvalue, Eigenvector and fibre direction determination

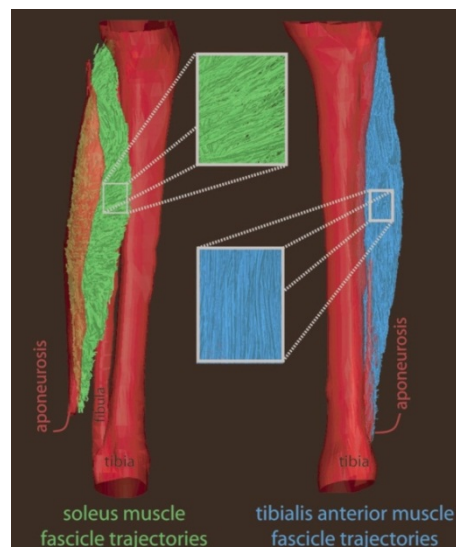


Figure 2.26: Fascicle trajectory mapping in skeletal muscle tissue.

### 2.3.10.3 Phase contrast MRI

Phase contrast MRI is another motion induced phase shift based technique. This time the spin movement of interest is macroscopic. The principles are the same, two magnetic gradients fields are employed separated in time, one to create a phase shift and other to attempt to return the system to phase coherence. As mentioned before the net phase found due to movement is proportional to the velocity. Through phase sensitive imaging data can be constructed where each voxel has a magnitude due to signal intensity and a phase related to the velocity (strictly speaking displacement between gradients) of the proton spins in that voxel <sup>81</sup>. Phase contrast MRI (PCMRI) aims to image the velocity of proton spins within the time between the gradients. The strength of the gradients and the interval between them sets the velocity scale which may be reliably detected, there exists a maximum velocity due to the fact that motion resulting in a phase change equal to  $360^\circ$  appears the same as  $0^\circ$  and cannot be distinguished from slower movements <sup>81</sup>. Figure 2.27 (reproduced from <sup>101</sup>) explains the PCMRI process. In order to reduce the influence of phase changes not related to movement (e.g. due to field heterogeneities) <sup>82</sup>, <sup>101</sup> the phase contrast image velocity map in one direction is obtained after a reference phase image is subtracted from the obtained velocity encoded image. One velocity component can be measured at a time. However through the combination of multiple repeated acquisitions at varying orientations (e.g. three mutually orthogonal directions) the 3D velocity vector can be computed throughout the image volume.

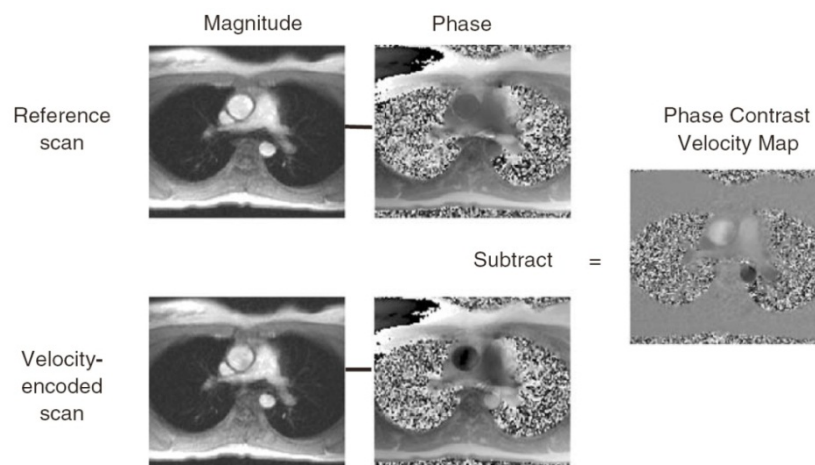


Figure 2.27: Phase contrast MRI

In principle the phase and therefore a measure of velocity can be obtained for each voxel. However in practise the signal to noise ratio limits requires averaging of the signal of adjacent voxels. This limits the effective spatial resolution of this technique <sup>82</sup>. The signal

to noise ratio also limits the accuracy of the corresponding derived displacements due to integration error<sup>82</sup>. The fact that multiple repeated image sets need to be acquired in order to generate one phase contrast map results in long acquisitions times. PC MRI has been widely used to study the motion of the heart (e.g.<sup>81,101-110</sup>) however it has also been applied to imaging of movement in skeletal muscle<sup>111-115</sup>.

#### 2.3.10.4 Magnetic Resonance Elastography

MR Elastography (MRE) is another technique based on phase shift imaging and aims to image mechanical property derived tissue parameters. Soft tissue is mechanically excited via an acoustic device generating low strain (e.g. <1%) shear waves in the tissue (frequencies of 90 to 150 Hz are typically used in skeletal muscle<sup>28</sup>). Gradients synchronized to the mechanical vibrations are then used to measure phase shift, which, when the information from several directions is combined allows for derivation of 3D displacement measures (due to these shear waves) at each voxel. Through inverse analysis of the shear wave propagation and attenuation it is possible to derive estimates of the theoretical shear modulus and viscosity of the tissue for the low strain levels and frequencies applied. Figure 2.28 (reproduced from<sup>32</sup>) demonstrates how the phase contrast MRI data can be post processed to obtain an image representing shear wave displacement (Figure 2.28a) and an image representing shear stiffness estimates (Figure 2.28b).

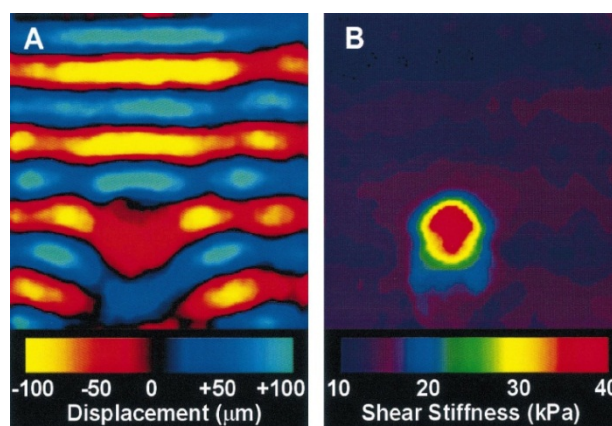


Figure 2.28: MR elastography of an agarose gel phantom with an embedded stiffer object (stiffer gel). A displacement image a) showing shear waves (300Hz) propagating through the phantom gel and a shear stiffness image b) showing the stiffer object.

MRE has been applied to various tissue types including skeletal muscle (e.g.<sup>28,116-121</sup>). Inverse analysis methods that allow for the derivation of the mechanical parameter estimates are often based on assumptions of isotropy (although recently also transversely

isotropy<sup>122</sup>) and linear elasticity or employ simple rheological models such as the Voigt model (see section 2.2.12.1 ). Due to the assumptions and current limitation to small strain the mechanical property estimates are more useful for diagnostic purposes (e.g. to imaging of breast lesion mechanical property alterations<sup>25</sup>) rather than for detailed anisotropic, non-linear and large strain constitutive property analysis.

### 2.3.11 *Tagged Magnetic Resonance Imaging*

As discussed in section 2.3.5 , it is possible using RF pulses to alter the state of hydrogen proton spins and the resulting magnetization vector e.g. to flip the net magnetization at a desired angle. This can be done selectively in space e.g. to excite only a certain region of interest. It is however also possible to use RF pulses to perturb the local magnetization. In such regions the signal can be reduced to background noise. This concept of introducing such an artificial manmade removal of signal is known as spin tagging and was first used to study blood flow by Morse and Singer 1970<sup>123</sup> and later Zerhouni *et al.* 1988<sup>124</sup> used this concept to analyse myocardial mechanics. Axel and Dougherty 1989<sup>125</sup>, <sup>126</sup> improved the MRI tagging further and developed a technique called SPAtial Modulation of Magnetization (SPAMM) that uses non-selective excitation to produce a periodic modulation of the magnetisation and parallel tag surfaces (initially planar) throughout the entire imaging volume within a few milliseconds. Figure 2.29 shows a schematic illustration of the SPAMM tagging process. An RF pulse is used to induce a flip angle to the magnetisation vector. A dephasing gradient is then used such that phase now varies in space along the direction of the gradient. This leads to the conical magnetisation vector distribution shown in the bottom left of Figure 2.29. A second RF pulse then flips the conical magnetisation by the same angle as the initial. This induces the flipped cone shown in the bottom right of Figure 2.29 where phase angle within the cone is dependent on the location in space along the gradient direction. Hence the Z-magnetisation magnitude varies sinusoidally in space along the gradient direction since some vectors are aligned with the Z-axis resulting in no net change of Z-magnetisation while for those at the bottom of the cone the Z-magnetisation is reduced. Therefore this technique creates sinusoidal signal modulation along the gradient direction visible as dark saturated surfaces or tag surfaces. Figure 2.29 illustrates what is known as first order or 1-1-SPAMM tagging. Higher order SPAMM modulations further approximate a block

function modulation rather than the sinusoidal modulation of 1-1-SPAMM. The perturbed magnetisation (bottom right in Figure 2.29) relaxes back to equilibrium (top left in Figure 2.29) as a function of  $T_1$  relaxation. Hence the low intensity tag surfaces fade back to normal signal due to as a function of  $T_1$  (for skeletal muscle tissue  $T_1$  times are around 0.9-1.4 s, see Table 2-1). However prior to this the tag pattern is temporarily locked in the tissue and tissue deformation occurring after tag pattern deposition is reflected in the deformation of the tag pattern.

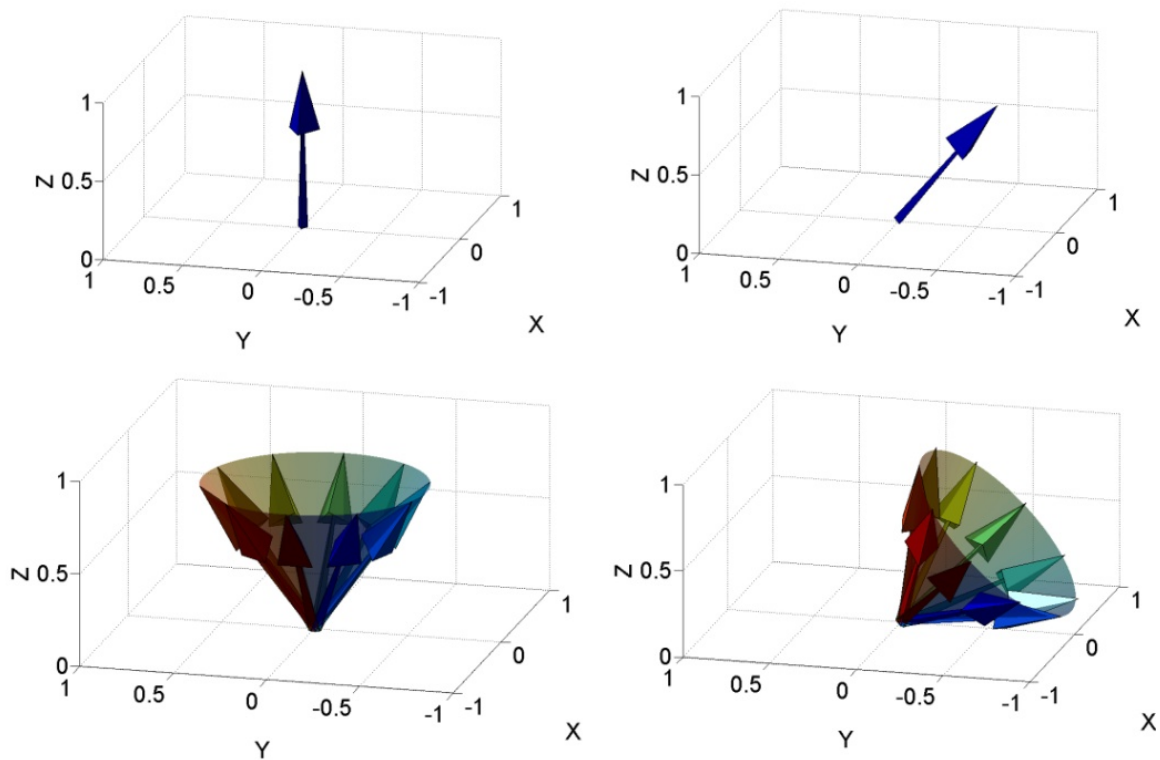


Figure 2.29 Equilibrium magnetisation (top left), RF pulse induced magnetisation vector tilt (top right), gradient induced dephasing results in cone-like magnetisation vector distribution (bottom left), a second RF tilts the cone resulting in a sinusoidally modulated Z-magnetisation (bottom right).

Figure 2.30 (reproduced from<sup>34</sup>) shows a normal series of cardiac MRI (left) and a series of SPAMM tagged MR images (right). In this case two orthogonal directions were used to create a grid pattern. Basic tag sequences of this type are now integrated within the pulse sequence libraries of all clinical MRI machines<sup>34</sup>. Many variations of this technique have been developed to measure cardiac motion such as: CSPAMM<sup>127</sup> (Complementary SPAMM) in which tags are maintained longer, DANTE<sup>128</sup> consisting of a series of short RF pulses, effective on small imaging systems. Hybrid tagging and phase contrast related methods have also been developed, such as DENSE (Displacement Encoding with Stimulated Echoes<sup>129</sup>) and HARP (Harmonic Phase<sup>130</sup>), in which a uniform pattern of phase modulation is encoded into the tissue and the deformation of that pattern is



detected<sup>34</sup>. However these techniques require acquisitions of additional repetitions with respect to traditional SPAMM.

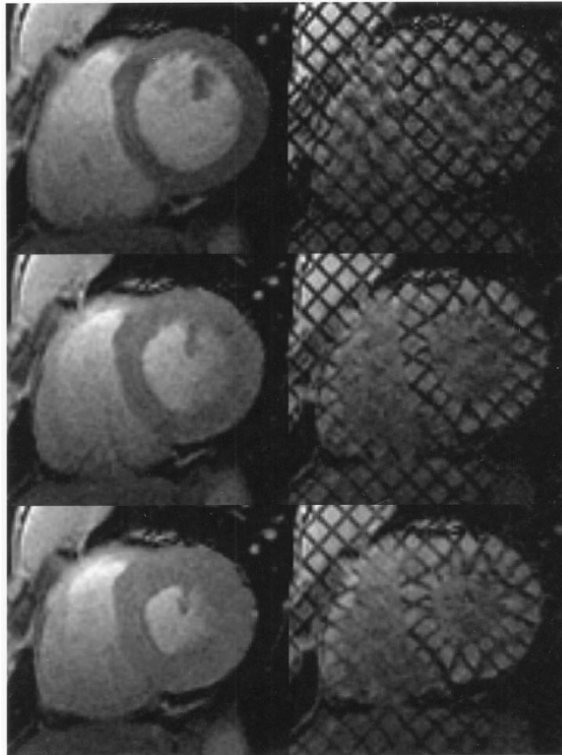


Figure 2.30 Left: standard cardiac MR images. Right: for the same heart, location, and cardiac phase, the corresponding tagged MR images.

The spatial resolution of the strain computed from the tagged images is often defined as the distance between two adjacent tags<sup>49</sup>. In practice, the tag spacing must be chosen such that tag pairs can be resolved by image processing, requiring for instance 5–7 voxels separation between tags<sup>34</sup>. The optimal tag thickness (half the tag modulation period) has been reported in the range of 0.8 to 1.5 voxels<sup>131</sup>.

## 2.4 Basics of image processing

### 2.4.1 Introduction

A large portion of the current study involves 3D image processing. Hence the basics of image processing are here briefly highlighted. Since the current study involves mainly 3D imaging this is the focus of this section. For a more detailed description the reader is referred to more specialised literature (e.g. on medical imaging<sup>73</sup>, image processing<sup>132, 133</sup>).

### 2.4.2 Background on image data

A general definition of an image is a discrete representation or visualisation of a multidimensional measured signal or mathematical function. Figure 2.31 shows examples of how continuous functions (left) can be discretely represented or sampled to obtain 2D (A) or 3D (B) images (right). Image data is generally visualised using regular tessellations whereby the area (2D) or volume (3D) is subdivided in a finite number of equal image elements. In the case of 2D imaging the image elements represent area units referred to as pixels and are generally rectangular. For 3D imaging image elements represent volume units referred to as voxels and are usually hexahedral.

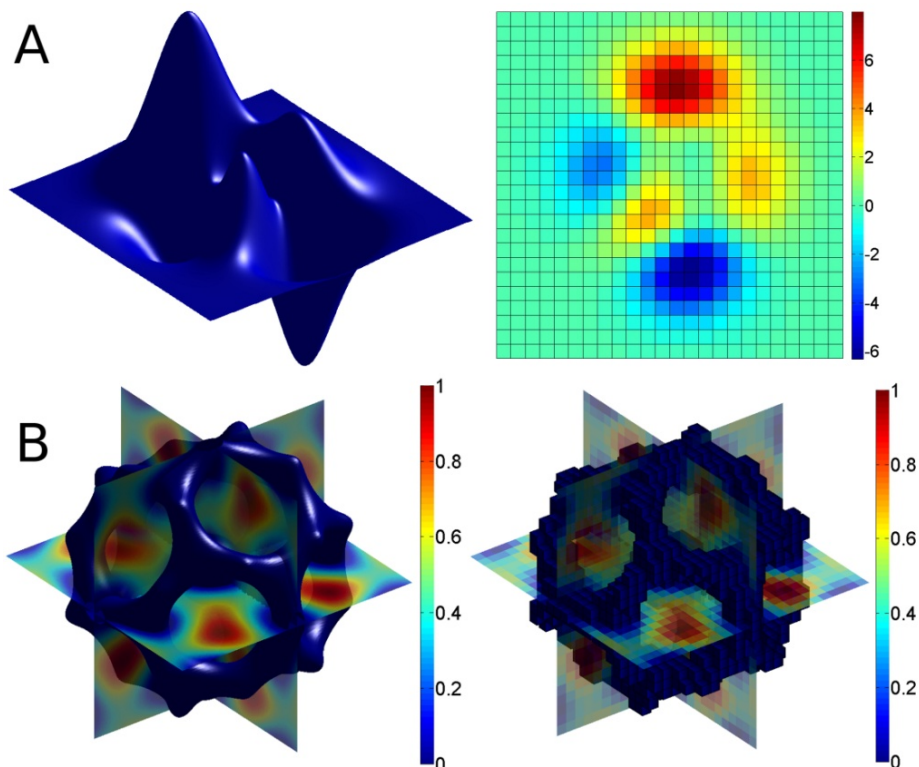


Figure 2.31: Examples of a 2D image where the signal represents height of a surface visualised using coloured pixels (B) and a 3D image where the signal represents signal value/intensity in space visualised as coloured voxels and pixel-slices (C). On the left ideal continuous descriptions and on the right discrete image representations.

A 3D image takes the form  $f(i, j, k)$  and can be represented as a 3D matrix. The variables  $(i, j, k)$  belong to the image coordinate system whose orthonormal basis is aligned with the image matrix row, column and slice directions respectively. Since an image is effectively signal intensities in space stored in matrix form it enables image processing using various mathematical and matrix operations. The image coordinate system is convenient since integer valued image coordinates are simply indices of voxels within the image matrix. However the image coordinate system does not take into account the possibly non-uniform voxel dimensions (the spacing in the row, column or slice direction), or the location and orientation in space of the imaging field of view (FOV) (see Figure 2.32). Other coordinate systems may be formulated that do take these into account. For instance the voxel dimensions can be taken into account using a so called local Cartesian coordinate-system  $(x, y, z)$  which is relatable to the image coordinate-system as:

$$(x, y, z) = \left( v_j \left( j - \frac{1}{2} \right), v_i \left( i - \frac{1}{2} \right), v_k \left( k - \frac{1}{2} \right) \right) \quad 2-111$$

where  $v = (v_i, v_j, v_k)$  are the voxel dimensions (the offset of  $\frac{1}{2}$  is due to the fact that the first voxel has the index  $(1,1,1)$  and its corner forming the image origin at  $(\frac{1}{2}, \frac{1}{2}, \frac{1}{2})$ ). In some cases the FOV is defined with respect to an external coordinate system in which it is translated and rotated. If this orientation is of interest the local Cartesian coordinates  $(x, y, z)$  can be translated and rotated accordingly to define the image data within a global external Cartesian coordinate system  $f(x', y', z')$ . This is often useful in order to appropriately overlay image data from repeated and varying FOV orientations and voxel sizes.

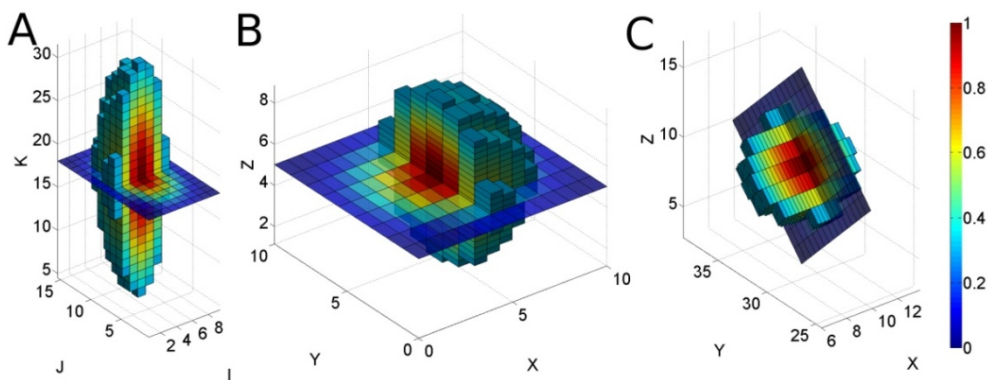


Figure 2.32 Spherical symmetric Gaussian function partially visualised using a mid-slice and voxels. Visualisation based on: Image coordinates showing (false) isotropic voxel appearance and distorted shape (A), Local Cartesian coordinate system taking voxel dimensions into account, note anisotropic voxels (B), Example global Cartesian coordinate system taking into account voxels dimensions, and their location and orientation in a global frame of reference (i.e. the field of view was translated and rotated with respect to some arbitrarily adopted reference coordinate system).

Two types of imaging processes can be defined (see Figure 2.33): 1) *at each voxel the signal value matches the signal sampled at the voxel centre*, or 2) *at each voxel the signal matches the average of the signal across volume of the voxel*. The former is thus a pure sampling of a function at discrete locations (and visualisation using points would strictly speaking be more appropriate than volume elements) while the latter volume averaging can be viewed as a discrete convolution of the continuous function with the voxel element. The latter is most common in imaging applications including photography and MRI.

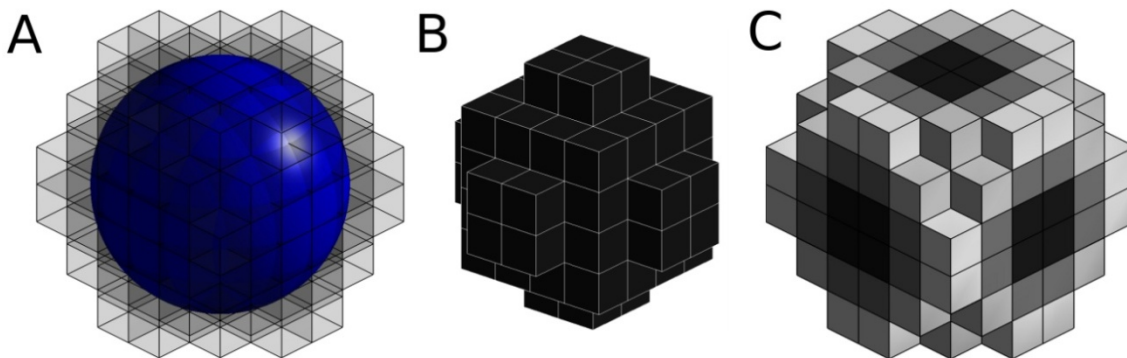


Figure 2.33 A solid sphere function (signal is 0 or black inside and 1 or white outside) imaged using a finite (shown as transparent) set of voxels (A), imaging of the sphere by sampling the function at the voxel centre coordinates leading to voxel signal intensities of either zeros or ones (B), the same sphere imaged by averaging the function across each voxel volume leading to intermediate signal due to partial volume effects (C).

### 2.4.3 Segmentation and filtering

Image segmentation or feature extraction techniques aims to convert image matrices to binary logic arrays whereby ones describe the feature of interest and zeros the rest of the image. The simplest form of segmentation is thresholding whereby the feature of interest is assumed to exhibit specific intensity characteristics (for instance the blue feature in Figure 2.31B can be segmented as all voxels with intensities lower than 0.2). More complex feature extraction methods involve filtering techniques.

A common operation in image processing is filtering or masking. Figure 2.34 shows an example where a Gaussian filter is used to average or blur signal intensities allowing for the suppression of noise.

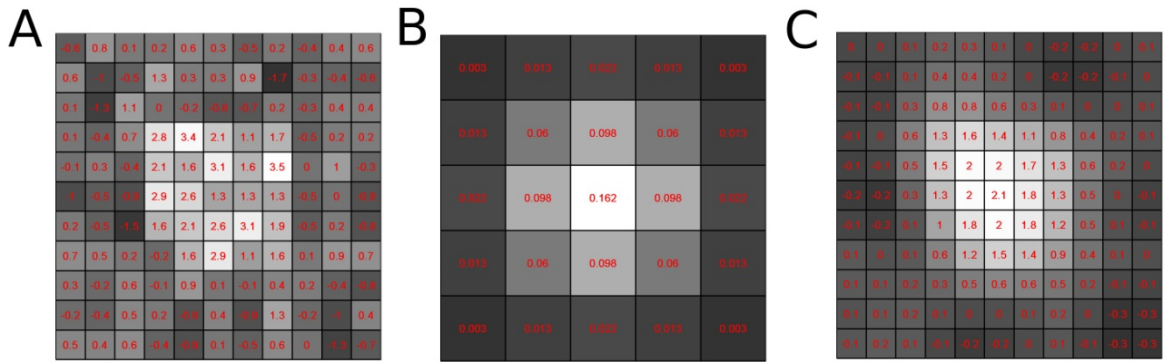


Figure 2.34 A 2D image containing a central high signal (white) square eroded by noise (A), a Gaussian blurring or averaging filter (B), the filtered result showing suppressed noise at the cost of blurring (C).

In the case of Figure 2.34 a 2D 5x5 filter was employed. The filtering occurs by marching this filter across the image and for each voxel a new signal is derived by taking the sum of the multiplication between its filter environment (here rectangular 5x5 region surrounding voxel) and the filter. The filter generally sums to 1 such that it does not induce signal alterations in homogeneous image regions. For a hexahedral filter  $\mathbf{F}$  and image  $\mathbf{M}$  the filtered image  $\mathbf{M}_f$  can be derived using:

$$\mathbf{M}_f(i, j, k) = \sum_{i_f=1}^{2n_i-1} \sum_{j_f=1}^{2n_j-1} \sum_{k_f=1}^{2n_k-1} \mathbf{M}(i + i_f - n_i, j + j_f - n_j, k + k_f - n_k) \mathbf{F}(i_f, j_f, k_f) \quad 2-112$$

with  $(n_i, n_j, n_k)$  denoting the index for the middle element in  $\mathbf{F}$ . The operation of marching across the images is referred to as convolution and can be written as:

$$\mathbf{M}_f = \mathbf{M} * \mathbf{F} \quad 2-113$$

where the operator  $*$  denotes convolution. For large image data sets convolution can be computationally expensive. However following the convolution theorem, convolution in the image domain is equivalent to multiplication in the Fourier domain leading to the more computationally efficient expression:

$$\mathbf{M}_f = \mathcal{F}^{-1}\{\mathcal{F}\{\mathbf{M}\}\mathcal{F}\{\mathbf{F}\}\} \quad 2-114$$

where  $\mathcal{F}\{ \}$  and  $\mathcal{F}^{-1}\{ \}$  represent the Fourier transform and inverse Fourier transform respectively.

Filters can be specifically designed to suppress or enhance features of interest. For instance Gaussian filters, as mentioned earlier, may be employed for blurring and noise suppression while other filters can be employed for enhancement of line or edge features in image data.

## 2.4.4 Spatial transformations

The coordinate descriptions for images can be subjected to spatial transformations including rigid (translations and rotations) and non-rigid transformations (deformations). The spatial transformations can also be subdivided into: 1) *Global spatial (or affine) transformations, acting homogeneously on the entire image*, or 2) *locally varying transformations*.

Global spatial transformations can be reduced to the following form:

$$\begin{bmatrix} x' \\ y' \\ z' \\ 1 \end{bmatrix} = \mathbf{T} \begin{bmatrix} x \\ y \\ z \\ 1 \end{bmatrix} \quad 2-115$$

whereby the original coordinates  $(x, y, z)$  are transformed or mapped to  $(x', y', z')$  using a transformation matrix  $\mathbf{T}$ . A transformation matrix can be decomposed as  $\mathbf{T} = \mathbf{DRS}$  defining a displacement  $\mathbf{D}$ , rotation  $\mathbf{R}$  and a deformation transformation tensor  $\mathbf{S}$  respectively. These can be defined as:

$$\mathbf{D} = \begin{bmatrix} 1 & 0 & 0 & d_x \\ 0 & 1 & 0 & d_y \\ 0 & 0 & 1 & d_z \\ 0 & 0 & 0 & 1 \end{bmatrix}, \mathbf{R} = \begin{bmatrix} e_{11} & e_{21} & e_{31} & 0 \\ e_{12} & e_{22} & e_{32} & 0 \\ e_{13} & e_{23} & e_{33} & 0 \\ 0 & 0 & 0 & 1 \end{bmatrix} \text{ and} \quad 2-116$$

$$\mathbf{S} = \begin{bmatrix} S_{xx} & S_{xy} & S_{xz} & 0 \\ S_{xy} & S_{yy} & S_{xy} & 0 \\ S_{xz} & S_{xy} & S_{zz} & 0 \\ 0 & 0 & 0 & 1 \end{bmatrix}$$

where the displacement is defined by the vector  $\mathbf{d}$  components and the rotation is defined by the components of the rotated orthonormal basis vectors  $\{\mathbf{e}_1, \mathbf{e}_2, \mathbf{e}_3\}$ . Finally a global deformation is defined using the tensor  $\mathbf{S}$  where the diagonal elements represent uniform scaling or stretch and the off diagonal components represent shearing. The coordinate transformation discussed in section 2.4.2 for mapping between the image coordinate system and Cartesian coordinate systems is a type of rigid transformation and can thus be formulated using displacement, rotations, and scaling tensors (whereby the displacement and rotation define the Cartesian orthonormal basis with  $\mathbf{d}$  defining the origin and  $\{\mathbf{e}_1, \mathbf{e}_2, \mathbf{e}_3\}$  the axis orientations, and the voxel dimensions defining the scaling with  $S_{aa} = v_a$ ). Examples of global deformations, due to  $\mathbf{S}$ , are as illustrated in Figure 2.35. Such type of deformations result in a homogeneous image deformation.

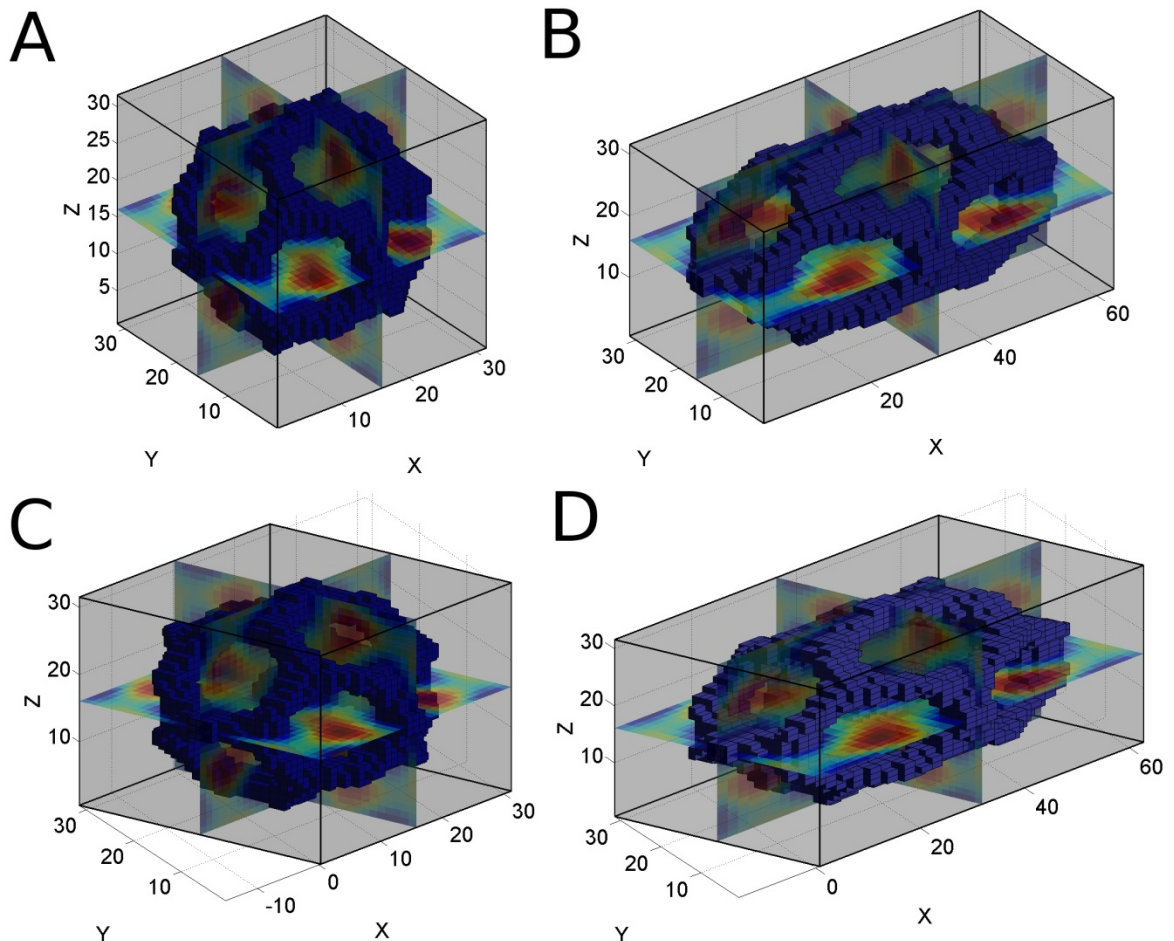


Figure 2.35 An example image (A) subjected to global scaling in the x-direction (B), shear in the x-direction (C) and combined scaling and shear in the x-direction (D).

For local, non-rigid transformations, deformation is a function of space and can thus be inhomogeneous. Local non-rigid transformations are common in image registration techniques (see section 2.4.5) whereby multiple image sets of similar objects, which may be deformed with respect to each other, are matched using deformation maps. A large array of local non-rigid geometric transformations have been proposed (see review article<sup>134</sup>) including those based on mechanical material models (e.g. linear elasticity). In general the local non-rigid transformations employed impose a smoothness and regularization on the deformation and thus effectively involve assumptions on the nature of the deformation and mechanical properties of the imaged object (e.g. level of homogeneity, isotropy, elasticity and compressibility).

### 2.4.5 Image correlation and registration

The above spatial transformations can be used to correct for motion that occurred between repeated acquisitions or for overlaying of image data derived from different imaging modalities. Methods to achieve this are digital image correlation (DIC) (e.g.<sup>135</sup>)

and image registration (review articles<sup>134, 136</sup>). With these techniques image pairs are adjusted with respect to each other using spatial transformations such that a similarity measure for the image sets is maximised. In addition to matching shifted or deformed image data sets for direct comparison, the techniques allow for the quantification of the motion and deformation between two image sets. Since DIC is relevant to this thesis it is highlighted in more detail.

In DIC displacement is derived from images of a surface undergoing motion and deformation. If the images are acquired at two orientations using for instance two camera angles, 3D surface displacements can be derived. In essence the technique relies on matching of points between an un-deformed reference image and a deformed image set. However due to disturbances such as noise and non-uniqueness of pixels, matching individual pixels is not possible. Instead the technique aims to match signal distributions within small regions in the image known as subsets. This illustrates the necessity for appropriate contrast within the subsets and hence surfaces are often painted with a random speckle pattern. Figure 2.36 highlights the DIC technique and illustrates subsets (green regions) in an example reference image (A) and an image of a deformed state (B). The reference image subset (Figure 2.36A) is moved and deformed until an appropriate match (Figure 2.36C) is obtained with the target image (the true image of the deformed state Figure 2.36B). The deformation is generally assumed uniform within each subset.

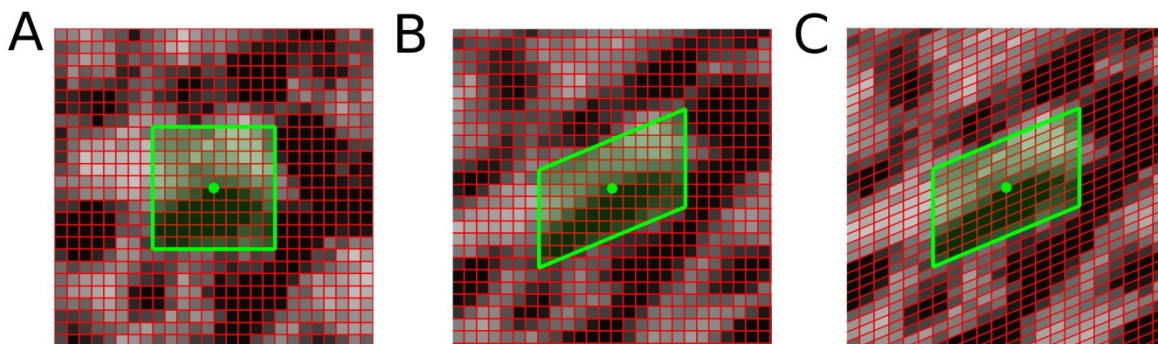


Figure 2.36 An example reference image (A), an image of a deformed state (B) and the reference image deformed to obtain a match to the image of the deformed state (C). A subset is shown outlined in green

To obtain a correlation between the two image-sets the subsets are iteratively altered (using optimisation routines) until a similarity measure has been maximised. Derivation of similarity measures requires a comparison between the target image and the deformed reference image. However, as the differences in pixel grid lines (red mesh lines) in Figure 2.36B and Figure 2.36C show the deformed reference image cannot simply be compared to the target image. First the deformed image of the reference state needs to be defined



on the same grid as the target image. This is done through (e.g. bilinear or cubic) interpolation.

Various similarity measures are in use in DIC (and image registration), an example is the normalised cross correlation coefficient  $C$  defined by:

$$C = \frac{\sum M_t M_d}{\sqrt{\sum M_r^2 \sum M_d^2}} \quad 2-117$$

where  $M_t$  and  $M_d$  represent the target image (the image for the deformed state) and the reconstructed (interpolated on the same grid as  $M_t$ ) deformed reference image respectively.

# 3 LITERATURE REVIEW

## 3.1 Introduction

This thesis involves the formulation of a framework for the non-invasive determination of the passive anisotropic and non-linear material properties of living human skeletal muscle tissue using non-invasive imaging and inverse FEA. Hence the following topics are discussed: 1) *The anatomy and physiology of skeletal muscle and its relation to the mechanical properties*, 2) *A review of experimental and computational modelling studies on the mechanical properties of skeletal muscle tissue*, 3) *A brief discussion on non-invasive imaging modalities*, 4) *MRI compatible actuators and sensor devices*, 5) *MRI based measurement of soft tissue deformation* and finally 6) *Validation of MRI derived motion and deformation*

## 3.2 Skeletal muscle anatomy and physiology

### 3.2.1 *Introduction*

Over 40% of human weight is composed of muscle tissue. Together the three types: skeletal, cardiac and smooth muscle tissue are responsible for all types of active mechanical movement within the human body. The skeletal muscles in the human body perform a variety of functions. Less obvious but very important functions are to aid in breathing (muscles in the chest), vision (ocular muscles that adjust eye orientation and provide focus) and hearing (muscles of the middle ear influencing movement of the auditory ossicles). Most of the functions are mechanical in nature such as to: produce skeletal movement, maintain active and passive body posture and position, provide support and protection for soft tissues (protection against impact), guard entrances and exits. However not all of skeletal muscle tissue's functions are mechanical in nature, it also aids in the maintenance of body temperature and the storage of nutrient reserves.

The mechanical behaviour of muscle tissue is a function of its particular constituents and structural architecture. Depending on muscle type skeletal muscle is composed of about 70-80% water, 3% fat and 10% collagen<sup>137</sup>. Elastin represents less than 1% of muscle tissue dry weight<sup>138</sup>. This section describes the structure and physiology of skeletal muscle tissue relevant to the current study. Since the mechanical properties of passive skeletal muscle are of interest the focus will be on the structure and function related to the passive (rather than active) mechanical properties of muscle tissue. The general anatomical information presented here, unless otherwise referenced was summarised from<sup>139-141</sup>.

### 3.2.2 *Skeletal muscle tissue architecture*

The levels of organisation of skeletal muscle are shown in Figure 3.1 (composed using images from<sup>142</sup>).

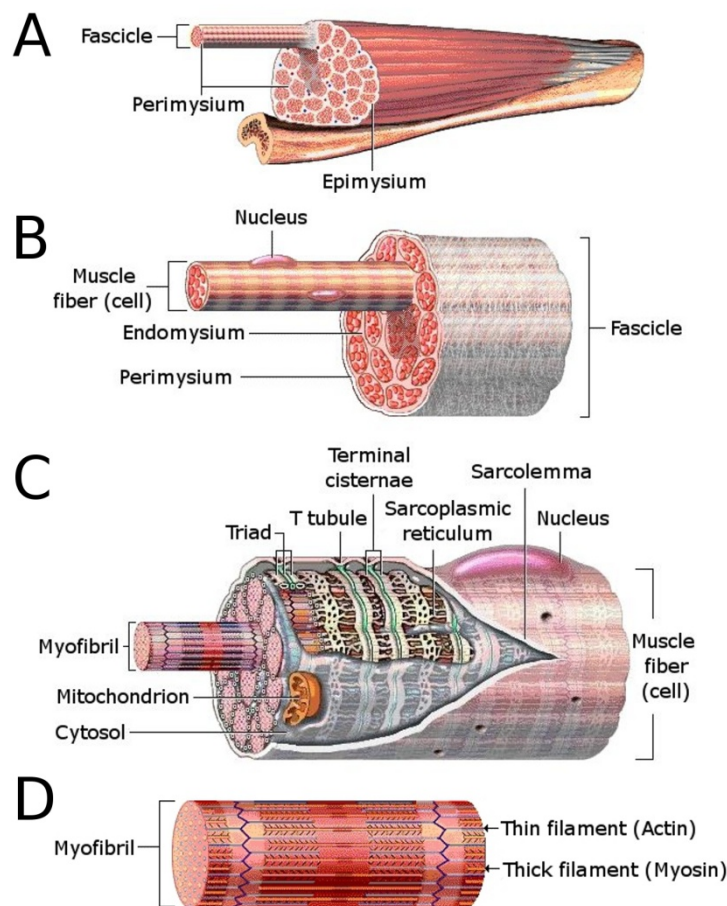


Figure 3.1 The organisation of skeletal muscle. The muscle body (A), the fascicle (B), the muscle cell/fibre (C) and the myofibril (D).

The outer surface of the muscles is wrapped in a dense layer of collagen fibres known as the epimysium. This layer separates the muscle from surrounding tissues and organs. As shown in Figure 3.2 (modified from<sup>143</sup>) the collagen fibres in the epimysium are arranged in two plies of parallel fibres at  $\pm 55^\circ$  with respect to the main fascicle direction<sup>143</sup>.

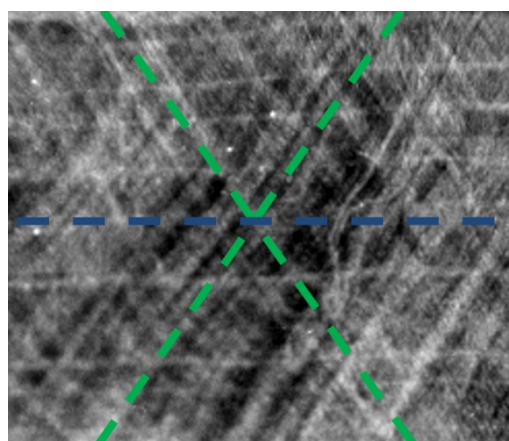


Figure 3.2 Light micrograph of collagen fibres of the epimysium of bovine skeletal muscle tissue. Blue and green lines highlight the muscle fascicle and collagen fibre orientations respectively.

Internally the epimysium is continuous with the perimysium which has a similar collagen network organisation and wraps around individual fascicles (Figure 3.1B) and connects

adjacent fascicles. The fascicles (Figure 3.1A-B) are bundles of muscle fibres (or muscle cells) (Figure 3.1C). The perimysium contains not only connective tissue fibres but also blood vessels and nerves that serve the muscle. Individual muscle fibres are separated by a connective tissue layer known as the endomysium which, at the margins of fascicles, are connected to the perimysium by perimysial junction plates<sup>144</sup>. The endomysium also loosely interconnects the adjacent muscle fibres and contains capillaries and nerve fibres that control the muscle fibre activation. Figure 3.3 (composed using images from<sup>145</sup>) shows the edomysial connective tissue in three levels of magnification showing its honeycomb-like tubular appearance in cross section (Figure 3.3A-B) and quasi-random collagen fibre arrangement (Figure 3.3C).

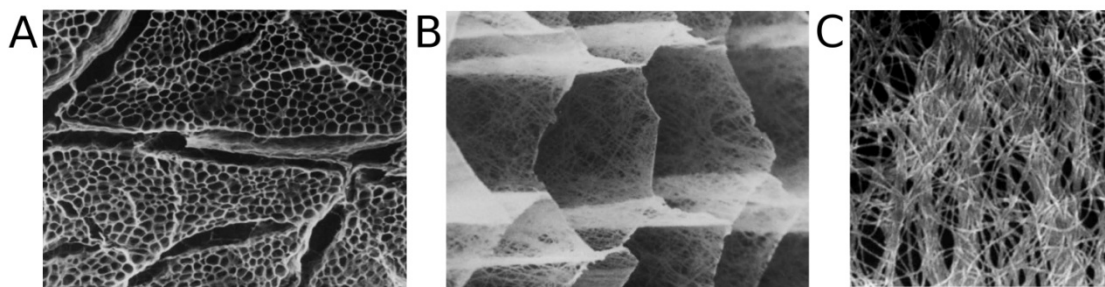


Figure 3.3 Scanning Electron Micrograph images following NaOH digestion of bovine sternomandibularis muscle. Cross sectional view of the collagen structures of the perimysium and endomysium (x100) (A), oblique view of approximately honeycomb-like endomysium structures (x3200) (B) and a close-up of the quasi-random felt-work of collagen fibre in the endomysium (x12200) (C).

At either end of the muscle the collagen fibres of the three connective tissue structures (epi-, peri- and endomysium) merge and become continuous with tendon or aponeurotic sheets, which in turn may become continuous with bone matrix at muscle attachment sites. The complex arrangement of the collagen fibres of the connective tissue structures have been reported to result in a non-linear elastic behaviour (e.g. for the epimysium<sup>146</sup>).

Muscle cells (Figure 3.1C) contain specialised protein filaments of actin and myosin located in myofibrils (Figure 3.1D) and are arranged into repeated groups (which give the cells a striated appearance). The basic contractile unit of myofibrils is known as the sarcomere (Figure 3.4 modified from<sup>140</sup>). When a muscle is activated the protein myosin forms bonds with actin and the filaments slide in relation to each other and allows for stiffness enhancement and powerful contraction. The actin and myosin filaments are also connected via a protein structure called titin (Figure 3.4). Titin filaments act like springs and have been reported to be the source of viscoelasticity of the sarcomere<sup>147</sup> and to be responsible for both the elasticity<sup>140, 148</sup> and the viscoelasticity of skeletal myofibrils<sup>149, 150</sup>.

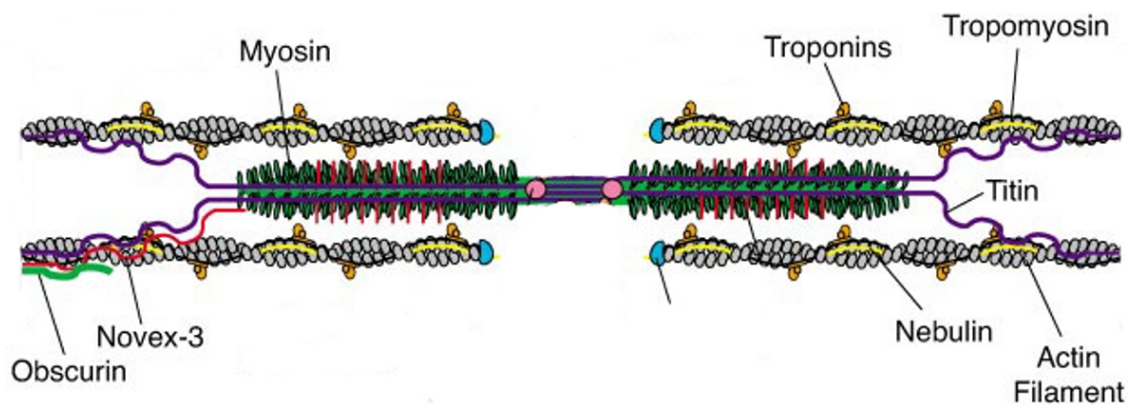


Figure 3.4: Schematic representation of part of the molecular structure of the sarcomere which is repeated along the muscle fibre length.

### 3.2.3 *Muscle tone and passive stiffness enhancement*

Nerve stimulation (e.g. through voluntary control) is able to trigger action potentials resulting in active contraction of muscles. However passive living skeletal muscle tissue (even during rest and deep sleep) maintains a certain level of activity. The goal of this activation is not to produce movement but to produce a certain amount of tension and therefore stiffness in the muscle tissue. This ‘resting’ activity resulting in tissue stiffness is referred to as muscle tone. Muscle tone serves to stabilise the positions of bones and joints and is involved in maintenance of balance and posture and aids in the protection against impact. In the current thesis skeletal muscle tissue is termed passive if it is not actively (e.g. voluntarily) contracted. However in the biomechanical literature the word ‘passive’ is also used for (freshly) dead muscle tissue which lacks muscle tone. However depending on time post-mortem, dead muscle tissue may present with enhanced stiffness and tension due to rigor mortis (see for instance<sup>151</sup>).

Muscle (and tendon) tissue also contain mechano-sensitive structures, such as muscle spindles, which allow protective stiffening or contraction of the muscle in response to muscle (e.g. sudden excessive) stretch. This protective effect is referred to as the myotatic reflex<sup>152</sup>. Living human passive muscle is therefore capable of increasing its stiffness as a response to elongating stretch and in shortening the opposite is true<sup>153, 154</sup>.

### 3.2.4 *Muscle fibre type, distribution and orientation*

Skeletal muscle tissue is composed of two main types of fibres: glycolytic and oxydative fibres. Glycolytic fibres, also called white or fast muscle fibres are large and densely packed with myofibrils. This type of cell is specialised to use stored reserves of glycol to produce fast powerful contractions. Oxidative fibres, also called red (since they contain a red protein called myoglobin similar to haemoglobin) or slow muscle fibres contain less myofibrils and are specialised for endurance. They therefore rely less on stored energy and more on a continuous supply and aerobic assimilation of glucose which is why they are surrounded by more capillaries. Since the concentration of myofibrils varies with fibre type it is not surprising that the mechanical properties of these fibre types also vary<sup>155-157</sup>. Since skeletal muscle generally possesses both strength and endurance they are often a mixture of both glycolytic and oxidative muscle fibres the ratio of which depends on the type of muscle and may alter as a function of its particular use in an individual.

Since muscle tissue is anisotropic its local mechanical properties also depend on local muscle fibre direction<sup>21, 158, 159</sup>. Figure 3.5 (anatomical images from<sup>141</sup>) shows some of the muscles in the upper arm and shoulder. As the figure demonstrates the fibre arrangement and orientations vary from one muscle to another. On the bottom of Figure 3.5 some schematic representations of simplified muscle fibre arrangements are shown. The largely parallel arrangement in the biceps brachii is known as fusiform while the arrangement of the pectoralis major muscle is known as convergent. Some other schematic representations of simplified muscle fibre arrangements such as a parallel (e.g. sartorius), unipennate (e.g. extensor digitorum longus), bipennate (e.g. rectus femoris) and multipennate (e.g. deltoid) are also shown.

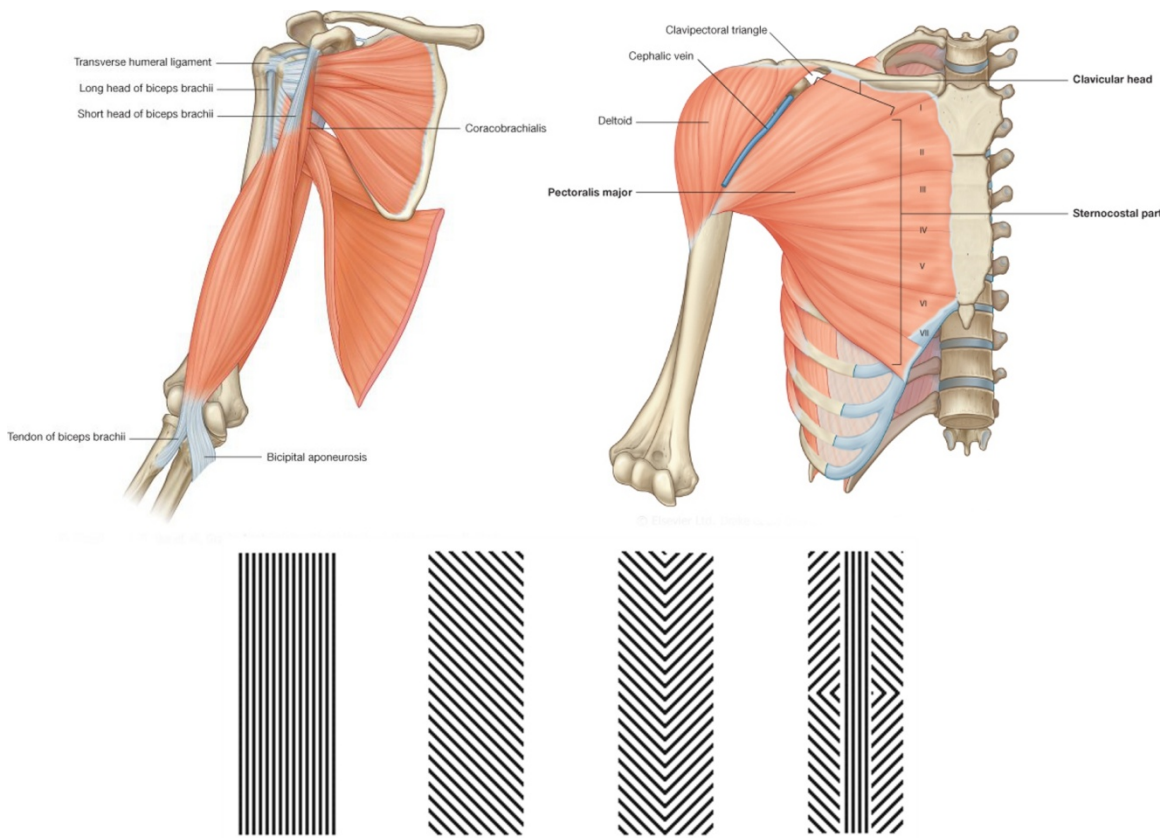


Figure 3.5: The musculature of the upper limb and chest (top left and right) and in the bottom schematic representations of typical fibre orientations within skeletal muscles. From left to right: A parallel, unipennate, bipennate and multipennate fibre arrangement.

### 3.2.5 Conclusions

Muscle tissue is anisotropic due to its fibre architecture. The non-linear mechanical behaviour of skeletal muscle tissue is due to the architecture and constituents of the muscle fibres (e.g. titin, actin and myosin features) and also its connective tissue structures. The latter are composed of complex collagen fibre arrangements which may relate to passive anisotropy of muscle tissue. Hence realistic modelling of the mechanical properties of muscle tissue should account for anisotropy introduced by both types of features.

Muscle fibres contain myofibrils with actin and myosin filaments which following activation produce active contraction and stiffness enhancement. However passive living muscle tissue at rest also presents with a mild degree of stiffness enhancement due to a rest activity called muscle tone. In addition muscle tissue is capable of enhancing stiffness (activity level) as a protective mechanism against (e.g. violent) stretch. Hence for passive mechanical property analysis induced muscle deformations should be mild



enough not to trigger this protective reflex. No data on (compressive) deformation rate/magnitude thresholds were found in the literature.

Depending of muscle site and particular function, muscles present with varying types of fibre arrangements. Fusiform muscles have largely parallel oriented fibres and this relative simplicity thus makes such muscles (e.g. the biceps brachii) most suitable for indentation and mechanical property investigation within the current thesis.

## 3.3 Skeletal muscle tissue mechanical behaviour

### 3.3.1 *Introduction*

The mechanical properties of materials describe its stress and strain relationship. In experimental mechanical property investigation the material response to known loading is analysed in order to understand the stress strain relationship of the material. Traditionally mechanical property investigation involves subjecting material samples to mechanical, such as tensile and compressive, testing. In the case of biological soft tissues this involves excising tissue samples and has thus largely been applied to animal tissue. However the mechanical properties of animal tissue may differ from human tissue. In addition biological materials may present with altered mechanical properties *in-vitro* and post-mortem (e.g. rigor mortis effects in skeletal muscle tissue, see<sup>151</sup>) with respect to living tissue *in-vivo* due to the altered biophysical conditions. Hence non-invasive approaches on living human tissue, mainly based on elasticity imaging, have also been developed.

This section reviews the relevant literature on the experimental investigation into the mechanical properties of passive skeletal muscle tissue and both invasive and non-invasive approaches will be discussed. Focus is placed on research relevant to constitutive modelling of passive 3D mechanical behaviour of muscle tissue.

### 3.3.2 *Invasive mechanical property assessment and analysis of excised tissue samples*

#### 3.3.2.1 **Compressive behaviour**

Some authors have investigated muscle behaviour using indentation tests. Gefen *et al.* 2005<sup>30</sup> performed indentation tests on surgically exposed rat gracilis muscles. Assuming

linear and isotropic behaviour they reported long term shear moduli in the range of 0.345-0.730 kPa. Similarly Palevski *et al.* 2006<sup>31</sup> performed high speed indentation tests on porcine gluteus maximus muscle samples. Muscle was considered as an isotropic linear (visco)elastic material with a long term shear modulus of  $0.700 \pm 0.300$  kPa.

Other authors have used compressive testing on excised tissue samples. Grieve and Armstrong 1988<sup>160</sup> conducted compression tests on porcine muscle samples and stress strain curves for samples subjected to unconfined uni-axial loading at varying load rates are shown in Figure 3.6 (reproduced from<sup>160</sup>). Samples were frozen on the day of slaughter and defrosted for testing and fibre orientation with respect to loading was not reported. However these curves demonstrate non-linearity and viscoelasticity of the tissue samples.

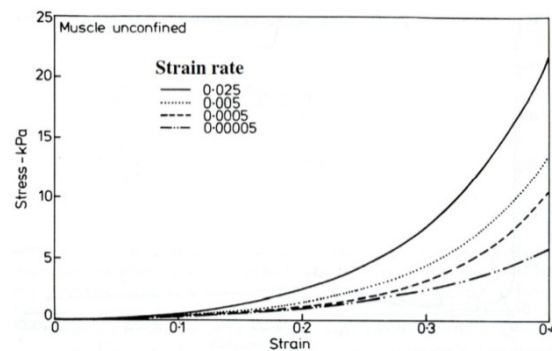


Figure 3.6: Unconfined compression of excised porcine muscle tissue at varying strain rates, reproduced from Grieve and Armstrong 1988.

Aimedieu *et al.* 2003<sup>161</sup> conducted dynamic compression (5-30 Hz) on porcine gluteus maximus samples. The analysis was however limited to simple Voigt model spring-dashpot parameters which are not directly usable for realistic (3D) constitutive modelling. The Voigt stiffness parameter showed a monotonous increase with load frequency (5 Hz: 8.5 kN/m up to 30 Hz: 347 kN/m).

Van Sligtenhorst *et al.* 2006<sup>162</sup> investigated the large strain (up to 80%) and high strain rate strain rate ( $1000 \text{ s}^{-1}$  up to  $2500 \text{ s}^{-1}$ ) compressive behaviour of bovine muscle tissue samples for loading in the fibre direction. Their results (Figure 3.7, reproduced from<sup>162</sup>) demonstrated that due to viscoelasticity the stress is highly dependent on the strain rate. However aged tissue (>200 hours post mortem) was used.

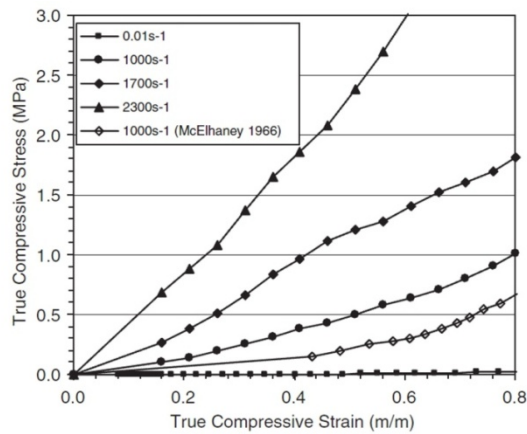


Figure 3.7: Typical stress strain data at various strain rates, reproduced from Sligtenhorst et al. 2006

Song et al. 2007<sup>163</sup> conducted high strain rate ( $540 \text{ s}^{-1}$  up to  $3700 \text{ s}^{-1}$ ) compression tests up to 50% on porcine muscle samples. Their results (Figure 3.8 reproduced from<sup>163</sup>) showed viscoelasticity and non-linearity in the compressive response in both the fibre and cross fibre directions and stresses were strongly dependant on strain-rate. They also reported anisotropy as this effect was found to be more pronounced in the cross fibre direction. The data was however presented in such a way that constitutive model evaluation is hindered.

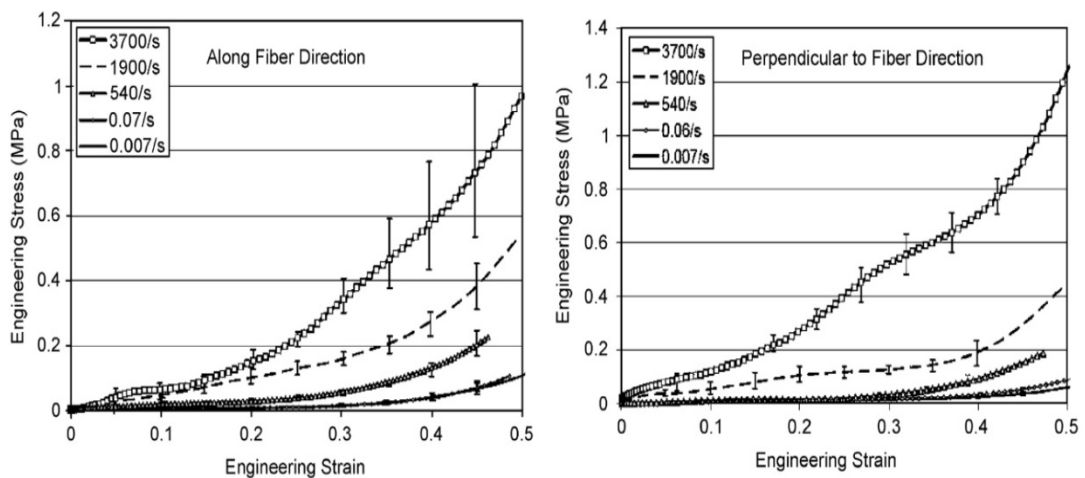


Figure 3.8: Stress-strain curves for a range of load rates for porcine muscle tissue in compression in the fibre (left) and cross-fibre (right) direction. Reproduced from Song et al. 2007

Bosboom et al. 2001 performed compression tests on surgically exposed rat tibialis anterior muscles in the transverse direction<sup>164</sup>. Ramp and hold (20 s) tests were conducted at constant speed (25 mm/s) at different strain levels. The results showed strain level dependant stress relaxation behaviour. Using plane stress FEA, and assuming isotropy, a constitutive law was formulated using a first order Ogden model ( $\mu = 15.6 \pm 5.4 \text{ kPa}$  and  $\alpha = 21.4 \pm 5.7 \text{ kPa}$ ) to capture elasticity and viscoelasticity was modelled

using a single term Prony series expansion ( $\gamma = 0.549 \pm 0.056$  and  $\tau = 6.01 \pm 0.42$  s) (see also section 2.2.12.2).

Van Loocke *et al.* 2006<sup>21</sup> investigated the non-linear elastic properties of muscle tissue by subjecting fresh (tested within 2 hours post-mortem) cuboid porcine gluteus maximus samples to uni-axial unconfined quasi-static (30% strain at  $0.05\% \text{ s}^{-1}$ ). In addition anisotropy was investigated by loading samples at the following angles  $\alpha=0^\circ$  (fibre direction),  $30^\circ$ ,  $45^\circ$ ,  $60^\circ$  and  $90^\circ$  (cross-fibre direction), with respect to the fibre direction. A schematic representation of the used loading configuration is shown in Figure 3.9. During the compression tests deformation was optically tracked with surface markers to compute Poisson's ratios. The quasi-static compression results are shown in Figure 3.10 (reproduced from<sup>21</sup>).

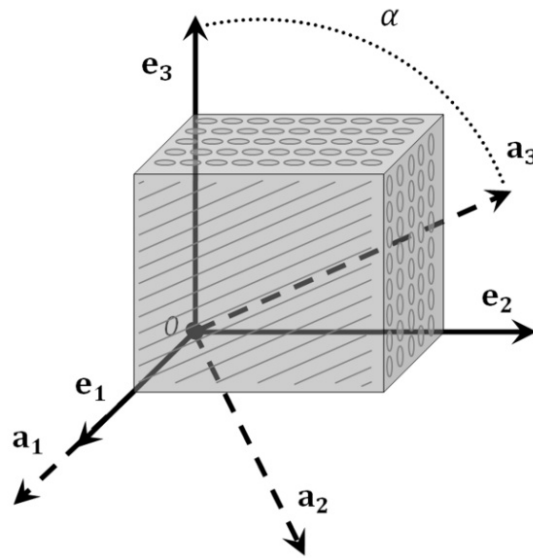


Figure 3.9. Schematic representation of a cuboid sample showing muscle fibre direction  $\mathbf{a}_3$  at an angle  $\alpha$  with respect to the loading axis  $\mathbf{e}_3$

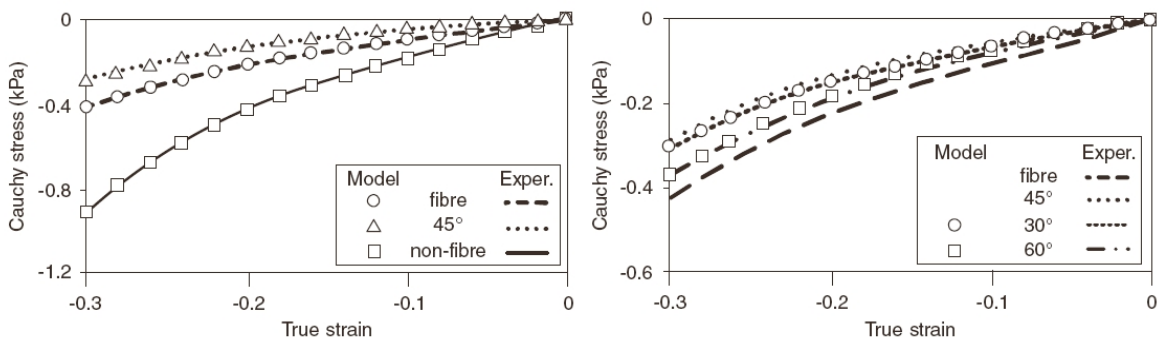


Figure 3.10: Experimental data from compression tests on fresh porcine samples fitted with the SYM model. The fibre,  $45^\circ$  and cross-fibre direction (left), the additional  $30^\circ$  and  $60^\circ$  orientations (right). Reproduced from Van Loocke *et al.* 2006

The cross-fibre direction was stiffest and loading at  $45^\circ$  produced the softest response indicating a complex anisotropic behaviour. The Poisson's ratios found are illustrated in Figure 3.11.

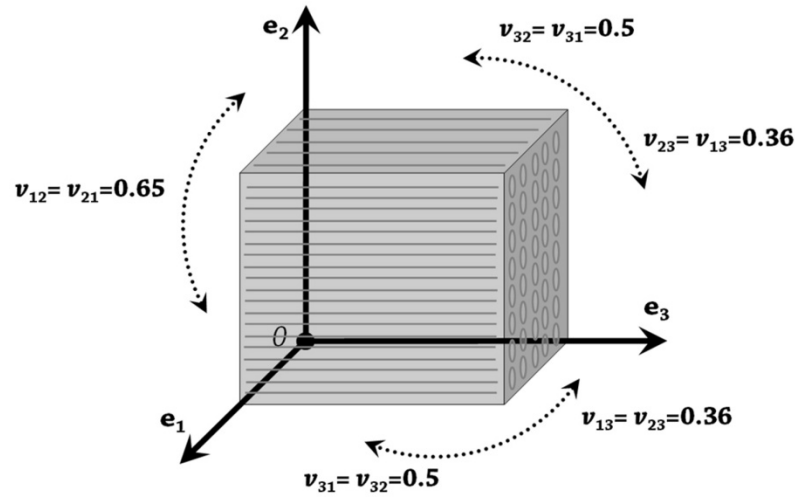


Figure 3.11. Schematic representation of a cuboid sample showing the various Poisson's ratios from Van Loocke *et al.* 2006 and the fibre direction aligned with  $e_3$ .

A constitutive model was proposed to describe the anisotropic behaviour based on classic (non-fibre reinforced, two stiffness directions) transverse isotropy. However unfortunately the Poisson's ratios measured and stiffness levels fitted are not compatible with a classic transversely isotropic model. For classic transverse isotropy  $\frac{\nu_{12}}{E_1} = \frac{\nu_{31}}{E_3}$  (with  $E_i$  Young's Moduli) and therefore  $\frac{E_3}{E_1} = \frac{\nu_{31}}{\nu_{13}} = \frac{0.5}{0.36} \approx 1.39$ , which dictates  $E_3 > E_1$ . However in order to let the cross-fibre direction be stiffest Van Loocke *et al.* 2006 enforced the opposite  $E_1 > E_3$  ( $E_1 = E_2$ ).

Due to near incompressibility when the muscle is loaded in (unconfined) compression the Poisson's effect induces a tensile expansion in the other directions. The Poisson's ratios measured by Van Loocke *et al.* 2006 indicate that when muscle is compressed transverse to the fibre direction ( $e_2$  in Figure 3.11) the fibre direction ( $e_3$  in Figure 3.11) resists this tensile loading more than the other transverse direction ( $e_1$  in Figure 3.11). This suggests a reinforcing structure exists in the fibre direction which is capable of resisting tension and which adds to the stiff response for transverse loading. In compressive loading in the fibre direction the Poisson's effect is homogeneous in both transverse directions. The fact that loading in this direction produces a softer response than for transverse loading indicates that apparently the reinforcing structure does not contribute to the same extent in compression. This suggests that the reinforcing fibrous components which acted during Poisson's effect induced tension for transverse loading are perhaps not contributing in compression due to fibrous buckling. This supports the hypothesis that the transverse and along fibre behaviour can be explained by a fibre reinforcing structure which is tension compression non-linear due to buckling of fibres in

compression. The measured Poisson's ratios and stiffness responses effectively exclude constitutive models that are not tension-compression non-linear.

In a later study by Van Loocke *et al.* 2008<sup>158</sup> similar experiments were conducted to study the viscoelastic behaviour of muscle tissue using stress-relaxation (30% strain at 0.5 %/s<sup>-1</sup>, 1 %s<sup>-1</sup>, 5 %s<sup>-1</sup> and 10 %s<sup>-1</sup>) compression tests on fresh porcine gluteus maximus samples. Loading was applied at  $\alpha=0^\circ$ , 45°, 60° and 90° with respect to the fibre direction. These experimental results are shown in Figure 3.12. The viscoelastic behaviour could be captured using a 5 term Prony series expansion (see also section 2.2.12.2 ) (however the elastic contribution was due to the transversely isotropic model proposed in Van Loocke *et al.* 2006<sup>21</sup>). These data demonstrate that muscle tissue is viscoelastic in compression and that the effect varies depending on fibre angle.

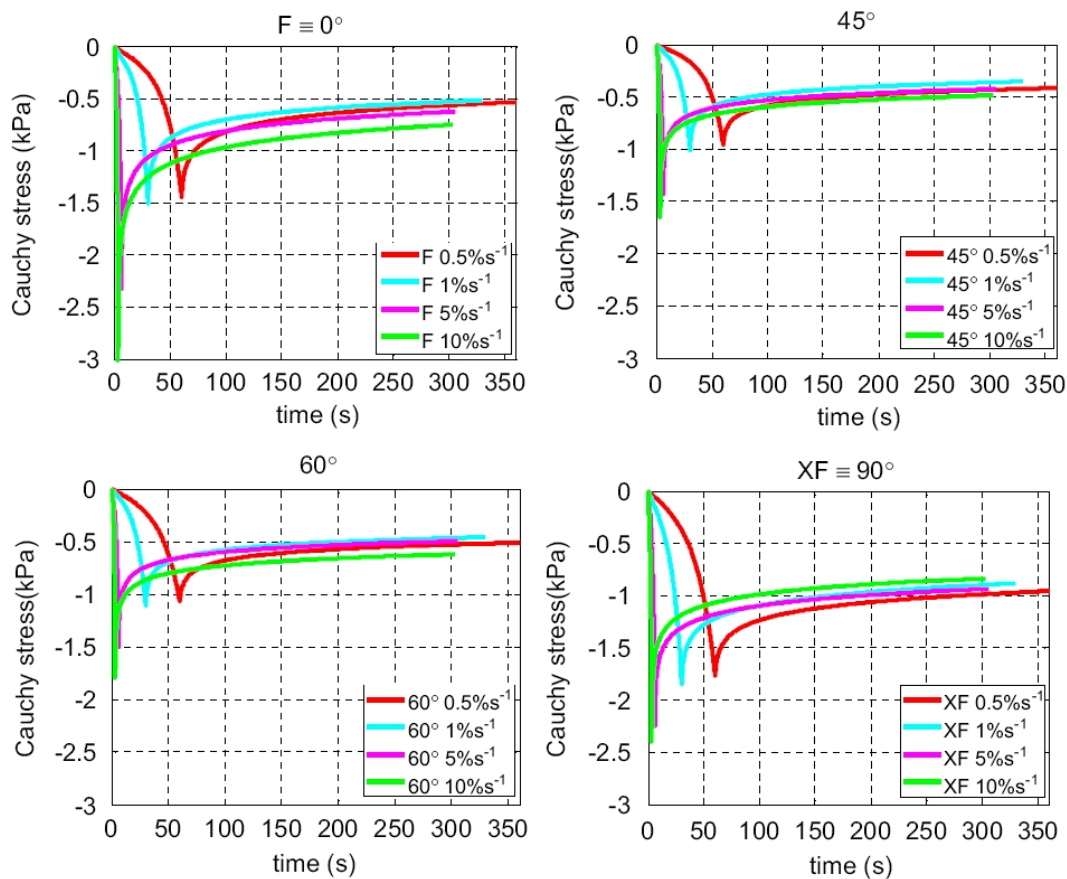


Figure 3.12: Stress-relaxation curves, from van Loocke *et al.* 2008, comparing muscle stress-relaxation behaviour at various (0.05% s<sup>-1</sup>, 0.5% s<sup>-1</sup>, 1% s<sup>-1</sup>, 5% s<sup>-1</sup> and 10% s<sup>-1</sup>) and various fibre orientations (0°, 45°, 60° and 90°).

### 3.3.2.2 Tensile behaviour

To date the passive tensile behaviour of skeletal muscle tissue has largely been limited to force length relationships when combined with active force-length models (e.g.<sup>165</sup>). Such data is however not directly suitable for detailed anisotropic mechanical property modelling and are thus not discussed. Only recently (many of the papers reviewed here

were published within the year of writing this thesis) has the passive tensile behaviour been investigated in more detail and for multiple fibre orientations.

Calvo *et al.* 2010<sup>24</sup> studied the passive tensile behaviour of fresh (tested within 10 minutes) rat tibialis anterior muscles samples in the fibre direction (up to stretch of 1.72 and a strain rate of 0.025 %s<sup>-1</sup>). A fibre reinforced transversely isotropic material model was fit to the experimental data with a strain energy density function described by:

$$\Psi_{total} = \Psi_{gm} + \Psi_f \quad 3-1$$

Where  $\Psi_{gm} = c_1(\tilde{I}_1 - 3)$  represents a Neo-Hookean ground matrix and the fibre strain energy function  $\Psi_f$  is defined by:

$$\Psi_f = \begin{cases} \frac{c_3}{c_4} e^{c_4(\tilde{I}_4 - \tilde{I}_{40})} - c_4(\tilde{I}_4 - \tilde{I}_{40}) - 1 & \tilde{I}_{4ref} > \tilde{I}_4 > \tilde{I}_{40} \\ c_5\sqrt{\tilde{I}_4} + \frac{1}{2}c_6 \ln(\tilde{I}_4) + c_7 & \tilde{I}_4 > \tilde{I}_{4ref} \\ 0 & \tilde{I}_4 < \tilde{I}_{40} \end{cases} \quad 3-2$$

With  $\tilde{I}_4$  the isochoric pseudo-invariant relatable to the fibre stretch as  $\tilde{\lambda}_f = \sqrt{\tilde{I}_4}$  (see also section 2.2.11 ). Here  $\tilde{I}_{40}$  represents the stretch at which fibres start to act and  $\tilde{I}_{4ref}$  where they are straightened. The mean experimental data (the mean parameters presented are ignored since average parameters of separate non-linear fits are invalid) and a model fit ( $c_1 = 1.00 \cdot 10^{-3}$  MPa,  $c_3 = 5.39 \cdot 10^{-2}$  MPa,  $c_4 = 0.78$ ,  $c_5 = 5.74$ ,  $c_6 = -9.04$ ,  $c_7 = -4.88$ ,  $\tilde{I}_{40} = 1.25$ ,  $\tilde{I}_{4ref} = 3.19$ ) are shown in Figure 3.13. The experimental data clearly show non-linearity in tension which the constitutive model is able to capture. However with the large amount of parameters used the uniqueness of the fit may be questioned. Especially given that the parameters were only fitted for fibre direction tensile loading which perturbs both the ground matrix and fibres simultaneously hindering the clear separation of their respective contributions. The parameters for the ground matrix were more than an order of magnitude lower than for the fibre contribution. It is likely that this difference is due to the rather linear Neo-Hookean ground matrix used, which means that the non-linearity in this model is almost solely due to the fibre contribution. The parameter  $\tilde{I}_{40}$  was 1.25, hence the model predicts isotropic Neo-Hookean behaviour (no influence of fibres) until a fibre stretch of  $\sqrt{\tilde{I}_{40}} \approx 1.12$  has been exceeded which is not in agreement with findings by other authors which demonstrate anisotropy in this region (e.g. <sup>22, 166, 167</sup>). In addition since the

parameter  $\tilde{I}_{4ref}$  was 3.19 the model contains straightened fibres after a fibre stretch of  $\sqrt{\tilde{I}_{4ref}} \approx 1.79$  has been exceeded. However the muscle test results used were only up to a tensile stretch of 1.72. Therefore it seems that during the curve fitting optimisation  $\tilde{I}_{4ref}$  was pushed beyond the test range. Hence it appears that the curve fitting based optimisation did not allow fibres to be straightened yet in the range tested. Therefore the parameters:  $\tilde{I}_{4ref}$ ,  $c_5$ ,  $c_6$  and  $c_7$  do not have any contribution for the range tested and their values are not validated by the test data. This model was recently expanded by Grasa *et al.* 2011<sup>168</sup> to include muscle pre-strain and evaluation for along fibre stretch only was presented.

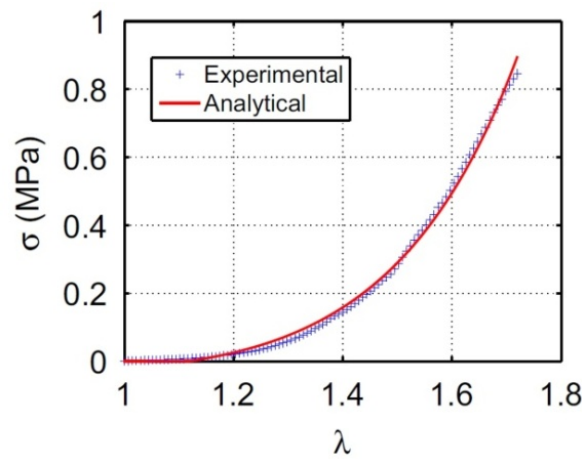


Figure 3.13: Average rat skeletal muscle stress –stretch curve and model fit. Reproduced from Calvo *et al.* 2010.

In a recent study by Nie *et. al.* 2011<sup>166</sup> fresh porcine muscle tissue was subjected to tensile loading in the fibre and cross-fibre directions at strain rates of 0.05 %s<sup>-1</sup>, 0.4 %s<sup>-1</sup>, 0.4 %s<sup>-1</sup>, 700 %s<sup>-1</sup>, 1400 %s<sup>-1</sup> and 2100 %s<sup>-1</sup>. The results (Figure 3.14) show a non-linear tensile stress-strain response for both the fibre and cross-fibre direction. The response was also found to be highly dependent on strain rate in both directions due to viscoelasticity. Anisotropy in tension is evident and the cross-fibre directions presented with higher stress responses than the fibre directions.



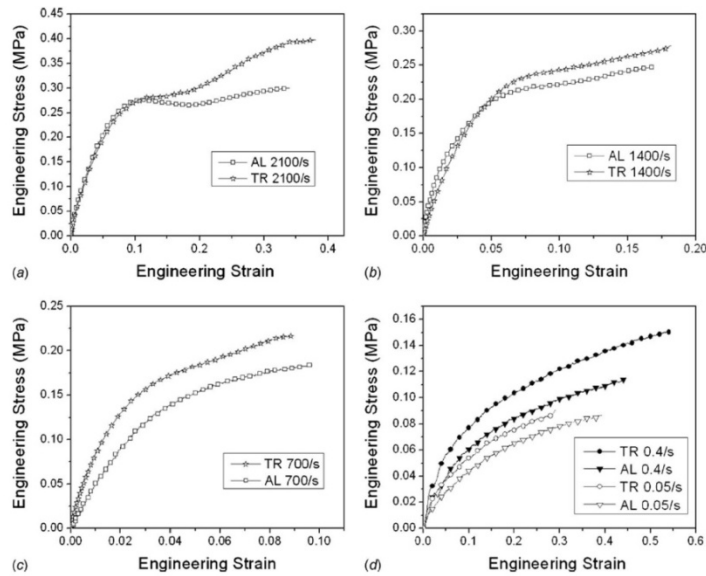


Figure 3.14.: Stress-strain curves of porcine muscle samples for the fibre direction (AL) and cross-fibre direction (TR). Reproduced from Nie *et al.* 2011.

Morrow *et al.* 2011<sup>167</sup> applied tensile testing to rabbit (extensor digitorum longus) muscle tissue samples. Tensile load at a strain rate of  $0.05\ \%s^{-1}$  was applied in the fibre and cross-fibre directions and longitudinal shear tests were performed. Due to the way the data is presented it is not usable for detailed anisotropic constitutive model fitting. Instead Morrow *et al.* 2011 present linear moduli (average slope of curves in linear regions) which were  $447 \pm 97.7$  kPa,  $22.4 \pm 14.7$  kPa and  $3.87 \pm 3.39$  kPa respectively for the fibre tension, cross-fibre tension and along fibre shear tests respectively.

In a recent study by Takaza *et al.* (unpublished)<sup>22</sup> the tensile behaviour of fresh (within two hours post-mortem) porcine skeletal muscle tissue was investigated in great detail. Similar to the approach by Van Looke *et al.* 2006<sup>21</sup> for compression, samples (approximately  $10 \times 10 \times 50$  mm) were subjected to uni-axial quasi-static tension at a strain rate of  $0.05\ \%s^{-1}$  for the following fibre angles with respect to the load axis:  $\alpha = 0^\circ$  (fibre direction),  $30^\circ$ ,  $45^\circ$ ,  $60^\circ$  and  $90^\circ$  (cross-fibre direction) (see also Figure 3.9). The average experimental curves are shown in Figure 3.15. The tissue was clearly anisotropic in nature as the response varied greatly with fibre angle. It appears that in tension the transverse direction plays an important role since the stress response increases dramatically as the fibre angle is rotated from  $0^\circ$  to  $90^\circ$  with respect to the load axis. The degree of non-linearity however appears to decrease with fibre angle.

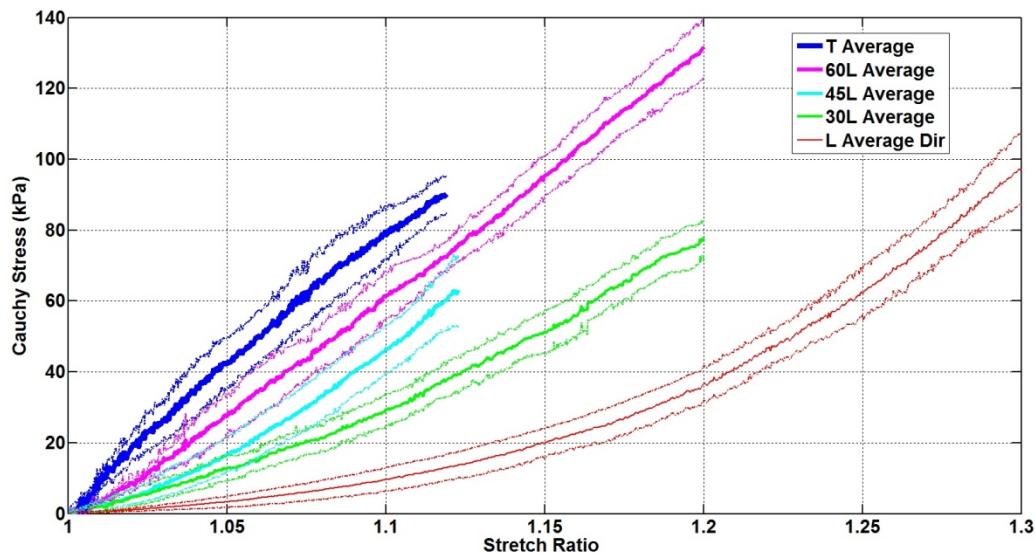


Figure 3.15: The tensile response of porcine muscle tissue at various fibre orientations ( $0^\circ$ ,  $30^\circ$ ,  $45^\circ$ ,  $60^\circ$  and  $90^\circ$ ). Thick curves describe the mean and thin curves above and below plus and minus one standard deviation. Reproduced from Takaza et al. (unpublished).

Takaza et al. (unpublished)<sup>22</sup> also recorded deformation using optical tracking of surface markers. This led to the derivation of Poisson's ratios for tension which are schematically illustrated in Figure 3.16.

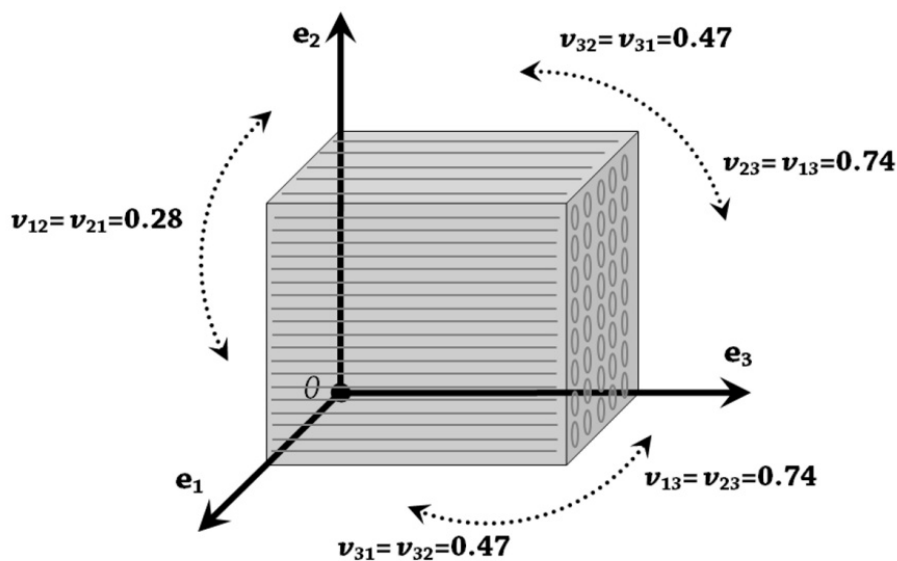


Figure 3.16. Schematic representation of a sample showing the various Poisson's ratio from Takaza et al. (unpublished) and the fibre direction aligned with  $e_3$ .

Due to near incompressibility of muscle tissue tensile loading induces compressive contractile loads in the orthogonal directions to the load. The Poisson's ratios measured by Takaza et al. (unpublished) indicate that for unconfined tensile loading in the transverse direction ( $e_2$  in Figure 3.16) the fibre direction ( $e_3$  in Figure 3.16) contracts more than the other transverse direction ( $e_1$  in Figure 3.16). This indicates that the fibre

direction is more compliant in Poisson's effect induced contraction than the transverse or cross fibre direction.

Takaza et al. (unpublished) also compared their fibre (L) and cross-fibre (T) results with the before mentioned papers by Calvo et al. 2010, Nie et al. 2011 and Morrow et al. 2010, see Figure 3.17 (modified from<sup>22</sup>).

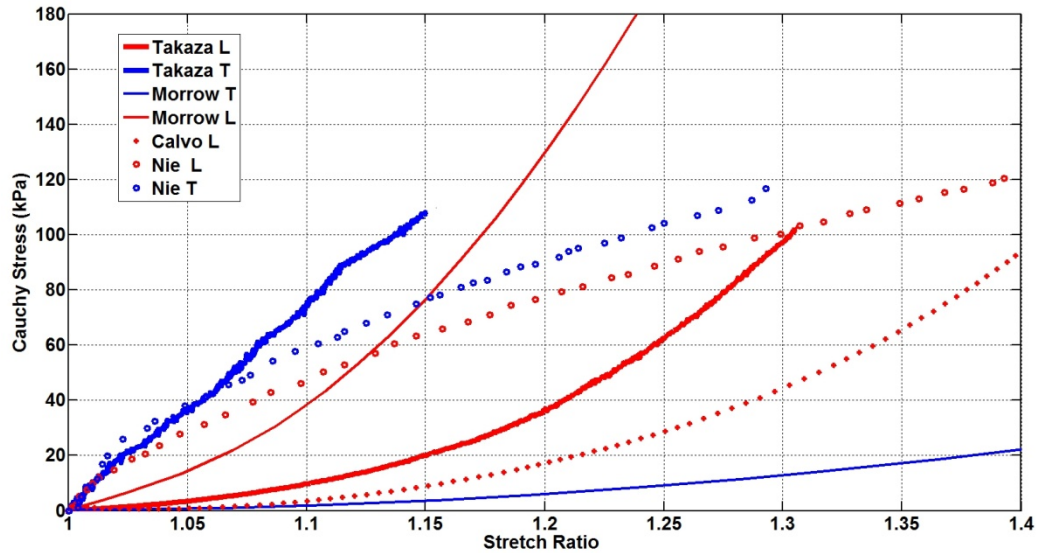


Figure 3.17: Comparison of fibre (L) and cross-fibre (T) tensile stress-stretch data from the literature. Modified from Takaza et al. (unpublished).

As Figure 3.17 shows a large degree of variation exists in the literature. However all authors agree on non-linearity and anisotropy of muscle tissue in tension and the cross-fibre direction is often reported to be stiffer than the fibre direction.

### 3.3.3 *Non-invasive mechanical property assessment*

In general the non-invasive analysis of the mechanical properties of soft tissue follows three main steps: 1) *Mechanical excitation of the tissue of interest (e.g. indentation or vibration)*, 2) *Measurement of experimental boundary conditions (geometry, loading conditions and resulting mechanical state of the tissue i.e. deformation)*, 3) *inverse analysis of the experimental boundary conditions to yield constitutive parameters (e.g. inverse FEA of the mechanical experiment)*. Experimental set-ups may vary depending on the mechanical property of interest. For instance the study of linear elasticity may involve quasi-static deformations and force measurements. Non-linear elasticity requires multiple and large strain measurements. Anisotropy requires analysis of tissue architecture and detailed 3D deformation measurement. Viscoelasticity requires dynamic measurements. This section summarises efforts found in the literature to analyse the mechanical properties of muscle

tissue non-invasively. The focus is on large strain (e.g. indentation) studies since these are most relevant to the current thesis.

Several authors have conducted indentation experiments to non-invasively derive soft tissue mechanical parameter estimates. For instance Zheng et al. 1999<sup>169</sup> performed indentation on volunteer leg soft tissue sites using a 9 mm in diameter hand-held ultrasound transducer. During indentation tissue thickness, a measure of compression level, was derived through ultrasound while probe indentation force was measured using a load-cell. The mechanical behaviour of skin, adipose and muscle tissue was jointly modelled assuming isotropic linear elasticity and Young's modulus estimates could be derived through analytical solutions for the indentation problem. Similarly Vannah and Childress 1996<sup>170</sup> studied the quasi-static bulk properties of muscular tissue *in-vivo* using indentation tests on volunteer posterior lower legs while indenter displacement and force were recorded. The mechanical behaviour was evaluated following CT scan derived FE modelling. Within the FE model skin, adipose and muscle tissue were jointly modelled as a single homogeneous and isotropic hyperelastic material. In comparable work by Tönük et al. 2004<sup>171</sup> subject specific elastic and viscoelastic material behaviour of lower extremity residual limb soft tissue in amputees were studied. Here a soft tissue indenter was applied and assuming local homogeneity, isotropy and axisymmetric loading conditions (through inverse axisymmetric 2D FEA) constitutive parameters could be derived. However, all the above indentation studies assume isotropic behaviour and jointly model skin, adipose and muscle tissue as a single material and the inverse analysis is based on mostly external boundary conditions (indentation force and displacement) only or limited to ultrasound based tissue thickness measurement rather than 3D tissue deformation. Hence these methods find their main application in the estimation of mechanical conditions in amputee tissue and prosthesis interactions (e.g.<sup>5</sup>) and they do not allow for the investigation of anisotropic 3D constitutive behaviour.

In a study focussed on the evaluation of the treatment of prophylaxis and venous disorder using compressive garments (tight leg socks), Dubuis et al. 2011<sup>172</sup> performed inverse analysis to determine mechanical parameters of lower leg soft tissue. Compressive socks were applied to volunteers and CT scans were taken before and after sock application providing the initial and target geometry for FEA (see Figure 3.18, composed using images from<sup>172</sup>). Using knowledge on the mechanical properties of the sock material and the CT scan derived geometric boundary conditions material

parameters were determined using inverse FEA. The model parameters were adjusted until a best match was achieved for a cost function defined on the contour radii along the length axis of the bone (Figure 3.18D). The soft tissues were assumed to be nearly incompressible, homogeneous, isotropic and Neo-Hookean hyperelastic using the following decoupled Neo-Hookean formulation:

$$\Psi(\tilde{I}_1) = \frac{\mu}{2}(\tilde{I}_1 - 3) + \frac{\kappa}{2}(J - 1)^2 \quad 3-3$$

With  $\mu$  the Neo-Hookean shear modulus and  $\kappa$  the bulk modulus. Bone was effectively modelled as rigid and two soft tissue material groups were modelled 1) *skin and adipose tissue*, 2) *muscle and tendonous tissue* (Figure 3.18).

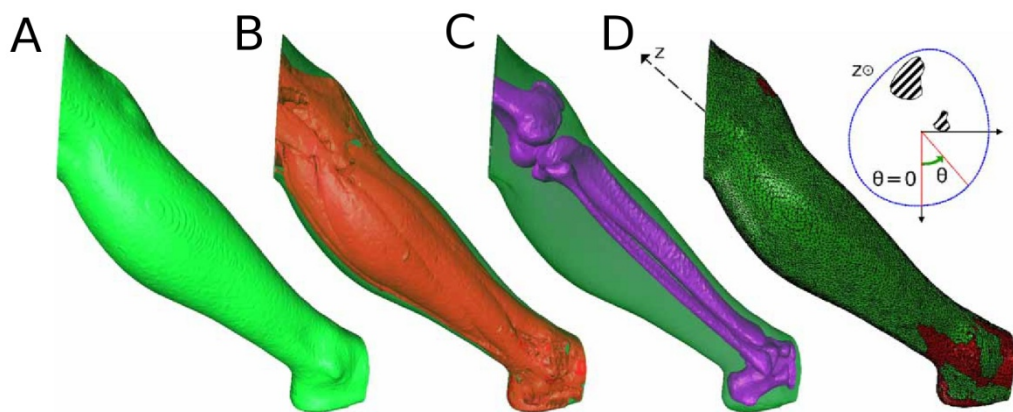


Figure 3.18. CT derived geometry (A), material boundaries (B), bone boundary (C) and FE model and a schematic illustration of the z axis and angle dependant contour radius for the cost function (D). Composed using images from Dubuis et al. 2011.

The material parameters which minimized the cost function were  $\mu = 11.1$  kPa and  $\kappa = 1.06$  MPa for material group 1 and  $\mu = 5.8$  kPa and  $\kappa = 1.16$  MPa for material group 2. The methods presented are appropriate for bulk material property assessment however anisotropic model evaluations require more detailed measures of internal strains rather than contour shape matching.

Using an MRI compatible loading device Tran *et al.* 2007<sup>173</sup> subjected volunteers to indentation (driven by static weights) of forearm soft tissue and applied 2D inverse FEA to derive isotropic Neo-Hookean hyperelastic (similar to equation 3-3) parameters for skin (epidermis, dermis and hypodermis) and muscle tissue. As shown in Figure 3.19, the 2D inverse FEA parameter optimisation minimized the difference between simulated and experimental forces and MRI derived 2D contour shapes. The average Neo-Hookean parameters found for muscle were  $\mu = 7.28 \pm 0.52$  kPa and  $\kappa = 143.78 \pm 74.98$  kPa.

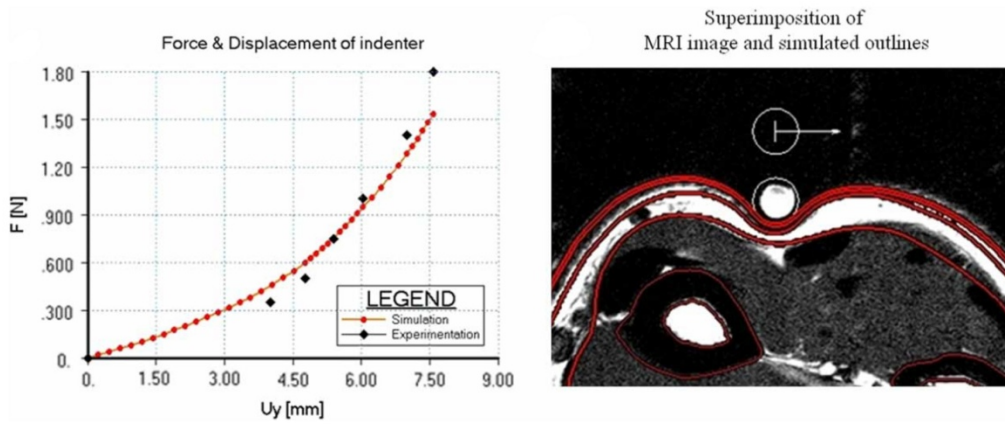


Figure 3.19. Experimental and simulated force displacement (left) and 2D contour shape (right) comparison for indentation of the forearm. Composed using images from Tran et al. 2007.

Ceelen et al. 2008<sup>174</sup> used an approach akin to the current thesis. Indentation was applied to rat lower leg muscles inside an MRI scanner. During indentation the resulting tissue deformation was studied using 1D SPAMM tagged MRI (Figure 3.20A-B) and indenter force was also recorded. The latter was used for verification of indentation timing with respect to imaging. The SPAMM derived deformation data was used not for constitutive parameter identification but rather for the validation of the inverse FEA (Figure 3.20C, composed using images from) based estimation of strain levels *in-vivo*. Strain levels were estimated from 2D plane stress FEA under the assumption of a single incompressible and linear Neo-Hookean material behaviour for all soft tissues (skin, adipose and muscle) of the leg. Since the FEA derived stresses were normalised with respect to the Neo-Hookean stiffness parameter the constitutive model served only as a means of capturing the incompressibility and deformation levels observed.

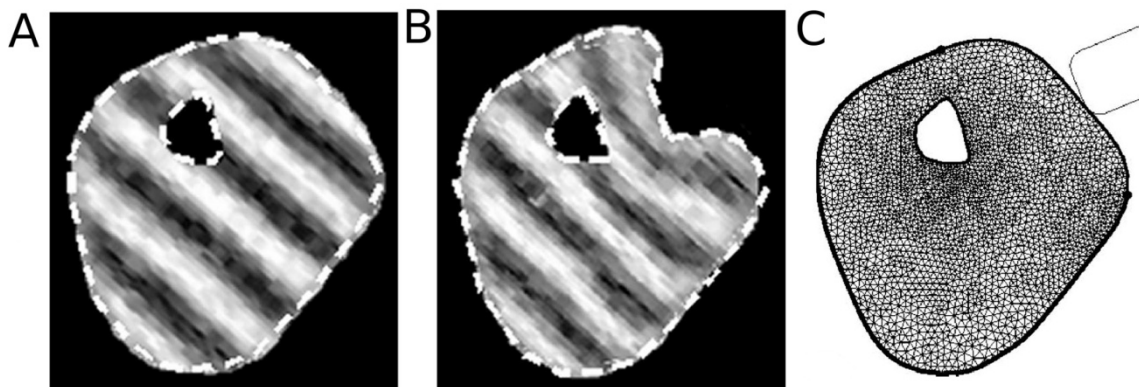


Figure 3.20. 2D SPAMM tagged MRI in a rat leg in un-deformed (A) and deformed configuration (B) and an MRI derived 2D FEA model. Composed using images from Ceelen et al. 2008.

Blemker et al. 2005<sup>23, 24</sup> proposed a model for the passive and active behaviour of muscle tissue. An anisotropic strain energy density function was proposed of the form:

$$\Psi(J, \beta_3, \beta_4) = \Psi_{vol}(J) + \Psi_{dev}(\beta_3, \beta_4, \lambda, \alpha) \quad 3-4$$

Where  $\Psi_{vol}(J) = \frac{\kappa}{2} \ln(J)^2$  describes the dilatational response and  $\Psi_{dev}(\beta_3, \beta_4)$  the deviatoric response defined by:

$$\Psi_{dev}(\beta_3, \beta_4, \lambda, \alpha) = \Psi_1(\beta_4(\tilde{I}_4, \tilde{I}_5)) + \Psi_2(\beta_3(\tilde{I}_1, \tilde{I}_4, \tilde{I}_5)) + \Psi_3(\lambda(\tilde{I}_4), \alpha) \quad 3-5$$

with  $\tilde{I}_i$  the modified deviatoric strain invariants,  $\beta_i$  the invariants due to Criscione *et al.* 2001<sup>66</sup> (see section 2.2.11 and equations 2-86),  $\lambda$  the fibre stretch. The strain energy components  $\Psi_1$  and  $\Psi_2$  are given by:

$$\begin{aligned} \Psi_1(\beta_4) &= c_1 \beta_4^2 \\ \Psi_2(\beta_3) &= c_2 \beta_3^2 \end{aligned} \quad 3-6$$

where  $c_1$  and  $c_2$  represent along-fiber shear and cross-fibre shear material parameters respectively. Blemker *et al.* 2005<sup>23</sup> modelled the along fibre strain energy as  $\Psi_3(\lambda(\tilde{I}_4), \alpha) = \Psi_{passive}(\lambda(\tilde{I}_4)) + \Psi_{active}(\lambda(\tilde{I}_4), \alpha)$  with  $\alpha$  a muscle activity parameter. However only the passive response  $\Psi_{passive}(\lambda(\tilde{I}_4))$  is relevant to the current thesis and was formulated (similar to equation 3-2 used by Calvo *et al.* 2010<sup>24</sup>) such that the passive force in the fibre  $f_{passive}(\lambda)$  becomes:

$$f_{passive}(\lambda) = \begin{cases} c_3 \left( e^{c_4 \left( \frac{\lambda}{\lambda_{ofl}} - 1 \right)} - 1 \right) & \lambda_{ofl} < \lambda < \lambda^* \\ c_5 \frac{\lambda}{\lambda_{ofl}} + c_6 & \lambda \geq \lambda^* \\ 0 & \lambda \leq \lambda_{ofl} \end{cases} \quad 3-7$$

Here  $P_i$  are material parameters,  $\lambda^*$  is the stretch at which the fibre behaviour becomes linear and  $\lambda_{ofl}$  (so called optimal fibre stretch) is the stretch at which fibres start to act. The material model was partially evaluated by comparing regional strain averages from FEA simulations and *in-vivo* experimental deformation estimates derived from phase contrast MRI during (64 repetitions per image slice) biceps brachii contractions (from Pappas *et al.* 2002<sup>175</sup>). However since Blemker *et al.* 2005<sup>23</sup> used  $\lambda_{ofl} = \lambda^* = 1.4$  the passive response is isotropic until a fibre stretch of 1.4 has been exceeded and once this has occurred the passive fibre response is linear (i.e. condition  $\lambda_{ofl} < \lambda < \lambda^*$  is never satisfied in equation 3-7). In addition for uni-axial loading (e.g. tension up to 1.4 or compressive loading) in the fibre direction  $\lambda \leq \lambda_{ofl}$  leads to a zero contribution in the fibre direction and, since for this type of loading  $\beta_3 = \beta_4 = 0$ , the total deviatoric stresses are zero. Therefore in this case the material response is solely dictated by the

volumetric hydrostatic pressure term  $\Psi_{vol}(J)$ . The passive material stiffness for this model is thus not fully defined for all types of loading directions.

Another common approach to non-invasive investigation of the mechanical properties of soft tissue is elastography. In elastography the tissue surface is oscillated with a known frequency resulting in strain waves which propagate through the material. Through non-invasive imaging of the tissue deformation and inverse analysis of the speed and attenuation of the measured shear waves, theoretical shear stiffness and viscosity parameters can be derived for the specific deformation level and stimulus frequency. In general, elastography methods assume linear elasticity and local homogeneity. Two types of elastography methods are commonly applied to soft tissue 1) based on MRI, MR Elastography (MRE) (see review article<sup>32</sup> and section 2.3.10.4 ) and 2) based on ultrasound imaging Ultrasound Elastography (USE) (see review article<sup>176</sup>). Figure 3.21 summarises MRE<sup>116, 119, 121, 177-180</sup> and USE<sup>181, 182</sup> based shear modulus measures for muscle tissue reported in the literature. As demonstrated a formidable degree of variation exists in the values in the literature as the shear moduli reported vary more than an order of magnitude. Even for the same muscle type in human volunteers shear moduli ranging from  $0.92 \pm 0.55$  kPa<sup>182</sup> up to  $29.3 \pm 6.2$  kPa<sup>117</sup> are reported. The difference found may be due to subject variation, experimental set-up and hardware, muscle regions, analysis orientations, imaging modalities and inversion methods employed. In relation to inversion methods it has been shown that shear moduli may be under-/overestimated depending on how realistic the mechanical model is that is assumed in the inversion of the wave data<sup>183</sup>. In addition the incorporation of viscoelastic effects, which is not always included, is important for the accurate derivation of the shear modulus measurements<sup>184</sup>. It has also been shown that the local geometry effects (e.g. due to wave reflections and interactions) influence the measured wave speeds and may lead to artefacts in the elastic parameter derivation<sup>185</sup>.

The majority of elastography methods in the literature assume linear elasticity and viscosity, isotropy and local homogeneity. In addition tension-compression non-linearity is not incorporated. Recently inversion methods have been employed which also incorporate viscoelasticity and anisotropy (e.g.<sup>120, 180, 186</sup>). However in many cases simple rheological models such as the Voigt model<sup>120, 186</sup> are employed. Due to the parallel spring and dashpot arrangement this model does not allow instantaneous elasticity and is therefore not suitable for constitutive modelling. Due to the current small strain (e.g.  $<3$



%) limitations of elastography methods, and the assumptions of linearity currently required in the inversion of the image data, the techniques are thus more appropriate for diagnostic imaging of tissue stiffness changes (e.g. to detect lesions<sup>25</sup> or liver fibrosis<sup>187</sup>) rather than for constitutive modelling.

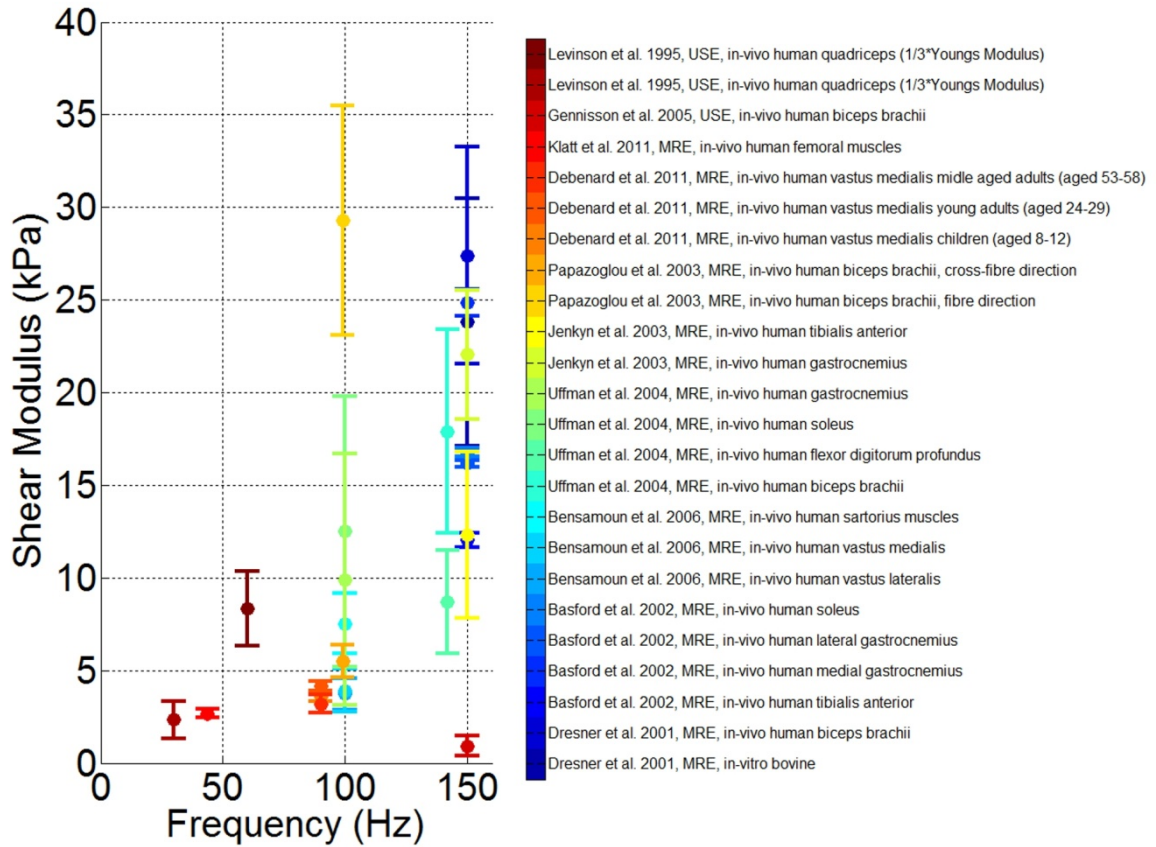


Figure 3.21. Summary of elastography derived shear modulus values for muscle tissue in the literature. Data entries are coloured according to study as indicated by the colorbar.

### 3.3.4 Comments on constitutive modelling of skeletal muscle tissue

The previous sections already highlighted some of the constitutive modelling approaches in relation to experimental investigations. In small strain non-invasive elastography studies where the focus lies on small strain properties, soft tissue is often represented as linear and isotropic (see review article<sup>32</sup>). In large strain non-invasive external loading experiments (such as leg compression<sup>172</sup>) tissue is often represented by isotropic hyperelastic formulations. However skeletal muscle is anisotropic in both tension<sup>22</sup> and compression<sup>21</sup>. In the current thesis modelling of the non-linear anisotropic behaviour of muscle is of interest.

The most common approach to modelling of transverse isotropy is to assume a strain energy function of the following general form:

$$\Psi = \Psi_{gm} + \Psi_f \quad 3-8$$

where  $\Psi_{gm}$  and  $\Psi_f$  represent an isotropic ground matrix and a fibre contribution respectively. The fibre contribution is modelled using a single fibre family aligned with the axis of transverse isotropy. Inherent in this modelling approach is that  $\Psi_f$  is *added* as a *reinforcing* structure to an isotropic ground matrix. Often tension compression non-linearity is induced by letting  $\Psi_f$  take a form similar to:

$$\Psi_f = \begin{cases} \Psi_{f\_tension} & \tilde{\lambda}_f > 1 \\ 0 & \tilde{\lambda}_f \leq 1 \end{cases} \quad 3-9$$

where  $\Psi_{f\_tension}$  is the strain energy function for tension and  $\tilde{\lambda}_f$  the deviatoric fibre stretch. Therefore the reinforcing effect of  $\Psi_f$  is strongest in tension and smallest (i.e. zero in compression) hence in general these models predict an increase in the stress response for tensile loading when the load angle is rotated from being orthogonal to being aligned with the fibre orientation and the opposite for compression. This approach may therefore not enable modelling of more complex anisotropic behaviour (e.g. the intermediate angle softening observed by Van Looke *et al.* 2006<sup>21</sup>).

Recently other so called polyconvex hyperelastic approaches to modelling anisotropy based on generalised structure tensors have been proposed (e.g. Schröder *et al.* 2003<sup>188</sup>, Ehret *et al.* 2007<sup>63</sup>) and related model formulations have been applied to the study of combined active and passive skeletal muscle behaviour (e.g. Odegard *et al.* 2008<sup>189</sup>, Mathyr *et al.* 2010<sup>10</sup> and Ehret *et al.* 2011<sup>190</sup>). For instance Ehret *et al.* 2011<sup>190</sup> who modelled the passive properties of muscle using the strain energy function:

$$\Psi = \frac{\mu}{4} \left\{ \frac{1}{\alpha} (e^{\alpha(I_p-1)} - 1) + \frac{1}{\beta} (e^{\beta(\tilde{K}-1)} - 1) \right\} \quad 3-10$$

here  $\mu$ ,  $\alpha$  and  $\beta$  are material parameters,  $\tilde{I}_p$  and  $\tilde{K}$  are so called generalised invariants:

$$\begin{aligned} \tilde{I}_p &= \frac{w_o}{3} \text{tr}(\mathbf{C}) + (1 - w_o) \text{tr}(\mathbf{CA}) \\ \tilde{K} &= \frac{w_o}{3} \text{tr}(\mathbf{C}^{-1}) + (1 - w_o) \text{tr}(\mathbf{C}^{-1}\mathbf{A}) \end{aligned} \quad 3-11$$

$$\text{with } \det(\mathbf{C}) = 1$$

with  $w_o$  a weight factor (material parameter) for the isotropic ( $w_o$ ) and muscle fibre behaviour ( $1 - w_o$ ). The texture tensor  $\mathbf{A} = \mathbf{a} \otimes \mathbf{a}$  is defined by the unit vector  $\mathbf{a}$  specifying the fibre direction. The term  $\text{tr}(\mathbf{CA})$  is the square of the stretch in the fibre

direction and  $\text{tr}(\mathbf{C}^{-1}\mathbf{A})$  relates to squared cross-sectional area of the fibre in the transverse direction. In this constitutive formulation the fibre reinforcement is not nulled in compression. Hence this transversely isotropic formulation predicts that the stiffer favoured direction is stiffer both in tension and compression. However the model was only evaluated for passive along fibre extension (experimental data from<sup>191</sup>). Nonetheless the authors agree that a single stress–stretch curve is insufficient to uniquely determine the material parameters of an anisotropic material. Recently Bøl *et al.* 2011<sup>192</sup> employed the above model for passive skeletal muscle tissue in a study on the passive and active behaviour of muscle tissue *in-vivo*. A volunteer performed arm movements inside a scanner and multiple static anatomical MR images were acquired allowing FEA model construction. The passive model parameters were however derived again from only a single passive along fibre extension curve (experimental data by Calvo *et al.* 2010<sup>24</sup>). This model has not been widely implemented in available FEA software.

In addition recently micromechanical modelling approaches have also been developed (see for instance Bøl *et al.* 2010<sup>193</sup> and Sharafi *et al.* 2010<sup>194</sup>). However these modelling approaches have not been widely implemented in available FEA software and are beyond the scope of this thesis.

There are many different non-linear viscoelastic constitutive laws in the literature (see review by Drapaca *et al.* 2007<sup>68</sup>). The theory of quasi-linear viscoelasticity, also referred to as Prony series expansions (see and section 2.2.12.2 ) has been implemented for FEA (see implementation by Puso and Weiss 1998<sup>70</sup>) and has been most widely used for the modelling of biological tissues (e.g. skeletal muscle<sup>158, 159</sup>, collagen<sup>195</sup>, ligaments and tendon<sup>196</sup>, plantar tissue<sup>197</sup>, arterial tissue<sup>198</sup>, kidney<sup>199</sup> and brain<sup>200</sup>).

### 3.3.5 Conclusions

After reviewing the literature it becomes clear that mechanical properties of skeletal muscle tissue have been extensively researched. The literature available reports the mechanical behaviour of passive skeletal muscle tissue to be non-linear, anisotropic and viscoelastic in both tension and compression. In addition muscle tissue presents with tension compression non-linearity. The most detailed experimental investigations into the large strain and anisotropic non-linear elastic behaviour of skeletal muscle tissue is due to Takaza *et al.* (unpublished)<sup>22</sup> and Van Loocke *et al.* 2006<sup>21</sup> for tension and

compression respectively. These experimental data may provide the basis for the formulation of constitutive laws for the anisotropic and non-linear elastic behaviour. In addition the viscoelastic property investigation for compression presented by Van Loocke *et al.* 2008<sup>158</sup> allows for modelling of viscoelasticity for compression e.g. using Prony series expansion.

Non-invasive attempts to characterise the mechanical properties of muscle tissue include:

1) *Indentation and external force displacement based analysis*, whereby tissue properties are assumed isotropic and the constitutive behaviour of skin, adipose and muscle tissue is jointly modelled.

2) *Ultrasound and MR elastography*, are successful diagnostic stiffness assessment techniques whereby only small strain (<3%) mechanical property estimates have been presented based on assumptions of linearity, local homogeneity and often isotropy. The sensitivity of elastography derived parameters to experimental conditions (e.g. geometry) and mechanical property assumptions (e.g. linearity, Voigt behaviour) has resulted in literature values varying more than an order of magnitude.

3) *MRI based deformation measurement and model evaluation*. Whereby MRI based deformation measurement such as phase contrast MRI or (1D) SPAMM tagged MRI is employed in combination with inverse analysis. These have largely been limited to isotropic model evaluations (e.g.<sup>174</sup>) or averaged regional strain estimates (in the case of<sup>23</sup>). Detailed 3D deformation measurement combined with anisotropic model evaluation has not been performed for skeletal muscle to date.

To date the majority of constitutive modelling approaches for the non-linear elastic behaviour of passive muscle tissue have focussed on isotropic hyperelastic formulations. Transversely isotropic formulations are generally based on summing an isotropic hyperelastic ground matrix response and a single reinforcing fibre direction which only reinforces in fibre tension. Since the fibre contribution is added to the isotropic ground matrix as a reinforcing agent the approaches may not enable modelling of more complex anisotropic behaviour (e.g. the near 45 degree load angle softening observed by Van Loocke *et al.* 2006<sup>21</sup>). In addition the models proposed have not been extensively validated using multi-directional anisotropic stress-strain information.

## 3.4 Non-invasive imaging modalities

In the current thesis the mechanical properties of living human muscle tissue are of interest. In order to study living human muscle tissue *in-vivo* non-invasive imaging methods are required. A suitable imaging modality should fulfil the following requirements:

1. Capable of 3D high resolution and high contrast imaging of human soft tissue anatomy allowing for segmentation of tissue types and for the construction of FEA models.
2. Capable of 3D high resolution imaging of the muscle fibre architecture allowing mapping of fibre directions for FEA implementation of anisotropy.
3. Capable of 3D fast and high resolution non-invasive imaging of complex 3D soft tissue deformation of muscle tissue.
4. The modality should be flexible to allow image acquisition at positions and orientations freely defined by the user.
5. The modality should not have significant negative biological and health side effects and preferable not employ ionizing radiation.

The only imaging modality found to match these requirements is MRI. The available soft tissue contrast in MRI is currently the highest among all medical imaging modalities<sup>79</sup>. MRI is non-invasive and employs non-ionizing radiofrequency waves and at present demonstrates no untoward biological effect<sup>79</sup>. In addition MRI provides the best combined sensitivity and specificity compared to conventional radiographs, nuclear medicine studies, musculoskeletal computer tomography (CT), and ultrasound<sup>79</sup>. The nature of the MR signal allows for multiple types of analysis which enables imaging of anatomy, diffusion (and muscle fibre arrangements, e.g.<sup>33</sup>) and 3D tissue deformation (see review article<sup>34</sup>) and elasticity (see review article<sup>201</sup>). MRI was therefore chosen as the imaging modality for the current thesis. Further chapters therefore focus on MRI based investigations.

## 3.5 MRI compatible actuator and sensor devices

As discussed in section 3.3.3 the non-invasive analysis of the mechanical properties of soft tissue requires mechanical excitation, non-invasive measurement of experimental boundary conditions and inverse analysis. Mechanical excitation requires the

implementation of actuators (to mechanically palpate/excite the tissue) and sensor devices to measure the applied load. MRI safe and compatible actuation and sensing is non-trivial<sup>202</sup> and therefore this section discusses MRI compatible actuator and force sensors. Since large strain analysis is of interest in the current thesis actuators relevant to indentation are the focus. In addition force sensors in the range relevant for soft tissue (around 0-15N) are discussed. Two main groups of actuators and sensors for the MRI environment can be distinguished: 1) *Systems employing electric principles and/or ferromagnetic components in the MRI room and/or close to the imaging region* and 2) *Systems which are intrinsically MRI compatible since they employ non-conducting and non-ferromagnetic materials and sensor signal transmission occurs using magnetically inert media within the MRI room*. Of interest to the current thesis are actuator (indenter) systems which are intrinsically MRI compatible such that the devices do not significantly affect imaging and can safely be used in close proximity to the subject without posing safety risks. Such systems do not require device and cable shielding, signal filtering strategies or device anchoring. This group of sensor and actuator devices therefore forms the focus in this thesis.

A large array of MRI compatible actuators (see review<sup>203</sup>) and sensor systems (see review<sup>204</sup>) have been proposed. These have mainly been developed for application to MRI robotics (e.g.<sup>35, 36</sup>), MRI and guided surgical interventions (e.g.<sup>37-39</sup>), MRI based catheterisation (e.g.<sup>40</sup>) and functional MRI studies (e.g.<sup>41, 42</sup>). MRI compatible actuators and force sensors have also been applied, to a limited extent, to MRI based soft tissue mechanical property investigation. To date these have been limited to quasi-static deformation analysis<sup>26, 43, 173, 205-208</sup>, the evaluation of isotropic hyperelastic constitutive models<sup>26, 43, 173, 205-208</sup>, estimation of strain from 2D imaging<sup>26, 205, 209</sup> or from finite element simulations<sup>26, 208</sup>. Force measurement is sometimes based on the application of static weights<sup>173</sup> or by repeating the experiment outside the MRI environment<sup>208</sup> or electric force sensors which suffer from MRI scanning induced electromagnetic interference<sup>43</sup>.

The only computer controllable MRI compatible indenter and dynamic force sensing system for non-invasive tissue investigation found in the literature was presented in Stekelenburg *et al.* 2006<sup>43</sup>. This system was recently used by Ceelen *et al.* 2008<sup>174</sup> to study rat lower limb muscle deformation (as discussed in section 3.3.3 ). However, currently the system is not applicable to human studies since it was developed

for animal experiments in a small bore (95 mm in diameter) MRI scanner. In addition it incorporates an electric force sensor the application of which is not of interest to the current thesis.

To date a large array of MRI compatible force sensors have also been developed. Piezoelectric sensors have been proposed; however, these cannot be used to measure static forces<sup>37</sup> and are therefore not ideally suited for quasi-static and viscoelastic (ramp and hold type) tissue property investigation. In addition they may induce image artefacts<sup>37</sup> depending on proximity to the imaging region. MRI compatible force sensors for the application of needle deflection and force feedback measurement during catheterisation have also been developed<sup>40, 210</sup> however these are applied to forces in the range 0-0.5N. Tada *et al.*<sup>211</sup> presented an optical MRI compatible tri-axial force sensor based on a deformable structure and optical micrometry. A total of 5 optical fibres were used: 1 emitting fibre mounted on a movable component and 4 receptor fibres allowing monitoring of motion of the emitting fibre and thus derivation of force. The system was calibrated in the range of 0-15N and showed errors under 3 %. This complex force sensing system has also been applied to quasi-static compression tests to the human finger-tip for inverse FEA of the assumed isotropic hyperelastic mechanical properties<sup>207</sup>. During quasi-static compression tests in 5 steps up to 3.48 N the force was measured at 1Hz. However the static force measurements showed standard deviations ranging from 0.11 N (for a mean force of 1.7 N) up to 0.3 N (for a mean force of 2.35 N). The causes for the increased deviations, with respect to the calibration which reported errors under 3%, were not discussed. In addition the hydraulic compressor system used was not described in detail.

Recently Song *et al.* 2011<sup>39</sup> designed an advanced fibre Bragg grating (FBG) based tri-axial force sensor system for the tip of a robot arm for application to minimally invasive surgery. FBG sensors are optical fibres containing periodic perturbations of the refractive index along the fibre which act as local strain and temperature dependant wavelength specific reflectors. Monitoring of the reflected Bragg wavelengths due to fibre strain thus provides a force sensing mechanism. The system was calibrated for forced up to around 10 N and a maximum force error of 0.5 N was recorded. This force range is rather low for application to soft tissue indentation and the robot arm features metallic components and hence the manipulator and force sensor design are not directly applicable to the current thesis. However FBG based force sensing in the MRI environment does seem to

have advantages over other force sensing systems. Song *et al.* 2011<sup>39</sup> highlights that since the measurand in FBG is wavelength encoded, the sensors are self-referencing, rendering it independent of fluctuating light levels. In addition FBG based sensors allow for miniaturisation of sensors due to their compact design.

To the authors knowledge to date no combined computer controllable MRI compatible indenter and dynamic force sensor systems have been developed for application to human soft tissue indentation.

## 3.6 MRI based measurement of soft tissue deformation

Since MRI allows fast and 3D imaging with excellent soft tissue contrast without exposing subjects to ionizing radiation, it is an ideal modality for the study of soft tissue motion. As such, a large variety of MRI based methods to non-invasively analyse soft tissue deformation have been developed. These can roughly be subdivided into; 1) *methods that rely on anatomical features* (e.g. using correlation methods<sup>212, 213</sup> or deformable models and non-rigid image registration<sup>214</sup>) and, since anatomical features may be insufficient, 2) *methods that rely on implanted markers*<sup>215</sup>, and finally 3) *methods that rely on specialized MRI sequences and signal modulation*, where phase contrast MRI methods<sup>129, 216</sup> or methods based on SPAtial Modulation of the Magnetization (SPAMM)<sup>124, 125</sup> are common<sup>34, 46, 49, 217</sup>. The latter is the focus of this thesis since it offers a relatively direct and possibly constraint free method for the derivation of large 3D strain measurements using comparatively low numbers of repetitions.

In SPAMM tagged MRI sequences (see also section 2.3.11 ) the magnetization is modulated using radiofrequency pulses and magnetic field gradients, resulting in saturated bands in the magnetization distribution and, as a consequence, contrasting patterns in the image data. These patterns act as temporary markers locked in the tissue whose appearance reflects any underlying tissue motion. Typically SPAMM tagged MRI methods are gated and image acquisition is synchronized with the motion cycle (e.g. towards heartbeats using electrocardiograms). In addition they are fast, as only part of the k-space is acquired with each cycle, and acquisitions from multiple motion cycles are used to compose a dataset representing a single motion cycle. This has confined the application of SPAMM tagged MRI to the analysis of highly repeatable and periodic



movements such as those of the heart<sup>46, 48, 49</sup>. Recently other tissue types have also been analysed for repeatedly induced motions of the tongue<sup>50</sup> (16 volunteer speech repetitions per slice), brain<sup>51</sup> (144 volunteer rotational head accelerations) and eyes<sup>52</sup> (>135 repeated left to right eye movements).

Recently faster approaches have been developed for estimation of 2D lung tissue movement<sup>218</sup>, but these cannot be applied to other tissue sites or to a clinical setting as inhaled hyperpolarized <sup>3</sup>He gas was used as a contrast medium, accelerating the image acquisition. Apart from repeatability constraints, discomfort and health issues may preclude the use of large numbers of repetitions limiting the applicability of current SPAMM tagged MRI approaches and analysis of tissue viscoelasticity and hysteresis is limited. In addition clinical conditions may impair the repeatable natural movement of tissues (e.g. cardiac arrhythmia).

A wide array of advanced post-processing methods have been proposed for SPAMM tagged MRI; for instance using deformable models<sup>219, 220</sup>, spline models<sup>221-223</sup>, non-rigid image registration<sup>224, 225</sup>, optical flow methods<sup>226</sup>, 3D tag surface analysis<sup>227</sup> and harmonic phase methods<sup>228</sup>. The post-processing methods in the literature involving deformable models, spline models and non-rigid image registration all inherently require assumptions on the nature of the deformation and/or the mechanical properties and models of the underlying tissue. Harmonic phase methods require non-trivial and error prone phase unwrapping. In addition, many of these methods require computationally intensive iterative optimization methods to be employed. It is possible to use the above approaches to investigate mechanical properties. However the constitutive model evaluation is limited to the model adopted and difference measures are based on the image data rather than more mechanically meaningful experimental parameters such as 3D deformation, strain and strain rate. This thesis focusses on post-processing methods which allow derivation of the complex 3D deformation while minimizing assumptions on the mechanical properties or the nature of the deformation.

### 3.7 Validation of MRI derived motion and deformation

The techniques for tracking tissue deformation from (for example tagged) MRI are complex and require validation using an independent measure of deformation. Since

physically implanting markers is not feasible and anatomic landmarks are either absent or difficult to track, alternative methods have been employed. Young et al.<sup>229</sup> recorded angular displacement of a silicone gel phantom using tagged MRI and evaluated the results using FEA and 2D surface deformation derived from optical tracking of lines painted on the phantom surface. Similarly, Moore et al.<sup>230</sup> used optical tracking of surface lines on a silicone rubber phantom to validate MRI based deformation measures. However simple tensile stretch was applied and only a 2D measure of surface deformation was used. There were also temporal synchronisation issues between the optical and MRI data. In both of the optical validation studies above the error related to the optical tracking method was not quantified. Other authors have used implantable markers. For instance Yeon et al.<sup>231</sup> used implanted crystals and sonomicrometric measurements for validation of tagged MRI of the canine heart. However the locations of the crystals were verified manually by mapping with respect to surface cardiac landmarks in the excised heart and matching problems between MRI and sonomicrometric measurements occurred. Neu et al.<sup>232, 233</sup> evaluated a tagged MRI based deformation tracking technique for cartilage using spherical marker tracking in a silicone soft tissue phantom. However the marker centres were determined by manually fitting a circle to each marker in two orthogonal directions and imaging was performed on *in-vitro* samples using a non-clinical small bore 7.05 T scanner.

This review shows that validation of *in-vivo* medical imaging techniques and image processing algorithms is challenging partially due to the lack of appropriate reference data. Although experimental validation methods using soft tissue MRI phantoms can be developed, the data derived from these often suffers uncertainties similar to those present in the target soft tissue. Therefore the validation method itself often lacks an appropriate reference.

## 3.8 Summary and proposed approach

Section 3.2 reviewed the architecture of skeletal muscle tissue demonstrating that it is anisotropic due to its fibre architecture and contains a complex connective tissue arrangement consisting of the main longitudinal muscle fibres which are interconnected and reinforced by connective tissue structures which are oriented transverse and oblique to the main fibre direction. Realistic modelling of the mechanical properties of muscle

tissue should account for anisotropy introduced by both types of features. This point is addressed in study VI, chapter 0.

Section 3.3 reviewed experimental and computational studies on the mechanical properties of skeletal muscle tissue. It was shown that mechanical properties of skeletal muscle tissue have been extensively researched for both tension and compression. Although a large degree of variation is observed the literature available reports the mechanical behaviour of passive skeletal muscle tissue to be non-linear, anisotropic and viscoelastic in both tension and compression. In addition muscle tissue presents with tension compression non-linearity. The most detailed experimental investigations into the large strain and anisotropic non-linear elastic behaviour of skeletal muscle tissue is due to Takaza *et al.* (unpublished)<sup>22</sup> and Van Loocke *et al.* 2006<sup>21</sup> for tension and compression respectively. These experimental data may provide the basis for the formulation of constitutive laws for the anisotropic and non-linear elastic behaviour.

Non-invasive attempts to characterise the mechanical properties of muscle tissue have so far been largely limited to the analysis of isotropic behaviour or grouped bulk behaviour of different tissue types. Elastography methods have been limited to small strain and often assume linear isotropic properties.

MRI based deformation measurement such as phase contrast MRI or SPAMM tagged MRI have been employed in combination with inverse analysis. However once again analysis has been limited to isotropic model evaluations (e.g.<sup>174</sup>) or averaged regional strain estimates (in the case of<sup>23</sup>). Detailed 3D deformation measurement combined with anisotropic model evaluation has not been performed for skeletal muscle to date.

Constitutive modelling approaches for the non-linear elastic behaviour of passive muscle tissue have so far largely focussed on isotropic hyperelastic formulations. Transversely isotropic formulations are generally based on summing an isotropic hyperelastic ground matrix response and a single reinforcing fibre direction which only reinforces in fibre tension. Hence contributions due to transverse (or other non-longitudinal) fibrous structures are not modelled. In addition the models proposed have not been extensively validated using multi-directional anisotropic stress-strain information. These points are addressed in study VI, chapter 0.

Section 3.4 highlighted that MRI offers excellent soft tissue contrast and is the only non-invasive and non-ionizing imaging modality allowing fast, high resolution and 3D imaging of all required boundary conditions of interest to the current study, such as anatomy, deformation and fibre architecture.

Section 3.5 reviewed currently available MRI compatible actuator systems and force sensors and concluded that to date no combined computer controllable MRI compatible indenter and dynamic force sensor systems have been developed for application to human soft tissue indentation. Hence such a system is proposed in study I, chapter 4.

Section 3.6 reviewed current MRI based soft tissue deformation measurement techniques and demonstrated that current methods require the combination of large numbers of repetitions which result in repeatability constraints and for the current thesis volunteer discomfort during indentation. Therefore study IV chapter 7 and V chapter 8 focus on static and dynamic methods respectively following a minimum of repetitions.

Section 3.7 demonstrated that MRI based motion measurement techniques require validation and that to date validation techniques have been limited or the error related to the validation methods is unknown. To address validation study III chapter 6 proposes a silicone gel phantom containing trackable spherical markers.

Non-invasive mechanical property assessment requires mechanical excitation, non-invasive boundary condition measurement and inverse analysis. The current thesis focusses on the development of an experimental and computational framework for the non-invasive analysis of the complex (anisotropic, non-linear and viscoelastic) mechanical properties of passive skeletal muscle tissue.

Figure 3.22 shows a diagram for the proposed approach. First an appropriate constitutive model and initial parameters are formulated based on data from the literature and are implemented in FEA. Then an indentation experiment is performed on healthy volunteers during which experimental boundary conditions are measured such as: 1) the geometry and fibre architecture, and 2) the indentation force and tissue deformation. The former is used for the construction of the FE model and for mapping of

the per element fibre directions. The indentation is then simulated using FEA yielding simulated measures of indentation force and soft tissue deformation. These are then compared to the true experimental force and deformation to derive difference measures for the optimisation based derivation of a new material parameter set. An iterative optimisation process composed of the following is then repeated until the difference measures are minimised: 1) *FEA simulation*, 2) *comparison of FEA and experimental boundary conditions* and 3) *material parameter optimisation*. This thesis relates to setting up and validating all the experimental and computational methods required in the diagram of Figure 3.22.

In study II chapter 5, the proposed framework in Figure 3.22 is evaluated with an alternative to MRI since implementation for MRI and anisotropic tissue presented with initial challenges. Therefore instead, the more limited but more straightforward non-invasive imaging technique, Digital Image Correlation (DIC) (see also section 2.4.5 ) was explored as an alternative to MRI based deformation boundary condition assesment.

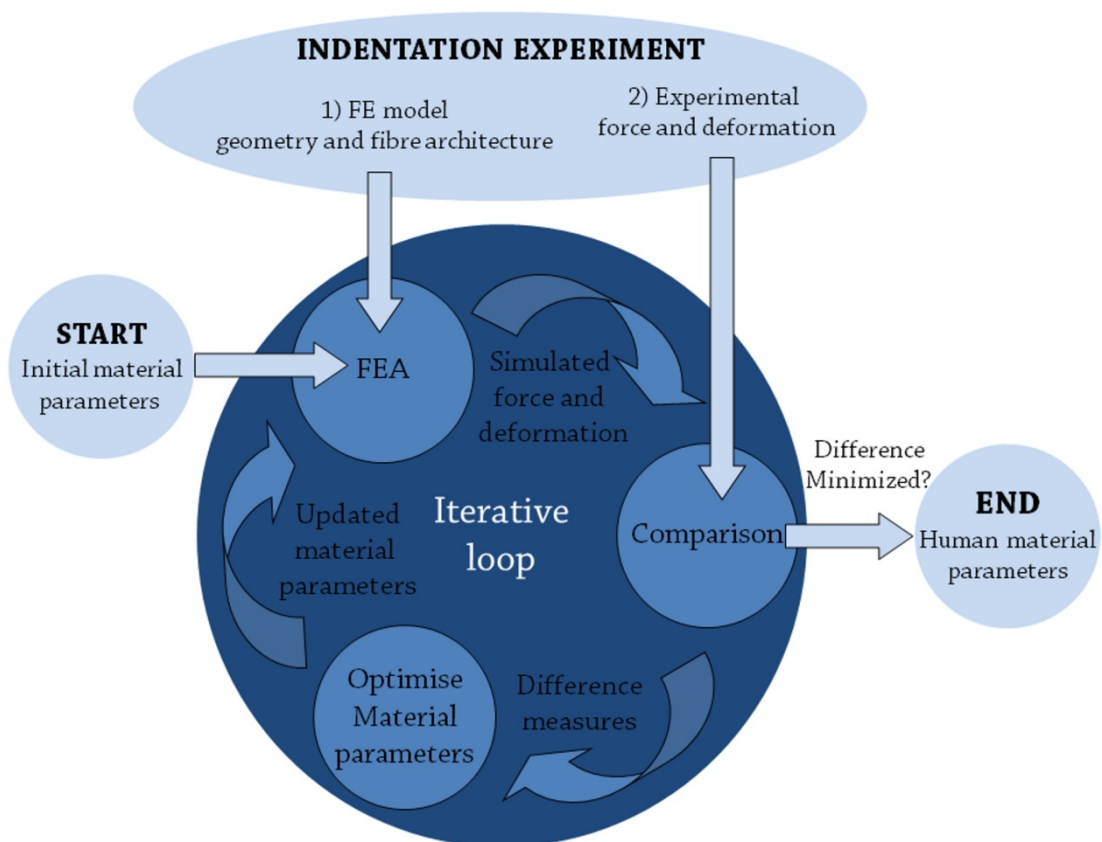


Figure 3.22 Diagram showing the proposed experimental and inverse FEA based determination of constitutive parameters.



## 4 STUDY I

# A Novel MRI Compatible Soft Tissue Indentor and Optical Fibre Bragg Grating Force Sensor

## 4.1 Introduction

Section 3.5 of the literature demonstrated that to date no combined computer controllable MRI compatible indenter and dynamic force sensor systems have been developed for application to human soft tissue indentation. This study focusses on the design and validation of such a system for muscle tissue indentation.

MRI based biomechanical soft tissue investigations often require the implementation of actuators (to mechanically palpate/excite the tissue) and sensor devices (to measure the applied load). Designing such devices to be safe within the MRI environment and compatible with the imaging is non-trivial<sup>202</sup>. This study presents a novel MRI compatible soft tissue indenter implemented with a Fibre Bragg Grating (FBG) based optical force sensor for application to non-invasive soft tissue mechanical property investigation. When combined with the MRI based measurement of boundary conditions such as geometry, architecture and soft tissue deformation, it allows for inverse FEA based evaluation of constitutive laws.

As discussed in section 3.5 systems which are intrinsically MRI compatible are of interest to the current thesis. These employ non-conducting and non-ferromagnetic materials and sensor signal transmission occurs using magnetically inert media within the MRI room. In addition these devices do not significantly affect imaging and can safely be used in close proximity to the subject without posing safety risks and do not require device and cable shielding, signal filtering strategies or device anchoring. As such a master slave system is presented here featuring an MRI compatible slave actuator (indenter) system composed of non-ferromagnetic and non-conducting materials. Embedded in the MRI actuator is a novel high speed MRI compatible force sensor based on optical FBG. This chapter outlines the design of the MRI compatible indenter system including the master-slave control system and force sensor. The system is evaluated for an MRI based investigation of soft tissue biomechanics using indentation of the upper arm of volunteers.

## 4.2 Methods

This section describes: 1) *Fibre Bragg Grating Based optical force sensing*, 2) *The soft tissue indenter system*, 3) *Optical force sensor calibration* and 4) *Evaluation of the indenter system*



performance. All signal and image processing methods were developed in MATLAB (The Mathworks Inc., USA).

#### 4.2.1 Fibre Bragg Grating Based optical force sensing

In FBG a periodic perturbation of the refractive index is introduced along an optical fibre acting as a local wavelength specific reflector<sup>234, 235</sup>. The reflected (Bragg) wavelength  $\lambda_B$  for a specific grating is defined by<sup>236</sup>:

$$\lambda_B = 2\eta_{eff}\Lambda \quad 4-1$$

Here  $\eta_{eff}$  is the effective refractive index of the fibre core and  $\Lambda$  is the period of the grating. From this equation it is clear that  $\lambda_B$  is both strain and temperature dependant since  $\eta_{eff}$  varies with temperature and  $\Lambda$  is altered following longitudinal fibre strain and thermal expansion/contraction<sup>236</sup>. Under isothermal conditions a linear relationship exists between reflected wavelength and the applied strain where tensile and compressive strains increase and decrease the wavelength reflected respectively. For the current study only the mechanical strain induced effect is of interest since it is linearly dependent on the force exerted on the optical fibre. In order to separate the effect of mechanical strain from the effects of temperature fluctuations two gratings are placed close together in series whereby one is subjected to both mechanical strain and local temperature variations, while the other is isolated from mechanical strain and acts as a (temperature) reference grating. The wavelength reflected from the latter reference grating  $\lambda_T$  is thus purely a function of temperature and, together with the wavelength reflected from the former (strain) grating  $\lambda_S$ , can be used to derive the mechanical fibre strain  $\varepsilon$  as<sup>237</sup>:

$$\varepsilon = \frac{1}{S_\varepsilon} \left[ \log \left( \frac{\lambda_S}{\lambda_{S0}} \right) - \log \left( \frac{\lambda_T}{\lambda_{T0}} \right) \right] \quad 4-2$$

Here  $S_\varepsilon = 1.2 \pm 0.03 \text{ pm}/\mu\varepsilon$  represents the strain sensitivity. The subscript 0 denotes initial values and initial wavelengths which can be measured for an unloaded fibre prior to each testing session by taking the mean signal (e.g. across 1000 samples, over 10 seconds) for both gratings.

For the current study a high strength optical fibre (GeO<sub>2</sub> doped silica glass fibre, ORCOMER® coated, 125  $\mu\text{m}$  in diameter) containing two FBG gratings (Draw Tower Grating pair, FBGS International, Belgium) was used. The nominal Bragg wavelengths for the gratings used are 1532 nm and 1530 nm for the strain and reference grating respectively (hence as tensile strain is applied the reflected wavelength increases away

from the reference grating wavelength). The reflected wavelength peaks were acquired at 1 kHz using an optical interrogator (SM130-700, Micron Optics Inc., USA). However for the current study the data was stored using a 10 point data interleave (running average of 10 consecutive data samples) resulting in an effective acquisition frequency of 100 Hz.

Due to the brittle nature of the fibre material it is best to load fibres in tension rather than compression. In tension the fibres used are capable of supporting loads up to 50 N (corresponding to a 5 % breakage strain). This is sufficient for the current study since forces in the range of 0-15 N are of interest (i.e. loads occurring during mild indentation of soft tissue).

## 4.2.2 *The soft tissue indenter system*

This section discusses the soft tissue indenter system in the following steps: 1) *The MRI compatible soft tissue indenter assembly*, 2) *The MRI actuator assembly*, 3) *The indenter head and force sensor assembly*, 4) *Actuator motion control and data acquisition*. For each section the most relevant parts are discussed with reference to an associated figure.

### 4.2.2.1 **The MRI compatible soft tissue indenter assembly**

The design for the MRI compatible soft tissue indenter assembly will now be discussed with reference to Figure 4.1. The MRI actuator body (1) is mounted on a support bridge (2) which is attached to two side plates (3) that are mounted onto the bottom plate (4). The whole assembly can be fixed on the scanner bed using a slide rail (5) and support ridge (6). The actuator orientation (blue arrows) can be adjusted using the adjustment screws (7) and (8) and slot (A) to set desired loading angle and maximum depth. The maximum indentation is set by placing the piston in its maximum deployed position, moving the actuator down until a desired maximum tissue indentation is reached and then securing the adjustment screws on the support bridge and side plates. The bridge set-up shown in Figure 4.1 can be used for indentation of extremity soft tissue sites such as the biceps region of the upper arm or the tibialis anterior region of the lower leg. For other tissue regions a different mounting structure can easily be incorporated. All parts are made of polyamide except for the MRI compatible actuator body which is discussed in the following section.

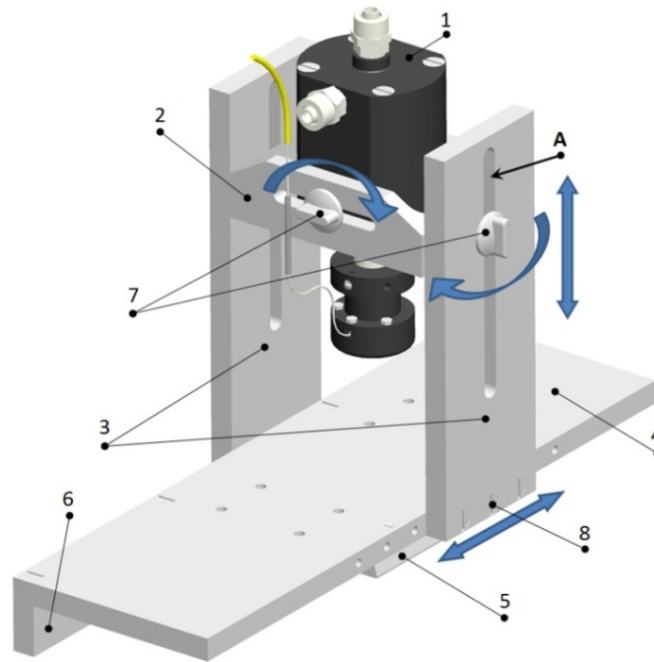


Figure 4.1 The MRI compatible indenter assembly.

#### 4.2.2.2 The MRI actuator assembly

This section discusses the MRI actuator assembly with reference Figure 4.2. The tube connector (1) allows water driven by the master cylinder to enter the actuator chamber formed via parts (2) and (3). The tube connector (4) and the rubber seal (5) form a manual valve which can be opened to allow for air removal during filling of the system. Parts (2) and (3) clamp a soft rubber diaphragm (6) which deforms under the influence of water pressure as the piston shaft (7), attached via the ring (8) is pushed downwards (see right side of Figure 4.2). The maximum stroke is 44 mm. The use of a diaphragm ensures low initial friction. The piston contains a flat face such that it can be constrained from rotating using part (9). The bottom part of the piston contains the indenter head and force sensor assembly (10) which is discussed in the following section. All black parts in Figure 4.2 are constructed of polyoxymethylene and all white parts are polyamide except for the piston which is made of polytetrafluorethylene to ensure low friction.

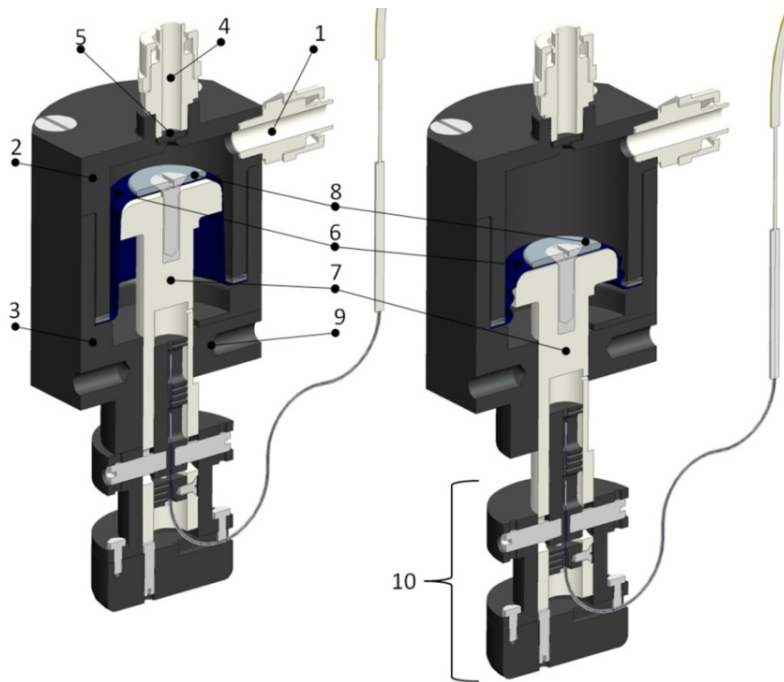


Figure 4.2 The MRI actuator assembly in a retracted (left) and outward state (right).

#### 4.2.2.3 The indenter head and force sensor assembly

The indenter head and force sensor assembly is discussed with reference to Figure 4.3. The bottom of the piston shaft (1) is inserted into the piston head parts (2-3) which are able to slide relative to the piston shaft by an amount limited by the set screw (4). The piston head is 45 mm in diameter with rounded edges 6 mm in radius. Using set screws (5) the piston head parts (2-3) are attached to part (6) of the force sensor assembly (right) which is inserted into the piston shaft (1). Part (7) of the force sensor assembly is fixed to the piston shaft via the screw (8). The FBG sensor fibre (9) enters the piston head at site (A) where it is supported using a bolt (10). The fibre reference and strain gratings (8 mm long each and 18 mm apart) are located at sites (B) and (C) respectively. The fibre (9) runs through a central hole in parts (6) and (7) where it is glued (EPO-TEK 353ND, Epoxy Technology Inc., USA) at sites (D) using the glue injection holes at (E). Thus when a compressive force  $F_C$  is applied to the bottom of the indenter head it slides with respect to the piston shaft, converting the load to a tensile force  $F_T$  at the strain grating (C) while the temperature reference grating (B) remains unloaded. The force  $F_C$  is directly proportional to the force  $F_T$ . Therefore due to the current design in the case of downward indentation with respect to gravity the weight of the indenter head components (0.94 N) first needs to be overcome. Hence for downward indentation only forces in excess of this weight can be recorded. Pre-tension can be introduced in the fibre using a screw (11)

which also ensures that the weight of the indenter head assembly does not buckle the fibre.

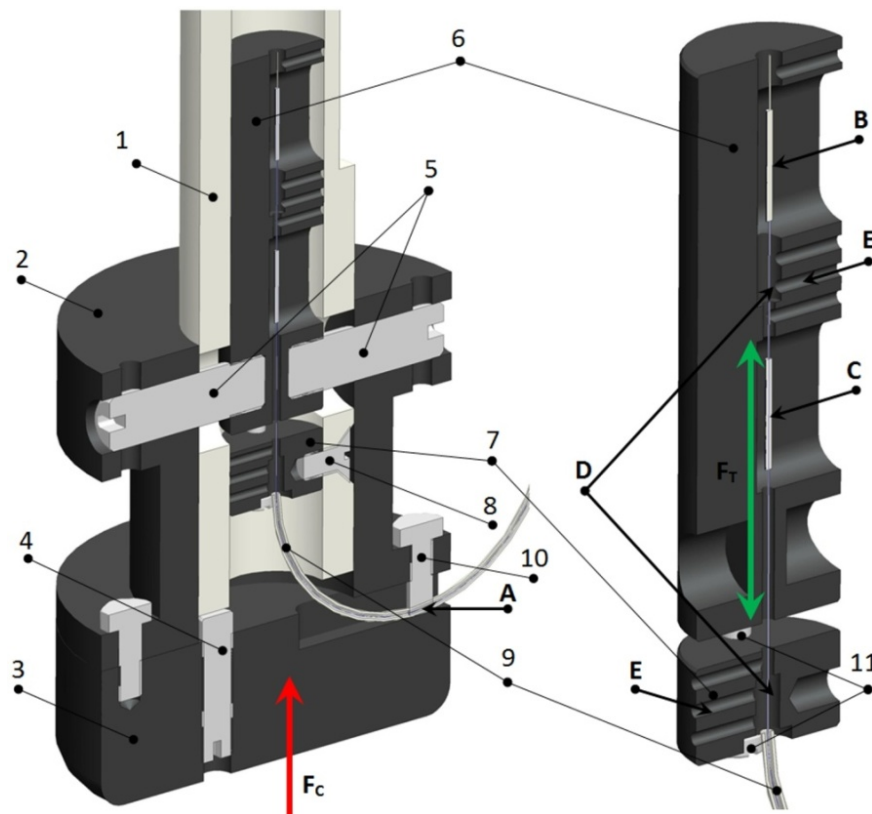


Figure 4.3 The indenter head (left) and force sensor assembly (right).

#### 4.2.2.4 Actuator motion control and data acquisition

The motion of the MRI compatible actuator discussed above is enabled via a computer controlled hydraulic master cylinder assembly placed outside the MRI room which will be discussed using Figure 4.4. A 24 V DC-motor (1) (FBG 0130821708, Bosch, UK) controls the movement of a steel hydraulic cylinder (2) (CP95SDB50-80, SMC Corporation, USA) via an attached stainless steel gear rack (3) forcing water in or out through the valve (4) which is linked to the MRI compatible actuator via a 12 mm diameter polyurethane tube. The DC-motor has an internal gear assembly with an internal to external gear-ratio of 62:1. The internal axis contains two 90° offset Hall sensors. Counting of the Hall sensor pulse edges (rising and falling for both sensors) thus provides 248 position references per external axis rotation which translates into approximately 1 positional reference for each 0.3 mm of MRI actuator motion. For the current study the Hall sensor outputs are used only for displacement control. Since the exact indenter placement and depth are set manually prior to scanning the actual indentation depth (final indenter displacement) was determined using segmentation of the indentation site from the MRI data.

The motion of the master cylinder (and thus the MRI actuator) is regulated by computer control of the DC-motor. Custom control hardware and software (LabVIEW 8.6, National Instruments Corporation, USA) incorporating two data acquisition units (USB 6009 and USB 6211, National Instruments Corporation, USA) were used for: 1) analysis of the Hall sensor signal, allowing position control and recording, 2) setting of FBG parameters and acquisition of FBG data over time based on TCP (Transmission Control Protocol) communication with the optical interrogator, and 3) motion triggering toward an MRI scanner generated TTL (Transistor-Transistor-Logic) trigger pulse. Motor speed was varied through pulse-width modulation of the input voltage. LabVIEW was run on a laptop PC, with a 32-bit Microsoft Windows Vista Business operational system, 3.5 Gb RAM, and dual core 2.1 GHz processors.

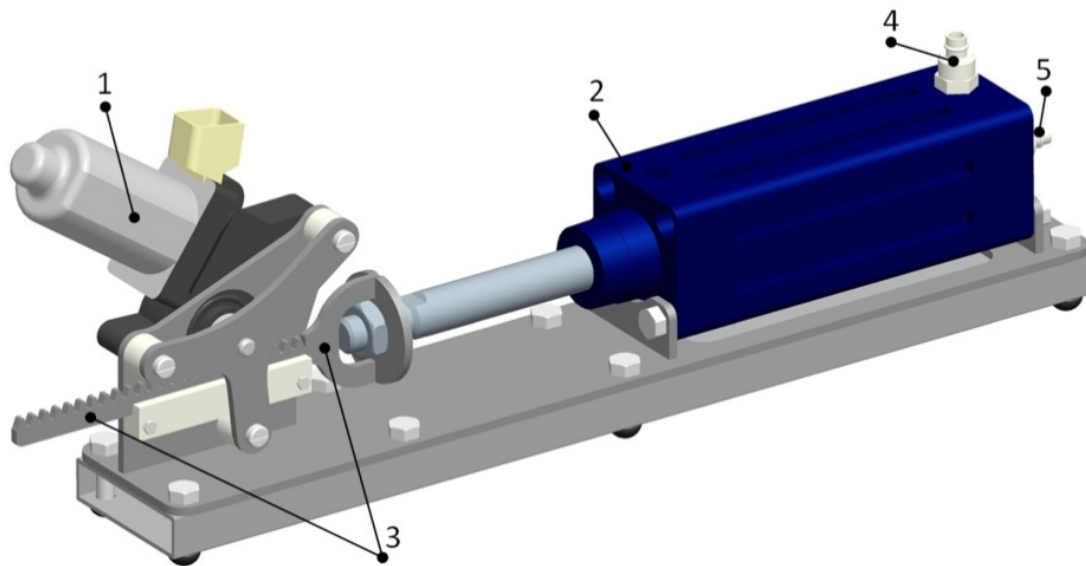


Figure 4.4 The hydraulic master cylinder assembly.

### 4.2.3 *Optical force sensor calibration*

In order to relate the FBG derived fibre strain measure in equation 4-2 to fibre force, uniaxial compression testing was done using a Zwick Z005 (Zwick GmbH & Co., Germany) equipped with a 50N load-cell. The system was subjected to three types of force controlled loading in the range of 0-15 N: 1) a stair case test (1 N steps at 0.25 N/s, followed by a 30 s hold phase, repeated 3 times), 2) a stair case test (1 N steps at 0.75 N/s, followed by 30 s hold phase, repeated twice) and 2) high speed ramp loading (ramp up to 15 N at 5 N/s followed by 10 second hold and ramp down to 0 N). A 0.5 N pre-load was used for all tests.

The staircase tests were used for calibration by segmenting the plateaus regions for both the load-cell and FBG strain curves. In order to determine a mapping from the FBG strain to force the average plateau forces for all tests (75 points, 15 for each of the 5 tests) were used simultaneously. Both linear (scaling based) and non-linear (cubic spline based) mappings were investigated. Following calibration based on the staircase tests, the force curve for the high speed ramp loading was then predicted using the stair-case based calibration and was thus effectively used for verification purposes.

#### 4.2.4 *Evaluation of the indenter system performance*

The intended application for the indenter is the non-invasive investigation of soft tissue mechanical properties whereby during indentation all boundary conditions required for inverse analysis are recorded. These boundary conditions include: 1) *the indentation force derived from the FBG sensor*, 2) *the complex soft tissue deformation acquired using SPAMM (SPAtial Modulation of the Magnetisation) tagged MRI<sup>238, 239</sup>*, 3) *the tissue geometry for the construction of FEA models derivable from anatomical MRI* and 4) *muscle tissue fibre architecture derivable from diffusion tensor MRI<sup>33</sup> to allow for analysis of anisotropic material behaviour*.

In order to evaluate indenter system performance for the above application it was applied (Figure 4.5) for indentation of a silicone gel phantom (see chapter 6) and the upper arm region of volunteers (ethical approval and informed consent obtained from the Medical Ethical Committee, Academic Medical Centre, Amsterdam, The Netherlands). All the above mentioned boundary conditions were recorded during the experiments. However only the measurements relevant to the indenter system performance are highlighted in detail here as the soft tissue deformation measurements are presented elsewhere (see chapters 7 and 8). Since the quality of these measurements also illustrates the utility of the indenter system they are briefly summarized in the discussion section.

The indenter system was evaluated in the following ways: 1) *force measurement within the MRI environment*, 2) *Evaluation of indenter motion repeatability*, 2) and 3) *Evaluation of MRI compatibility*.

All scans were performed on a 3.0 T scanner (Philips Intera, Philips Healthcare, Best, The Netherlands) and Figure 4.5A-B highlights coil placement of the flexible surface coils used (Flex-M, Philips Healthcare, Best, The Netherlands) and Figure 4.5C-D shows iso-surface visualisations of the indented configurations and sample SPAMM tagged MRI

slices. In order to compute 3D soft tissue deformation SPAMM tagged MRI data was acquired in three mutually orthogonal directions<sup>238, 239</sup>. However for both the phantom and volunteer data one of the three SPAMM tagged MRI directions was used for demonstration of indenter performance.

For the phantom tests repeated indentations were performed while a dynamic series ( $n = 60$ ) of SPAMM tagged MRI data were acquired (1-1 SPAMM, 123 ms delay, 177 ms 3D Transient Field Echo read-out,  $T_R/T_E$  2.53/1.28 ms, field of view 120x120x39 mm, acquisition matrix 80x52, 10 slices, reconstructed voxel size 0.93x0.93x1.5 mm). Timing of indenter motion with respect to imaging resulted in 11 image dynamics per indentation cycle and 5 complete repeated indentations per dynamic series.

For the volunteer tests repeated indentations were performed while a dynamic series ( $n = 250$ ) of SPAMM tagged MRI data were acquired (1-1 SPAMM, 100 ms delay, 177 ms 3D Transient Field Echo read-out,  $T_R/T_E$  2.42/1.19 ms, field of view 120x120x40 mm, acquisition matrix 80x60, 10 slices, reconstructed voxel size 0.94x0.94x2 mm). Timing of indenter motion with respect to imaging resulted in 71 image dynamics per indentation cycle and 3 complete repeated indentations per dynamic series.

Indentation cycles were triggered using a TTL pulse timed to start with the first dynamic or the first dynamic following completion of a deformation cycle.



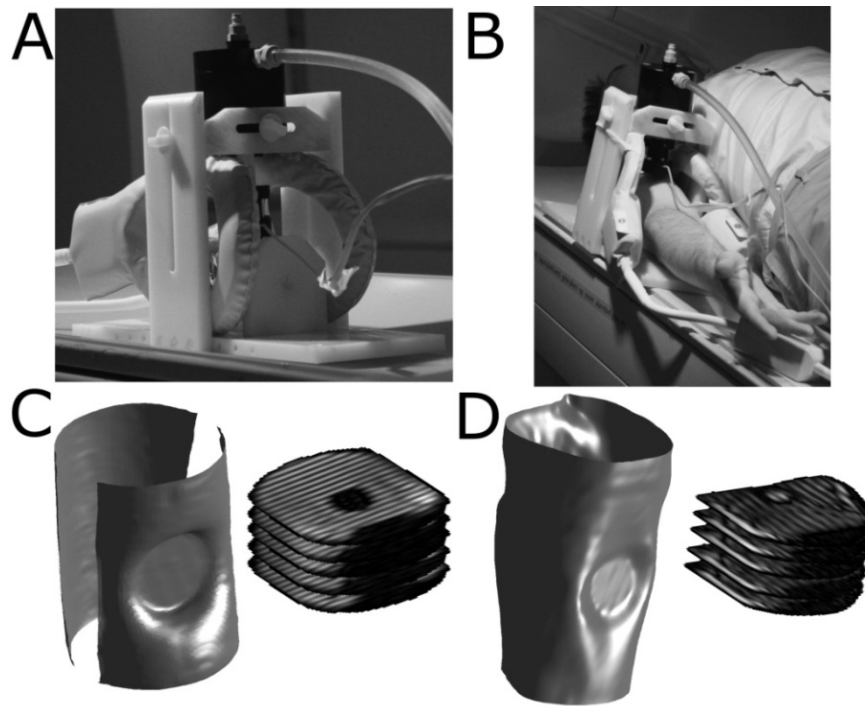


Figure 4.5 The MRI compatible indenter system positioned for indentation of the silicone gel phantom (A) and the upper arm of a volunteer (B). Coils are placed laterally to the regions of interest and can be secured to the side plates. In addition iso-surfaces illustrating the indentation sites and selected SPAMM tagged MRI data slices are shown for the phantom (C) and volunteer (D).

#### 4.2.4.1 Force measurement within the MRI environment

During the indentation experiments the FBG derived force was recorded at 100 Hz. Since the force sensor is optical fibre based no interference with the MRI imaging is expected. Since skeletal muscle tissue is highly viscoelastic<sup>158, 159</sup> it is expected that, for the indentation tests of ramp and hold type discussed above, force relaxation should be observed during the hold phase. To demonstrate the sensor's performance in the MRI environment for application to soft tissue biomechanics, its ability to register this viscoelastic force history is demonstrated for two load rates of 10 mm/s and 20 mm/s.

#### 4.2.4.2 Evaluation of indenter motion repeatability

In order to study repeatability of the indenter motion, the dynamic SPAMM tagged MRI series (see Figure 4.5C-D) for the phantom ( $n = 60$  dynamics) and for the volunteer ( $n=250$  dynamics) were analysed. The SPAMM tagging encodes for motion and are thus well suited for repeatability analysis. Each dynamic series can be represented as a 4D data set  $N_{i,j,k,d}$  where  $(i, j, k)$  represent voxel (row, column and slice) indices and  $d$  the index for dynamics. In case a repeated periodic motion occurred during the dynamic series some of these dynamics are thus equivalent to each other with the exception of

differences induced by noise. In order to establish whether the indenter motion was indeed repeatable a  $n \times n$  temporal sum of squared differences (SSD) matrix (SSDM) was created for both the phantom and volunteer data where all dynamics are compared to all others using:

$$SSDM_{p,q} = \sum_{i,j,k} (N_{i,j,k,p} - N_{i,j,k,q})^2 \quad 4-3$$

where each entry in the matrix at  $(p, q)$  reflects the sum of squared differences of dynamic  $p$  with respect to dynamic  $q$  for a random selection of 10000 voxels within the gel/tissue volume. The matrix SSDM is obviously symmetric around its diagonal where all entries are zero since here  $p = q$ . However if a repeated periodic motion occurred during the dynamic series other parallel diagonals with minimal differences are to be found. For instance if a repeated motion with period  $x$  (dynamics) occurred then multiple diagonal minima exist since the following entries in SSDM should all reflect only differences due to noise:  $[(p, p + x), (p + 1, p + 1 + x), (p + 2, p + 2 + x), \dots]$ . For the current study a period of 11 and 71 (see description of indentation experiment at the start of section 4.2.4 ) should therefore be observable in the data for the phantom and volunteer data respectively (e.g. for the phantom data dynamic 1 is repeated at dynamic 12, 23 etc.). Analysis of parallel diagonal locations in the SSDM, showing difference magnitudes expected for noise (i.e. similar to differences between multiple static repetitions) thus allowed for demonstration of repeatability.

#### 4.2.4.3 Evaluation of the system MRI compatibility

The MRI environment poses significant design challenges for the safe and appropriate functioning of both the device and the MRI scanner. In this study the following definition of MRI compatibility is used (for current definitions of MRI safety terminology see <sup>202,240</sup>. Although the term “MRI compatibility” is no longer favoured by the ASTM it is commonly used in the literature and hence also adopted here): *A device or system is Magnetic Resonance (MR) compatible if, when used in the MR environment, is MR safe and has been demonstrated to neither significantly affect the quality of the [MRI data or its] diagnostic information, nor have its operations affected by the MR device.* Since all of the device features presented, that are to be used in the MR environment are non-conducting (with the exception of the tap water used in the hydraulic system), non-metallic and non-magnetic the indenter system operation is not significantly affected by the MRI scanner and can be

termed MR safe using scientific rationale<sup>202</sup>. In addition all materials employed in the MRI environment (e.g. polyoxymethylene, polyamide, polytetrafluorethylene and polyurethane) exhibit appropriate magnetic susceptibility<sup>241</sup> for MRI and thus it is likely that their influence on MRI data quality is minimal. Nonetheless to evaluate the effect of the indenter on MRI data quality, system performance was analysed in the MRI environment. MRI data was acquired for a silicone gel phantom (Figure 4.5). In order to study the effect of the indenter presence on image quality a dynamic series (n=100) of MRI data was acquired with and without the indenter present. The same sequence as above was employed however without the SPAMM pattern (177 ms 3D Transient Field Echo read-out,  $T_R/T_E$  2.38/1.15 ms, field of view 120x120x40 mm, acquisition matrix 80x60, 20 slices, reconstructed voxel size 0.94x0.94x2 mm). To study the effect of the presence of the indenter for each dynamic series, per voxel temporal signal to noise (SNR) ratios  $tSNR$  were derived for each data set (with and without the indenter) using:

$$tSNR_{ijk} = \frac{\overline{\mu_{ijk}}}{\overline{\sigma_{ijk}}} \sqrt{n} \quad 4-4$$

where  $\overline{\mu_{ijk}}$  and  $\overline{\sigma_{ijk}}$  represents the mean and standard deviation of voxel  $(i, j, k)$  respectively across all dynamics.

## 4.3 Results

### 4.3.1 *Optical force sensor performance*

Figure 4.6 shows the staircase test force curves used for calibration (3 repetitions for 0.25 N/s and 2 for 0.75 N/s) and overlain the results for fitting based on the FBG strain signal. The current configuration of the sensor can only measure forces in excess of indenter head assembly weight. Hence all FBG derived force curves presented here start at 0.94N. Using linear scaling (scale-factor 970.20) followed by shifting (adding 0.94 N to compensate for the weight of the indenter head assembly) the FBG strain could be linearly related to force (Figure 4.6A). Although this showed an overall good correlation (Figure 4.6B) with the load-cell force ( $R^2=0.99$ ), force differences up to 0.16 N (corresponding to 3.2 % difference with respect to 5 N) occurred and a maximum difference percentage of 5.6 % was encountered (corresponding to a 0.056 N difference from 1 N). However all curves (Figure 4.6A) demonstrated a small degree of non-linearity of the FBG force sensor system. Linear mapping thus led to underestimation for low

forces where the curve was initially slightly concave followed by overestimation of larger >7N forces due to a mild convex curvature (see curvature in Figure 4.6B). Hence to take the mild non-linearity into account a cubic spline fit (MATLAB function *CSAPE*) was used to map the FBG strain to force (Figure 4.6C) producing a piecewise-polynomial form relating FBG-strain to force. The fit was constrained at the ends such that the end slopes match the slope of the cubic of the last 4 data points to allow for reasonable extrapolation in forces in the range 15-50 N (up to breakage). The cubic spline based mapping of the FBG strain to force, reduced the maximum error percentage to 3.1% (corresponding to a 0.031 N difference from 1 N) and the maximum force error magnitude to 0.043 N (corresponding to 0.7% difference with respect to 6 N). The mean and standard deviation of the differences with respect to the load-cell force were 0 N ( $-2.23 \cdot 10^{-5}$  N) and 0.015 N respectively. Figure 4.6B shows the high degree of correlation (Figure 4.6D) between the load-cell force and the FBG derived force ( $R^2=1.00$ ). The largest percentage difference coincided with the (1 N) first plateau measurements which is closest to 0.94 N, the lowest recordable force. If for all tests the first plateau is ignored, the maximum error percentage is 1.2 % (corresponding to a 0.024 N difference from 2 N).

After calibration based on the stair-case tests the response for a ramp test at 5 N/s was predicted (Figure 4.7). The differences with respect to the load-cell force were not found to increase for the higher load rate which is also apparent from the large degree of overlap in Figure 4.7.

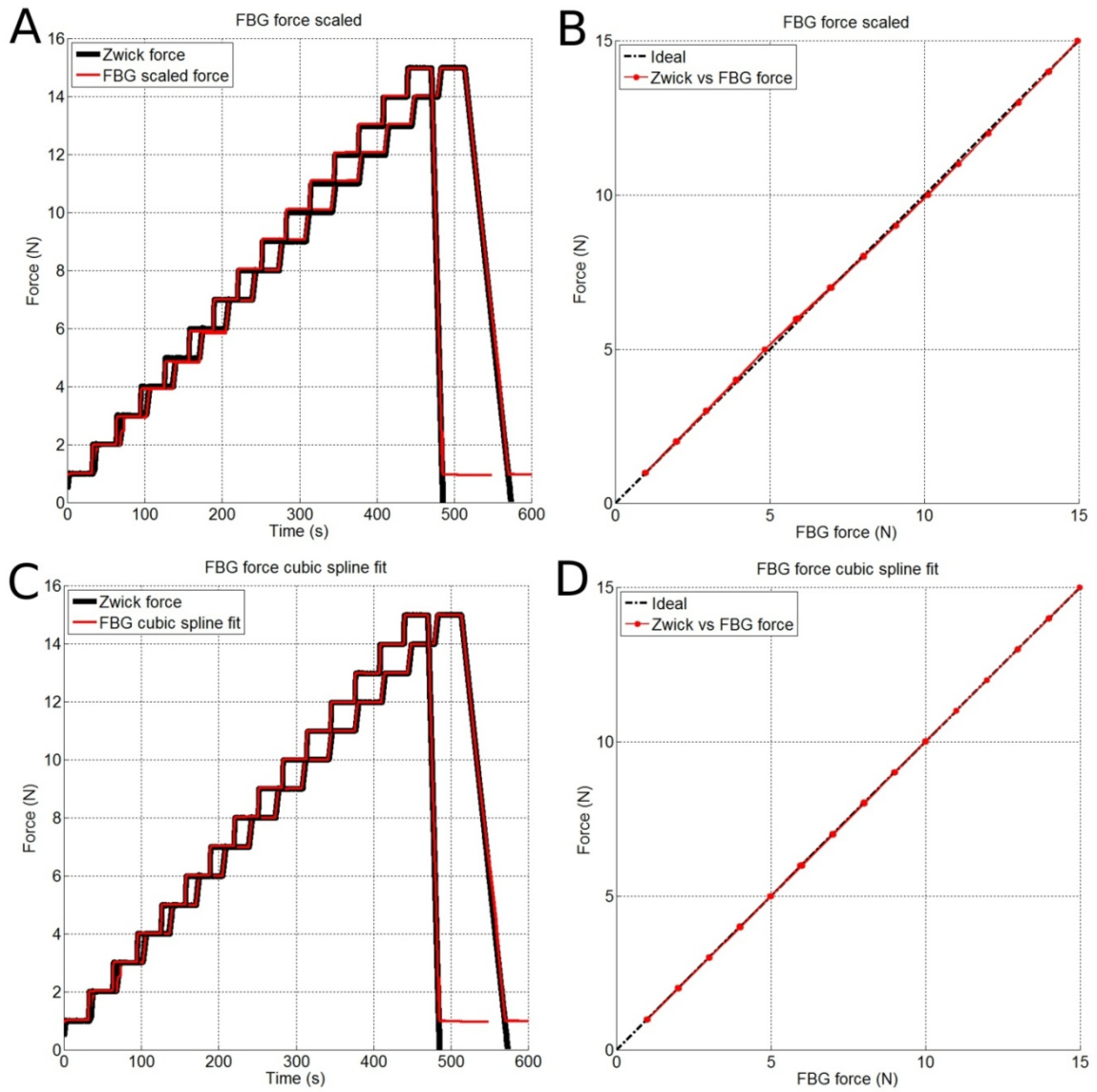


Figure 4.6 The load-cell (thick black) and, overlain, the FBG derived (red) force history curves for the stair-case tests (A-C) and, the load-cell and FBG derived plateau forces plotted against each other to show correlation (B-D). Images (A-B) are for linear scaling while (C-D) are for cubic spline based mapping of FBG-strain to force.

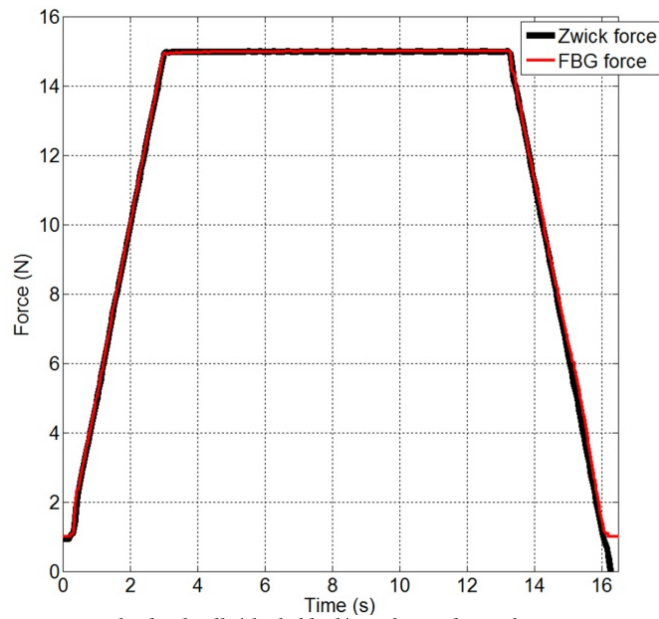


Figure 4.7 The load-cell (thick black) and, overlain, the FBG derived (red) force history

Figure 4.8 shows sample force and displacement history curves for volunteer upper arm indentation within the MRI scanner. As expected, no signal interference from the MRI scanner was observed. Both sets of curves in Figure 4.8 demonstrate viscoelastic force decay during the hold phase of the load. In addition preconditioning is observed (Figure 4.8B) as the peak force is reduced during the first motion cycles. This is not a repeatability artefact but a well-known empirical finding for biological soft tissue. The loading rate for the first volunteer in Figure 4.8A (a male volunteer aged 30) was twice as high for the second volunteer in Figure 4.8B (a female volunteer aged 25). Besides indentation depth and subject to subject variation it is likely that the increase in viscoelastic response observed in the second volunteer can be explained by the increase in loading rate.

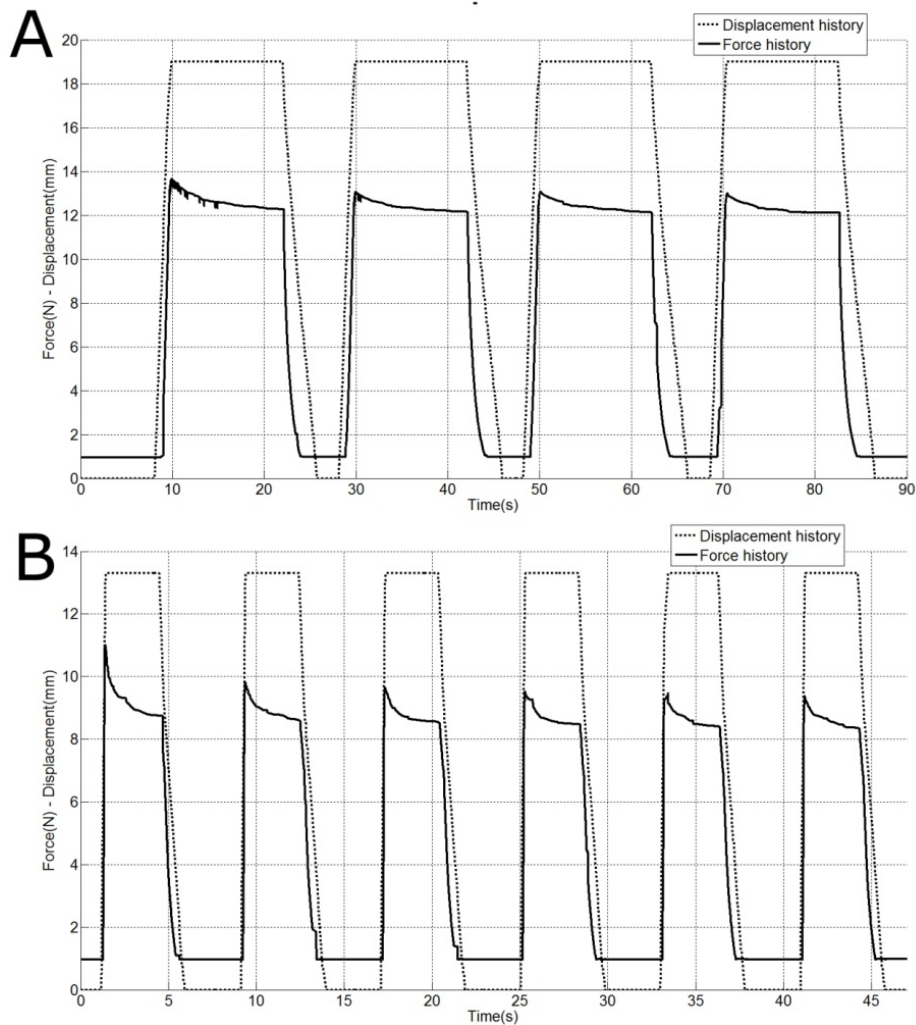


Figure 4.8 Sample displacement (dashed) and force (solid) curves for cyclic ramp and hold indentation tests for two different volunteer tests. Part (A) shows 19mm indentation at 10mm/s and a 12 s hold phase. Part (B) shows 13.3 mm indentation at 20mm/s and a 3s hold phase.

### 4.3.2 Repeatability of indentor motion

Figure 4.9A-D shows a visualisation of the sum of squared differences matrix (SSDM) for the phantom and volunteer data (due to symmetry only half of the matrix is shown). As mentioned in section 4.2.4.2, periodic motions should be reflected in the SSDM as parallel diagonals showing minimal differences. These are visible for both the phantom and volunteer data. Each row in the SSDM describes a periodic signal starting on the left, on the main diagonal, with a zero magnitude difference (difference with respect to itself) the magnitudes alter but return to a minimum every 11<sup>th</sup> and 71<sup>st</sup> entry in the rows for the phantom and volunteer respectively. In order to visualise this periodic nature for all rows more appropriately Figure 4.9B and E show shifted or synchronised SSDMs. Here, starting at the bottom, each row of entries in the SSDM was shifted to the left by an amount equivalent to its corresponding row (or dynamic) number minus 1 (e.g. first row

remains the same, second is shifted by 1, third by 2 etc.). This shifting effectively aligns or synchronises all the periodic difference variations in the SSDMs. The numbered labels in Figure 4.9B and E now clearly show that for the phantom and volunteer data the periodic signal exactly reflected the desired periods of 11 and 71 dynamics respectively. This is further illustrated in Figure 4.9C and F which are obtained by taking the mean of images Figure 4.9B and E in the row direction. As Figure 4.9C and F show clear minima exist at the appropriate locations (red dots) and differences rapidly increase to more than an order of magnitude higher for non-repeated dissimilar images. It was found that for static repetitions during the hold phases the mean and standard deviation of the SSD were  $1.13 \cdot 10^6$  and  $0.25 \cdot 10^6$  for the phantom data and  $4.14 \cdot 10^4$  and  $0.60 \cdot 10^4$  for the human data. These thus form the SSD values expected purely due to noise variations. The SSD values for acquisitions during indenter motion, which, according to applied indenter motion, should be equivalent, showed a mean and standard deviation of  $1.14 \cdot 10^6$  and  $0.52 \cdot 10^6$  for the phantom data and  $4.37 \cdot 10^4$  and  $0.94 \cdot 10^4$  for the human data. Hence it may be concluded that the indenter presents with a highly repeatable motion since the differences expected due to noise are of equivalent magnitude to the differences between repeated indenter motions.

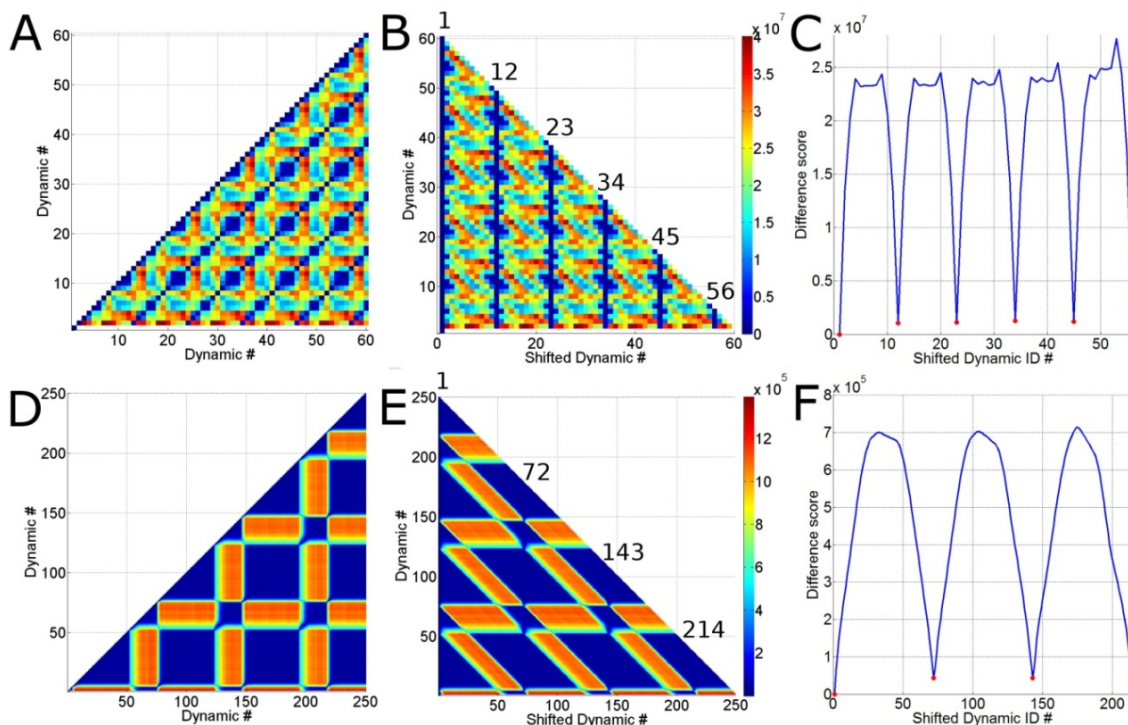


Figure 4.9 Motion cycle repeatability results for the phantom (A-C) and volunteer (D-F). (A-D) show the SSDM's. (B-E) show the shifted or "synchronised" SSDMs and (C-F) show derived mean SSD graphs (blue line) were red dots indicate the cycle repetition points.



### 4.3.3 MRI compatibility of indenter system

Figure 4.10 below shows temporal SNR images derived for the phantom without (A) and with indenter present (B). It was found that throughout the field of view the temporal SNR levels were not significantly altered by the presence of the indenter. The overall mean and standard deviation of the temporal SNR levels for the phantom volume without indenter present were 500.18 and 207.08 respectively. When the indenter was added this became 501.95 and 200.45 respectively. This result was invariant under permutation of read-out directions and or slice orientations. However since the MRI actuator contains tap water, which presents with signal, certain read-out directions may present with fold-over due to this signal. However this can easily be avoided by alternating the read-out direction or by employing fold-over suppression techniques.

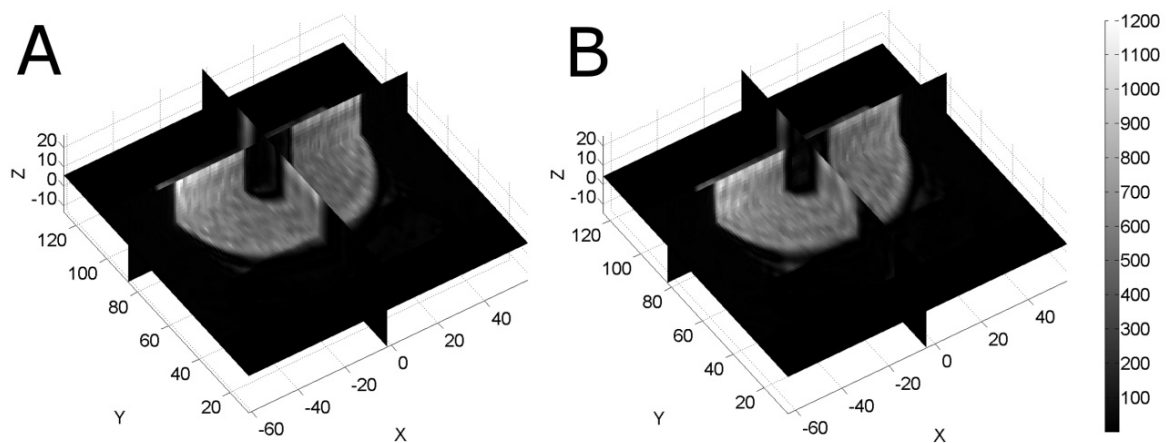


Figure 4.10 Temporal SNR images for the phantom without (A) and with indenter present (B).

## 4.4 Discussion

A novel MRI compatible soft tissue indenter system and optical FBG based force sensor have been presented. The computer controlled indenter motion is highly repeatable since MRI acquisitions during repeated indenter motions did not induce significant additional variation on top of what is expected due to noise. In addition the indenter device and force sensor are fully MRI compatible as they are manufactured from non-ferromagnetic materials. The MRI compatibility was also evident following evaluation inside an MRI scanner and no negative effects such as SNR decrease and or image artefacts were observed.

Following uni-axial compression testing the force sensor was calibrated for measurement of compressive forces up to 15 N and demonstrated a maximum force difference percentage of 3.1 % (corresponding to a 0.031 N difference from 1 N) and a

maximum force error magnitude of 0.043 N (corresponding to 0.7 % difference with respect to 6 N). Evaluation of the force sensor during soft tissue indentation demonstrated its ability to record viscoelastic force histories resulting from ramp and hold indentations. The MRI compatible force sensor and soft tissue indenter presented have a wide range of possible application such as MRI guided interventions<sup>37</sup> and functional MRI<sup>41</sup>. In addition, as is relevant to the current thesis, when combined with inverse analysis and measurement of soft tissue deformation, it allows for the non-invasive determination of the mechanical properties of living human soft tissue.

As referred to in section 4.2.4 the indenter system was evaluated for use in the non-invasive investigation of tissue biomechanics. Indentation tests were performed on a silicone gel phantom and the upper arm of volunteers. During indentation all boundary conditions required for inverse FEA analysis of the biomechanical tissue properties were acquired such as: 1) *the indentation force derived from the FBG sensor*, 2) *the complex soft tissue deformation acquired using SPAMM (SPAtial Modulation of the Magnetisation) tagged MRI<sup>238, 239</sup>*, 3) *the tissue geometry for the construction of FEA models derivable from anatomical MRI and 4) muscle tissue fibre architecture obtained from diffusion tensor MRI<sup>33</sup> to allow for analysis of anisotropic material behaviour*. Figure 4.11 shows sample results for indentation of a volunteer with the indenter system. Following application of SPAMM tagged MRI in three mutually orthogonal directions dynamic 3D deformation could be measured (Figure 4.11A-B). In addition diffusion tensor MRI allowed for characterisation of fibre architecture throughout the region of interest (Figure 4.11C) and anatomical MRI scans provided the basis for the construction of detailed FEA models (Figure 4.11D). The MRI compatible indenter set-up was used for validation of SPAMM tagged MRI based 3D soft tissue deformation measurements in a silicone gel phantom and the upper arm of a volunteer (see chapters 7 and 8). The repeatable indenter motion allowed for the quantification of deformation measurement accuracy and precision at sub-voxel levels, further demonstrating the high level of repeatability of the indenter motion.

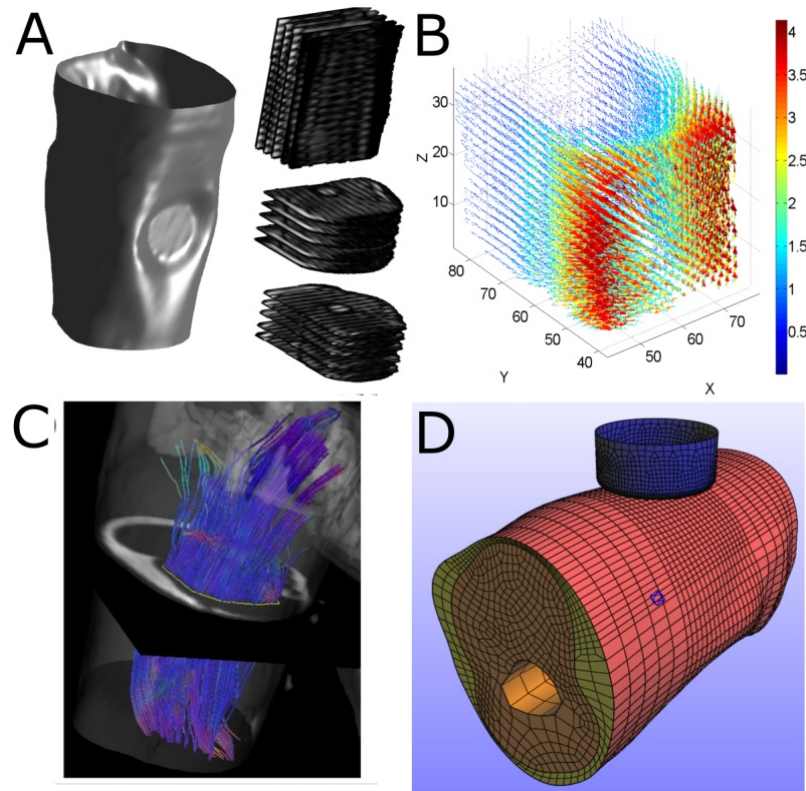


Figure 4.11 SPAMM tagged MRI acquired during indentation (A) allowing derivation of 3D dynamic deformation measurements (units mm) (B). Diffusion tensor measurements provide fibre architecture (C) which together with anatomical MRI data allows for the construction of detailed finite element models (D).

Figure 4.12 shows two alternative applications for the MRI compatible indenter system, large strain mechanical property investigation based on the combined use of SPAMM tagged MRI and MR Elastography (see Figure 4.12A and the preliminary study<sup>242</sup>) and for validation of motion compensation techniques for dynamic contrast enhanced imaging (Figure 4.12B). The indenter has also found application outside the MRI environment for inverse mechanical property analysis combined with digital image correlation<sup>243</sup>.

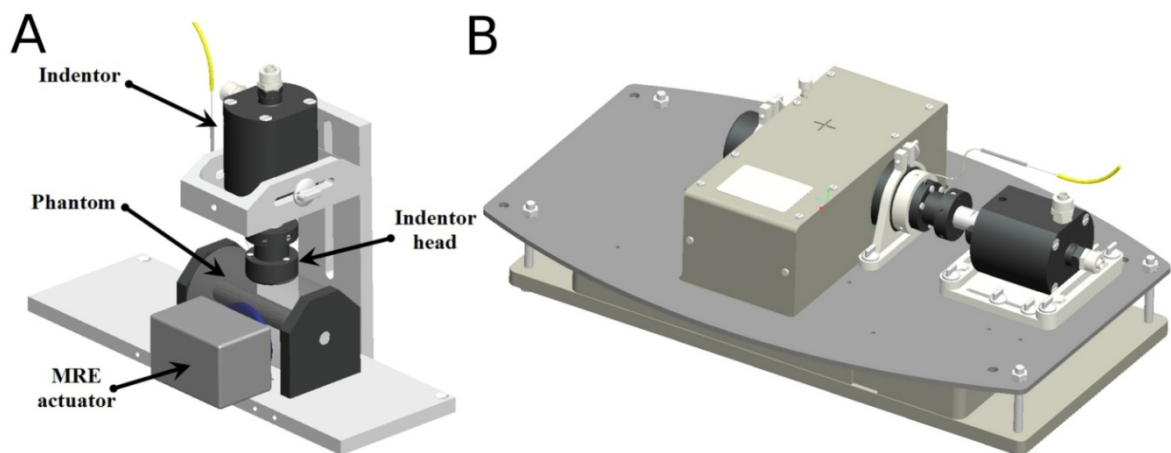


Figure 4.12 Example alternative applications of the MRI compatible actuator. For large strain MR Elastography (MRE) measurements (A) and mounted for use with a specialised coil and phantom for validation of motion compensation techniques during contrast enhanced imaging (B).

Various soft tissue loading devices have been used in the literature for MRI based tissue investigation. To date however: many have been limited to quasi-static deformation analysis<sup>26, 43, 173, 205-208</sup>, the evaluation of isotropic hyperelastic constitutive models<sup>26, 43, 173, 205-208</sup>, estimation of strain from 2D imaging<sup>26, 205, 209</sup> or from finite element simulations<sup>26, 208</sup>. Force measurement is sometimes based on the application of static weights<sup>173</sup> or by repeating the experiment outside the MRI environment<sup>208</sup> or electric force sensors which suffer from MRI scanning induced electromagnetic interference<sup>43</sup>. Recently Fu et al. 2011<sup>209</sup> used an MRI compatible indenter system to study leg tissue biomechanics and 2D strain estimates were derived for 7 frames per indentation cycle based on harmonic phase MRI. Detailed comparison to the current study is however hindered since the MRI compatible system was not fully described. To the authors' knowledge this is therefore the first study to demonstrate a computer controllable MRI compatible indenter with an integrated high sampling rate (100 Hz) force sensor suitable for the non-invasive analysis of the complex anisotropic, viscoelastic and 3D mechanical behaviour of human soft.

The current study employs FBG for MRI compatible force measurement and calibration demonstrated force difference percentages no larger than 3.1 % for forces up to 15 N (maximum force difference magnitude was 0.043 N). To date a large array of MRI compatible force sensors have also been developed. Piezoelectric sensors have been proposed; however, these cannot be used to measure static forces<sup>37</sup> and are therefore not ideally suited for quasi-static and viscoelastic (ramp and hold type) tissue property investigation. In addition they may induce image artefacts<sup>37</sup> depending on proximity to the imaging region. MRI compatible force sensors for the application of needle deflection and force feedback measurement during catheterisation have also been developed<sup>40, 210</sup> however these are applied to forces in the range 0-0.5 N. Tada *et al.*<sup>211</sup> presented an optical MRI compatible tri-axial force sensor based on a deformable structure and optical micrometry. A total of 5 optical fibres were used: 1 emitting fibre mounted on a movable component and 4 receptor fibres allowing monitoring of motion of the emitting fibre and thus derivation of force. The system was calibrated in the range of 0-15 N and showed errors under 3 %. This complex force sensing system has also been applied to quasi-static compression tests to the human finger-tip for inverse analysis of the assumed isotropic hyperelastic mechanical properties<sup>207</sup>. During quasi-static compression tests in 5 steps up

to 3.48 N the force was measured at 1 Hz. However the static force measurements showed standard deviations ranging from 0.11 N (for a mean force of 1.7 N) up to 0.3 N (for a mean force of 2.35 N). The causes for the increased deviations, with respect to the calibration which reported errors under 3 %, were not discussed. In addition the hydraulic compressor system used was not described in detail hindering comparison to the system proposed in the current study. Tokuno *et al.*<sup>244</sup> developed a force sensor based on optical micrometry and demonstrated accuracy within 1.6 % for forces up to 6 N. Song *et al.*<sup>39</sup> designed an advanced FBG based tri-axial force sensor system for the tip of a robot arm for application to minimally invasive surgery. Forces were calibrated up to around 10 N and a maximum force error of 0.5 N was recorded. As this review shows, the force sensor performance demonstrated in the current study is comparable to those in the literature.

Some limitations of the proposed MRI compatible indenter and force sensor system are now discussed. The indenter system employs a hydraulic (tap water driven) master slave system. If imaging is performed using read-out directions aligned with the water filled actuator signal fold-over may occur. However this can easily be dealt with using alteration of the read-out direction, field of view adjustments or fold-over suppression techniques.

At present the indenter stroke is limited to 44 mm. This is sufficient for application to (non-injury inducing) soft tissue indentation in human subjects. For other applications requiring a larger range of motion the design can be scaled up.

Due to the way that compressive forces are converted to tensile forces in the FBG sensor within the current design, measurement of forces in the range 0~0.94 N are currently not possible since the weight of the indenter head (0.94 N) assembly needs to be overcome (only the case for downward indentation). The force measurement range 0.94~15 N is however sufficient for many purposes including (non-damaging) large strain biomechanical soft tissue investigation.

Other researchers have developed more complex tri-axial force sensor systems (e.g.<sup>39, 211, 244, 245</sup>) for MRI. However the uni-axial force measurements presented here ensured a simple and compact indenter design and are sufficient for comparison to inverse FEA as the same resultant uni-axial force can easily be generated as an output.

For the current study the FBG signal was acquired at 1 kHz however a 10 point data interleave was used for the optical interrogator leading to an effective acquisition

rate of 100 Hz. Although 100 Hz is deemed sufficient for the applications of the current study, a sample rate up to 1 kHz is feasible with the employed optical interrogator (or higher using more advanced interrogators). However acquiring the sensor at 1 kHz was not possible in the current study given the limitations in computer speed and of the indenter control and data acquisition software used. The computer control system has to simultaneously record the FBG signals and record and control the DC-motor behaviour and monitor the MRI TTL pulse in real-time. As such in the future force measurement of up to 1 kHz will be possible with this indenter given improvements in computational power and improvements in the data acquisition software.

With the exception of the optical interrogator system the proposed MRI compatible indenter system is relatively low cost. The MRI compatible indenter slave system components (used within MRI environment) are fabricated from non-conducting non-ferromagnetic materials which are all common engineering polymers (e.g. polyoxymethylene). All non-standard components can be manufactured using simple mill and rotating bench operations and all screws, tubes, fittings, the DC-motor and master cylinder are commercially available. If readers are interested in the design specifications or computer aided design files (based on Pro/Engineer, Parametric Technology Company, MA, USA) these can be made freely available upon request.

Future work will focus on the application of the proposed MRI compatible indenter and force sensor system to the non-invasive investigation of skeletal muscle tissue mechanical properties. Since the system allows for dynamic force measurement and can be combined with the MRI based 3D fibre architecture and dynamic deformation measurement it thus allows for the evaluation of the complex (non-linear elastic, anisotropic and viscoelastic) 3D mechanical properties of soft tissue.

## 4.5 Conclusions

A novel MRI compatible indenter system is presented for the investigation of soft tissue biomechanics. A master slave system was developed whereby a computer controlled hydraulic master cylinder was used to provide highly repeatable motions to an MRI compatible actuator. To evaluate the system in the MRI environment and demonstrate its usefulness for soft tissue biomechanics investigation the system was used for indentation of a silicone gel phantom and the upper arm of volunteers. Repeatability was

evident from the fact that MRI data for static repetitions showed similar variations as those from dynamic motion repetitions. All indenter components in the MRI room are non-ferromagnetic and non-conducting and hence MRI safe and can be used in close proximity to the imaging subject. MRI compatibility was demonstrated following imaging of a phantom and the presence of the MRI actuator did not induce any artefacts or significant SNR changes. Embedded in the indenter assembly is a novel high sampling speed (currently 100 Hz) optical FBG based force sensor. The force sensor was calibrated for forces up to 15 N and demonstrated a maximum force difference of 3.1% (maximum force difference magnitude was 0.043 N). Application of the force sensor in volunteer upper arm indentation showed the sensor's ability to register viscoelastic force decay resulting from ramp and hold indentation.

Together with MRI modalities such as SPAMM tagged MRI, the indenter system allows for analysis of all boundary conditions required for the non-invasive investigation of the complex mechanical properties of soft tissue. Future work will focus on the use of the proposed system for the analysis of the non-linear elastic, anisotropic and viscoelastic mechanical properties of skeletal muscle tissue with application to the field of impact biomechanics and pressure ulcer prevention.

## 5 STUDY II

# DIC and inverse FEA for the Determination of the Mechanical Properties of Soft Tissue



## 5.1 Introduction

As discussed in section 3.8 the current thesis aims toward a framework for the inverse FEA based non-invasive analysis of the mechanical properties of muscle tissue. The implementation with MRI and anisotropic tissue property assessment presented with initial challenges. Hence the more limited straightforward imaging method, digital image correlation (DIC), was assessed as an alternative to MRI in the inverse FEA based mechanical properties assessment of bulk soft tissue.

DIC has been applied to biological soft tissues e.g. using 2D DIC: on the human tympanic membrane<sup>246</sup>, sheep bone callus<sup>247</sup>, human cervical tissue<sup>248</sup> and recently also using 3D DIC: for the bovine cornea<sup>249</sup> and mouse arterial tissue<sup>250</sup>. In all these studies the analysis is limited to planar tissue and/or superficial properties of excised tissue samples and thin tissue layers. The potential of using the surface measurements of 3D DIC to assess mechanical states throughout the bulk of a tissue has been suggested<sup>251</sup> but not yet attempted. This chapter assesses, for the first time, the use of 3D DIC and inverse FEA to non-invasively determine the bulk material properties of a soft tissue phantom which could be applied *in-vivo*.

## 5.2 Methods

DIC is an optical method which uses tracking and image registration to measure high resolution 3D deformation. Using a two camera set-up (Figure 5.1A) and tracking of unique features such as speckles, within small image subsets (Figure 5.1B). DIC can be combined with an iterative FEA procedure to optimise the parameters of a constitutive model. To verify this method, indentation tests were performed on a silicone gel (SYLGARD® 527 A&B dielectric, Dow Corning, MI, USA) phantom (Figure 5.1C). The material parameters for a hyperelastic Neo-Hookean material model of the gel were determined by regression (using Prism 4.0, GraphPad Software Inc.) of the model against uni-axial compression tests up to 50 % strain on cubic samples (~10mm). The Neo-Hookean strain-energy density is defined by:

$$\Psi(\tilde{\lambda}_1, \tilde{\lambda}_2, \tilde{\lambda}_3, J) = \frac{\mu}{2} (\tilde{\lambda}_1^2 + \tilde{\lambda}_2^2 + \tilde{\lambda}_3^2 - 3) + \frac{\kappa}{2} (J - 1)^2 \quad 5-1$$

Where  $\tilde{\lambda}_i = J^{-\frac{1}{3}} \lambda_i$  represent the modified principal stretches and  $J$  the Jacobian. The parameters  $\mu$  and  $\kappa$  define material stiffness and the Poisson's ratio as:

$$\nu = \frac{3\left(\frac{\kappa}{\mu}\right) - 2}{6\left(\frac{\kappa}{\mu}\right) + 2} \quad 5-2$$

The material was assumed nearly incompressible and thus in the fitting procedure  $\kappa$  was constrained to yield a Poisson's ratio of 0.4997. The parameters found were:  $\mu= 1.71$  kPa,  $\kappa=2857$  kPa ( $R^2 =0.9979$ ).

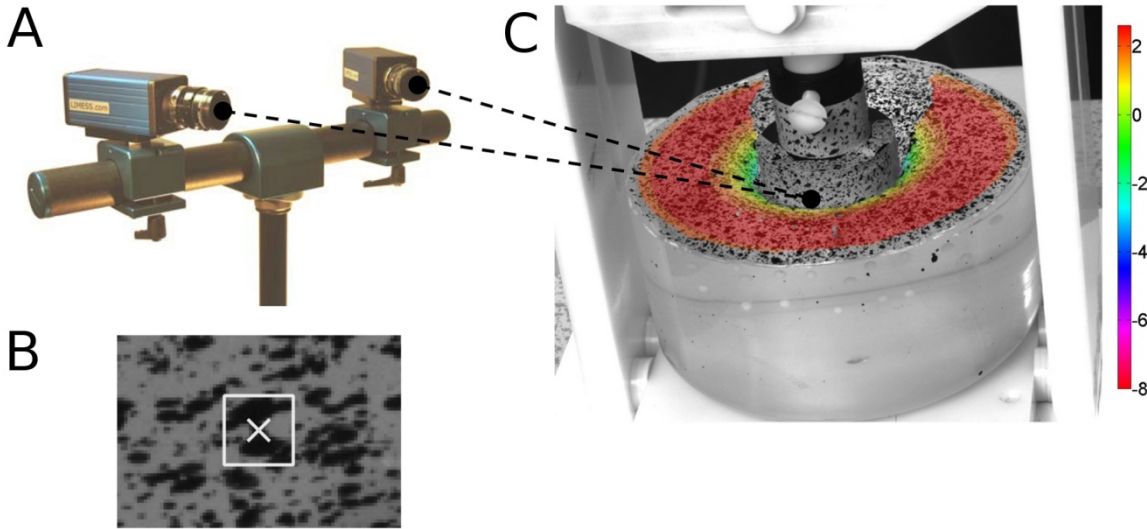


Figure 5.1 The two camera DIC set-up (A), a close-up of speckles showing a subset (B) and the silicone gel phantom model and indenter piston with overlain the DIC derived top surface displacement (C).

The soft tissue phantom (Figure 5.1C) was moulded in a cylindrical polypropylene container and black paint speckles (0.2~2mm) were applied to the top surface of the gel. A circular indenter was then used to apply compression. A two camera DIC configuration (Limes Messtechnik & Software GmbH, Pforzheim, Germany) was used to record the deforming phantom and the movement of the speckle pattern for static compression up to 11.7 N load applied to the gel through the indenter. The indenter set-up was similar to that described in chapter 4 however the optical force sensor was not implemented and instead forces were applied to the top of the indenter using a set of known weights. Analysis software VIC-3D (DIC Software, Correlated Solutions, Inc., Columbia, SC, USA) was then used to calculate the deformation of the top surface of the gel and the indenter displacement (Figure 5.1C). To simulate the compression experiment an axisymmetric FEA model of the gel indentation was created using Abaqus 6.7-1 Standard (Dessault Systèmes, Suresnes Cedex, France). The container was assumed rigid (no deformation of the container was observed) and simulated by constraining the gel nodes that would be in contact with the container from moving in all directions. The piston was modelled as rigid and the gel phantom was modelled using the Neo-Hookean hyperelastic material

model and meshed using 4-node quadrilateral elements. Since the silicone gel is sticky the gel/piston contact was modelled with no slip. The experimental displacement was applied to the piston. The material parameters were then iteratively altered until a good match with both the experimental indenter force and deformation was obtained. The upper region of the FEA model is shown in its initial and deformed state in Figure 5.2A and B respectively.

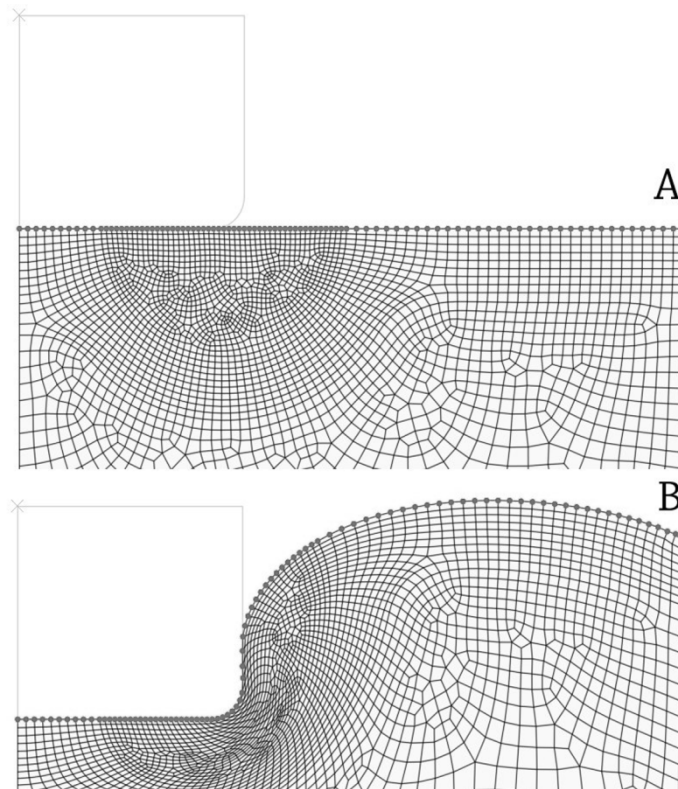


Figure 5.2 Top surface region of FEA model: (A) Initial FEA mesh, (B) deformed FEA mesh

## 5.3 Results

The experimental and FEA results were compared using Matlab 7.4 R2007a (The Mathworks Inc., USA). The best match to the experimental data was achieved using  $\mu=1.80$  kPa and  $\kappa=2999$  kPa ( $\nu=0.4997$ ) which are a close match to the parameters derived from uni-axial compression ( $\mu =1.71$  kPa,  $\kappa=2857$  kPa). The experimental DIC results are 3D coordinates of points tracked on the top surface of the phantom and are shown in Figure 5.3.

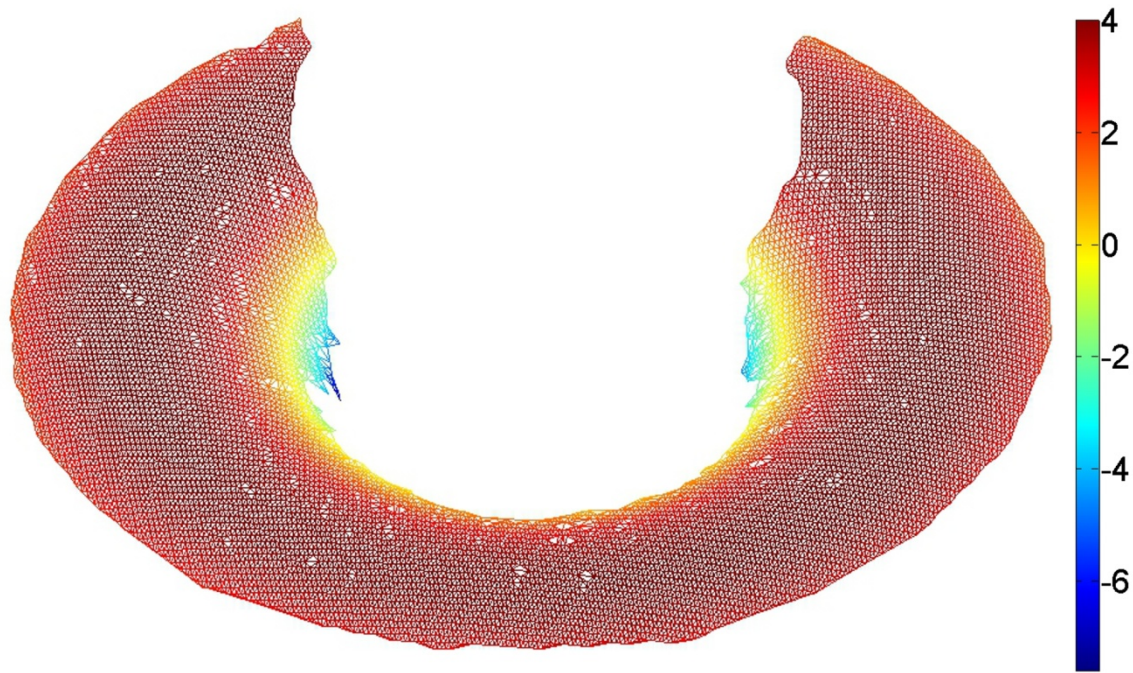


Figure 5.3 A Delaunay triangulation of the data points tracked using DIC. Edges are shaded towards displacement magnitude (mm).

In order to compare the 3D experimental deformation data with the axisymmetric 2D FEA deformation data, the 3D data was revolved around the central axes. This effectively “wrapped” all data points around the central axes and mapped them into a single plane. Figure 5.4A is a top view of the experimental surface at the maximum compression depth (16.75mm). The surface is shaded depending on the difference magnitude (mm) with the FEA results. The average difference magnitude observed is 0.4 mm with the largest differences around the centre near the indenter edge where correlation was poorer due to the inward curvature of the gel. A mirrored representation showing the 2D FEA results and the wrapped DIC results are shown in Figure 5.4B. The shape of the top surface in the FEA simulation forms a good match to the experimental shape ( $R^2=0.81$ ).

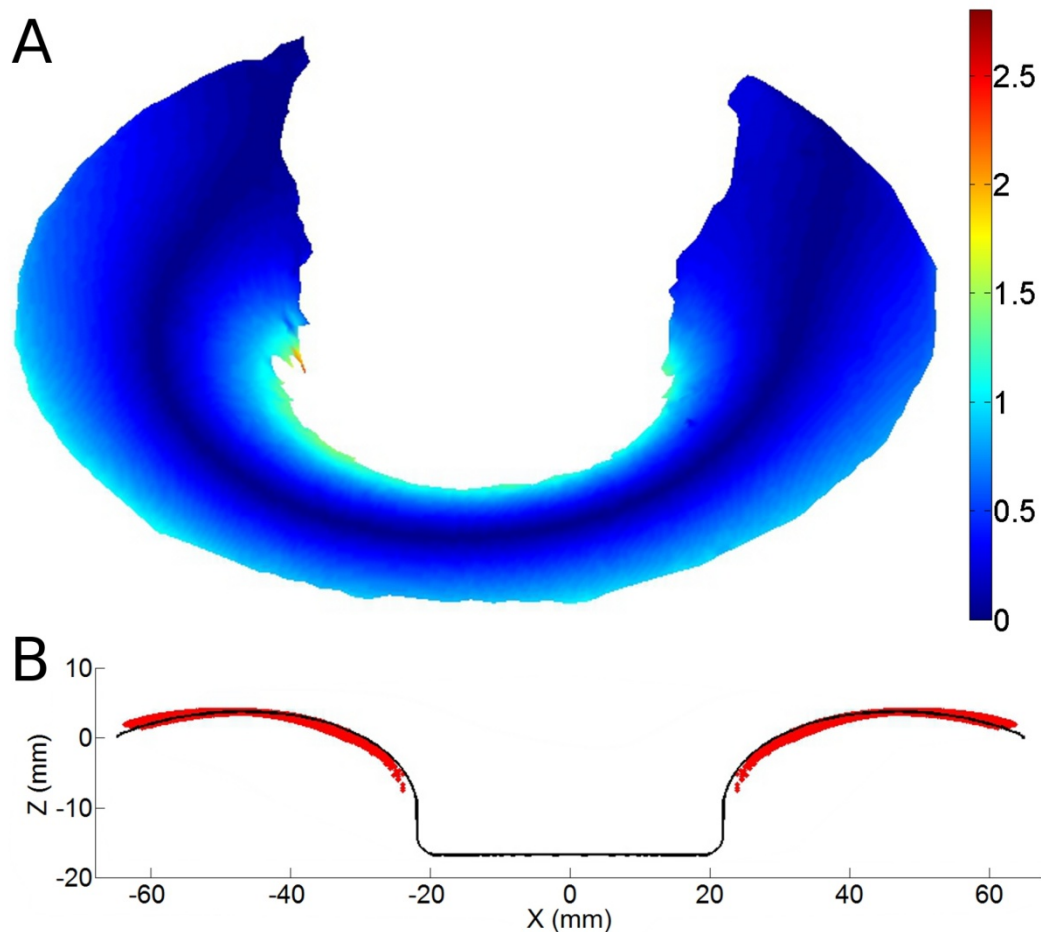


Figure 5.4 Comparing DIC and FEA deformation data. A 3D comparison of revolved FEA top surface with DIC surface (A), surface is coloured according to the error magnitude (mm). A 2D comparison showing the mirrored FEA top surface (black curve) and DIC points (red).

Figure 5.5 demonstrates that near incompressibility was a good assumption, as lowering  $\nu$  results in divergence from the experimental deformation ( $\mu$  was held constant).

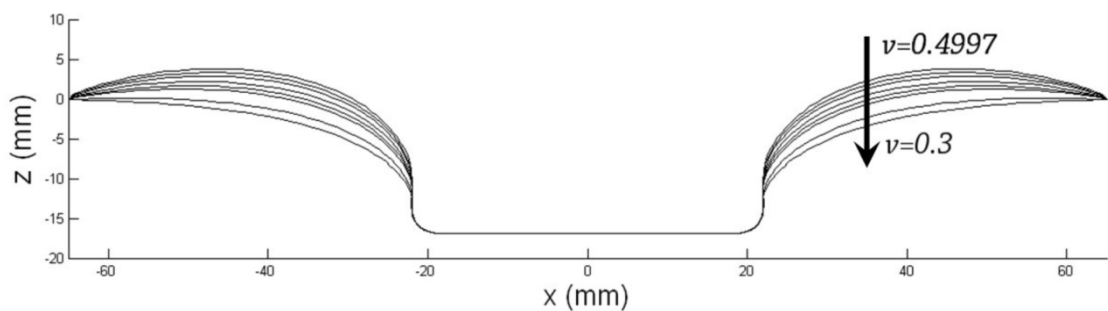


Figure 5.5 Influence of choice of Poisson's ratio on resulting FEA deformation at piston depth of 16.74mm. From top to bottom surface deformation for  $\nu=0.4997$  (best match),  $\nu=0.495$ ,  $\nu=0.49$ ,  $\nu=0.48$ ,  $\nu=0.47$ ,  $\nu=0.45$ ,  $\nu=0.4$  and  $\nu=0.3$

A parametric analysis for the parameter  $\mu$  was performed using FEA simulations. The resulting indenter force displacement curves are shown in Figure 5.6. In addition to the experimental indenter force displacement data, curves are shown for the best match (using  $\mu=1.80$  kPa) and the  $\mu$  derived from regression to uni-axial data ( $\mu=1.71$  kPa). To

indicate how altering  $\mu$  influences the indenter force response, curves for  $\mu=1.37$  kPa and  $\mu=2.05$  kPa (20 % lower and 20 % higher than 1.71 kPa respectively) are also shown.

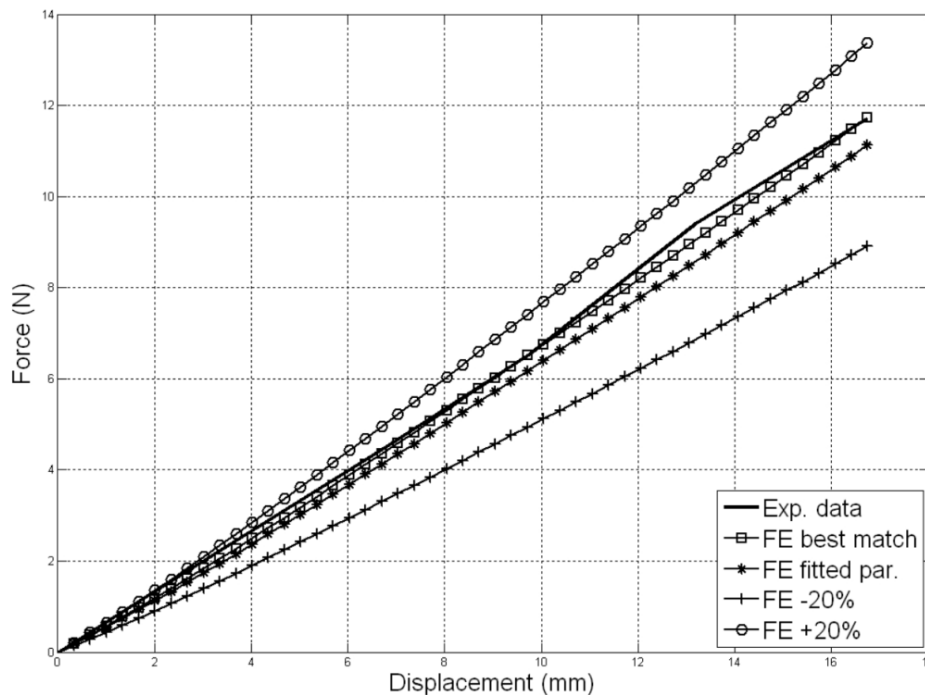


Figure 5.6 Indenter force displacement curves. Experimental (solid), FEA best match to experimental (solid, square), FEA using fitted parameters (solid, star), FEA using 20% lower  $\mu$  (solid, plus), FEA using 20% higher  $\mu$  (solid, circle).

## 5.4 Discussion and conclusions

Figure 5.4, Figure 5.5 and Figure 5.6 demonstrate that the experimental indenter force and shape boundary conditions could be reproduced using  $\mu=1.80$  kPa and  $\kappa=2999$  kPa (such that  $\nu=0.4997$ ). The shape of the top surface in the FEA simulation mainly depends on the choice of the Poisson's ratio (Figure 5.5) and the force mainly on the choice of  $\mu$  (Figure 5.6).

The  $\mu$  parameter for the best match ( $\mu=1.80$ ) closely matches the derived from independent uni-axial compression tests ( $\mu=1.71$ ). Using  $\mu=1.71$  in the FEA simulation results in predicted indenter force of 11.14 N which is a 95 % match to the experimental force (11.7 N). However it may be that the experimental indenter force was lower than 11.7 N because of possible friction in the indentation device due to the application of static weights on the indenter top.

Furthermore, the shape of the deformed finite element surface in Figure 5.4 is a close match ( $R^2=0.81$ ) to the experimental shape. The small difference may partially be related to the fact that the gel surface meniscus was not modelled (the initial surface in the FEA model is flat).

Overall these results demonstrate that when the correct bulk material properties are applied, the FEA model has a good capability of reproducing the experimental boundary conditions. It is therefore concluded that a two camera DIC configuration to record 3D surface deformation, in combination with FEA modelling, can be used to determine the bulk constitutive parameters of hyperelastic Neo-Hookean materials. The present work is limited to isotropic and elastic materials and thus application to anisotropic and viscoelastic materials requires further research. DIC is more straightforward than other imaging modalities such as MRI and, combined with FEA modelling, has the potential to characterize not only the superficial properties but also the underlying bulk constitutive properties for materials with arbitrary shapes undergoing large deformations.

## 6 STUDY III

# A Validation Framework for MRI Based Deformation Measurement



## 6.1 Introduction

As discussed in section 3.7 the techniques for tracking tissue deformation from (for example tagged) MRI are complex and require validation using an independent measure of deformation. In addition it was concluded that validation of *in-vivo* medical imaging techniques and image processing algorithms is challenging partially due to the lack of appropriate reference data and for common validation methods employed the errors associated with the validation methods are not quantified. In this chapter a novel technique for the validation of a 3D MRI based motion and deformation tracking is presented. The validation method, based on marker tracking in a novel silicone gel soft tissue phantom, was evaluated (and validated) using simulated magnitude MRI data since this allows full control and knowledge of marker locations and thus provides a ‘gold standard’ for method evaluation. In addition this allows for the independent analysis of geometric bias and of method performance across a wide range of realistic noise conditions.

### 6.1.1 *The tissue phantom*

The proposed validation configuration is a MR compatible indenter used to apply deformation to a phantom and provide an independent measure of deformation allowing validation of MRI based motion and deformation tracking. A silicone gel soft tissue phantom (Figure 6.1) was developed to represent deformation modes expected in the human upper arm due to external compression, as such the phantom resembles a cylindrical soft tissue region containing a stiff bone-like core. The gel (SYLGARD® 527 A&B Dow Corning, MI, USA) has similar MR<sup>252</sup> and mechanical properties<sup>243</sup> to human soft tissue and has been used in numerous MRI based studies on soft tissue biomechanics<sup>229, 232, 253-260</sup>. Embedded in the gel are contrasting spherical polyoxymethylene balls of  $3\pm 0.05$  mm diameter (The Precision Plastic Ball Co Ltd, Addingham, UK). The lack of signal in the markers in comparison to the high gel signal allows tracking.

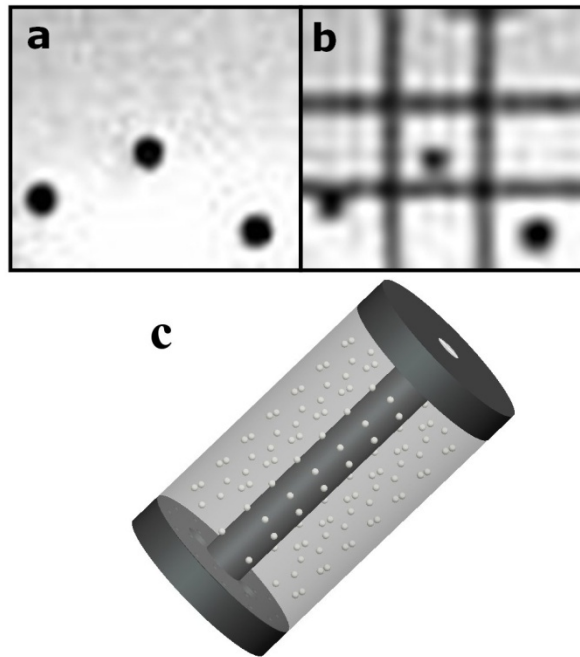


Figure 6.1 An MR image of a gel region with markers (A), a tagged MRI region and (B) and the silicone gel soft tissue phantom containing the contrasting spherical markers (white balls) (C)

### 6.1.2 MR Imaging

The type of image data used in the current study is T2 magnitude MR images. Deformation can be measured using marker tracking methods applied to full volume scans taken at each deformation step. A full volume scan was performed on the tissue phantom using a 3 T scanner (Philips Achieva 3 T, Best, The Netherlands), isotropic 0.5 mm voxels were used and the data was stored using the DICOM (Digital Imaging and Communication in Medicine) format. Figure 6.1 A and B show an example of an MR image and tagged MR image of a region of the phantom respectively. The voxel intensities of the images are 9 bit unsigned integers with values ranging from 0-511. The data was imported into Matlab 7.4 R2007a (The Mathworks Inc., USA) for image processing. The image data was normalised producing an average gel intensity of 0.39, while the average marker intensity was zero.

### 6.1.3 Marker tracking method

To track the movement of markers from the 3D MR data an image processing algorithm was developed in Matlab (The Mathworks Inc., USA). The centre point of each marker at each time-step can be found using 3 main steps: (1) *masking*, (2) *adjacency grouping* and (3) *centre point calculation*.

### 6.1.3.1 Masking

Masking was performed to identify the central voxels for each marker. To reduce computational time the mask was only applied to voxels that qualify (based on intensity threshold) as potentially belonging to a marker. In addition a sparse cross-shaped mask was designed (Figure 6.2A) with just 12 voxels (significantly less than non-sparse cubic or spherical masks which would be around 729 and 250 voxels respectively). When the mask operates on a voxel  $v$  with image coordinates  $(i, j, k)$ , the image coordinates of the 12 (surrounding) mask voxels  $(i_m, j_m, k_m)$  can be defined as:

$$\begin{pmatrix} i_m \\ j_m \\ k_m \end{pmatrix} = \begin{pmatrix} i + (1, -1, 0, 0, 0, 0, 4, -4, 0, 0, 0, 0) \\ j + (0, 0, 1, -1, 0, 0, 0, 0, 4, -4, 0, 0) \\ k + (0, 0, 0, 0, 1, -1, 0, 0, 0, 0, 4, -4) \end{pmatrix} \quad 6-1$$

Image processing masks are generally used as a spatial filter, however in this case the mask was used as a logic operator to find voxels matching the following criterion: A voxel  $v$  at location  $(i, j, k)$  is classified as a central marker voxel when all the central cross mask voxels (see cross shape in Figure 6.2A) have intensities smaller than the intensity threshold  $T$  and all of the outer voxels (see outer voxels in Figure 6.2A) have intensities higher than or equal to the intensity threshold  $T$ . In other words the following pseudo equation needs to be true:

$$\begin{pmatrix} i_m(1:6) \\ j_m(1:6) \\ k_m(1:6) \end{pmatrix} < T \quad \wedge \quad \begin{pmatrix} i_m(7:12) \\ j_m(7:12) \\ k_m(7:12) \end{pmatrix} \geq T \quad 6-2$$

Here all of the first six mask voxels (indicated with 1:6), of the mask coordinate collection  $(i_m, j_m, k_m)$ , represent the central cross elements and the last six (indicated with 7:12) represent the outer elements (see Figure 6.2A). Depending on the marker appearance in the image (see next section) up to 8 central marker voxels match this criterion and were found per marker.

### 6.1.3.2 Adjacency grouping

Calculating the marker centre point using only the central marker voxels identified using masking does not provide an accurate centre point determination (accurate to within a voxel at best) and is sensitive to marker appearance. The more voxels that are included (e.g. all) the better. To find and group voxels deemed to belong to the same marker a grouping algorithm was used. The central marker voxels found using masking were used

as starting points to group objects using adjacency analysis. The adjacency grouping is a stepwise process. Adjacency coordinate groups (ACGs) are created for all the voxels found using masking. The process starts with one of the voxels found using masking  $v'$  and is assigned to be part of marker group  $G$ . The coordinates  $(i_g, j_g, k_g)$  of the ACG for this voxel  $v'$  with coordinates  $(i', j', k')$  is defined as:

$$\begin{pmatrix} i_g \\ j_g \\ k_g \end{pmatrix} = \begin{pmatrix} i' + (1, -1, 0, 0, 0, 0) \\ j' + (0, 0, 1, -1, 0, 0) \\ k' + (0, 0, 0, 0, 1, -1) \end{pmatrix} \quad 6-3$$

The ACG contains all the directly adjacent voxels of the voxel  $v'$  (its direct upper, lower, front, back, left and right neighbours). Any voxel  $v$  with coordinates  $(i, j, k)$  is added to the marker group  $G$  when its intensity is lower than  $T$  and its coordinates are found within one of the ACGs of the marker group  $G$ . When a voxel is added to the marker group  $G$  its ACG is added to the set of ACGs belonging to  $G$  and this process is repeated. Voxels are added to a marker group until the group is no longer growing. Figure 6.2B shows how, starting with one central voxel, the surrounding low intensity voxels within the coordinate group  $(i_g, j_g, k_g)$  are added and when this is repeated all voxels representing the marker are grouped. After grouping the dimensions and number of voxels of the object were compared to what is expected for normal markers (e.g. a diameter of ~6 voxels and consisting of under 250 voxels) to filter out possible objects other than markers.

### 6.1.3.3 Centre point calculation

The centre point for each marker group was determined using weighted averaging. The centre coordinates  $(i_c, j_c, k_c)$  of a marker composed of  $N$  voxels is defined as:

$$(i_c, j_c, k_c) = \left( \frac{\sum_{a=1}^N w_a i_a}{\sum_{a=1}^N w_a}, \frac{\sum_{a=1}^N w_a j_a}{\sum_{a=1}^N w_a}, \frac{\sum_{a=1}^N w_a k_a}{\sum_{a=1}^N w_a} \right) \quad 6-4$$

Here  $(i, j, k)$  represent the coordinates of each of the voxels in the marker group. Since those voxels with intensities close to zero are more likely to belong to a marker than voxels with intensities close to the gel intensity, the weight  $w_a$  for a voxel with intensity  $z_a$  was defined as:

$$w_a = \left( 1 - \frac{z_a}{T} \right), \text{ with } w_a = 0 \text{ if } z_a > T \quad 6-5$$

Here  $T$  represents a threshold which for a noiseless image could be set equal to the gel intensity (weights then represents the volume fraction of the gel present in the voxel).

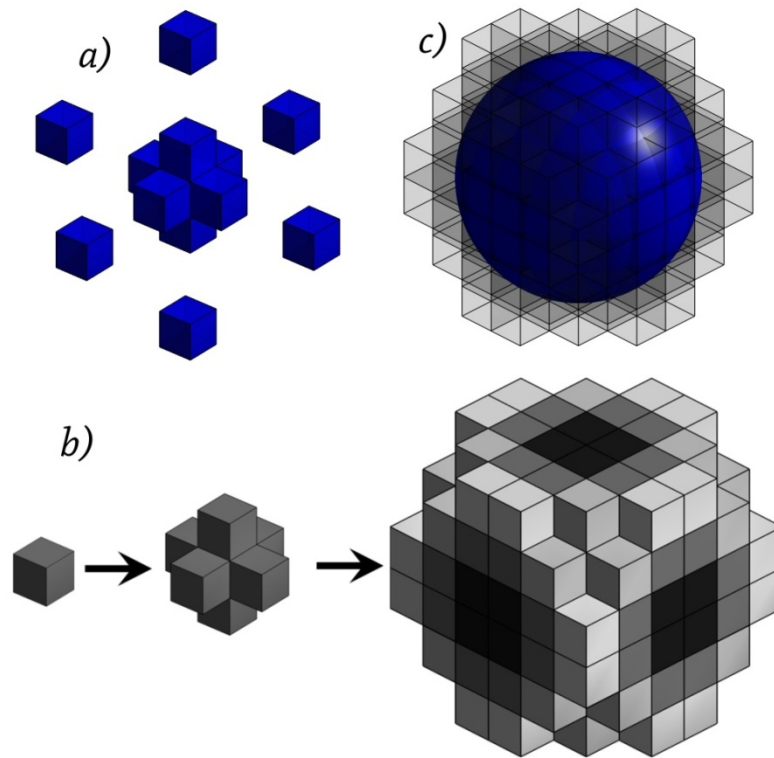


Figure 6.2 The cross-shaped mask (A), the adjacency based grouping process (B), a 3 mm diameter sphere placed at the calculated marker centre (C).

#### 6.1.4 Evaluation of marker tracking method using simulated magnitude MR image data

The marker tracking method was evaluated using simulated magnitude MRI data because this allows full control and knowledge of marker locations and thus provides an appropriate ‘gold standard’ for method evaluation. The simulated data also allow one to isolate and study errors from different sources. The marker tracking method was evaluated using algorithms developed in Matlab (The Mathworks Inc., USA) and involves the following steps: (1) *Simulation of a noiseless image and analysis of geometric bias, and* (2) *Simulation of noisy magnitude MR data and analysis of the noise effects.* The final noisy image data allows one to evaluate the performance of the method under varying noise conditions while the noiseless image allows for evaluation of the geometric bias implicit in the method.

### 6.1.5 *Simulation of a noiseless image and analysis of geometric bias*

Since the marker image intensity values are zero, image data were simulated by multiplying an image representing gel volume fractions by the average normalised gel intensity. A 3D image space can be defined containing only markers and gel and can be expressed as a continuous binary function  $f(i, j, k)$  where  $f(i, j, k) = 0$  for all marker coordinates and  $f(i, j, k) = 1$  for all gel coordinates. When this function is represented across voxels intermediate intensities arise as averaging occurs at each voxel where intensity is equivalent to the gel volume fraction within the voxel. The continuous binary function can however be approximated by a high resolution binary image. In order to simulate a volume fraction image at the desired (lower) resolution (cubic 0.5 mm voxels) involves simple averaging of the high resolution representation. High resolution binary images were created at 25 times the acquisition resolution. A 2D mid-slice of a high resolution (cubic 0.02 mm voxels) binary image is shown in Figure 6.3A. At this resolution the marker sphere is represented by over 1.7 million voxels and the volume is represented with less than 0.07% error. Figure 6.3B shows the corresponding volume fraction image at the averaged, acquisition resolution (cubic 0.5 mm voxels). By multiplying the obtained volume fraction image with the appropriate gel intensity (average normalised intensity 0.39) a noiseless simulated image is obtained.

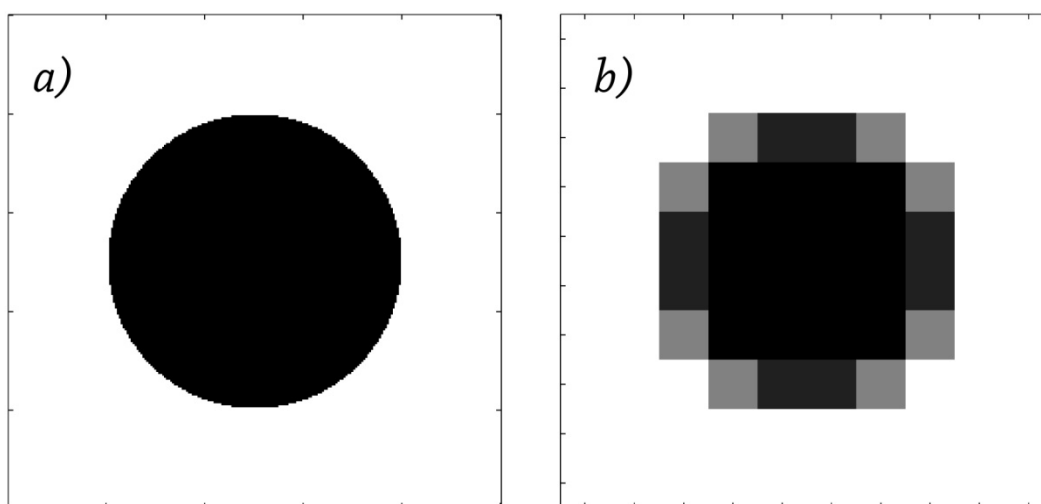


Figure 6.3 A high resolution (uniform 0.02mm voxels) binary mid-slice image of a marker (A) and corresponding mid-slice at the MR acquisition resolution (uniform 0.5mm voxels) (B).

The appearance in Figure 6.3B is symmetric because the marker centre point coincides with a voxel corner. However the appearance of objects in images varies depending on

their location due to averaging across the voxels, which leads to a geometric bias affecting the marker tracking method. Figure 6.4A shows a marker sphere and the voxel in which its centre point is found. This voxel is named the Object Central Voxel (OCV), as previously described (Figure 6.4B). When a marker centre point coincides with the centre of its OCV appearance 1 is obtained. Similarly 2 up to 4 demonstrate the appearance of a marker when its centre coincides with the middle of a voxel face, the middle of a voxel edge and a voxel corner respectively. Appearances 1-4 are the most symmetric appearances obtainable. Other appearances however can be asymmetric such as case 5 which is obtained when the marker centre coincides with the centre of the tetrahedron in Figure 6.4. Obviously when a marker is translated exactly one voxel in any orthogonal direction its appearance has not changed but simply shifted. In fact due to symmetry all possible appearances are uniquely defined by the tetrahedron shown in Figure 6.4B. All other appearances can be obtained by rotation and mirroring of the appearances in this tetrahedron. Since the centre point calculation in the marker tracking method is based on an average of marker voxel coordinates, it is sensitive to symmetry of the marker appearance and as such the error is also related to asymmetry.

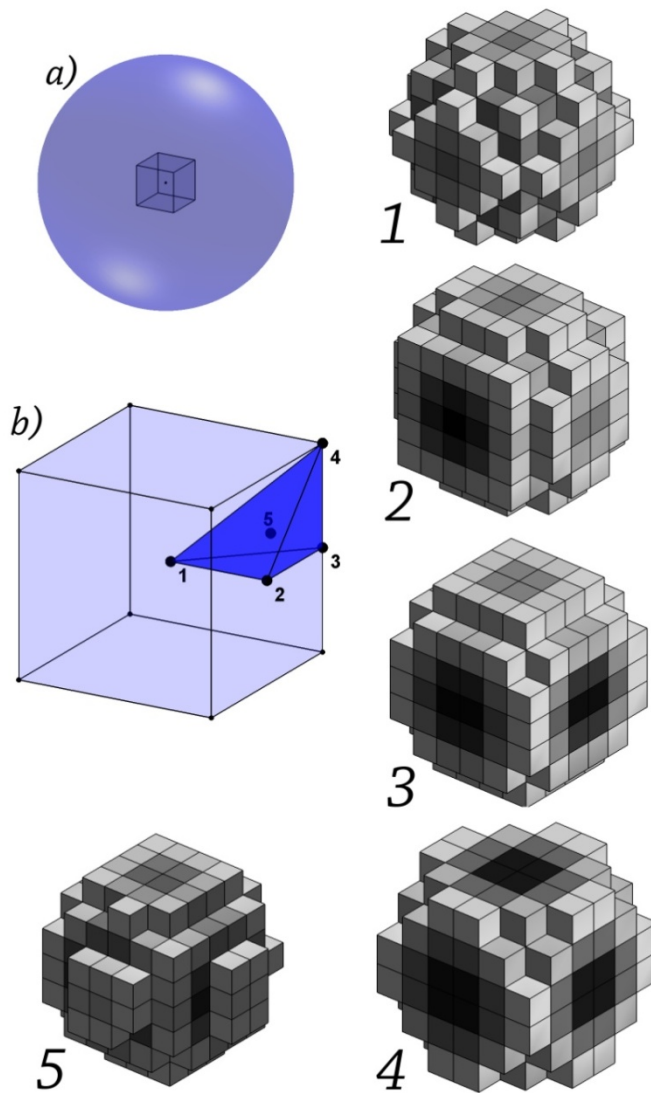


Figure 6.4 A marker sphere showing OCV (A), an OCV showing the tetrahedron in which the appearance of markers varies uniquely (B). The most symmetric appearances mid voxel (1), mid face (2), mid edge (3) and voxel corner (4) and an asymmetric appearance for the middle of the tetrahedron (5).

Due to the repeated periodic appearance under translation in any of the orthogonal directions the marker appearances and geometric bias function therefore have a triple periodic form with minima coinciding with the symmetry points 1-4 discussed in Figure 6.4. It is thus hypothesised that the magnitude of the geometric bias  $E$  should follow a form similar to:

$$E \approx \sqrt{\frac{1}{3}(\sin(i)^2 + \sin(j)^2 + \sin(k)^2)} \quad 6-6$$

Figure 6.5A illustrates an OCV for such a function whereby its elements are shaded toward the expected geometric bias if a marker were to be centred on that location. Figure 6.5B shows that the best regions of such a pattern coincide with OCV points 1-4



and the worst regions furthest away from these regions with the worst points one quarter into the OCV in all directions.

The geometric bias was investigated by simulating markers with their centre points coinciding with various locations within an OCV in the absence of noise. Due to the symmetry in the appearances as discussed above, simulations were performed in 1 octant of the OCV only using a grid of points. For visualisation purposes the results were then mirrored to obtain bias measures across the full OCV producing a 19x19x19 grid. A finer grid was then applied around the maximum bias to closely approximate the location of the real maximum bias. This process was repeated until the found maximum no longer varied significantly.

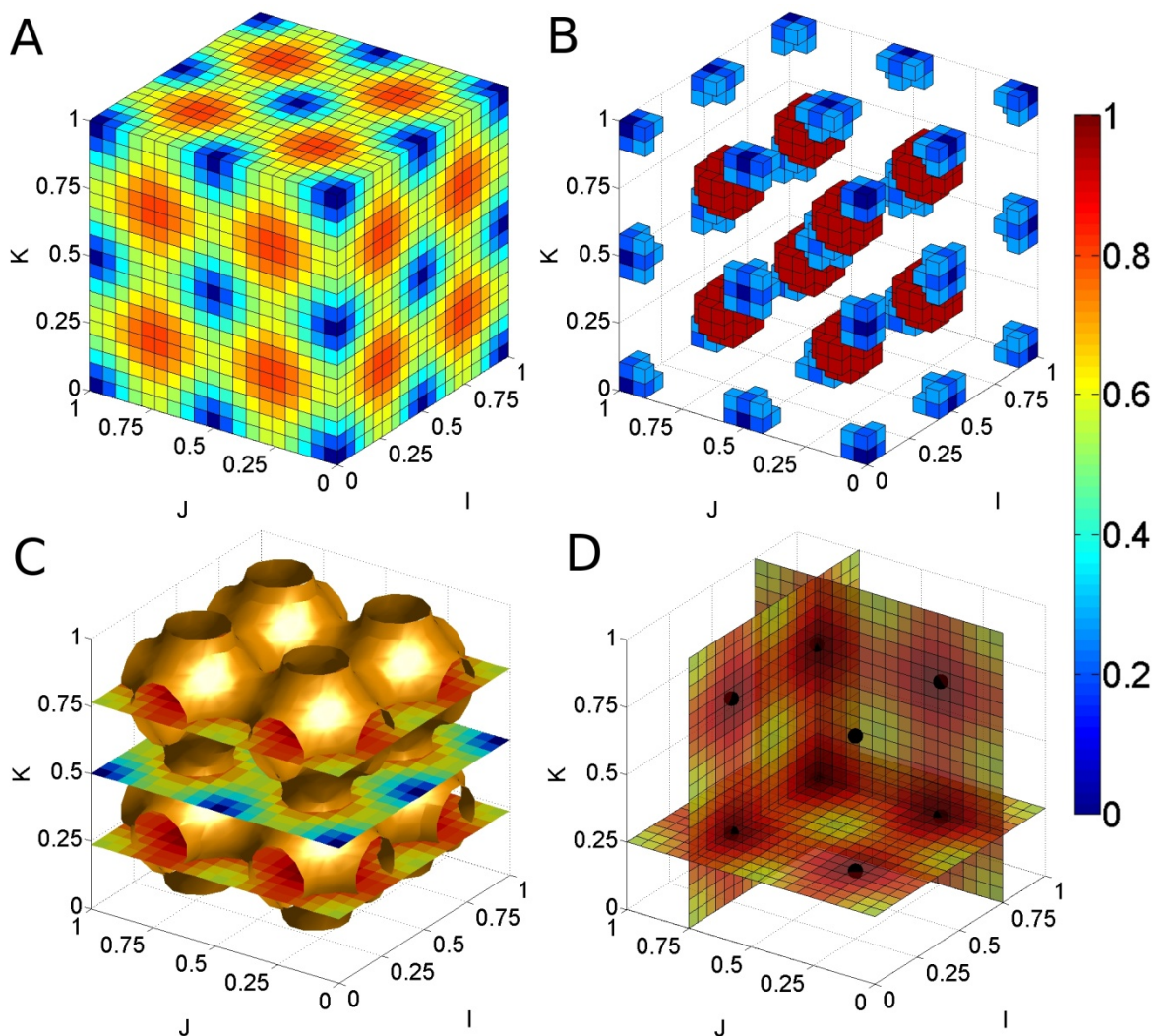


Figure 6.5 The OCV showing the expected pattern for the magnitude of the geometric bias of the marker tracking method across the OCV (A), the best and worst regions highlighted (B), slice view and iso-surface for intermediate magnitude (C) and three slices through locations with the largest error magnitude with maxima shown as black dots (D).

## 6.1.6 Simulation of noisy magnitude MR data and analysis of the noise effects

Noise is present in all MR image data, and the performance of the marker tracking method needs to be evaluated in the presence of appropriate noise in the simulated image. During MRI, signal is acquired in the frequency domain using receiver coils. To move to the image domain the signal can be sampled at discrete locations and reconstructed using inverse Fourier Transforms. For each reconstructed image voxel in Cartesian space the signal  $s$  can be expressed as<sup>261</sup>:

$$s = s_R + s_I = A + n_R + in_I, \text{ with } i = \sqrt{-1} \quad 6-7$$

where a  $A$  is real signal (represents the noiseless simulated image) and  $n_R$  and  $n_I$  represent real and imaginary noise components respectively. These independent noise components are identically distributed (with zero mean) and their Probability Density Function (PDF) is Gaussian<sup>261-263</sup>. The magnitude  $m$  of a signal can be calculated using:

$$m = \sqrt{(A + n_R)^2 + n_I^2} \quad 6-8$$

The image intensities in magnitude MR images in the presence of noise follow a Rician distribution<sup>261-264</sup> with a PDF given by<sup>265, 266</sup>:

$$P_m(m|A, \sigma_g) = \frac{m}{\sigma_g^2} \exp\left(\frac{-(A^2 + m^2)}{2\sigma_g^2}\right) I_0\left(\frac{Am}{\sigma_g^2}\right) H(m) \quad 6-9$$

where  $\sigma_g$  represents the standard deviation of the Gaussian noise,  $H$  represents the Heaviside step function (ensuring  $P_m = 0$  for  $m = 0$ ) and  $I_0$  is the 0 order modified Bessel function of the first kind. Figure 6.6 shows a surface plot of the Rician PDF for a range of signal to noise (SNR) ratios  $\frac{A}{\sigma_g}$ . When the noise dominates and  $\frac{A}{\sigma_g}$  approaches zero the Rician PDF reduces to the Rayleigh PDF<sup>261, 262</sup> (see blue dots in Figure 6.6). However, when the signal dominates ( $\frac{A}{\sigma_g} > 2$ <sup>262</sup>) the Rician distribution behaves approximately Gaussian (red dots in Figure 6.6 are for a Gaussian PDF at  $\frac{A}{\sigma_g}=6$ )<sup>261, 262</sup>. With the knowledge that when  $A = 0$  the Rician PDF reduces to the Rayleigh PDF,  $\sigma_g$  can be estimated by analysis of background noise using<sup>264</sup>:

$$\sigma_g \approx \sqrt{\frac{1}{2N} \sum_{i=1}^N m_i^2}$$

6-10

Using this equation, and analysis of the background of a normalised T2 MR image of the silicone gel phantom,  $\sigma_g$  was estimated to be 0.02. Based on the average normalised gel intensity of 0.39 this corresponds to an SNR of 19.5. However, to evaluate the performance of the marker tracking method in the presence of noise, images were simulated at the worst location found by the geometric bias at a SNR of 5 up to 35. Simulations were performed 10000 times to obtain an estimate of the error distribution at the various SNR levels.

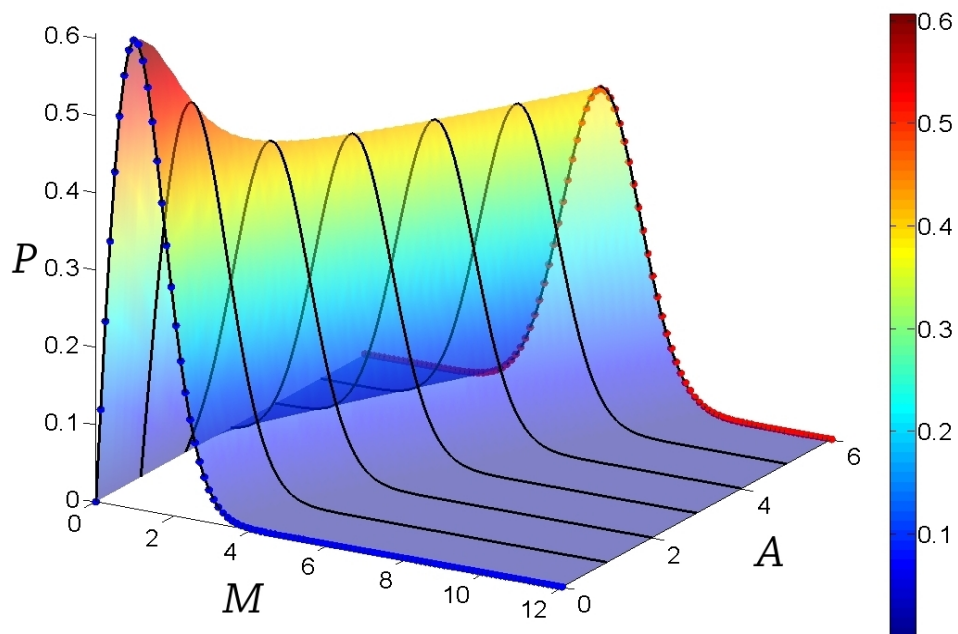


Figure 6.6 The Rician PDF at various  $A/\sigma_g$  ratios (0-6). When  $A/\sigma_g=0$  the Rician PDF reduces to the Rayleigh distribution (blue dots) however as  $A/\sigma_g$  becomes  $>2$  the Rician PDF behaves approximately Gaussian (red dots at  $A/\sigma_g=6$ )

## 6.2 Results

The results are presented in two steps: 1) *Evaluation of the geometric bias in the marker tracking method*, and 2) *Evaluation of the performance on the marker tracking method in the presence of noise*.

## 6.2.1 Evaluation of the geometric bias in the marker tracking method

Figure 6.7A shows the geometric bias error in the absence of noise in an Object Central Voxel (OCV). The colour in each element is the error (in units of voxels) of the marker tracking method for each point on the 3D grid. Figure 6.7B highlights the best and worst regions. Analysis demonstrated that overall the geometric bias of the marker tracking method ranges from 0 to a maximum of  $5.560 \times 10^{-3}$  (with a mean of  $3.149 \times 10^{-3}$  and a standard deviation of  $7.771 \times 10^{-4}$ ) voxels. The error is 0 for the symmetric cases (points 1-4 in Figure 6.4) while the maximum error occurs in locations close to one quarter into the OCV in all directions (0.23). The maximum errors are illustrated as black dots in Figure 6.7C.

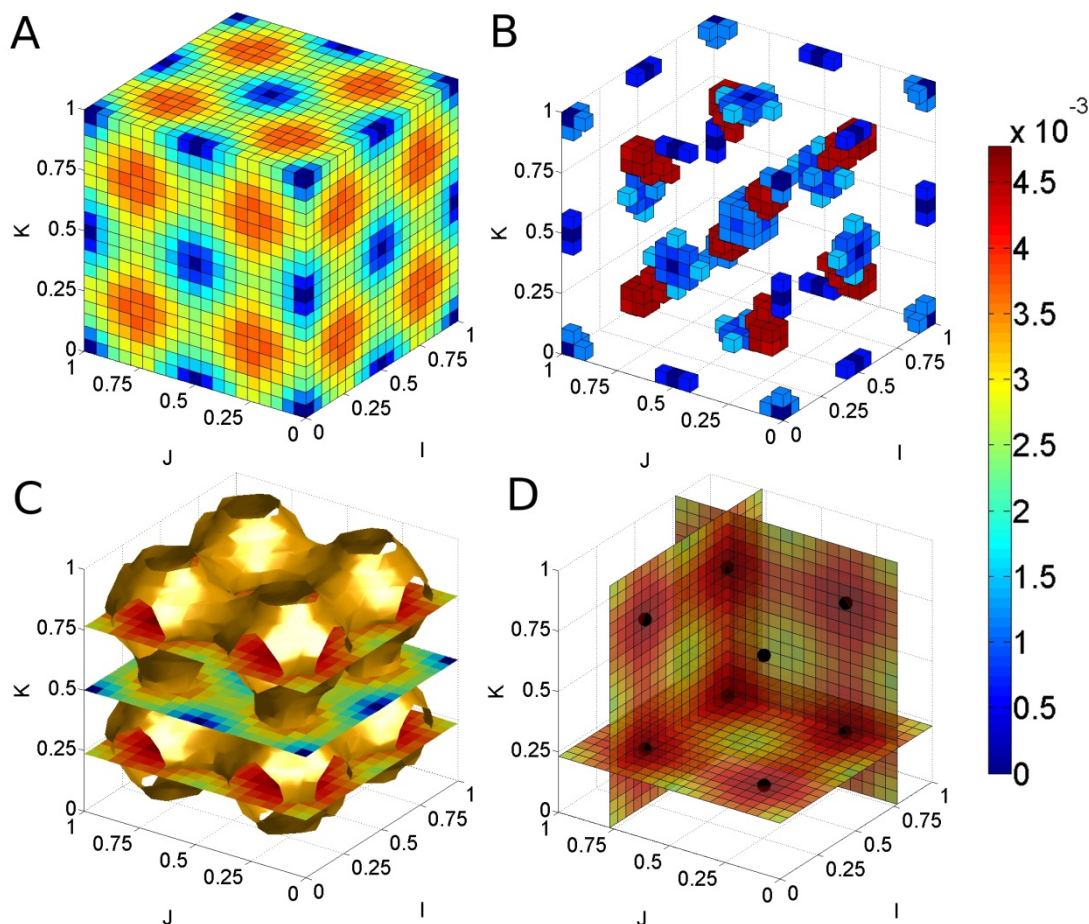


Figure 6.7 The OCV showing the magnitude of the geometric bias of the marker tracking method across the OCV (A), the best and worst regions highlighted (B), slice view and iso-surface for intermediate magnitude (C) and three slices through locations with the largest error magnitude with maxima shown as black dots (D).

## 6.2.2 Evaluation of the performance on the marker tracking method in the presence of noise.

The performance of the marker tracking method for the noisy magnitude MR image simulations obtained from the 10000 simulations at each SNR of 5 up to 35 is presented next. As the SNR increases from 5 to 35 the maximum, mean and minimum voxel errors vary according to Figure 6.8A. The standard deviation is plotted in Figure 6.8B. Although for  $T=0.26$  the maximum stays below 0.1127 in all cases, the method performs better when  $T$  is chosen depending on SNR. To illustrate this Figure 6.9 shows results for the SNR range 15-35 using  $T=0.32$ . Using a higher  $T$  means that the marker groups are composed of more voxels and thus a more accurate centre point can be calculated. The maximum voxel error for  $T=0.26$  at a SNR=19.5 (estimated SNR level) is  $4.25 \times 10^{-2}$  voxels however using a  $T=0.32$  in this case results in a more than threefold increase of the accuracy as the maximum error is reduced to  $1.16 \times 10^{-2}$  voxels. The optimum  $T$  value for a certain SNR can be determined using MR data simulations. Using simulations the error can be minimised for a given SNR by adjusting the  $T$  value.

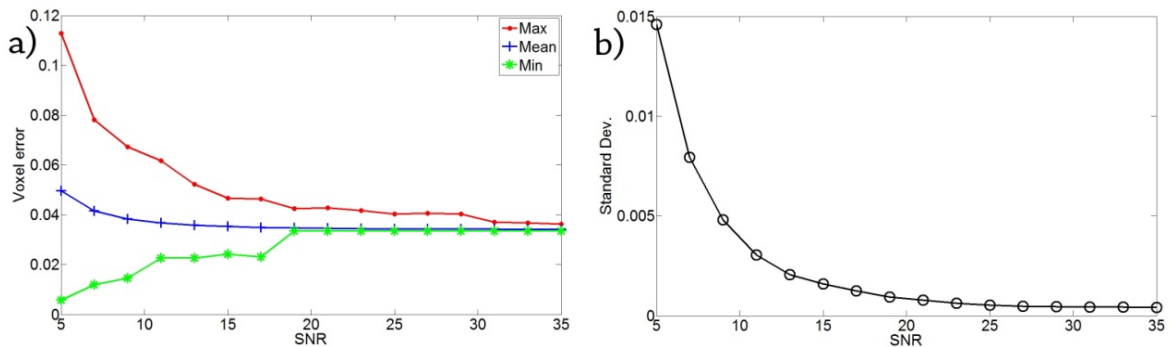


Figure 6.8 Results for SNR 5 up to 35 using  $T=0.26$ . The maximum (red dotted line), the mean (blue crossed line) and the minimum (green starred line) voxel error plotted against SNR (A), and the standard deviation plotted against SNR (B).

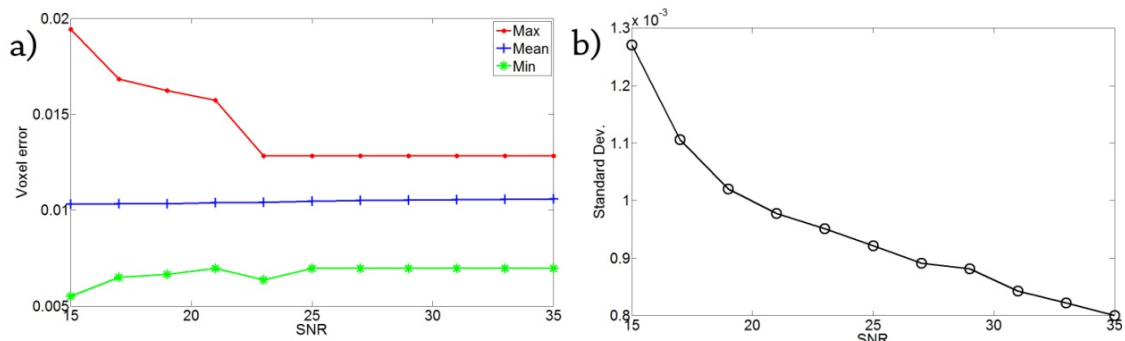


Figure 6.9 Results for SNR 15 up to 35 using  $T=0.32$ . The maximum (red dotted line), the mean (blue crossed line) and the minimum (green starred line) voxel error plotted against SNR (A), and the standard deviation plotted against SNR (B).

## 6.3 Discussion

Several MRI based motion tracking algorithms have been proposed in the literature: for example tagged MRI<sup>49</sup> and phase contrast MRI<sup>101</sup>, but these all rely upon validation of the algorithms proposed. A review of the literature showed that the validation methods used for existing techniques are frequently incomplete, and this chapter presents a novel validation method for MRI based on motion tracking using a marker tracking algorithm which itself is validated against simulated MR image data. Simulated data was generated for the noise-free case as well as for a variety of different Rician distributed noise levels. The noise-free image data allowed analysis of the error related to the geometric bias independently from other error sources. Therefore the method proved to be robust with geometric bias errors of between  $0-5.560 \times 10^{-3}$  voxels and errors due to noise remaining below 0.1127 voxels for all cases simulated with signal to noise ratios from 5-35. These results were achieved for a global threshold value  $T=0.26$ . However altering the threshold value, based on the SNR may result in a significant increase in accuracy. The optimum  $T$  value for a certain SNR can be determined using MR data simulations. Using simulations the error can be minimised for a given SNR by adjusting the  $T$  value.

The method proposed in this chapter has two main advantages. The first is that the data used for validation is simulated and therefore can be chosen to have desired levels of noise. This permitted evaluation of the marker tracking method for different levels of noise which has not been done previously. Secondly, since this validation method is based on MRI, the marker tracking experiment and the MRI based motion and deformation tracking can all be performed at the same time within the MR scanner. Although this method has been developed for application to tagged MRI on the upper arm, the methods presented here are not limited to this application and can be applied to validate other types of MRI based motion and deformation tracking techniques. Furthermore, these methods are independent of the chosen phantom shape.

## 6.4 Conclusions

A novel marker tracking method has been presented and validated using simulated MR image data. The marker tracking method is robust and the maximum geometric bias was  $5.560 \times 10^{-3}$  voxels while the error due to noise remains below 0.1127 voxels for Rician noise distributions with signal to noise ratios from 5 up to 35. This appears to be the only

marker tracking algorithm suitable for the validation of MR based motion and deformation tracking of soft tissue which has been validated against a 'gold standard'.

## 7 STUDY IV

# The MRI Based Measurement of Static 3D Soft Tissue Deformation



## 7.1 Introduction

As highlighted in section 3.6 SPAMM tagged MRI based methods to derive soft tissue deformation involve a large amount of repetitions e.g. depending on the temporal and spatial resolution from 16 per slice<sup>50</sup> to over a hundred<sup>51</sup>. Besides repeatability constraints, discomfort and health issues may preclude a large number of repetitions in practise. In the case of soft tissue indentation in the current thesis repeated indentations cause volunteer discomfort. In addition it hinders viscoelastic analysis. The purpose of the study presented here was therefore to reduce the number of repetitions required ensuring volunteer comfort and limiting repeatability artefacts and allowing expansion of SPAMM tagged MRI to less repeatable, and in the future, arbitrary and non-periodic movements for which there are currently no methods available.

A novel method was developed to segment tag surfaces and track tag surface intersection points. Nevertheless, as highlighted in section 3.7, the derived displacement measurements require validation against a “gold standard” reference measure. Since such a reference measure is often not present *in-vivo*, many studies have used numerical and physical models for validation. However in many cases the reliability of the reference itself is not known or evaluated. In one study validation with implanted crystals and sonomicrometric measurements was performed<sup>231</sup>, but crystal locations were verified manually and matching problems between MR and sonomicrometric measurements occurred. In chapter 6 a novel validation framework for MRI based deformation measurement was proposed based on a deformable silicone gel phantom containing contrasting spherical markers. The “gold standard” reference is made available through marker tracking. The validation methodology was itself independently validated using image simulations (error smaller than 0.12 voxels) and therefore provides a reliable “gold standard” for the evaluation of the SPAMM derived deformation measurement. This validation approach was therefore adopted here.

Since the purpose of the current study is to reduce the number of repetitions required, a novel non-triggered MRI sequence, based on SPAMM<sup>124, 125</sup> is presented for the measurement of 3D soft tissue deformation, whereby a parallel tag pattern is introduced using a single 1-1 (first order) SPAMM pre-pulse. Subsequently a full 3D volume is acquired following a single 3D read-out. Post-processing methods for deformation derivation often involve assumptions on the mechanical nature of the

material and its deformation. Representing tags as surfaces and tracking the intersections of these surfaces computed in 3D offers a relatively simple method to derive 3D deformation. In addition this avoids issues related to through-plane motion and assumptions of zero displacement in the parallel (within tag surface) direction associated with 2D approaches.

In order to derive 3D deformation the intersections of tag surfaces, which are segmented from three initially orthogonal 1-1 SPAMM data sets using a newly developed sheet marching algorithm are computed. This approach allows measurement of 3D deformation following just three motion cycles. To the best of our knowledge this makes the SPAMM tagged MRI based techniques presented here the fastest available for the non-invasive measurement of 3D soft tissue deformation. The deformation measurements were validated by indentation tests (using the custom designed MRI compatible soft tissue indenter described in chapter 4) and marker tracking (chapter 6) in a silicone gel phantom. In addition the performance of the method was evaluated *in-vivo* using indentation of the biceps region of the upper arm of a volunteer.

## 7.2 Methods

### 7.2.1 *MRI sequence design*

For the current study a novel non-triggered MRI sequence, based on SPAMM<sup>124, 125</sup> was used which forms an expansion of a sequence earlier developed for 1D bowel motion estimation<sup>267</sup> to the measurement of 3D soft tissue deformation. The sequence was applied to a silicone gel phantom for validation and to a volunteer for *in-vivo* evaluation. A schematic for the pulse sequence design is shown in Figure 7.1. A single 1-1 (first order) SPAMM pre-pulse (5ms) imposes a temporary sinusoidal modulation on the Z-magnetization and thus also on the signal magnitude causing it to vary sinusoidally from normal to severely reduced. The reduced signal regions form a parallel surface pattern in the tissue (visible as low intensity lines in 2D slices). These surfaces are generally referred to as tags. After the tag pre-pulse a time delay is introduced (which is set depending on desired T1 contrast and magnitude of deformation) during which the tissue indentation occurs. Subsequently a full 3D volume is acquired following a single read-out (Transient Field Echo,  $T_R/T_E=2.9/1.8$  ms, flip angle  $8^\circ$ ). A tag spacing of 6mm and 9mm were used

for the phantom and human volunteer respectively. A single SPAMM direction can be acquired in less than 1.5 s (pre-pulse 5 ms, time delay 300 ms, read-out 900 ms). The sequence was implemented on a 3.0 Tesla Philips Intera scanner (Philips Healthcare, Best, The Netherlands), scans were performed using two FLEX-M coils.

Since the tag surface pattern is temporarily locked in the tissue (fades due to T1 relaxation), the (static) deformation of the tissue, that occurred between pre-pulse and readout, is reflected in the deformation of the tag surface pattern. However in the absence of any within-surface reference points, a single set of tag surfaces only provides tag surface shape or an estimate of a single displacement component. To derive 3D displacements it is possible to combine three tag surface sets from initially orthogonal directions whereby each set provides a reference to within-surface deformation in the other directions. Therefore three data sets with mutually orthogonal tags were acquired for both the initial and deformed configuration. The intersection points of tag surfaces from three directions provide trackable material points, and three initial and three deformed data sets are required to derive 3D deformation.

In many SPAMM tagged MRI studies acquisitions are gated for instance in cardiac applications<sup>49</sup> by triggering the scan sequence towards the electrocardiogram in order to synchronize imaging with the heart motion cycle. However in the current study external loading (indentation) is applied to induce deformation and no physiological trigger is available. As such the external trigger dependence was removed. Instead the scanner was used to generate a 4 ms Transistor-Transistor Logic (TTL) pulse allowing for the appropriate and repeatable timing of the indentation. Scans were repeated for validation purposes according to the diagram shown in Figure 7.1. Table 7-1 provides a summary of the scanning parameters and configurations used in this study and illustrates three slices for each data set recorded. A continuous set of SPAMM dynamics (n=20) were acquired for each direction such that multiple initial and deformed data sets were obtained. However acquisitions continued as the indenter was slowly returned to its original position but these un-loading configurations were not used in the current study. Scanning parameters were optimized for each scan direction, leading to varying scan durations and thus the varying numbers of acquired initial and deformed configurations for each scan direction shown in Table 7-1.

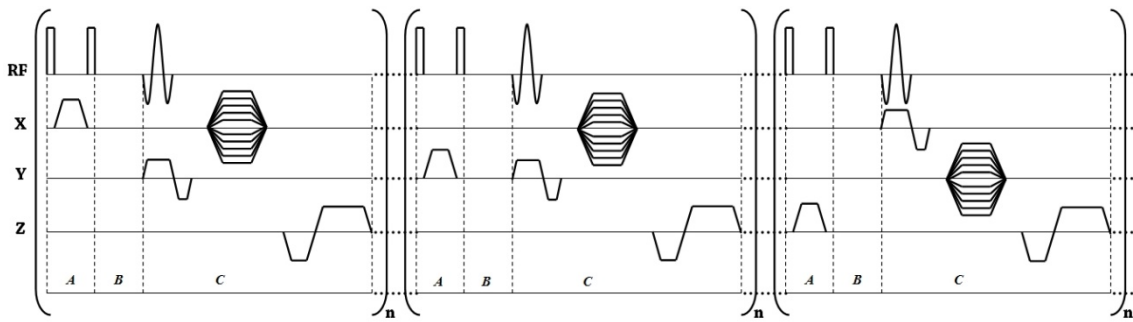


Figure 7.1 Diagram of the SPAMM pulse sequence. The 1-1 SPAMM pre-pulse (phase A) modulates the signal followed by a desired time delay (phase B) after which a full volume read-out takes place (phase C). This can be repeated  $n$  times for each direction.

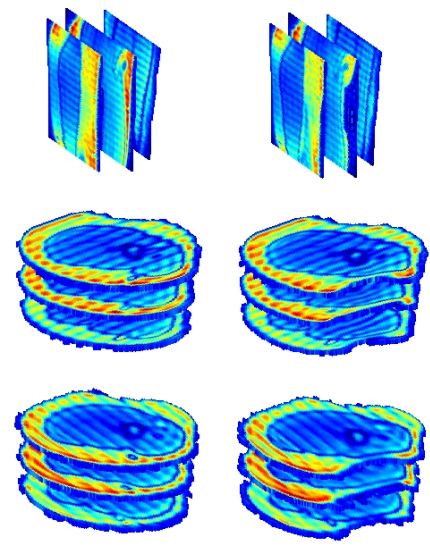
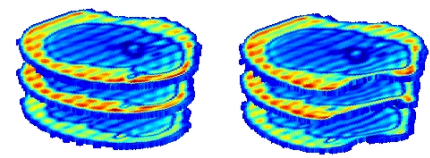
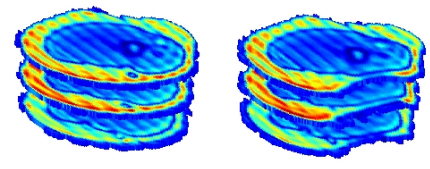
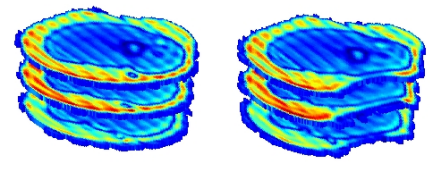
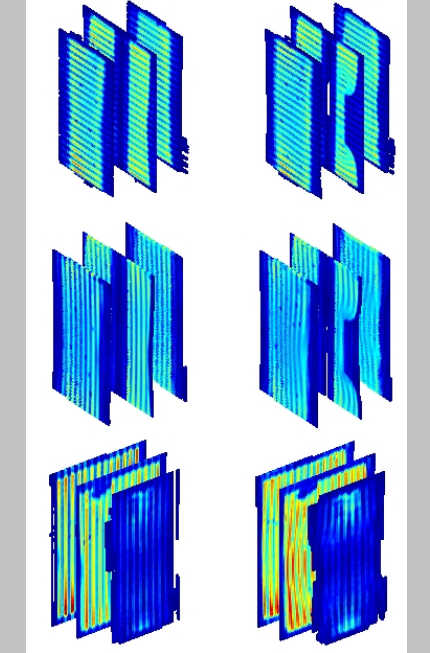
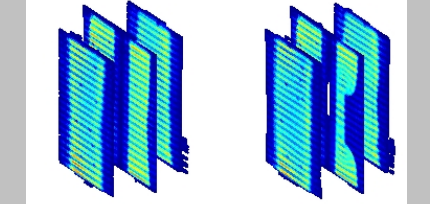
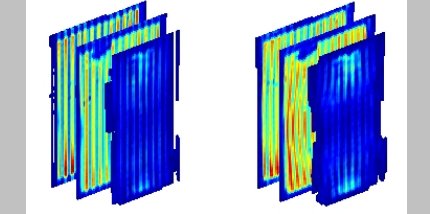
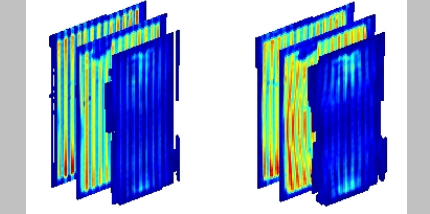
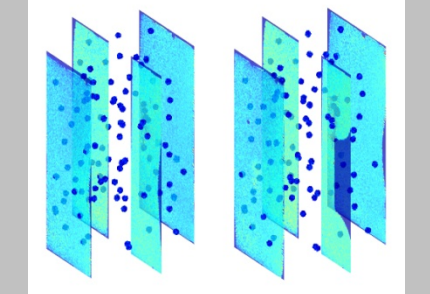
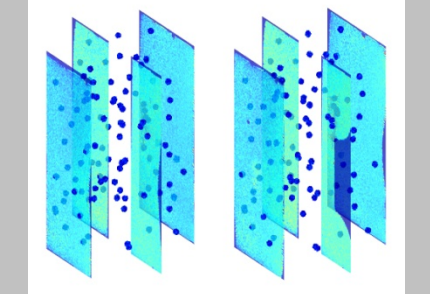
Initial configuration	Deformed configuration	Number of acquisitions	Scan type	Field of view size (mm)	# slices	Voxel dim. (mm)
		6 Initial	XY 1-1	130x130x52.5	35	1.35x1.35x1.5
		7 Deformed	SPAMM YZ slices			
		4 Initial	XZ 1-1	253x253x45	15	0.88x0.88x3
4 Deformed	SPAMM XY slices					
		4 Initial	YZ 1-1	253x253x45	15	0.88x0.88x3
		4 Deformed	SPAMM XY slices			
				10 Initial	XY 1-1	130x130x67.5
5 Deformed	SPAMM YZ slices					
10 Initial	XZ 1-1			130x130x52.5	35	1.35x1.35x1.5
5 Deformed	SPAMM YZ slice					
		10 Initial	YZ 1-1	130x130x67.5	45	1.25x1.25x1.5
		5 Deformed	SPAMM XZ slices			
				1 Initial	T2	120x120x80
1 Deformed	Weighted XZ slices					

Table 7-1 The MRI acquisition matrix

## 7.2.2 *The validation set-up: indenter and soft tissue phantom*

Validation of the soft tissue deformation measurement was achieved using indentation tests on a silicone gel phantom (Figure 7.2A). The phantom's cylindrical shape (120mm long and 80mm in diameter) and stiff poly-oxy-methylene (POM) "bone-like" core (20mm in diameter) represents an idealized geometry of the upper arm, allowing simulation of comparable deformation modes. The silicone gel (SYLGARD® 527 A&B Dow Corning, MI, USA) simulates soft tissue as its stiffness<sup>243</sup> and MRI properties<sup>252</sup> are within the range of human soft tissue, and it has been used in numerous MRI based studies on soft tissue biomechanics<sup>229, 232, 253-260</sup>. The "gold standard" reference is created through the use of spherical POM balls of  $3\pm 0.05$ mm diameter (The Precision Plastic Ball Co Ltd, Addingham, UK) embedded within the gel volume. These markers have low signal compared to the gel and can be tracked from high resolution (0.5mm isotropic voxels) T2 weighted images to provide an independent measure of deformation thus allowing for the evaluation of accuracy of the deformation measurement. The bottom row in Table 7-1 shows three slices for the  $T_2$  weighted data in the initial and deformed configuration, in addition the segmented markers are shown as voxels. The marker tracking methods were described in chapter 6 and demonstrated errors under 0.12 voxels (0.05 mm). In addition to the phantom validation the ability to measure soft tissue deformation *in-vivo* was demonstrated using indentation tests on the biceps region of the upper arm (see Figure 7.2B) of a healthy volunteer (female, age 24, height 1.65 m, weight 65 kg, ethical approval and informed consent obtained).

The gel phantom and the volunteer's upper arm were subjected to static transverse ramp (~12 mm) and hold (3 s) indentations (at a speed of ~40mm/s) using a custom designed, hydraulically powered and MRI compatible soft tissue indenter (Figure 7.2B and chapter 4). The indenter head is cylindrical (45 mm in diameter) and its speed and depth can be varied via a computer controlled hydraulic master cylinder. As mentioned before appropriate and repeatable timing of the indentation was achieved via triggering towards a 4 ms TTL pulse generated by the scanner prior to imaging.

Figure 7.2C and 2D illustrate several image slices with the tag-lines for the phantom and volunteer data in the initial and deformed configuration. In addition iso-surfaces are

shown which clearly indicate the circular indentation sites in the deformed configuration. For clarity all figures are presented with a similar 3D orientation such that the reader maintains a reference towards the orientation and location of the indentation.

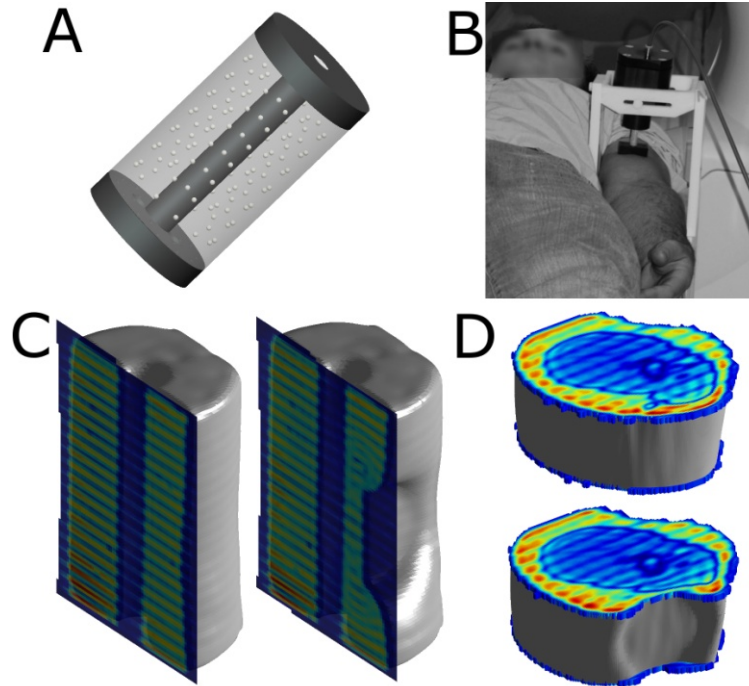


Figure 7.2 The silicone gel soft tissue phantom (A), the MRI compatible indenter placed at volunteers upper arm (B), iso-surface plot showing the indentation sites for the phantom (C) and volunteer (D).

### 7.2.3 Deriving tissue deformation from the SPAMM tagged MRI data

In order to extract soft tissue deformation from the SPAMM tagged MRI data was analysed using novel post-processing methods developed in Matlab (The Mathworks Inc., Natick, MA, USA). The MRI data (DICOM files) were uploaded and slices were combined into 3D volume matrices and the data was normalized towards maximum intensity. No filtering was applied. Post-processing was performed in the following steps: A) *Logic masking*, to identify potential tag-voxels, B) *Connectivity analysis*, to remove irregularities (e.g. anatomical disturbances), C) *Sheet marching* to segment the tags and fit surfaces, and finally D) *Calculation of tag surface intersections*, whereby tag surface intersection points for the initial and deformed configuration were used to derive the displacement vector field. The latter two geometric operations (C and D) occur in a regular Cartesian space (patient coordinate system) whereby the non-uniform voxel dimensions are taken into account.

### 7.2.3.1 Logic masking

Logic masking was used to determine the tag surface orientation and to identify potential tag voxels. A 3D cross shaped mask was used to act as a logic operator testing the mask environment for certain criteria. The mask dimensions can be altered according to the tag thickness. The logic masking checks whether the outer mask elements are of higher intensity than the voxel it is centred on. The cross-shaped mask can be seen as being composed of three mutually orthogonal segments. The overall dominance of any one of these segments allows for the detection of global tag surface orientation. For voxels that are part of a tag surface there is at least one higher intensity element on both sides of one of the orthogonal segments. The result of this analysis step was a binary logic matrix. Figure 7.3A shows XZ 1-1 SPAMM data for the human volunteer. In Figure 7.3B the tag voxels for these slices, identified using masking are overlaid as voxels (grey and black). However MRI is complicated by noise, possible artefacts and, in addition anatomical features may induce additional intensity variations *in-vivo*. Such disturbances may result in false positives tag voxels (e.g. at the muscle/fat boundary in Figure 7.3). However tag surfaces are by definition continuous structures (in the absence of shearing) and this knowledge can be used *a priori* to correct for possible false positive tag voxels using the connectivity analysis presented next.

### 7.2.3.2 Connectivity analysis

In order to remove false positive tag voxels connectivity analysis was performed. A voxel's tag connectivity in a certain direction was defined as the number of tag voxels it is connected to in this direction. For instance each tag voxel in a column of  $n$  tag voxels has a connectivity of  $n$  in the column direction. If a voxel is part of a continuous tag its connectivity in the perpendicular direction should reflect the thickness of the tag, while in the parallel directions it should reflect the local tag width and length respectively. These connectivity measures distinguish false positives from tag voxels and allows for their removal. Voxels discarded in this way, e.g. those near the bone and the muscle/fat boundary, are shown in grey in Figure 7.3B. For the phantom tag voxels that formed bridges between two adjacent tags (due to markers) were removed.



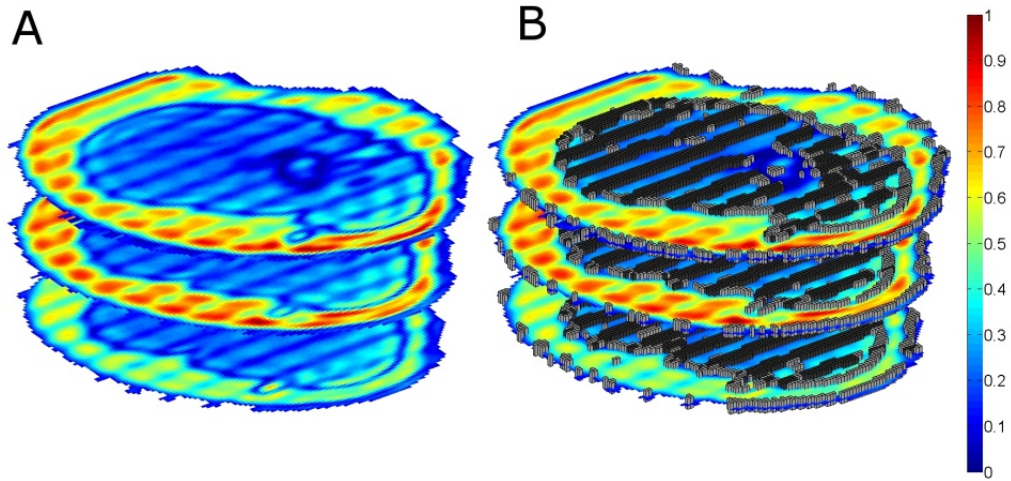


Figure 7.3 Three slices for the human XZ 1-1 SPAMM data (A) and the same slices with overlaid tag-voxels, those that pass the connectivity analysis are shown in black while those that are discarded are shown in grey (B).

### 7.2.3.3 Sheet marching

Segmentation of the tag surfaces was achieved using a novel sheet-marching algorithm in which tag surfaces were represented by cubic spline surfaces that “grow” using two moving fronts from manually determined start and end locations. Each surface grows from the extremities inwards and marches towards the opposite side guided by the tag voxels identified using masking and connectivity analysis. This process consists of two main steps which are repeated until the surface was complete: 1) *Extrapolation of surface fronts*, 2) *Update extrapolated fronts using weighted averaging*.

#### Extrapolation of surface fronts

Tag surfaces were represented as a cubic spline surfaces using a cubic smoothing spline function  $f$  which minimizes (see Matlab *csaps* function and<sup>268</sup>):

$$(1 - \mu) \sum_{i=1}^n (y_i - f(x_i))^2 + \mu \int_{x_0}^{x_n} \left( \frac{d^2 f}{dx^2} \right)^2 dx \quad 1$$

here  $y_i$  represents the data value at coordinate  $x_i$  and  $\mu \in [0,1]$  controls the degree of smoothing, i.e. the “stiffness” of the marching sheet ( $\mu=0$  produces a linear least-squares fit while  $\mu=1$  produces the “natural” cubic spline interpolant), here  $\mu = 0.05$  was used. Using the cubic spline formulation and the currently defined tag surface (initially only the start and end points) the coordinates of the next steps inwards (on both fronts) are estimated using extrapolation.

### Update extrapolated fronts using weighted averaging

The next step is to update the extrapolated fronts using a weighted average of the potential tag voxels that are found on the tag surface and up to one tag thickness offset from the tag surface in both perpendicular directions. The manually determined tag surface start and end locations are also updated to remove possible user bias. The averaging weights are linearly derived from the voxel intensities such that low intensity voxels are favoured. These are more likely to be part of tags and this ensures that the surface closely follows the centre of the tags. After this update the next steps are extrapolated until the two moving fronts reach the opposite side of the field of view. The fronts thus cross each other after meeting in the middle and each coordinate is effectively updated twice. This is to remove possible “overshoot” and “undershoot” bias due to the marching direction of the sheet. Once the fronts have reached the opposite side a final surface is fitted to all data points using  $\mu = 0.05$ . At surface locations where no tag-voxels are found a void is introduced in the surface. Figure 7.4 illustrates the stepwise sheet marching for one of the phantom tag surfaces. Tag surfaces were segmented for both the phantom and volunteer data and for all directions and repetitions (see column 3, Table 7-1). In addition a single average surface set was constructed from the various repetitions for each direction (Figure 7.5).

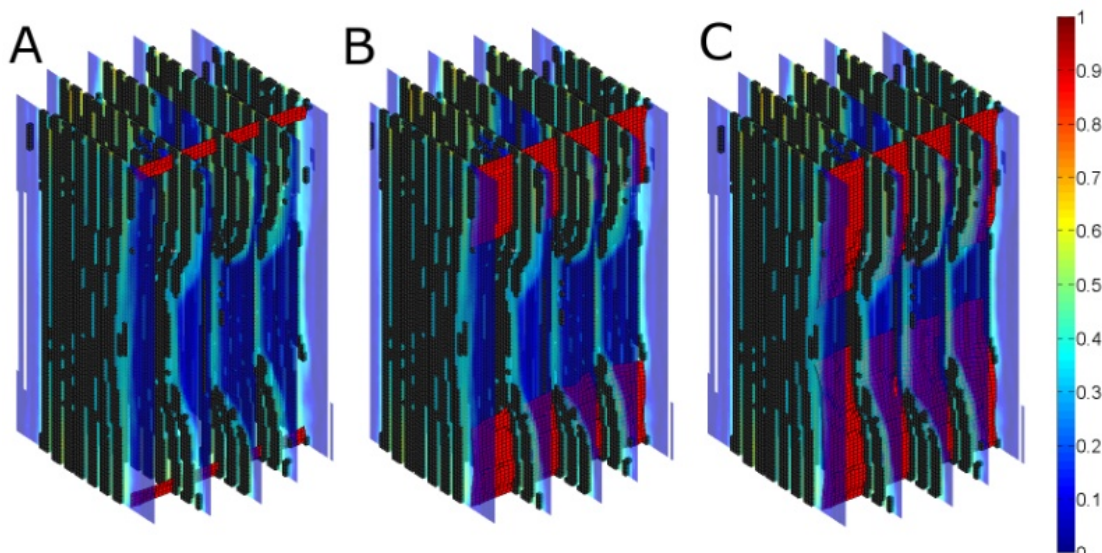


Figure 7.4 Several slices for the phantom showing, from A to C a tag surface as it marches from the periphery of the data inwards. Tag voxels that guide the process are shown in black.

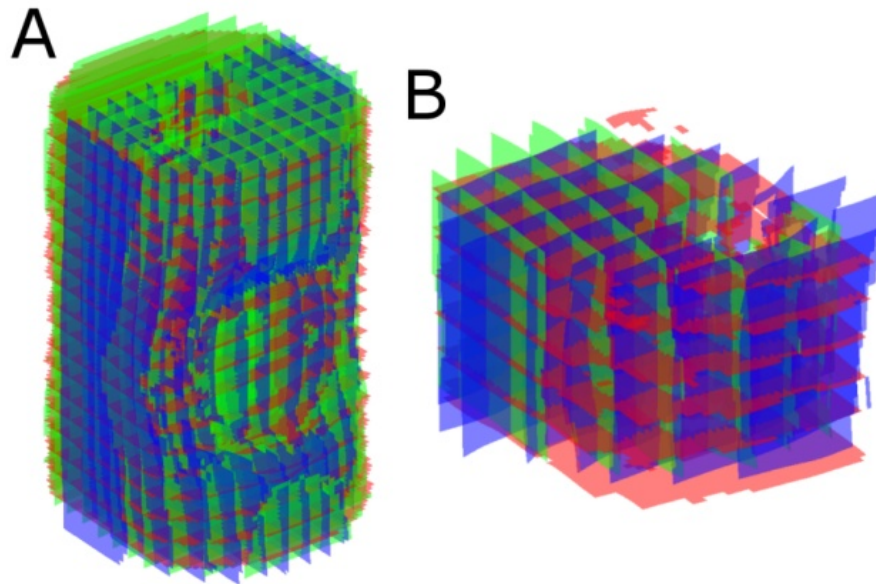


Figure 7.5 The segmented tag surfaces for the phantom (A) and volunteer data (B) in the deformed configuration.

#### 7.2.3.4 Calculation of tag surface intersections and displacement fields

Figure 7.5 demonstrates how the average tag surfaces for the three orthogonal directions intersect each other. The next step was to find the intersections for these surfaces as these represent material points that can be tracked over time. This was done as follows: first the shape of a first surface was sampled onto all coordinates defining the second surface. Then the intersection curve of these two surfaces was found by solving where the subtraction of these surfaces equals zero. Finally the intersection point of all three surfaces can then be found by calculation of the intersection of this curve with the third surface. Using this approach all intersection points or tag points for the initial and final configurations could be found. Since tag surfaces were numbered this provided a reference to match corresponding tag points in both configurations. As such the initial and final coordinates could easily be used to construct a 3D displacement vector field, whereby the displacement was simply defined as the difference between the deformed and initial coordinate sets. This approach was followed for all individual surface sets and also for the overall average surface sets. Figure 7.6 shows the average vector fields (derived from the average surface sets) obtained for the phantom and volunteer data. The arrow orientations indicate displacement direction and the arrow lengths the magnitude of displacement. For both the phantom and volunteer data the displacement field demonstrates the inhomogeneous nature of the deformation induced by the indentation.

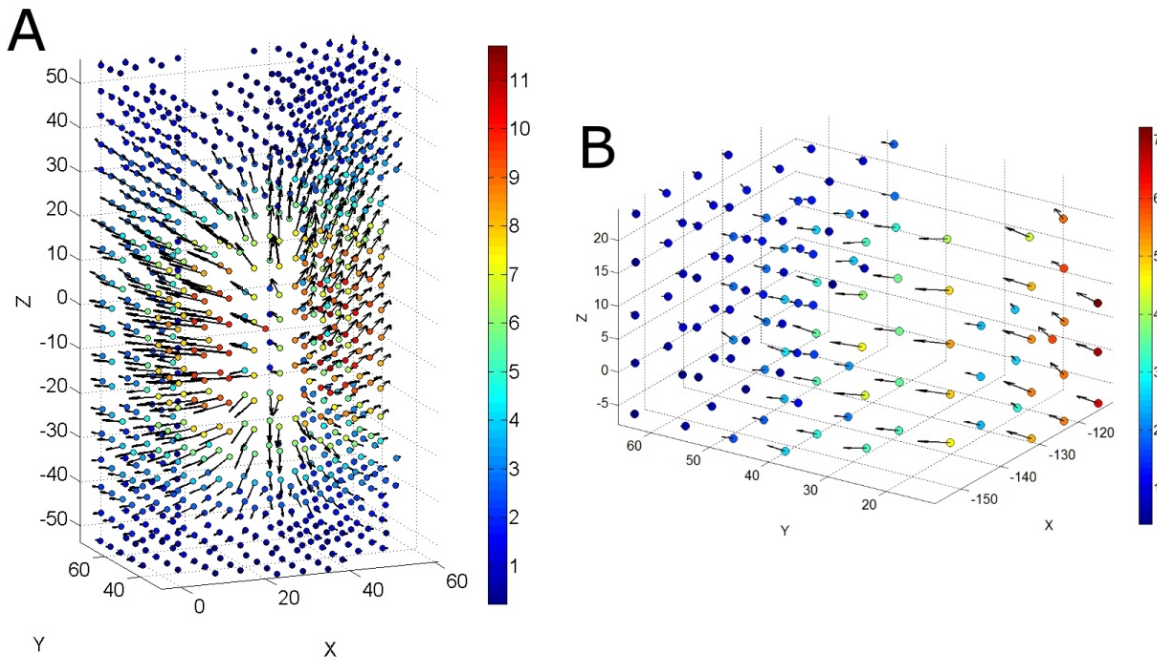


Figure 7.6 The average displacement fields for the phantom (A) and human volunteer data (B). Initial points are coloured towards the displacement magnitude (in mm) and the displacement vector arrows point towards the tag points in the deformed configuration

#### 7.2.4 Analysis of precision and accuracy

For the current study the following precision and accuracy measures were evaluated: 1) Precision of tag point location, 2) Precision of displacement magnitude and 3) Accuracy of displacement measurement in the phantom.

As shown in column 3 of Table 7-1 each tagging direction was repeated several times. This allows for the generation of a large number of combinations of initial and deformed surface sets whose intersections yield the initial and deformed tag point sets. For instance, for the phantom data, there were 700 ( $10 \times 10 \times 7$ ) possible combinations of initial and 150 ( $5 \times 5 \times 6$ ) combinations of deformed tag point sets, resulting in 105000 ( $700 \times 150$ ) possible displacement field combinations. The repetitions and combinations can be used to analyse the precision of the methods employed. However to limit computational time the precision was analysed by using 20 random combinations of initial and deformed surface sets which resulted in 20 initial and deformed tag point sets and 400 ( $20 \times 20$ ) displacement vector fields for both the volunteer and phantom data set. Each coordinate set was compared to the overall average coordinate sets to evaluate precision of tag point locations. Similarly, the precision of the displacement magnitude was assessed by comparison to the overall average displacement magnitude. Finally for the phantom the average displacement field was compared to the “gold standard”

displacement measured using marker tracking. This was done by using the average displacement field and the initial marker locations to predict (using interpolation) the marker locations in the deformed configuration. The difference between this predicted displacement and the actual marker displacement provides a measure of the accuracy of the SPAMM tagged MRI based displacement measurement. Gaussian mixture distributions (see Matlab *gmdistribution* function and<sup>269</sup>) were used for statistical analysis of the tag point location precision and the displacement accuracy. The overall mean was defined as the quadratic mean of the means in the X, Y and Z directions while the overall standard deviation was defined as the square root of the mean Eigen-value of the covariance matrix. In addition root mean square (RMS) values were computed for comparison to values in the literature.

## 7.3 Results

### 7.3.1 *Precision of tag point location*

As outlined in section 7.2, 20 random tag point sets were evaluated for both the initial and deformed configuration. For each tag point the location difference with respect to the corresponding average tag point was calculated. For the phantom and volunteer data 41040 (2052 tag points/set and 20 random combinations) and 5760 (288 tag points/set and 20 random combinations) tag points were evaluated. Figure 7.7 shows scatter plots for all tag point location differences for the phantom (Figure 7.7A-B) and volunteer data (Figure 7.7C-D). Note that most points are concentrated at the centre and therefore overlap.

For the phantom data the overall mean location difference and standard deviation were 3  $\mu\text{m}$  and 42  $\mu\text{m}$  respectively for the initial configuration. Similarly for the deformed configuration the overall mean and standard deviation were 5  $\mu\text{m}$  and 59  $\mu\text{m}$ . The RMS values were 74  $\mu\text{m}$  and 103  $\mu\text{m}$  for the initial and deformed configuration respectively. The largest tag point location difference in the initial and deformed configurations was 1.41 mm and 1.46 mm respectively. These outliers (differences larger than 250  $\mu\text{m}$ ) represented less than 1 % for both the initial and deformed configuration and are always found at the edges and corners of surfaces and surface interruptions (e.g. bone like core) where surface segmentation is based on less information.

Similarly for the volunteer data the overall mean and standard deviation were  $3\ \mu\text{m}$  and  $118\ \mu\text{m}$  respectively for the initial configuration and  $7\ \mu\text{m}$  and  $137\ \mu\text{m}$  for the deformed configuration. The RMS values were  $204\ \mu\text{m}$  and  $238\ \mu\text{m}$  for the initial and deformed configuration respectively. The largest tag point location differences for the initial and deformed configuration were  $0.75\ \text{mm}$  and  $1.27\ \text{mm}$  respectively. Again these differences represented isolated cases that were rare in occurrence as differences of magnitudes over  $0.5\ \text{mm}$  represented only  $0.9\ \%$  and  $1.5\ \%$  for the initial and deformed configurations respectively.

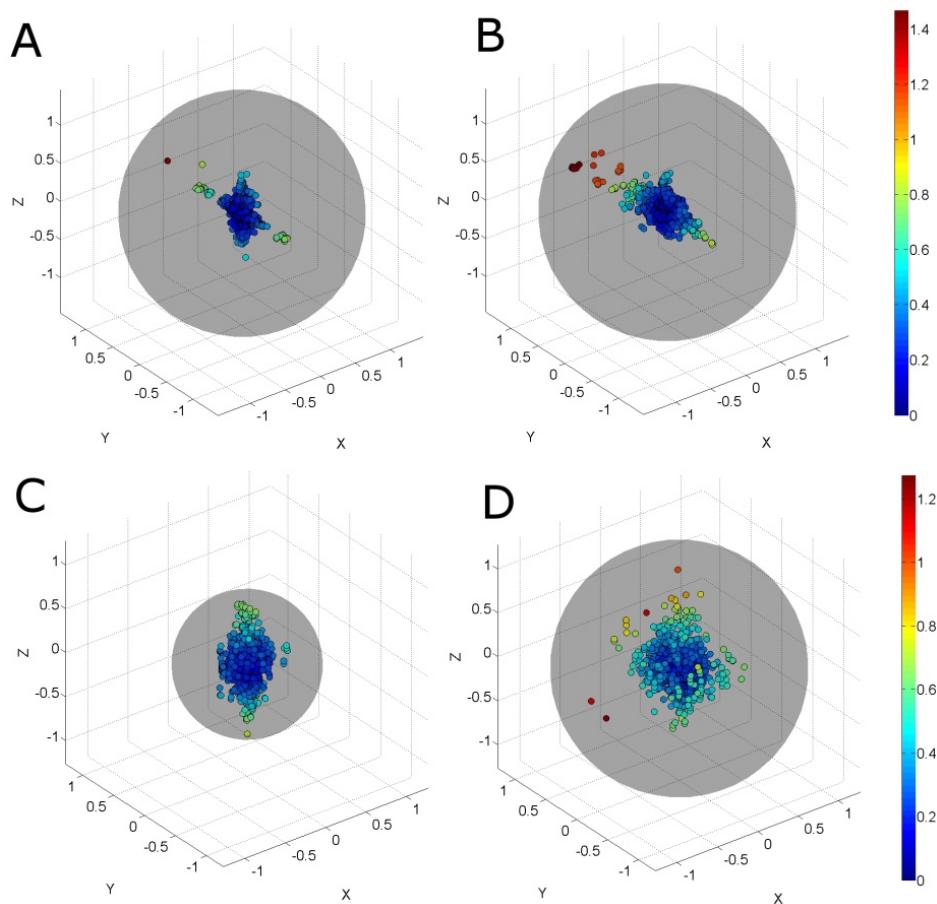


Figure 7.7 Tag point location difference scatter plots for the phantom (A and B) and human volunteer data (C and D) for both the initial (A and C) and deformed configuration (B and D). Color represents differences with respect to average (in mm), outer sphere radius is equal to the maximum difference.

### 7.3.2 Precision of displacement magnitude

For both the phantom and volunteer data a total of 400 displacement fields were derived from the 20 random tag point sets in the initial and deformed configurations. For each location the difference in displacement magnitude with respect to the corresponding average displacement magnitude (derived from the average surface set intersections see section 7.2.3.4 and 7.2.4 ) was calculated. To study the effect of displacement on the

precision of displacement magnitude measurement Figure 7.8A shows the distribution of displacement magnitude differences for the phantom data as a function of the average displacement magnitude. Figure 7.8B is a plot of the mean and standard deviation of the displacement magnitude differences as a function of the average displacement magnitude of the phantom data. Similarly for the volunteer data this is shown in Figure 7.8C-D. For both datasets the mean displacement magnitude differences varied little with increasing displacement. The overall mean and standard deviation for the phantom data was 6  $\mu\text{m}$  and 75  $\mu\text{m}$  respectively and for the volunteer data the mean and standard deviations were 5  $\mu\text{m}$  and 169  $\mu\text{m}$  respectively. However there were some outliers present for the higher displacement levels up to a maximum of 1.48 mm for the phantom and 1.13 mm for the volunteer data. Displacement magnitude differences larger than 0.5 mm represented only 0.1 % and 0.2 % for the phantom and volunteer data respectively. As expected the larger differences occurred in locations where reduced surface information was available in the initial and or deformed configurations (see also section 7.3.1 ). These were similarly identifiable allowing exclusion if desired. Since the deformation mode was indentation against a bone (or bone-like core), the larger displacements also coincide with locations where segmentation of tag surfaces was more challenging and or incomplete, e.g. the gap introduced by the bone. This therefore partially explains the slight increase in variation with displacement magnitude visible in Figure 7.8B-D.

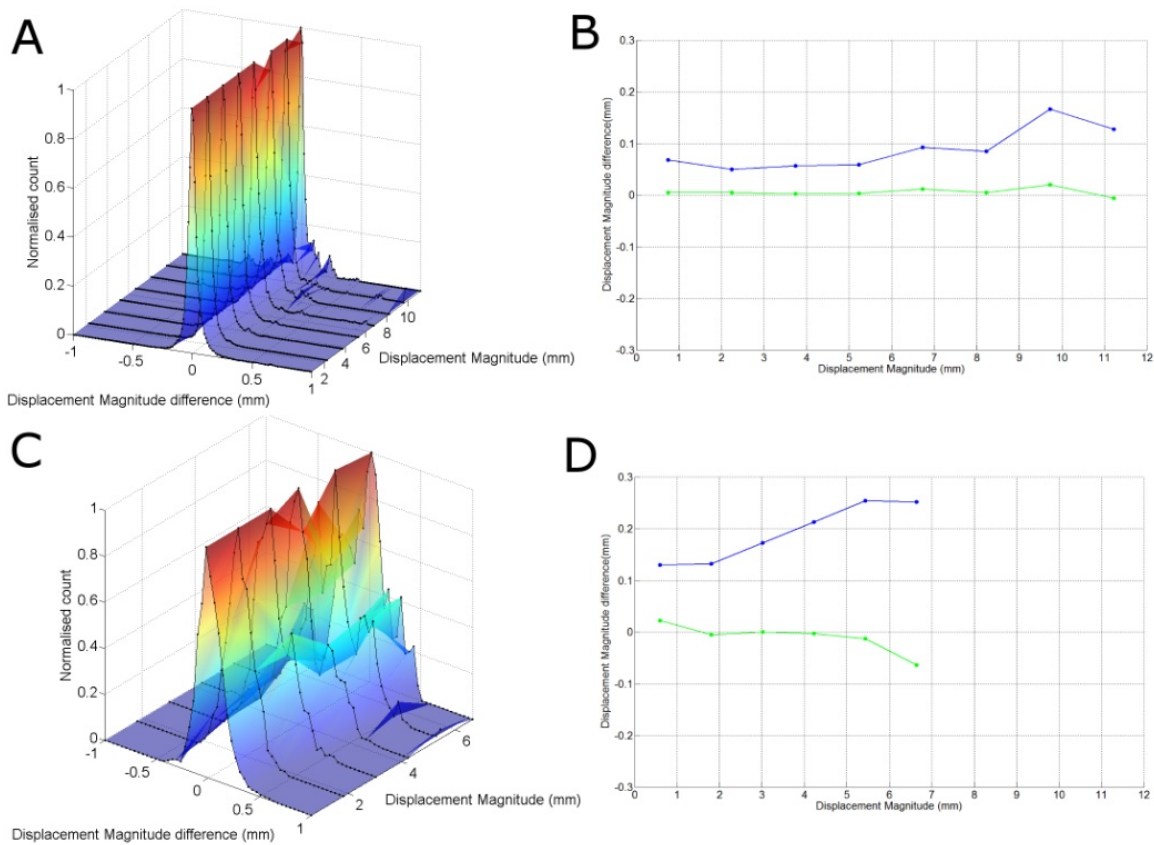


Figure 7.8 The normalised distributions of the displacement magnitude differences as a function of the average displacement magnitude for the phantom (A) and human volunteer data (C), and the mean displacement magnitude difference (green) and standard deviation (blue) as a function of the displacement magnitude for both the phantom (B) and human volunteer data (D).

### 7.3.3 Accuracy of displacement measurement in the phantom

Figure 7.9A shows the marker locations in the initial (blue) and deformed configuration (green) for markers ( $n=34$ ) that were properly embedded within (the convex hull) of the average displacement field (Figure 7.6A). Following comparison with marker displacement the accuracy of the tag point displacement measurement was evaluated. Using the average displacement field the marker locations in the deformed configuration were predicted (red in Figure 7.9A). Note how the predicted and measured marker locations in the deformed configurations overlap. The difference between the predicted marker displacement and the actual marker displacement provides a measure of the accuracy of the displacement measurement. Figure 7.9B shows the differences as a 3D scatter plot. The spheres shown are centred on the mean,  $72 \mu\text{m}$ , and the inner sphere has a radius equal to the overall standard deviation,  $289 \mu\text{m}$ , while the outer sphere radius represents the maximum difference observed ( $891 \mu\text{m}$ ). The RMS values for the



displacement differences in the X, Y and Z directions were 253  $\mu\text{m}$ , 354  $\mu\text{m}$  and 278  $\mu\text{m}$  respectively. The maximum difference was found near the edge of the displacement field where predictions were more limited due to the reduced amount of displacement information available here. No relationship with displacement magnitude was observed.

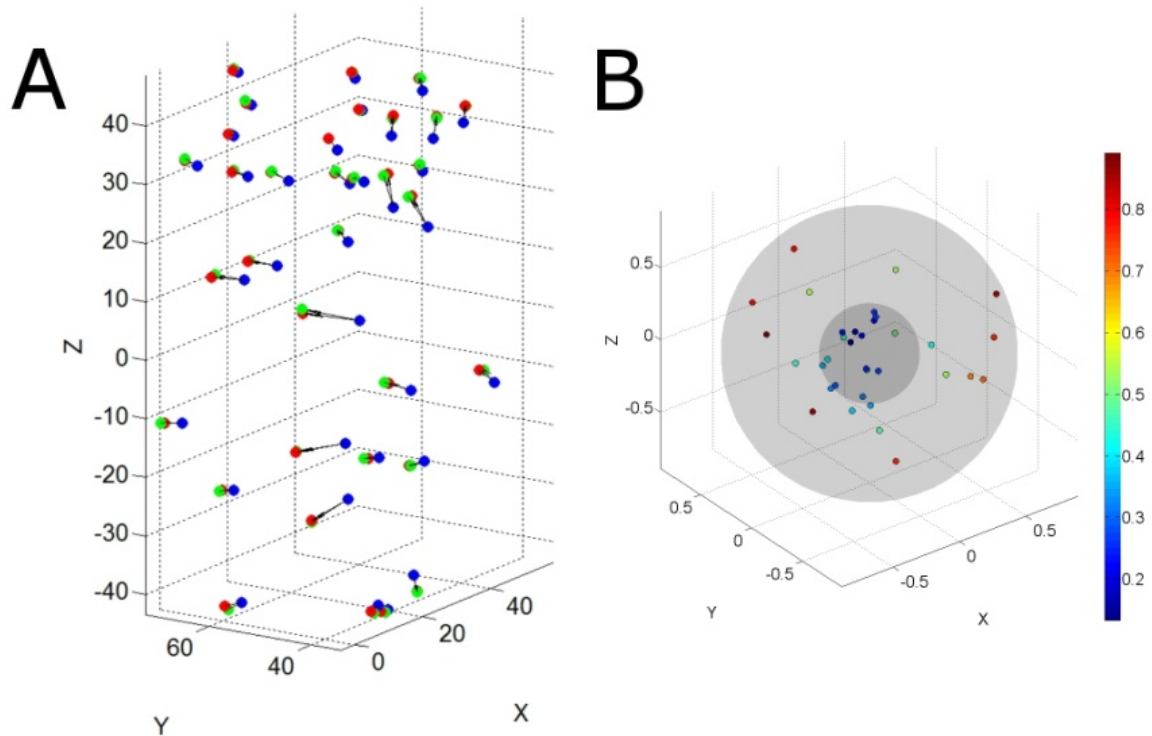


Figure 7.9 The 34 markers in their initial (blue), deformed (green) and predicted deformed locations (red) (A), and a scatter plot for the difference between the measured and predicted marker locations in the deformed configuration. Points are colored towards the magnitude of the difference (mm)

## 7.4 Discussion

Current SPAMM tagged MRI approaches to non-invasively measure human soft tissue deformation *in-vivo* require the combination of many repeated motion cycles. This has so far generally limited the biomechanical and clinical applications of SPAMM tagged MRI to the study of highly repeatable and periodic movements such as those present in the heart<sup>46, 48, 49</sup>. Besides repeatability constraints, discomfort and health issues may not allow large numbers of repetitions. Therefore the current study presents the validation of a method aimed to reduce the number of repetitions required in recording soft tissue motion.

A novel non-triggered MRI sequence based on SPAMM<sup>124, 125</sup> for the measurement of soft tissue deformation following just three deformation cycles has been presented. The tag surface patterns were introduced following a single 1-1 (first order) SPAMM pre-pulse followed by a time delay during which the tissue was indented. Subsequently a full 3D

volume read-out was performed to acquire the data from a single motion cycle. To derive true 3D deformation three tag surface sets from initially orthogonal directions were combined, whereby each set provides a reference to within surface-deformation in the other directions. Therefore for the current study, three mutually orthogonal tag data sets were acquired for both the initial and deformed configuration. Tag surfaces were segmented using a custom developed sheet marching algorithm. The intersection points of the segmented tag surfaces from three directions provided trackable material points throughout the volume and allowed for the measurement of 3D deformation. To our knowledge the presented methodology is the fastest SPAMM tagged MRI method available for the non-invasive measurement of 3D soft tissue deformation.

Indentation tests using an MRI compatible soft tissue indenter and marker tracking were performed on a silicone gel soft tissue phantom to validate the ability of the proposed methodology to measure 3D soft tissue deformation. The derived displacement demonstrated sub-voxel accuracy with a mean displacement difference of 72  $\mu\text{m}$  and a standard deviation of 289  $\mu\text{m}$ . The performance of the methodology *in-vivo* was also demonstrated using indentation of the biceps region of the upper arm of a volunteer. In addition, several precision measures were evaluated for both the phantom and volunteer data. For the silicone gel phantom the tag point location precision showed a mean and standard deviation of 3  $\mu\text{m}$  and 42  $\mu\text{m}$  respectively for the initial configuration, and 5  $\mu\text{m}$  and 59  $\mu\text{m}$  respectively for the deformed configuration. Similarly for the volunteer, the tag point location precision showed a mean and standard deviation of 3  $\mu\text{m}$  and 118  $\mu\text{m}$  respectively for the initial configuration, and 7  $\mu\text{m}$  and 137  $\mu\text{m}$  respectively for the deformed configuration. In addition displacement magnitude precision was evaluated for both data sets. For the phantom the displacement magnitude precision showed a mean and standard deviation of 6  $\mu\text{m}$  and 75  $\mu\text{m}$  respectively and, similarly for the volunteer, a mean and standard deviation of 5  $\mu\text{m}$  and 169  $\mu\text{m}$  respectively. The sub-voxel accuracy and precision demonstrated in the phantom in combination with the precision comparison between the phantom and volunteer data provide confidence in the methods presented for measurement of soft tissue deformation *in-vivo*.

Comparison of the validation results with previous studies is difficult since among other things the deformation modes and magnitudes investigated and the nature of the reference measure vary greatly. However, some comparison with previous methods is appropriate to demonstrate the benefits of the new approach. Young et al. 1993<sup>229</sup>

recorded angular displacement of a silicone gel phantom using tagged MR images and evaluated the results using numerical and analytical modelling and 2D surface deformation derived from optical tracking of lines painted on the phantom surface. A root mean square (RMS) error for the longitudinal translation between magnetic tags and the analytical model (verified by comparison with the optically measured deformation of the painted stripes) was 0.24 mm. Similarly, Chen et al. 2010<sup>219</sup> recently validated their tagging methods using a numerical phantom and reported RMS errors ranging from 0.15~0.37 mm (depending on cardiac phase). Xu et al. 2010<sup>226</sup> validated 3D tagging analyzed using optical flow methods using simulated deformation. The displacement in X, Y and Z direction demonstrated RMS errors of 0.43 mm, 0.45 mm and 1 mm respectively. For the current study the measurement of deformation was validated using marker tracking in a silicone gel soft tissue phantom demonstrating sub-voxel accuracy with a mean displacement difference of 72  $\mu\text{m}$  and a standard deviation of 289  $\mu\text{m}$  (RMS values for the displacement differences in the X, Y and Z directions were 253  $\mu\text{m}$ , 354  $\mu\text{m}$  and 278  $\mu\text{m}$  respectively). This demonstrates that despite the fact that only three deformation cycles were used, the accuracy and precision of the methodology presented are of similar order of magnitude to recent methods involving many repetitions.

The present study has several limitations. The methods presented here have only been evaluated for static deformation measurement, since for each motion cycle the deformation only occurred during the time delay introduced between the pre-pulse and read-out phase. Future work will focus on the evaluation of the methods presented for dynamic motion analysis.

Initial tag surface locations are currently determined from three initial configuration data sets. These can be acquired rapidly in series (each requiring less than 1.5 s). It is however possible to avoid the use of these initial configurations through certain assumptions about the initial state of tag surfaces. If tag surfaces in the deformed configuration can be segmented successfully and are sufficiently continuous (not sheared), and if their initial state is assumed planar, and if no rigid body movement occurred, then the planar segments of the tag surfaces in un-deformed regions can be used for approximation of initial tag surface shapes and locations. However this may result in inaccuracies as field in-homogeneities are known to result in non-planar initial tag surface shapes.

Presently the sheet marching algorithm is seeded using manually determined start and end tag surface locations. However the validation presented here is independent of these

manually determined initial estimates since they were updated and replaced by coordinates based on the data. In the future it is possible to replace the manual seeding by automatic start and end location identification.

Although only three motion cycles were combined to measure 3D deformation, allowing for the expansion of SPAMM tagged MRI to less repeatable motions. Ideally a full set of data should be acquired following a single acquisition, but currently the SPAMM tagged MRI sequence presented employs a single 1-1 SPAMM pre-pulse, thus providing a single direction for each read-out. Although this does not allow 3D analysis, it does allow for the estimation of 1D displacements associated with arbitrary and non-periodic tissue movements<sup>267</sup>.

## 7.5 Conclusions

A novel MRI sequence based on SPAMM for the measurement of 3D soft tissue deformation following just three deformation cycles has been developed. Its ability to measure soft tissue deformation was validated through indentation tests (using an MRI compatible soft tissue indenter) and marker tracking in a silicone gel phantom. In addition the technique's ability to measure soft tissue deformation *in-vivo* was demonstrated using indentation of the biceps region of the upper arm of a volunteer. Following comparison to marker tracking in the phantom, the SPAMM tagged MRI derived displacement demonstrated sub-voxel accuracy and precision with a mean displacement difference of 72  $\mu\text{m}$  and a standard deviation of 289  $\mu\text{m}$ . Displacement magnitude precision was evaluated for both data sets. The standard deviations of displacement magnitude with respect to the average displacement magnitude were 75  $\mu\text{m}$  and 169  $\mu\text{m}$  for the phantom and volunteer data respectively. The sub-voxel accuracy and precision demonstrated in the phantom in combination with the precision comparison between the phantom and volunteer data provide confidence in the methods presented for measurement of soft tissue deformation *in-vivo*. Since only three motion cycles are required the presented methodology is, to our knowledge, the fastest currently available for the non-invasive measurement of 3D soft tissue deformation. This therefore allows for the expansion of the application of SPAMM tagged MRI to the analysis of less repeatable motion and to cases where a large number of repetitions is not clinically

feasible. Future work will focus on the evaluation of the methods presented for dynamic motion analysis.

## 8 STUDY V

# The MRI Based Measurement of Dynamic 3D Soft Tissue Deformation

## 8.1 Introduction

As discussed in section 3.6 in SPAMM tagged MRI the tissue is temporarily magnetically tagged using a periodic signal modulation and tracking of the tag pattern allows measurement of deformation.

Typically SPAMM tagged MRI methods require segmented acquisitions whereby an image set reflecting a single motion cycle is composed via repeated imaging of multiple motion cycles. In some studies of tissue biomechanics motions were repeated over a hundred times (e.g. 144 volunteer rotational head accelerations<sup>51</sup>, and >135 repeated left to right eye movements<sup>52</sup>). Hence SPAMM tagged MRI has mainly found application in the study of highly repeatable motions such as those occurring in the heart<sup>46, 48, 49</sup>. In the previous chapter indentation induced 3D skeletal muscle tissue deformation measurement was presented requiring the use of only 3 motion cycles. However the methods were validated only for static deformations (limiting viscoelastic analysis) and the post-processing methods were semi-automatic. The focus of the current study is thus to expand these methods to dynamic deformation measurements using automated analysis methods while maintaining the minimum of three repeated motions. Within the current study this ensures reduction of repeatability artefacts. However it also has the potential to widen the clinical application from the current analysis of highly periodic motion, to cases where motion is less repeatable or where large numbers of repetitions are not clinically feasible.

Section 3.6 also discussed current post-processing methods for SPAMM tagged MRI (for instance using deformable models<sup>219, 220</sup>, spline models<sup>221-223</sup>, non-rigid image registration<sup>224, 225</sup>, optical flow methods<sup>226</sup>, and harmonic phase methods<sup>228</sup>). Many of the post-processing methods in the literature inherently require assumptions on the nature of the deformation and/or the mechanical properties of the underlying tissue or require computationally intensive iterative optimization methods to be employed.

This chapter therefore presents a simple, computationally efficient and fully automatic post-processing framework featuring Gabor filtering based tag segmentation and orthogonal weighted averaging based triangulated surface fitting. Deformation is measured following tracking of mutually orthogonal surface triplet intersections. Since no regularizing (deformable/spline) model is required for computation of deformation, the post-processing framework presented avoids many of the assumptions on the tissue

deformation and is thus ideal for the analysis of complex deformation (i.e. involving tissue non-linearity, anisotropy and sliding induced shearing).

A novel (non-segmented) SPAMM tagged MRI and post-processing framework is presented enabling fully automatic and continuous sampling of complex 3D dynamic tissue deformation using 3 motion cycles only. For validation the techniques are applied to the measurement of complex dynamic deformation in the silicone gel phantom containing markers (see chapter 6) which, when tracked, provide a reference measure of deformation enabling derivation of technique accuracy. In addition the techniques are applied to indentation induced deformation measurement in the upper arm of a volunteer for *in-vivo* evaluation.

## 8.2 Methods

### 8.2.1 *The experimental set-up: indenter and soft tissue phantom*

In the current study 3D dynamic deformation is measured using continuously sampled dynamic SPAMM tagged MRI (section 8.2.2 ) applied in three orthogonal directions during three motion cycles. In order to validate the deformation measurements performance was evaluated in a silicone gel tissue phantom and *in-vivo* in the upper arm of a volunteer (Figure 8.1). A computer controlled MRI compatible indenter (chapter 4) with a flat circular (45 mm in diameter) head was used to apply repeated transverse indentation (~20 mm deep) to a silicone gel phantom and the biceps region of the upper arm of a volunteer. Since three repeated motion cycles are required for derivation of 3D deformation the indenter motion was triggered (using a scanner generated TTL pulse) to start after the first dynamic of each acquisition series. This first dynamic thus provides the initial un-deformed tag pattern state. A single motion cycle is defined as an indentation phase, a hold phase and a retraction phase. For validation of the deformation measurement the silicone gel soft tissue phantom (200 mm long and 120 mm in diameter containing a stiff 20 mm in diameter bone-like core) contains contrasting (low signal) spherical markers ( $3\pm 0.05$  mm in diameter). These markers were tracked (chapter 6) from  $T_2$ -weighted scans (0.5 mm isotropic) of the same field of view for the initial un-deformed and the final deformed configuration. In addition phantom and *in-vivo*



accuracy measures could be derived from the fact that the displacement paths should return to their original location as displacement is recorded up to the end of the retraction phase of the motion cycle. For more information on the experimental set-up the reader is referred to chapters 4 and 7.

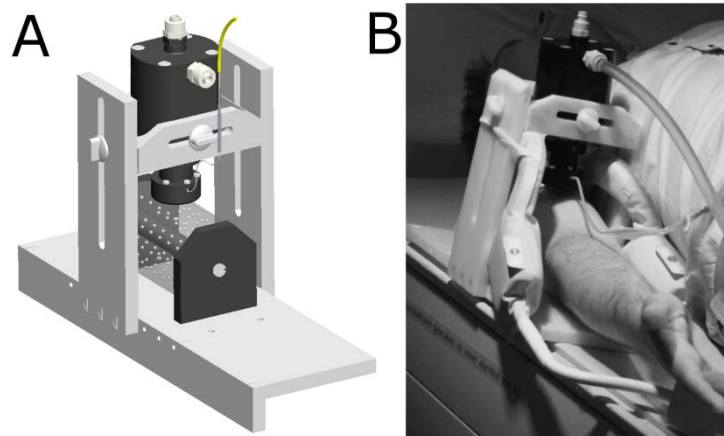


Figure 8.1 The experimental set-up showing the MRI compatible indenter used for indentation of a silicone gel phantom (A) and volunteer upper arm (B).

### 8.2.2 MRI sequence

For the current study a (non-ECG triggered) single-shot SPAMM tagged MRI sequence was employed which is a dynamically optimized version (read-out acceleration and delay reduction) of the sequence presented in chapter 7. A schematic for the pulse sequence design is shown in Figure 8.2. Table 8-1 provides a summary of the scanning parameters and configurations used in this study and illustrates several slices for each data set recorded. As the sequence diagram shows, following a 1-1 SPAMM tag pre-pulse (parts A) a short delay (parts B) was introduced during which the tissue and tag pattern deforms. Subsequently the image data is acquired using a single 3D Transient Field Echo (TFE) read-out (parts C). The 3D TFE read-out was configured with a Cartesian acquisition mode in k-space, the profile order was set to low-high, a radial turbo direction was used and half-Fourier was applied for acceleration (0.625 in the readout direction and 0.8 in the first phase encode direction). All scans were performed on a 3.0 T (Intera, Philips Health Care, Best, The Netherlands) MRI scanner using flexible surface coils with two elliptical elements (diameters of 14 and 17 cm) placed laterally to the upper arm (Figure 8.1B). Each individual acquisition was non-segmented and not repeated and entire image volumes were acquired consecutively in time for each direction. For the phantom and volunteer imaging the motion was thus effectively continuously sampled at 3.3 Hz (123 ms delay + 177 ms read-out) and 3.6 Hz (100 ms delay + 177 ms read-out) respectively.

Full 3D dynamic deformation measurement is achieved through the combination of dynamic SPAMM data from 3 orthogonal directions, thus requiring 3 motion cycles. However for validation purposes multiple motion cycles (see Table 8-1) were recorded for each acquired SPAMM direction allowing analysis of technique accuracy and precision both in the phantom and *in-vivo*. Thus for the phantom and volunteer tests 11 and 37 consecutive dynamics per motion cycle were acquired respectively (5 during indentation phase 1 during hold phase and 5 during retraction phase for the phantom, and 9 during indentation phase, 15 during hold phase and 13 during retraction phase for the volunteer). For the volunteer indentation was applied at a lower speed to ensure comfort and with a longer hold phase to allow for viscoelastic recovery. Although the overall deformation magnitudes are similar to those tested in chapter 7 the individual deformations for each dynamic were relatively low (compared to those occurring in chapter 7) since the deformation (occurring at ~12 mm/s) was continuously sampled at 3.3-3.6Hz.

During each dynamic acquisition motion is allowed to continue during the read-out. Therefore temporal blurring may cause mild underestimation of the motion. The amount of underestimation is related to many factors including the nature of the read-out and the deformation (speed and directions). The spatial characteristics of SPAMM tags correspond with specific peaks in the k-space domain, which define the bulk of the deformation information encoded in the tag pattern. However frequency components from the whole of the k-space domain contribute to the more detailed local deformation information encoded in the tag pattern. Therefore, since the read-out profile order was low-high, the latter is acquired towards to the end of the read-out sequence. As such it is expected that significant motion features are still acquired towards the end of the read-out and no compensation of the possible underestimation is required.

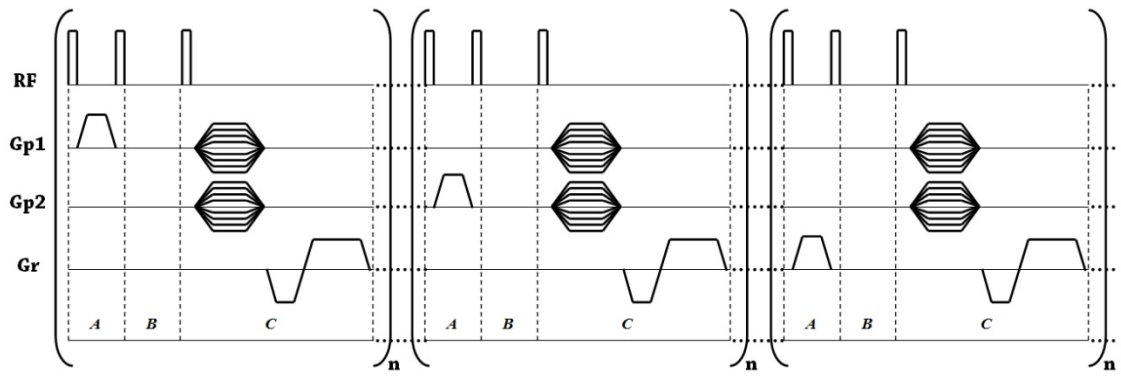


Figure 8.2 Diagram of the SPAMM pulse sequence and 3D TFE read-out. The 1-1 SPAMM pre-pulse (A) modulates the signal followed by a desired time delay (B) after which a 3D volume is acquired (C). The acquisition can be repeated  $n$  times for each direction.

MRI data visualisations: Iso-surface of indented state, and a selection of 5 evenly spaced slices for each image data set	Scan type # dynamics, # indentations $T_R/T_E$ (ms) Read-out time (ms)	Field of view (mm), Acquisition matrix, # slices Reconstructed voxel size (mm)	Slice orientation, Tag parameters: $p_t$ (mm), $\theta_t$ ( $^\circ$ ), $\psi_t$ ( $^\circ$ ) Delay time (ms)
<b>Phantom imaging</b> 	1-1 SPAMM 12, 1 2.39/1.16 177	120x120x39 80x80, 13 0.93x0.93x1.5	Sagittal 4, $0.5\pi$ , 0 123
	1-1 SPAMM 48, 4 2.38/1.53 177	120x120x39 80x52, 13 0.93x0.93x1.5	Transversal 4, 0, 0 123
	1-1 SPAMM 48, 4 2.53/1.28 177	120x120x39 80x52, 13 0.93x0.93x1.5	Transversal 4, $0.5\pi$ , 0 123
	T2-weighted 2, 1 2500/638 10min	120x120x80 240x240, 160 0.47x0.47x0.5	Sagittal N.A. N.A.
<b>Volunteer imaging</b> 	1-1 SPAMM 150, 4 2.45/1.21 177	100x100x40 68x52, 10 0.89x0.89x2	Coronal 6, $0.5\pi$ , 0 100
	1-1 SPAMM 150, 4 2.42/1.19 177	120x120x40 80x60, 10 0.94x0.94x2	Transversal 6, 0, 0 100
	1-1 SPAMM 150, 4 2.57/1.30 177	100x100x40 68x52, 10 0.89x0.89x2	Transversal 6, $0.5\pi$ , 0 100

Table 8-1 The MRI acquisition matrix

### 8.2.3 Spatial characteristics of SPAMM tags

To aid the description of the analysis methods in section 8.2.4 the spatial characteristics of SPAMM tags are first briefly discussed. For a more detailed discussion on SPAMM tagged MRI the reader is referred to<sup>49</sup>. SPAMM tagging induces a periodic modulation on

the signal profile across the image volume and in the case of 1-1 (first order) SPAMM is approximately sinusoidal. Thus an un-deformed tagged image  $M_t$  can roughly be expressed as the following type of modulation of a magnitude image  $M$ :

$$M_t \approx \left| M \cdot \left( m + A \cdot \cos\left(\frac{2\pi x_r}{p_t}\right) \right) \right| \quad 8-1$$

Here  $p_t$ ,  $m$  and  $A$  set the spatial tag period (or spacing), mean and amplitude of the modulation respectively across the direction  $x_r$ . Throughout this chapter tag modulations are expressed along  $x_r$  belonging to the coordinates  $(x_r, y_r, z_r)$  formed following rotation of  $(x, y, z)$ , expressed in a regular Cartesian coordinate system:

$$(x_r, y_r, z_r) = R_t \cdot (x, y, z) \quad 8-2$$

Where  $R_t$  represents the rotation matrix:

$$R_t = \begin{bmatrix} \cos(\theta_t) & 0 & \sin(\theta_t) \\ 0 & 1 & 0 \\ -\sin(\theta_t) & 0 & \cos(\theta_t) \end{bmatrix} \begin{bmatrix} \cos(\psi_t) & -\sin(\psi_t) & 0 \\ \sin(\psi_t) & \cos(\psi_t) & 0 \\ 0 & 0 & 1 \end{bmatrix} \quad 8-3$$

expressed using the Euler angles  $(\theta_t, \psi_t)$  which define an x-axis and z-axis rotation consecutively. The initial and un-deformed tag orientation and period are set during scanning. In the current study three mutually orthogonal SPAMM directions were applied and their orientation and frequency characteristics in the above notation are presented in Table 8-1.

For each image data set a local Cartesian coordinate system  $(x, y, z)$  is defined which is aligned with its image axes (voxel row, column and slice directions). The field-of-view location and orientation which are set during scanning determine the local coordinate system's origin location and axes orientations. Local coordinate systems thus vary for each image data set and generally do not coincide with the overall scanner coordinate system (based on bore axis and perpendicular directions). The tag orientation parameters  $(\theta_t, \psi_t)$  are defined with respect to the local (not overall scanner) coordinate system. Thus for two image sets with orthogonal tag features in space (the overall scanner coordinate system) the respective tag orientation parameters  $(\theta_t, \psi_t)$  may be equivalent (Table 8-1) as long as the set field-of-view orientations are mutually orthogonal. Although throughout the work presented here computations are mainly performed in the overall scanner coordinate system the methods and results are presented in local coordinates systems for clarity as features may be oblique with respect to the global scanner coordinate system.

Although an un-deformed tagged image will have the features discussed above, tissue deformation causes them to vary spatially depending on the nature of the deformation (e.g. local orthogonal tension or compression will increase or decrease  $p_t$  respectively and bending will locally perturb  $\theta_t$  and  $\psi_t$ ). However this can be taken into account during analysis and the periodic nature will remain advantageous in segmentation as will be discussed in section 8.2.4.1 . In addition field inhomogeneity and local material property differences may cause the tag features to be non-planar prior to the onset of deformation. As such for the current study dynamics acquired in the absence of motion were used as the reference state.

The extrema (maxima and minima) of the periodic modulation are here referred to as tags or tag features and surfaces fitted to them as tag surfaces. An intersection point for a tag surface triplet is referred to as a tag point. In order to derive deformation the current study applies segmentation of the extrema and tracking of mutually orthogonal tag feature derived tag points. This leads to a trackable grid of tissue points with a  $\frac{p_t}{2}$  mm spacing (2x2x2 mm and 3x3x3 mm for the phantom and volunteer data respectively).

## 8.2.4 *Deriving tissue deformation from the SPAMM tagged MRI data*

In order to derive full 3D dynamic soft tissue deformation from the continuous dynamic SPAMM tagged MRI data a post-processing framework was created and implemented using MATLAB (7.8 R2009a The Mathworks Inc., Natick, MA). Magnitude MRI data was imported and normalized for each dynamic and post-processing was performed in the following 5 steps:

- 1) *Gabor filter analysis*: The goal of this analysis step is *a)* to derive (filtered) image data sets which will aid in the successful segmentation of tags, and *b)* to derive per voxel tag surface normal orientations which will aid the surface fitting methods presented.
- 2) *Tag feature segmentation*: The goal of this analysis step is to segment and separately group tags based on the Gabor image data sets.
- 3) *Orthogonal weighted-mean surface fitting*: Using the per voxel tag orientations estimated from the Gabor filter bank a triangulated surface description is created where surface points are derived using orthogonal weighted means.

4) *Tag surface intersection determination*: Using the triangulated surface descriptions tag intersection points from the three mutually orthogonal directions are derived producing the tissue points trackable over time.

5) *Derivation of displacement fields*: This analysis step produces the dynamic and cumulative displacement fields.

### 8.2.4.1 Gabor Filter Analysis

Due to the specific spatial characteristics of SPAMM tags (discussed in section 8.2.3 ) they can be enhanced using a filter which shares these characteristics, the Gabor filter<sup>270</sup> (see Figure 8.3A-B). A Gabor filter is a wavelet constructed by modulating a Gaussian envelope with a harmonic function (Figure 8.3A and B visualize a 1D and 3D example). For the current study magnitude SPAMM tagged MRI data is used and is analysed using the following type of 3D Gabor filter:

$$G(x_r, y_r, z_r, \sigma_p, \sigma_s, p_g) = e^{-\frac{1}{2}\left(\left(\frac{x_r}{\sigma_p}\right)^2 + \left(\frac{y_r}{\sigma_s}\right)^2 + \left(\frac{z_r}{\sigma_s}\right)^2\right)} \cdot \left(\pm \cos\left(\frac{2\pi x_r}{p_g}\right)\right) \quad 8-4$$

Here  $p_g$  is the central period of the harmonic modulation and the parameters  $\sigma_p$  and  $\sigma_s$  define the size of the Gabor filter since they represent the perpendicular, and within-tag surface standard deviations respectively for the ellipsoidal Gaussian envelope. The  $\pm$  denotes alteration of sign when tracking of the maxima (+) or minima (-) is of interest. Analogous to the equations and notation introduced in section 8.2.3 the modulation acts along the  $x_r$  direction in the coordinate system  $(x_r, y_r, z_r)$  formed following rotation of the system  $(x, y, z)$  with a rotation matrix defined using the Gabor angles  $(\theta_g, \psi_g)$ . Given its particular frequency, size and orientation, convolution with the Gabor filter will produce an image where features that locally resemble its appearance are amplified while others are suppressed. However, as discussed in section 8.2.3 , motion and deformation results in locally varying tag frequency and orientation. Therefore a common approach<sup>219, 271-273</sup> is to employ an array or bank of filters, all with different spatial and frequency characteristics. A single filtered image can then be reconstructed by taking the maximum response of all filters for each voxel. For computational efficiency all convolutions were computed as:

$$M_f = \mathcal{F}^{-1}\{\mathcal{F}\{M_t\} \cdot \mathcal{F}\{G\}\} \quad 8-5$$

Here  $M_f$  represents the filtered image and  $\mathcal{F}\{ \}$  and  $\mathcal{F}^{-1}\{ \}$  denote the Fourier and inverse Fourier transform respectively.

It is important to note that the choice of the Gabor parameters can affect the apparent deformation derived. For instance the standard deviations set the amount of blurring in their respective directions which might cause undesired averaging effects on the deformation. Therefore for the filter bank used  $\sigma_p$  was set at  $\frac{p_g}{3}$ . Hence in the direction orthogonal to the modulation the filters only act on a central and its two directly neighbouring extrema. For a visualisation of a similarly confined 1D Gabor wavelet see Figure 8.3A. The within-tag-surface standard deviation  $\sigma_s$  sets the amount of averaging across the surface (e.g. size of disks in Figure 8.3B) and large values will have a straightening effect on the tag shape while smaller values leave its original shape and detail intact. Using large standard deviations effectively has a smoothing and regularisation effect not only on the images, but also on the derived deformation. This however is desirable for segmentation as the effects of noise are suppressed allowing easy separation of more blur-scale invariant features such as tags. To harness this benefit without over-averaging the deformation the Gabor analysis presented here is split into two parts: a) *Gabor scale-space filtering*, and b) *Gabor Filter Bank analysis*. The former is only used as an aid in the separation and segmentation of tags while the latter is used for two purposes: a) Enhancement of tag appearance, b) Assessment of local tag orientation. The two types are schematically illustrated in Figure 8.4 and the parameters used are specified in Table 8-2.

For the Gabor scale-space the orientation and central period were held constant while for both the perpendicular and within-surface standard deviations a scale-path or range was specified going from  $p_t$  to  $\frac{p_t}{3}$  in 6 scale steps. For each scale-space filter a separate image was formulated leading to 6 scale-space images sets for each extrema (e.g. Figure 8.5B-C).

For the Gabor filter bank however the filter orientation and central frequency were varied across 27 filter combinations. The within-surface standard deviation was held constant while the perpendicular standard deviation was constrained  $\frac{p_g}{3}$  such that the filter design of Figure 8.3A is maintained. The maximum filter response (in the image domain) was used for each voxel producing two filtered image sets, one for each extrema (e.g. the maxima in Figure 8.5D). However the specific Gabor filter orientation that



produced the maximum response was also stored for each voxel as this is an estimate of the local tag surface orientation and can be used in surface fitting. Specifically it provides an estimate of the local surface normal vector  $\mathbf{n}_s$  since:

$$\mathbf{n}_s = \begin{bmatrix} \cos(\theta_g)\cos(\psi_g) \\ \sin(\psi_g) \\ -\sin(\theta_g)\cos(\psi_g) \end{bmatrix} \quad 8-6$$

The surface normal estimates are only appropriate for locations that resemble the filter such as the central voxels for the tag extrema. The surface normal orientations are thus only used for these voxels.

For each extrema type the Gabor filter analysis produced: 6 Gabor scale-space image sets (going from most to least blurred in 6 steps), a Gabor filter-bank optimized image set, and a surface normal estimation data set.

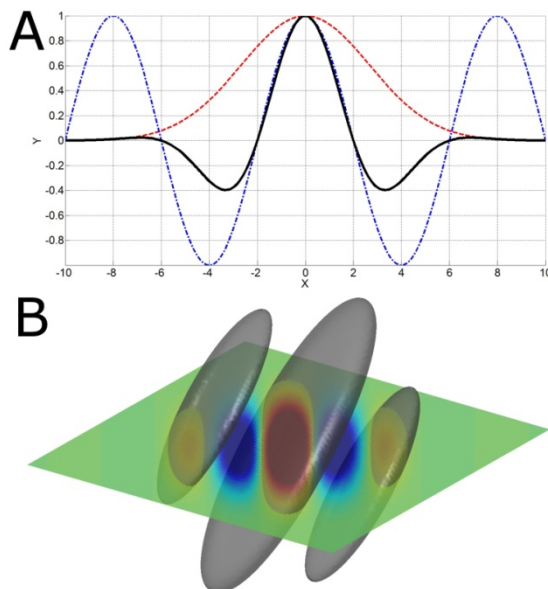


Figure 8.3 1D representation of a Gabor wavelet (solid) composed using multiplication of Gaussian (dashed) with harmonic function (dashed-dotted) (A), 3D visualisation of Gabor wavelet showing 2D mid-slice and iso-surfaces (B).

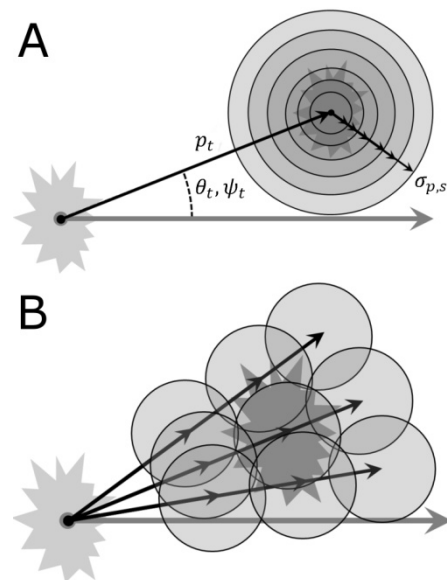


Figure 8.4 Schematic representation of the Gabor scale-space (A) and Gabor filter bank (B). Circle centre distance from origin, circle radius and location illustrate the Gabor central period, Gaussian envelope size and orientation respectively.

Gabor filter set type	x-axis tilt $\theta_g$ ( $^\circ$ )	z-axis tilt $\psi_g$ ( $^\circ$ )	Central period $p_g$ (mm)	Perpendicular standard deviation $\sigma_p$ (mm)	Within surface standard deviation $\sigma_s$ (mm)
Gabor scale-space filters (6 scale steps)	$\theta_t$	$\psi_t$	$p_t$	$p_t \rightarrow \frac{p_t}{3}$	$p_t \rightarrow \frac{p_t}{3}$
Gabor filter bank (all 27 combinations)	3 variations: $\theta_t - 20$ $\theta_t$ $\theta_t + 20$	3 variations: $\psi_t - 20$ $\psi_t$ $\psi_t + 20$	3 variations: $p_t - 1$ $p_t$ $p_t + 1$	$\frac{p_g}{3}$	$\frac{p_t}{3}$

Table 8-2 The Gabor filter designs

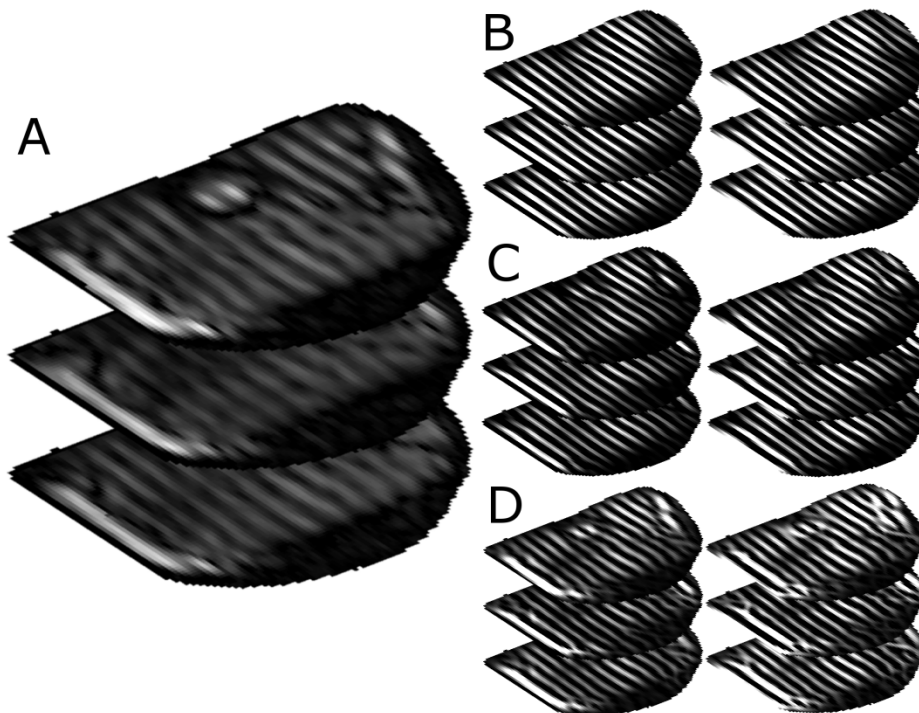


Figure 8.5 Image data that is unfiltered (A), and Gabor scale-space filtered images for the most blurred step (B) and an intermediate step (C) and Gabor filter-bank enhanced images (D). Maxima shown on the left, minima on the right. The scale-space images show separate and straightened tag features while the filter-bank images maintain tag feature curvature.

#### 8.2.4.2 Tag feature segmentation

The first step in tag segmentation is to produce logic images reflecting whether voxels in all the Gabor-filtered image sets are potential tag voxels. An appropriate and adaptive threshold  $T_{tag}$  was half the mean of all voxels within a set with an intensity higher than 0 (i.e. all significantly positively enhanced voxels, since features dissimilar or opposite in

nature to the Gabor filter become reduced or negative). The logic images  $L_{tag}$  for each Gabor image set  $M_f$  were derived using:

$$L_{tag} = \begin{cases} 1 & M_f \geq T_{tag} \\ 0 & M_f < T_{tag} \end{cases} \quad T_{tag} = \frac{\sum M_h}{2 \sum L_h} \quad M_h = \begin{cases} M_f & M_f > 0 \\ 0 & M_f \leq 0 \end{cases} \quad 8-7$$

$$L_h = \begin{cases} 1 & M_f > 0 \\ 0 & M_f \leq 0 \end{cases}$$

Then a simple grouping algorithm was implemented whereby all potential voxels that are touching each other with one of their 6 faces are grouped together to form a tag feature. The initial tag features are formulated by grouping in the most blurred Gabor filtered image (Figure 8.5B and Figure 8.6A) since here all tag features are appropriately separated. As Figure 8.6 demonstrates the threshold  $T_{tag}$  segments the tag features with a thickness of about  $\frac{p_t}{2}$ . Next the shape of each tag feature is adjusted using the following step wise process repeated for each less blurred Gabor scale-space image and finally also the Gabor filter-bank optimised image (thus a total of 7 tag feature adjustment steps):

- 1) An orthogonal weighted average (perpendicular to tag feature orientation) of the voxel coordinates of the current tag feature shape is taken to provide reference coordinates of the voxels at the centre of the tag (leaving the tag feature 1 voxel thick).
- 2) The tag feature shape for the next image set is then defined as all voxels that are classified as potential tag voxels and are touching one of the central tag voxels from the previous step (this regrows the tag features to their normal  $\frac{p_t}{2}$  thickness, this step can be repeated for tags with large  $p_t$  relative to the voxel size).

After the final step the tag shape has also been adjusted to the Gabor filter bank enhanced image which maintains features of deformation (Fig 5B). The segmentation also assigns each tag feature with a tag number enabling indexing of tag intersection points (section 8.2.4.4).

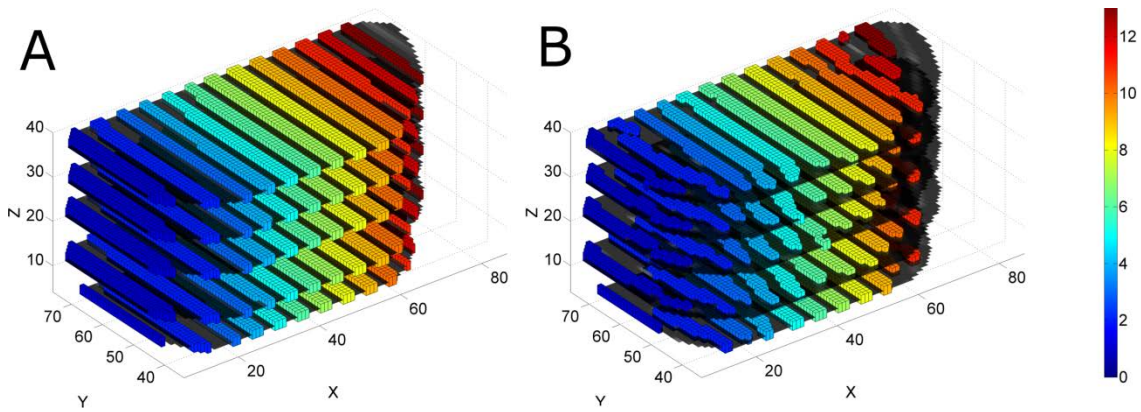


Figure 8.6 Segmented tag maxima features shown as voxels (shaded according to tag number) in the most blurred (A) and final Gabor bank filtered state (B). Axis units are in mm.

### 8.2.4.3 Orthogonal weighted-mean surface fitting

A simple yet flexible surface fitting approach was derived as it can fit surfaces of any orientation and severe deformation and voids due to shearing or gaps. The first step in the surface fitting is the specification of orthogonal masks (see Figure 8.7). These are constructed using the per voxel derived surface normal  $\mathbf{n}_s$  (see equation 8-6). For each tag voxel with orthogonal neighbours (i.e lying at the centre of a tag feature) and voxel coordinates  $\mathbf{p}_v$ , the orthogonal mask coordinates  $\mathbf{V}_m$  are defined as the collection of all voxels along the line (see arrows in Figure 8.7):

$$\{(\mathbf{p}_v - \mathbf{n}_s h_m), (\mathbf{p}_v + \mathbf{n}_s h_m)\} \quad 8-8$$

The parameter  $h_m$  is the mask height here set to  $\frac{p_t}{4}$ . For each tag voxel with orthogonal neighbors a tag surface point  $\mathbf{p}_s$  can be derived using the orthogonal weighted average:

$$\mathbf{p}_s = \frac{\sum \mathbf{V}_m \mathbf{W}_m}{\sum \mathbf{W}_m} \quad 8-9$$

where  $\mathbf{W}_m$  are the orthogonal mask weights linearly derived from the image signal intensities. When applied to all voxels with orthogonal neighbours this produces a set of points describing the surface where each point location was determined depending only on its local orthogonal neighbourhood. As such sharp transitions, gaps and shear interfaces are permissible and do not require special treatment. The next step is to assume a type of connectivity across these points to form the surface. This is done through a simple Delaunay triangulation whereby gaps and sheared interfaces are accounted for via removal of triangles with edge lengths longer than twice the largest voxel dimension of the image set (see gaps in Figure 8.8). Finally to suppress the effects of noise and to reduce the stepped appearance induced due to the discrete nature of voxels, the surfaces are mildly smoothed using surface smoothing (HC-Laplacian

smoothing<sup>274</sup> ensuring shape shrinkage is limited). The smoothing is based only on local connected neighbourhoods (Laplacian umbrella's) and does not occur across gaps and sheared interfaces and thus such sharp transitions are appropriately maintained.

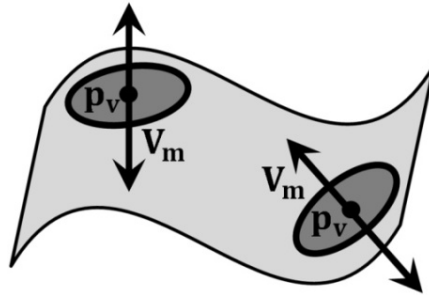


Figure 8.7 Schematic visualization of a tag surface, two tag voxel locations  $\mathbf{p}_v$  and associated orthogonal masks  $\mathbf{V}_m$ .

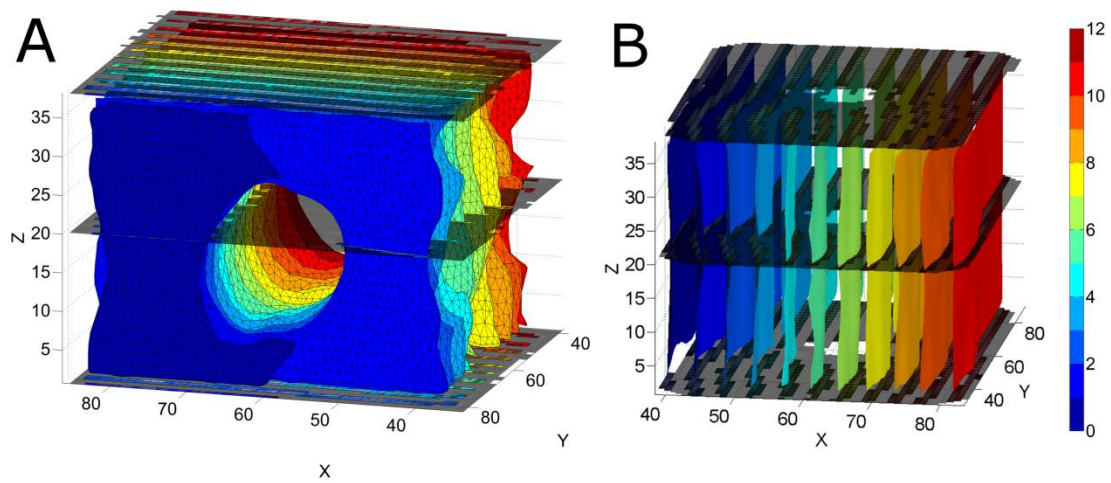


Figure 8.8 Segmented surfaces for two of the phantom data sets. Note the triangulated appearance of the surfaces in and how sheared interfaces and gaps e.g. at the core location are dealt with (A) and how curvature (due to indentation in Y direction) is captured (B). Axis units are in mm.

#### 8.2.4.4 Tag surface intersection determination

Since the prior analysis step produced triangulated surfaces a logical and simple method for obtaining tag surface intersections is to compute triangle intersections. Each intersection point is uniquely defined by the intersection of a triangle triplet. If each surface contains  $n$  triangles then  $n^3$  triplet combinations exist. Thus for computational efficiency the number of candidate triangles is first reduced. This is done by focusing the analysis only on those triangles that are closer than the longest occurring triangle edge length (based on nearest vertex search of Delaunay tessellation). For each surface this reduces the candidate triangles to only those located near a possible intersection point. The triangle intersection calculation is based on vector geometry. The intersection point  $\mathbf{p}$  for three planes (triangles) is defined by:

$$\mathbf{p} = \frac{(\mathbf{x}_1 \cdot \mathbf{n}_1)(\mathbf{n}_2 \times \mathbf{n}_3) + (\mathbf{x}_2 \cdot \mathbf{n}_2)(\mathbf{n}_3 \times \mathbf{n}_1) + (\mathbf{x}_3 \cdot \mathbf{n}_3)(\mathbf{n}_1 \times \mathbf{n}_2)}{\det([\mathbf{x}_1 \quad \mathbf{x}_2 \quad \mathbf{x}_3])} \quad 8-10$$

where  $\mathbf{x}_1$ ,  $\mathbf{x}_2$  and  $\mathbf{x}_3$  are arbitrary points on each plane and  $\mathbf{n}_1$ ,  $\mathbf{n}_2$  and  $\mathbf{n}_3$  are the face-normals. Next the validity of the intersection point (if existent) is determined by checking whether it is found either inside and/or on each of the triangle faces using:

$$L_{on} = \begin{cases} 1 & (\sum \mathbf{c}_1 = 0 \vee \sum \mathbf{c}_2 = 0 \vee \sum \mathbf{c}_3 = 0) \wedge (\sum \mathbf{c}_1 \geq 0 \vee \sum \mathbf{c}_2 \geq 0 \vee \sum \mathbf{c}_3 \geq 0) \\ 0 & \text{otherwise} \end{cases}$$

$$\mathbf{c}_1 = (\mathbf{v}_2 - \mathbf{v}_1) \times (\mathbf{p} - \mathbf{v}_1), \mathbf{c}_2 = (\mathbf{v}_2 - \mathbf{v}_3) \times (\mathbf{p} - \mathbf{v}_2), \mathbf{c}_3 = (\mathbf{v}_3 - \mathbf{v}_1) \times (\mathbf{p} - \mathbf{v}_3)$$

$$L_{in} = \begin{cases} 1 & d_1 = 1 \wedge d_2 = 1 \wedge d_3 = 1 \\ 0 & \text{otherwise} \end{cases} \quad 8-11$$

$$d_1 = \mathbf{c}_1 \cdot \mathbf{n}, d_2 = \mathbf{c}_2 \cdot \mathbf{n}, d_3 = \mathbf{c}_3 \cdot \mathbf{n}$$

$$L_v = \begin{cases} 1 & L_{in} = 1 \vee L_{on} = 1 \\ 0 & \text{otherwise} \end{cases}$$

Here  $\mathbf{v}_i$  represent the triangle vertex vectors and  $\mathbf{n}$  its face-normal. An intersection point  $\mathbf{p}$  is valid ( $L_v = 1$ ) if it is inside ( $L_{in} = 1$ ) or on ( $L_{on}=1$ ) each of the triangles.

Since the tag feature segmentation provides numbered indices for each tag surface, each intersection point, being an intersection point of a tag surface triplet for a certain dynamic, is thus uniquely specified by a 4 digit tag-index  $(T_1, T_2, T_3, d)$ , where  $d$  is the dynamic number and  $T_i$  the tag numbers for each direction. Thus each tag point position  $\mathbf{p}$  was stored in the tag point array  $\mathbf{P}(T_1, T_2, T_3, d)$ . This type of indexing avoids the need for tag intersection point tracking methods (e.g. point matching algorithms<sup>275</sup>).

#### 8.2.4.5 Derivation of dynamic deformation

In the current study deformation is measured following tracking of intersections of tag surfaces in three sets of mutually orthogonal tag surfaces (although other types of intersecting oblique orientations are permissible and would not require alteration of the methods presented here). Since field in-homogeneities may cause the initial tag shape to be non-planar displacement is defined with respect to tag points derived from tag-surfaces segmented for an initial configuration. The displacement array  $\mathbf{U}$  is thus defined by:

$$\mathbf{U}(T_1, T_2, T_3, d_i) = \mathbf{P}(T_1, T_2, T_3, d_i) - \mathbf{P}(T_1, T_2, T_3, d_0) \quad 8-12$$

where  $d_0$  is the appropriate reference or initial dynamic for the dynamic  $d_i$ . These per dynamic displacements are referred to as the individual displacement fields. The above is

schematically illustrated in Figure 8.9, as the tissue deforms the initial tags and intersections (light gray in Figure 8.9A) obtain a new location (dark gray in Figure 8.9A). This produces the first individual dynamic displacement field (green vectors in Figure 8.9A). For each consecutive dynamic the deformed tissue is re-tagged (hence its initial coordinates may represent the same spatial coordinates but not the same tissue points as the previous dynamic) and undergoes an additional displacement (red vectors in Figure 8.9B).

Figure 8.9C-D shows a schematic derivation of the so called cumulative dynamic displacement. The deformed state of the first (or prior) dynamic (light grey in Figure 8.9C) is mapped into the displacement field of the second (or current) dynamic (transparent vectors in Figure 8.9C). Through (natural neighbour and 3D Delaunay tessellation based) interpolation of the current displacement field onto the deformed state of the prior dynamic, it is possible to derive the displacement that the initial tissue points underwent during the second dynamic (dotted arrows in Figure 8.9C). The continuous mapping of the previous state into the current allows for the construction of a continuous cumulative displacement path over time (consecutive green and red arrows in Figure 8.9D).

Each individual dynamic displacement measurement is derived following a single initial and a single deformed state hence possible displacement measurement errors are a function of two measurements. For the cumulative dynamic displacement however each displacement field is a function of all past measurements and thus measurement errors may propagate. A common approach is to apply regularization techniques and assumptions on the nature of the deformation and underlying constitutive properties. However implementation of such assumptions is not of interest to the current study. Therefore the approach presented here does not require *a priori* knowledge of the geometry and nature of the deformation and mechanical properties. Therefore cumulative displacement is derived using simple natural neighbour interpolation instead.

For the current study the cumulative displacement measures are required in order to derive accuracy measures (e.g. marker displacement prediction, see section 8.2.5 ).

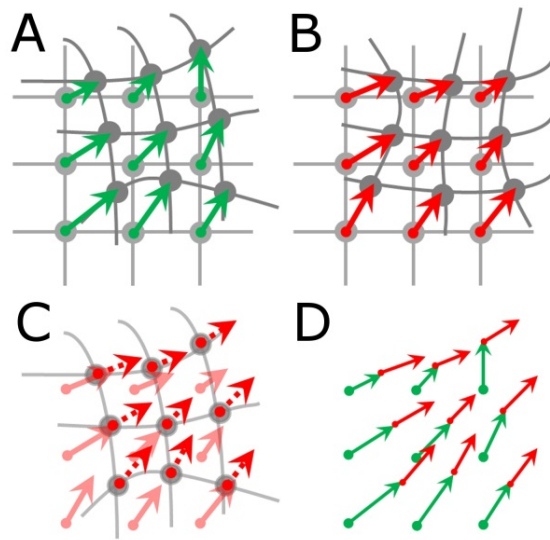


Figure 8.9 Derivation of dynamic displacement (A-B). Derivation of cumulative dynamic displacement (C-D).

### 8.2.5 Analysis of precision and accuracy

As shown in Table I continuous dynamic tagging was applied in each direction during repeated indentations. Due to the repetitions for each direction a multitude of combinations can be made for computation of tag surface intersections and displacement fields. In order to limit computational time random data set combinations were chosen leading to 6 tag point location sets per dynamic allowing computation of 36 individual displacement fields per dynamic. Using the mean of all combinations of individual displacement fields a single mean cumulative displacement field was derived. The following precision and accuracy measures were evaluated:

#### 1) Precision of tag point location

For each dynamic the difference of each tag point location combination ( $n = 6$ ) with respect to the mean tag point location for that dynamic was calculated. This allowed computation and analysis of difference scatter clouds for each dynamic.

#### 2) Precision of individual dynamic displacement

For each dynamic the deviation of displacement magnitude of each individual displacement field combination ( $n = 36$ ) with respect to the average individual displacement magnitude was calculated.

#### 3) Accuracy of cumulative dynamic displacement

Since deformation is tracked up to the end of the retraction phase of the motion cycle differences between the initial coordinates and the final locations of the total cumulative displacement are a measure of accuracy both in the phantom and *in-vivo*.



#### 4) *Accuracy of displacement compared to marker tracking in the phantom.*

Using the mean cumulative displacement of the indentation phase of the motion cycle the marker locations in the deformed state can be predicted and compared to the real measured marker locations<sup>276</sup>. Comparison of true independently measured and predicted marker displacement marker thus yields a measure of the accuracy of the methods applied to the phantom.

Statistical analysis was performed using fitting of Gaussian models (see Matlab *gmdistribution* function and<sup>269</sup>) to the various difference measures. Each overall mean was defined as the root mean square (RMS) of the means in the X, Y and Z directions while the overall standard deviations are defined as the square root of the mean Eigen-value of the co-variance matrix. In addition RMS values were computed where appropriate allowing for comparison to values in the literature.

## 8.3 Results

### 8.3.1 *Precision of tag point location*

For both the phantom and volunteer data 6 tag point location sets were derived for each dynamic and compared to the mean tag point locations for each dynamic. Figure 8.10A-B below shows the difference scatter plots for all tag points (all combinations and for all dynamics) where  $n=449495$  and  $n=232391$  for the phantom and volunteer data respectively.

For the phantom data the standard deviation was  $44\ \mu\text{m}$  (RMS of difference magnitudes  $76\ \mu\text{m}$ ). The largest tag point location difference was  $0.96\ \text{mm}$ . Such outliers are however rare as differences larger than  $0.28\ \text{mm}$  were found in less than 1 % of tag points. Similarly for the human data the standard deviation was  $92\ \mu\text{m}$  (RMS of difference magnitudes  $160\ \mu\text{m}$ ) and the largest tag point location difference found was  $1.73\ \text{mm}$ . However, again such outliers are however rare since differences over  $0.4\ \text{mm}$  were found in less than 1 % of tag points.

Figure 8.10C-D demonstrates that no clear relationship between the standard deviations and the respective dynamic exists for either the phantom or the volunteer data.

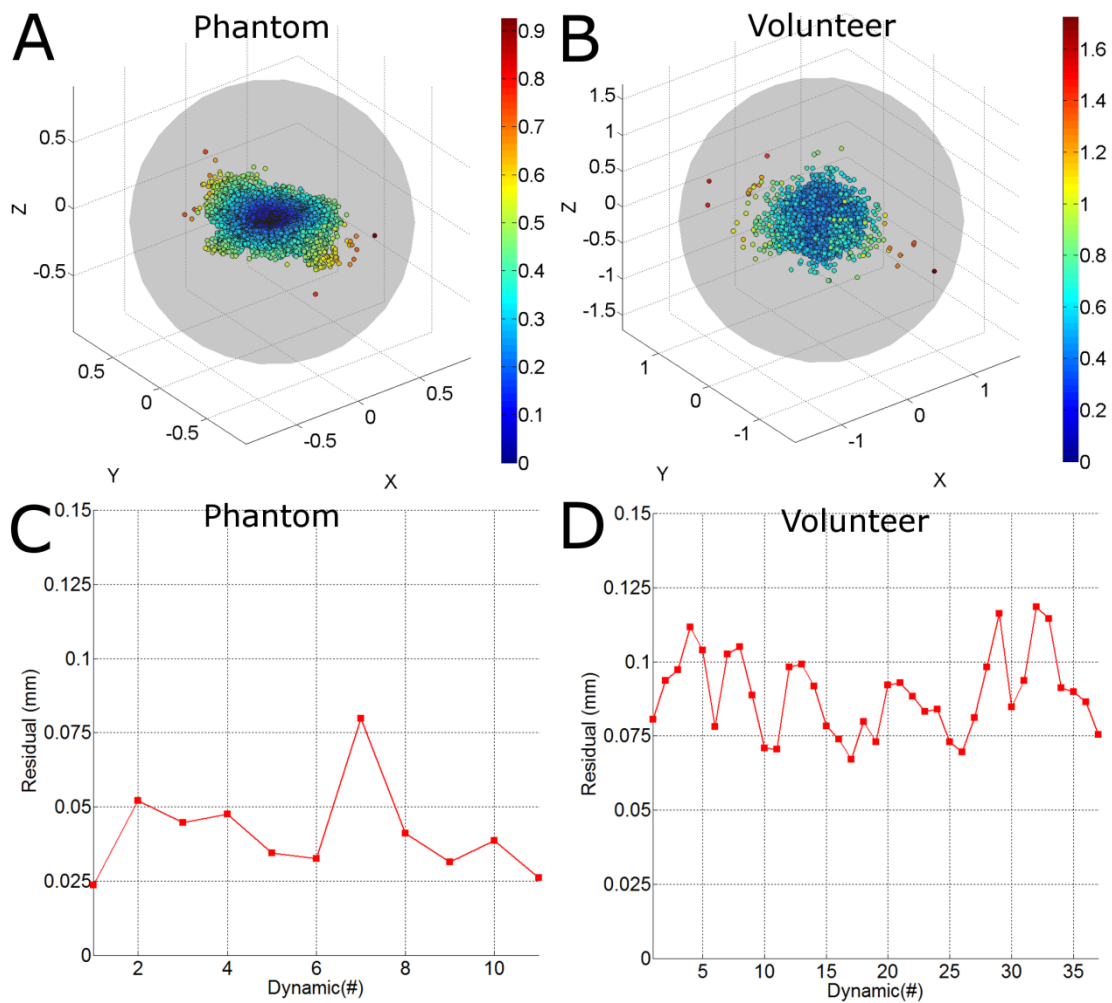


Figure 8.10 Tag point location difference scatter plots and circumspheres for all dynamics (A-B). Points shaded according to difference magnitude. In addition the means (dotted curve) and standard deviations (blocked curve) of the differences as a function of dynamic number (C-D). Images on the left are for the phantom and on the right are for the volunteer. All units are in mm.

### 8.3.2 Precision of individual dynamic displacement

For both the phantom and volunteer data a total of 36 individual displacement fields (Figure 8.11) were derived for each dynamic and compared to the mean individual displacement for each dynamic. For the phantom data the overall standard deviation for the displacement magnitude differences was 61  $\mu\text{m}$  (n=2567001). The largest difference found was 0.87 mm (outliers over 0.24 mm occurred in less than 1 % of cases). The standard deviation was 91  $\mu\text{m}$  for the volunteer data (n=1388343). The largest difference found was 1.44 mm (outliers over 0.29 mm occurred in less than 1 % of cases).

Similar to the tag-point precision results no relationship across dynamics was observed. In addition as the scatter plots and distributions in Figure 8.12 demonstrate, no relationship with displacement magnitude was observed as the standard deviation did not vary significantly with increasing displacements.

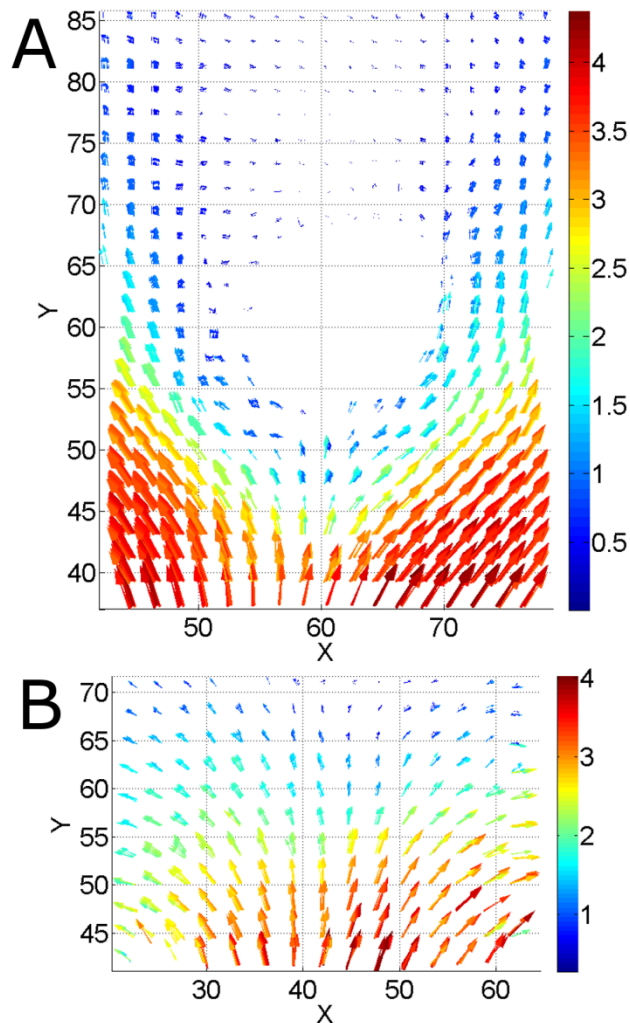


Figure 8.11 One of the individual displacement fields during the indentation phase for the phantom (A) and volunteer data (B). Displacement vectors are shown as arrows shaded towards magnitude. All units are in mm.

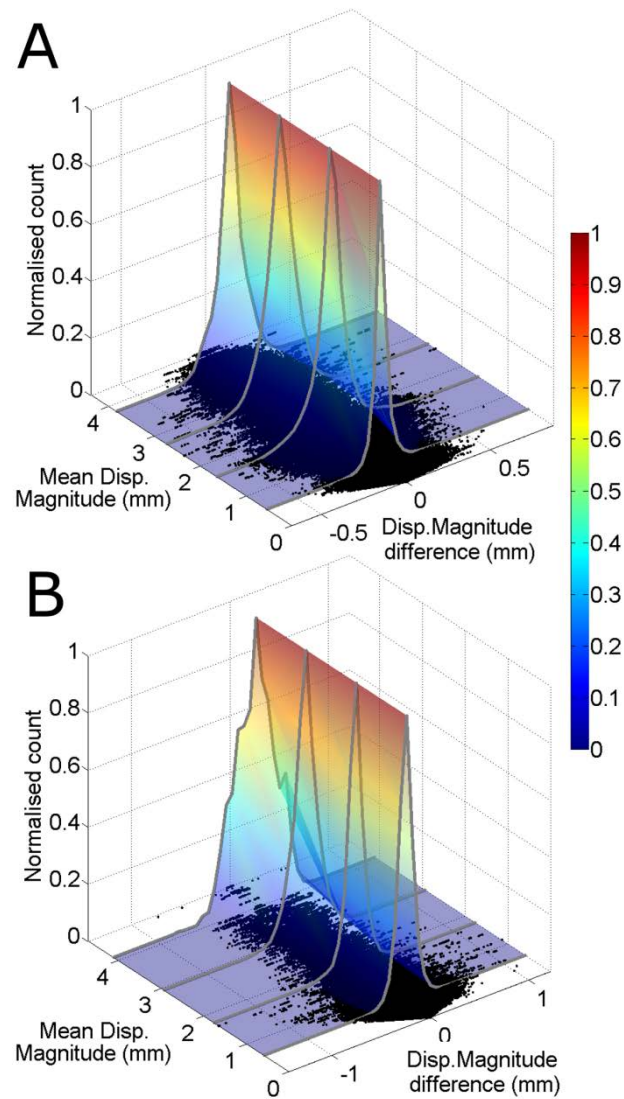


Figure 8.12 Normalized distributions (grey curves and shaded surface) of the displacement magnitude differences (for all combinations and all dynamics) as a function of the mean displacement magnitude for the phantom (A) and human volunteer data (B). The XY-planes of the graphs show scatter-plots (black dots) for all differences. All units are in mm.

### 8.3.3 Accuracy of cumulative dynamic displacement

Through analysis of the entire deformation cycle (indentation, hold and retraction phase) a complete cumulative displacement vector path could be reconstructed (Figure 8.13) for both the phantom and volunteer data. The complex nature of the deformation induced by the indentation is evident from the curved motion paths observed. For both the phantom and volunteer data sets the differences between the start and end locations of the motion paths were derived in order to calculate measures of accuracy of the cumulative displacement measurement. Figure 8.13D illustrates a selection of motions paths. For both the phantom and volunteer data it was found that differences were smallest for locations where displacement vectors maintain sufficient neighbours throughout all dynamics (such as region 1 in Figure 8.13D) while largest errors were

found at the periphery of the displacement field (e.g. region 2 Figure 8.13D) where natural neighbour interpolation used for computation of the cumulative displacement is more limited. Displacement vectors at the periphery were therefore not included in the further analysis. As is evident from the difference scatter plots in Figure 8.14 overall a good agreement was found with mean differences and standard deviations of 0.44 mm and 0.59 mm for the phantom (combination of 11 dynamics) and 0.40 mm and 0.73 mm for the human data (combination of 37 dynamics) respectively. As was mentioned in section 8.2.4.5 constraint free derivation of cumulative displacement may be sensitive to error propagation. Hence some large differences were found with maxima of 2.8 mm and 3.5 mm respectively for the phantom and volunteer data. As shown in Figure 8.15 no significant relationship with (cumulative) displacement magnitude was found and the mean of the differences did not vary significantly with displacement. However for the phantom the mean of the difference was lower for displacement magnitudes under 5 mm but remain constant for larger displacements.

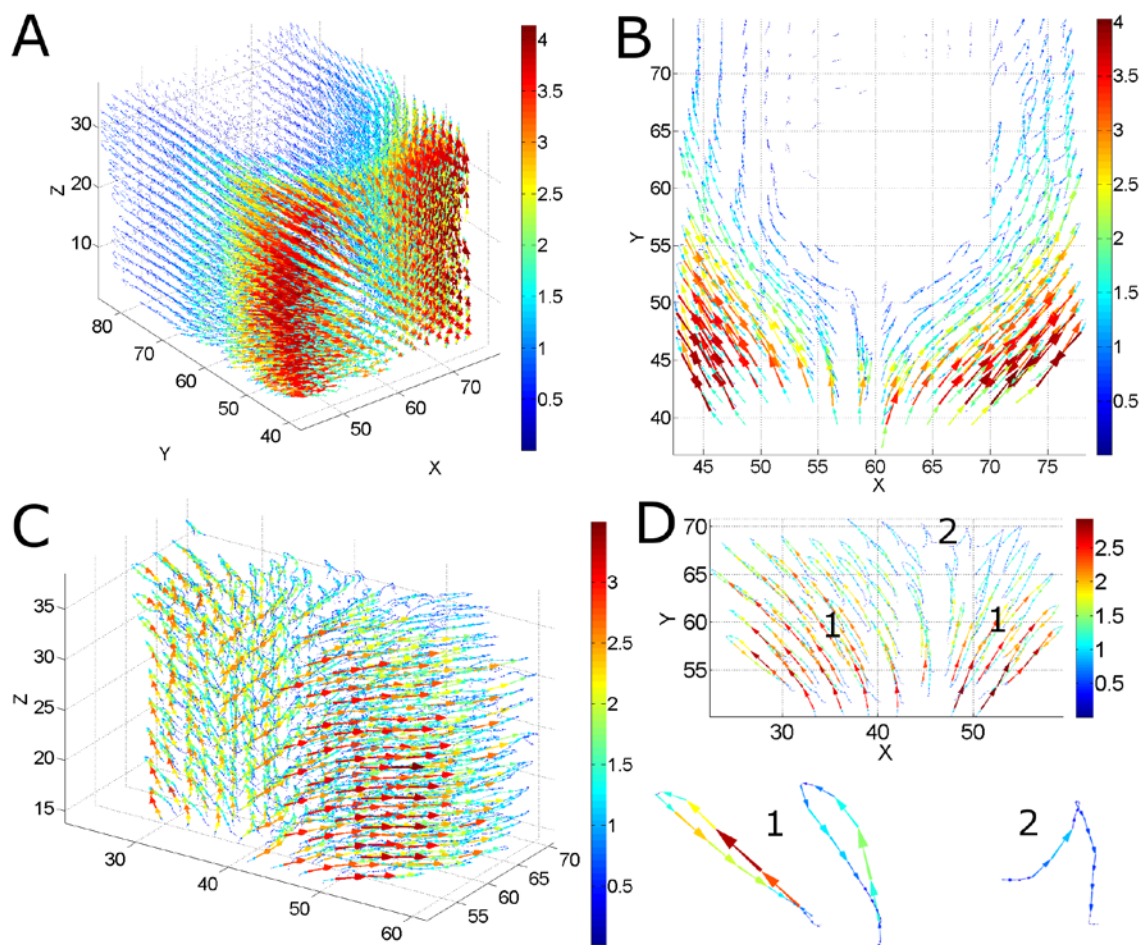


Figure 8.13 The cumulative displacement for the phantom (A-B) and volunteer data (C-D). Vector fields are shown and individual arrows shaded towards magnitude "Slice" views are shown in B and D. In addition a selection of motion paths are illustrated (bottom of D) to show results for locations embedded in (D-1) or on the edge of the displacement field (D-2). All units are in mm.

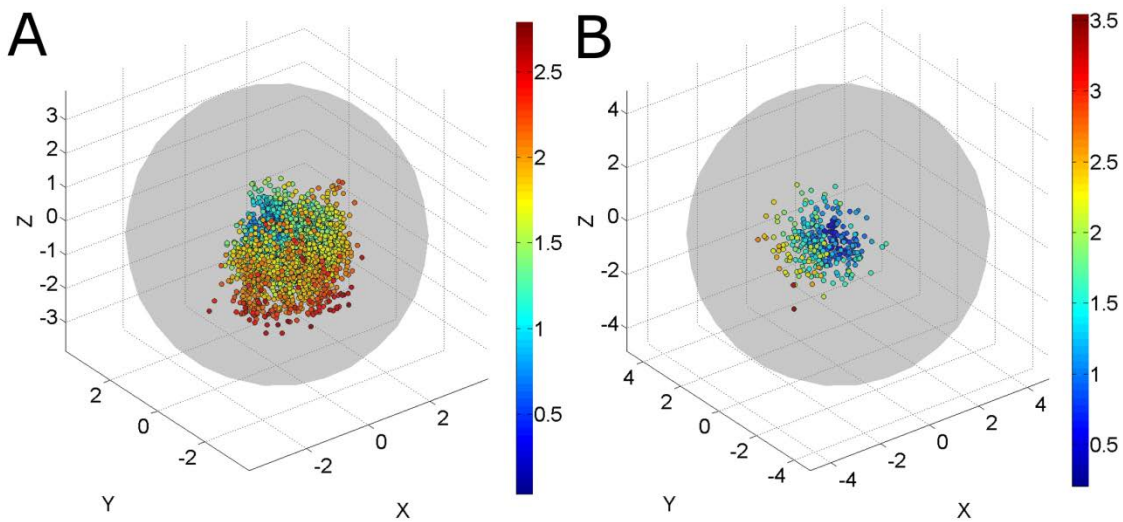
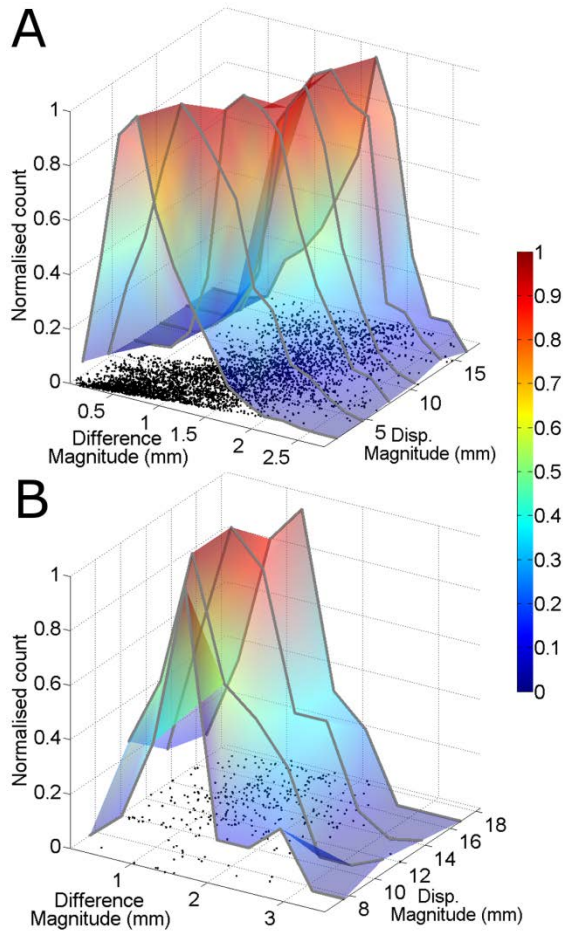


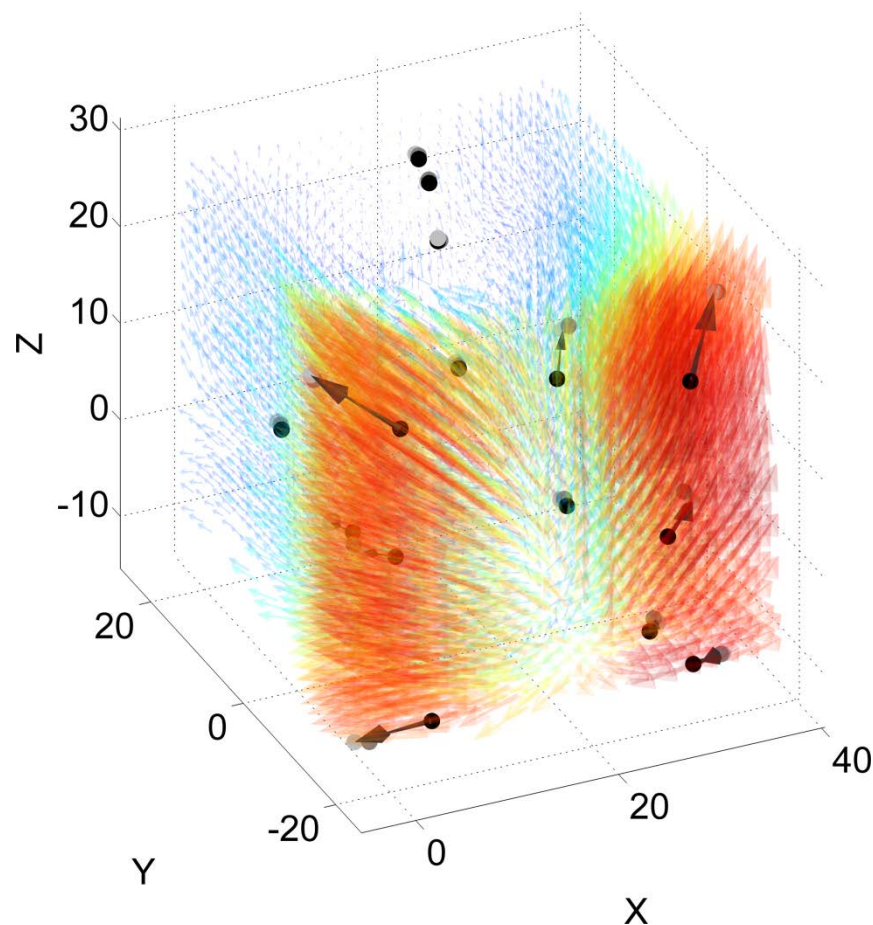
Figure 8.14 Scatter plots and their circumsphere for the cumulative displacement difference with respect to the initial for the phantom (A) and volunteer (B) data. Points are shaded according to difference magnitude. All units are in mm.



### 8.3.4 Accuracy of displacement in the phantom

Figure 8.16A shows the average cumulative displacement for the indentation part of the motion cycle and marker locations (n=15) within the field of view for the initial and final

deformed configuration. Using the average displacement field the marker locations in the deformed configuration were predicted (red in Figure 8.16A) and could be compared to the true independently measured locations. The difference between the predicted marker displacement and the actual marker displacement provides a measure of the accuracy of the displacement measurement. The differences showed a mean of 0.35 mm and a standard deviation of 0.63 mm (X,Y and Z RMS values were 0.59, 1.02 and 0.41 mm respectively). The difference demonstrated no relationship with displacement magnitude. The largest difference found was 2.65 mm for a marker close to the edge of the displacement field, where the interpolation based computation of the cumulative displacement and marker prediction is based on a relatively limited number of points.



## 8.4 Discussion

A novel SPAMM tagged MRI and fully automatic post-processing framework for the measurement of complex 3D dynamic soft tissue deformation following just three

repeated motion cycles was presented. The techniques presented demonstrate dynamic measurement of complex 3D soft tissue deformation at sub-voxel accuracy and precision and were validated for 3.3-3.6 Hz sampling of deformation speeds up to 12 mm/s.

A fully automatic post-processing framework is presented featuring the novel implementation of Gabor scale-space and filter bank assisted segmentation. In addition triangulated surfaces were fitted to the segmented tag extrema aided by Gabor filter bank derived estimates of local surface normal directions. Finally a dense grid (2x2x2 mm and 3x3x3 mm for the phantom and volunteer respectively) of tag points could be tracked following computation of tag surface triplet triangle intersections. Despite the fact that the post-processing methods are conceptually simple they are highly flexible as they enable tracking of tag features at any oblique orientation and undergoing complex deformations.

In the current study deformation is derived using 3 orthogonal SPAMM data sets and three repeated motion cycles only. This is a significant improvement over current methods involving many repetitions (e.g. in the order of 16 per slice<sup>50</sup>). Besides the reduction in scan time the presented methods have the potential to expand the application of SPAMM to the study of less periodic motions and motions which are (e.g. clinically) difficult to repeat. In this study the techniques are applied for indentation based biomechanical tissue investigation where the minimization to three motion cycles ensured volunteer comfort and avoided repeatability issues associated with tissue preconditioning.

The soft tissue deformation measurement techniques were validated against marker tracking in a silicone gel phantom and evaluated *in-vivo* for the upper arm. Sub-voxel accuracy and precision levels were found. Below a comparison to literature is presented however, comparison is challenging since deformation modes, speeds, magnitudes and validation measures vary considerably. Recently Chen et al. 2010<sup>219</sup> presented tagged MRI methods for cardiac deformation measurement whereby deformation was derived from the image data using Gabor filter banks, point matching and deformable models. Evaluation of their methods based a numerical phantom showed RMS displacement errors of 0.15~0.37 mm. Xu et al. 2010<sup>226</sup> derived deformation from tagged MRI using optical flow methods and presented evaluation of the methods using simulated deformations showing X, Y and Z direction RMS errors of 0.43 mm, 0.45 mm and 1 mm respectively. In our previous work <sup>238</sup> where a similar validation set-up was



used for static deformation measurement, comparison to marker tracking in a silicone gel phantom showed a mean difference of 72  $\mu\text{m}$  and a standard deviation of 0.29 mm. In addition displacement magnitude precision was analysed and the standard deviation for displacement differences with respect to overall mean displacement was 72  $\mu\text{m}$  for the phantom and 169  $\mu\text{m}$  *in-vivo*. The accuracy and precision levels presented in the current study are of a similar magnitude to those in the literature. For instance for the current study differences between true and predicted marker locations showed a mean of 0.35 mm and a standard deviation of 0.63 mm.

Since a major application of the work presented in this chapter is the non-invasive analysis of tissue mechanical properties a constraint free (no assumptions on the nature of the mechanical properties or deformation) methodology for the computation of cumulative displacement was employed. Methods for the derivation of cumulative displacement from individual displacement fields often involve deformable models<sup>219</sup> and are akin to non-rigid registration methods (e.g. related to deformable image registration and finite element analysis<sup>277</sup>). However these approaches require *a priori* knowledge and assumptions on the nature of the deformation and/or the mechanical properties of the tissue and were thus not of interest to the current study. In cases where the mechanical behaviour and deformation of tissue is well understood the implementation of these methods (combined with the individual displacement measurements presented) may provide an improvement on the accuracy achieved with the constraint free derivation of cumulative displacement presented here.

Some limitations need to be addressed. Due to the dynamic nature of the methods presented here motion occurring during the read-out is inevitable. This has a temporal averaging effect on the appearance of the tag features and as such may lead to underestimation of deformation. This effect is however deemed small especially given the presented results.

The current study presents the validation of the measurement of complex dynamic 3D soft tissue deformation for  $\sim 3.3$  Hz sampling of a 18 mm indentation (and retraction) at speeds of 12 mm/s leading to individual dynamic displacement magnitudes of up to 4 mm. Although the validation of higher speeds is not presented here the techniques are not limited to deformation speeds of 12 mm/s as the delay (which is user defined) and read-out (which depends on resolution but also scanner hardware) times can be adjusted for higher speeds e.g. to obtain similar displacements of 4mm in individual

dynamics. Hence the scanning protocol can be customized to the expected deformation speeds and magnitudes.

Since one of the future applications is musculoskeletal in nature the current study employs two flexible musculoskeletal coils and volunteer position constraints resulted in a suboptimal positioning at the edge of the bore. More advanced coil types and positioning may thus yield better results.

Currently three motion cycles are required for the computation of 3D deformation. Thus the methods presented are limited to the analysis of motion types which allow such repeatability reliably. For the application of computer controlled indentation presented such motions are easily and reliably repeated and synchronized using motion triggering. However un-triggered motion analysis of repeated motions can also be facilitated since temporal synchronization of the three SPAMM directions can be achieved in post-processing. Ideally however 3D deformation should be derivable from unrepeated motion. This would enable the imaging of non-periodic arbitrary motion (e.g. bowel motion<sup>267</sup>). Although non-segmented acquisitions of grid tagged volumes (simultaneous tag modulation tagging in 3 mutually orthogonal directions in a single image volume) is possible, the triple saturation pattern significantly reduces signal intensities hindering analysis of deformation at present.

Future work will focus on the combination of the current techniques with inverse finite element analysis for the analysis of the mechanical properties of human skeletal muscle tissue.

## 8.5 Conclusions

Novel SPAMM tagged MRI based methods are presented for high speed measurement of complex dynamic 3D soft tissue deformation following just 3 motion cycles. Deformation is derived using a novel and fully automatic Gabor filtering based post-processing framework. The techniques were validated using marker tracking in a silicone gel soft tissue phantom for indentation induced dynamic deformation measurement. In addition *in-vivo* evaluation for the measurement of indentation induced deformation of the biceps region of the upper arm was performed. The techniques presented demonstrate dynamic measurement of complex 3D soft tissue deformation at sub-voxel accuracy and precision and were validated for 3.3-3.6 Hz sampling of deformation speeds up to 12 mm/s. As

only 3 deformation cycles are required the techniques presented are to the authors' knowledge the fastest currently available for the derivation of 3D dynamic deformation. This allows for the expansion of the SPAMM tagged MRI based measurement of dynamic deformation to cases where motion is less repeatable or where large numbers of repetitions are not clinically feasible.

## STUDY VI

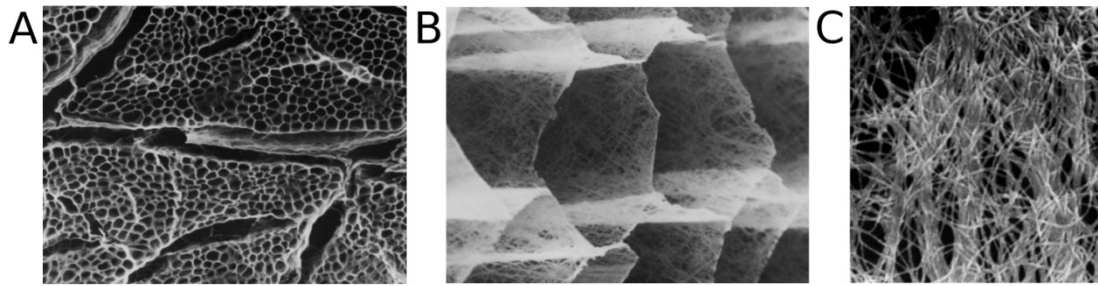
# Constitutive Modelling of Skeletal Muscle Tissue

## 8.6 Introduction

Section 3.2.2 of the Literature review highlighted that skeletal muscle contains a complex multi-layered collagen fibre arrangement which may relate to passive anisotropy of muscle tissue (see also Figure 8.17 modified from <sup>143</sup>). The passive mechanical properties of muscle tissue are thus not only a function of longitudinal connective tissue structures but also structures oblique to the fibre direction which are often not accounted for in constitutive modelling approaches.

Section 3.3 of the Literature review discussed that mostly the passive mechanical are represented as either isotropic or using single (longitudinal) fibre family reinforced transverse isotropy models. It was also discussed that these models are often only evaluated for longitudinal loading and sometimes also transverse loading. Using uni-axial testing at various load angles (0°, 30°, 45°, 60° and 90° were tested) for compression and tension respectively Van Looke *et al.* 2006 <sup>21</sup> and Takaza *et al.* (unpublished)<sup>22</sup> have shown that muscle tissue exhibits a complex anisotropic behaviour and also for intermediate load angles.

Since common constitutive modelling approaches have not been evaluated for performance for the intermediate load angles, in this study a multiple of constitutive models were implemented and evaluated for their suitability to model the non-linear elastic and anisotropic behaviour of muscle tissue in tension and compression. First the mechanical behaviour of muscle tissue is reviewed presenting visualisation of anisotropy landscapes, then constitutive models will be discussed followed by inverse FEA based constitutive parameter optimisation. In addition, motivated by the fact that both longitudinal and transverse connective tissue contributions are important to the overall passive mechanical properties, a novel constitutive law is proposed which accounts for multiple fibre orientations and transverse reinforcement.



## 8.7 Methods

Data processing and visualisation was performed using custom written MATLAB (7.8 R2009a The Mathworks Inc., Natick, MA) codes. In addition MATLAB based optimisation and iterative FEA control software was created. FEA was performed using the freely available software FEBio (open source version 1.3.0.1540, Musculoskeletal Research Laboratories, The University of Utah, USA).

### 8.7.1 *The anisotropic and non-linear elastic properties of muscle tissue*

As discussed in section 3.3.2 the anisotropic and non-linear elastic properties of skeletal muscle tissue were investigated for compression and tension by Van Looke *et al.* 2006<sup>21</sup> and Takaza *et al.* (unpublished)<sup>22</sup> respectively. Both authors subjected fresh porcine skeletal muscle tissue samples to uni-axial unconfined quasi-static loading (strain rate  $0.05\% \text{ s}^{-1}$ ) for load angles of  $\alpha=0^\circ$  (fibre direction),  $30^\circ$ ,  $45^\circ$ ,  $60^\circ$  and  $90^\circ$  (cross-fibre direction), with respect to the fibre direction. A schematic representation of the used loading configuration which will also aid discussion of constitutive modelling is shown in Figure 8.18. The muscle fibre direction, also termed the longitudinal direction, is defined by the vector  $\mathbf{a}_3$  oriented at an angle  $\alpha$  with respect to the loading axis  $\mathbf{e}_3$ . The transverse direction is defined by the plane described by  $\mathbf{a}_1$  and  $\mathbf{a}_2$ .

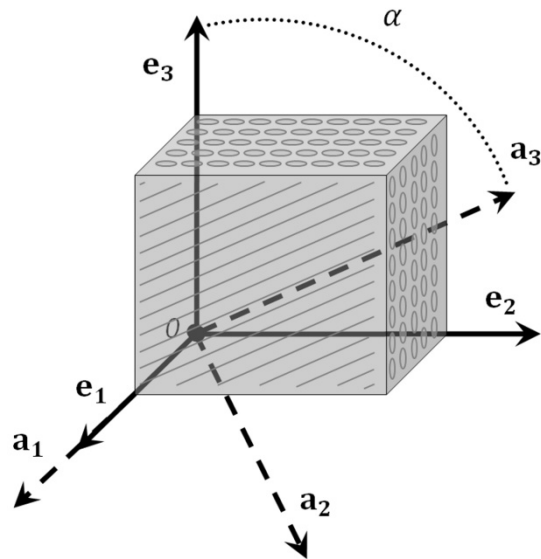
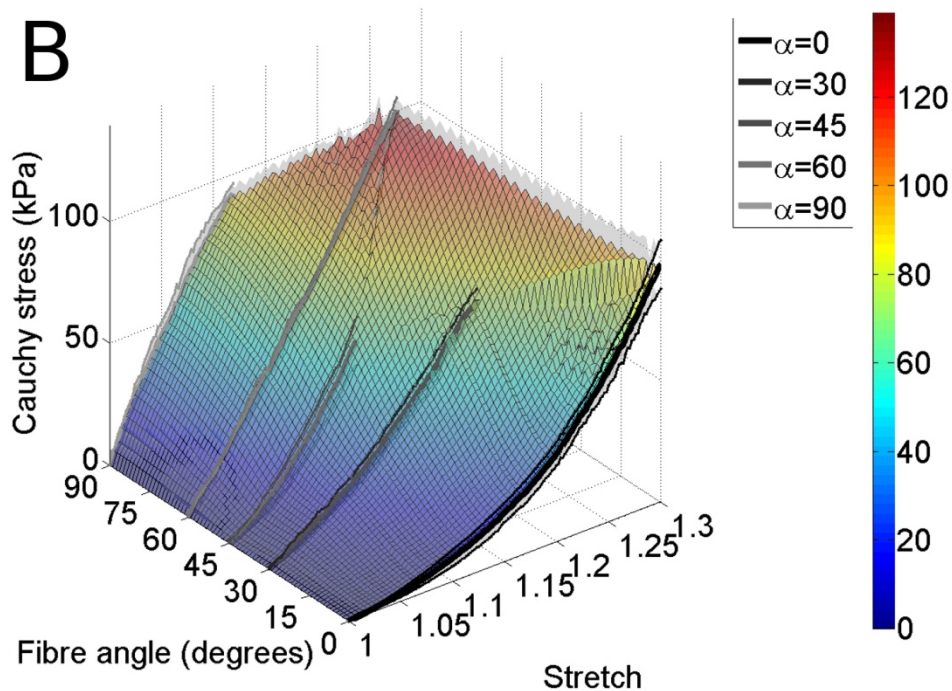
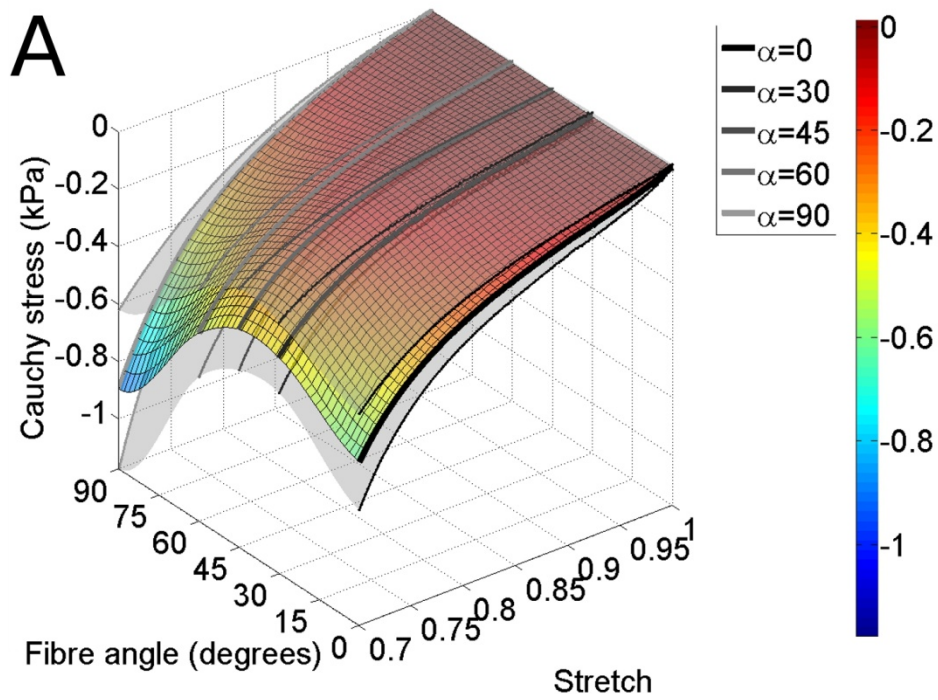


Figure 8.18. Schematic representation of a cuboid sample showing muscle fibre direction  $\mathbf{a}_3$  at an angle  $\alpha$  with respect to the loading axis  $\mathbf{e}_3$

In section 3.3.2 the quasi-static compression and tension test curves were discussed (see Figure 3.10 and Figure 3.15 respectively). Since the anisotropic behaviour is a function of both stretch and load orientation it can be represented by a surface. Hence to visualise the anisotropic behaviour more clearly periodic surface fits to the quasi-static load curves are shown in Figure 8.19. The complex anisotropic behaviour is now more clearly visible. Figure 8.20 shows the same surfaces except now the stresses have been normalised to the fibre direction loading response. Under the assumption of transverse isotropy these surfaces are periodic with load angle e.g. in the sense that the anisotropic response for loading at  $45^\circ$  is equivalent to that of  $-45^\circ$ .

For compression (Figure 8.19A and Figure 8.20A), a relative softening behaviour is observed for loading at angles between  $0^\circ$ - $90^\circ$  with an apparent minimum around  $45^\circ$ . Figure 8.20A shows that the fibre and cross-fibre directions are initially similar and that the cross-fibre direction gradually becomes stiffer in relation to the fibre direction. The intermediate angle softening is maintained across the loads tested (up to 30% compression) however this effect appears to reduce with increasing load. Geometrically this may be explainable by a gradual rotation of the fibres with respect the load axis since increasing levels of compression cause the fibres to become more orthogonal to the load axis, and thus more loaded in tension.

For tension (Figure 8.19B and Figure 8.20B), as the load angle is rotated from the fibre direction the response becomes gradually stiffer and more linear. The relative difference effect appears to decrease with increasing load as the fibre direction is more non-linear and increases in stiffness with load.

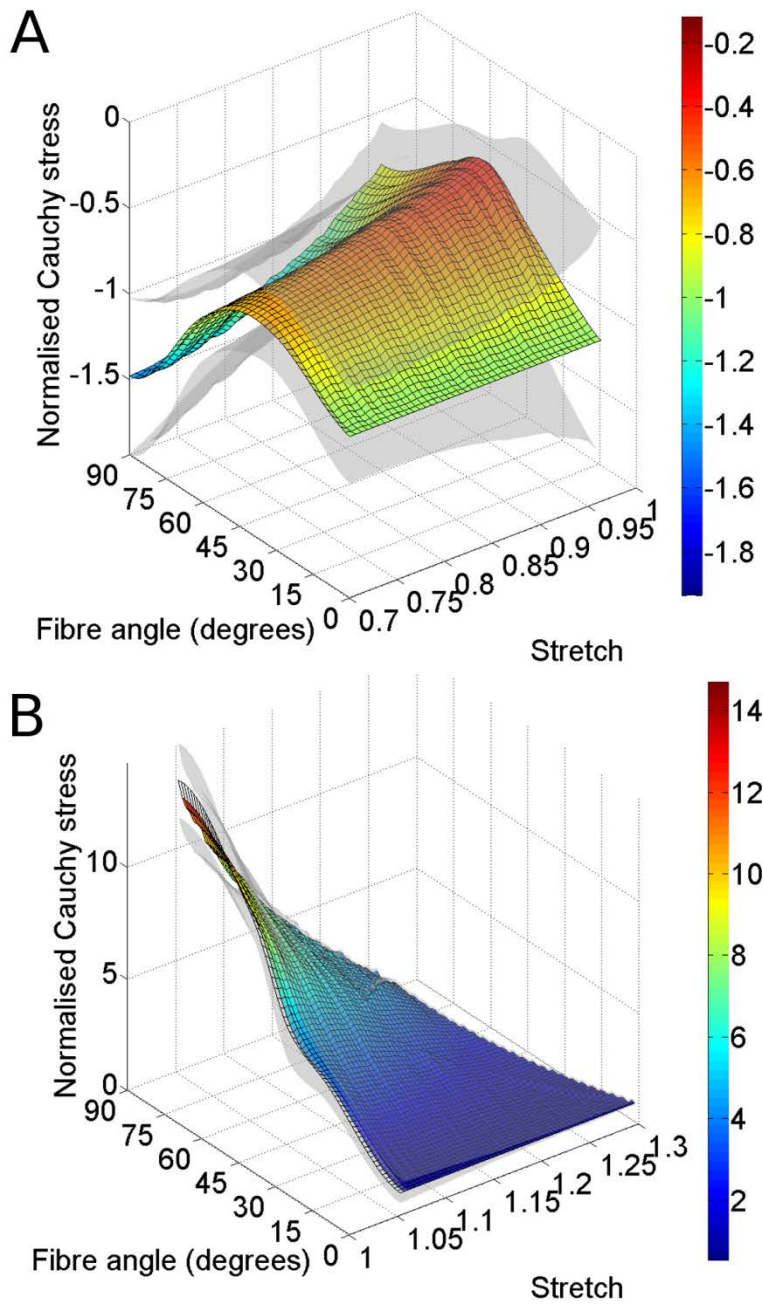


It appears that the stress response for compression and tension is dramatically different as the tensile response appears more than two orders of magnitude higher for all loading directions. The term tension-compression non-linearity refers to materials exhibiting differences in behaviour for the two loading types. However this generally refers to deviations along a certain loading direction. For instance for tension or compression of muscle along the fibre direction one could model the stiffer response in tension due to



fibre extension and the softer response in compression due to fibre buckling. Having assumed such an approach the tension only fibres would however have the same mechanical properties irrespective of how that tension was induced. For instance compression induced tensile volumetric deformation. According to the Poisson's ratios derived by Van Loocke *et al.* 2006 <sup>21</sup> (see section 3.3.2.1 ) a transverse compressive stretch of 0.7 would induce a fibre direction stretch of almost 1.14. For continuum mechanical models assuming fibre reinforcement the magnitude of the associated stress contribution is however equivalent irrespective of whether it was a "direct" tension or Poisson's effect induced tension. Hence modelling approaches assuming tension only fibres do not eliminate this type of linked tension compression behaviour. Instead such models would only present with tension compression non-linearity due to the geometric nature of the loading, i.e. along fibre stretch of 1.3 is associated with a fibre stretch of 1.3 while transverse compression at a stretch of 0.7 induces a tensile fibre stretch of 1.14.

Assuming the experimental data are accurate and can complement each other it would appear that muscle tissue presents with a "volumetric" type of tension-compression non-linearity. The nature of this effect in relation to the fibrous connective tissue and matrix components are not known. In the current study phenomenological models are formulated and an approach is proposed to allow the material parameters to vary depending on mode of loading: tension or compression.



### 8.7.2 Constitutive modelling of non-linear elasticity

In this study the following hyperelastic constitutive modelling approaches were evaluated using inverse FEA based fitting to the experimental tension and compression data discussed in the previous section: 1) *Isotropic Ogden hyperelastic (ISO)*, 2) *Fibre reinforced transversely isotropic Ogden hyperelastic (TISO)*, 3) *Tension compression non-linear orthotropic Ogden hyperelastic (TCNL)*, 4) *Ellipsoidal fibre distribution Ogden hyperelastic*

(EFD) and finally a novel constitutive formulation the 5) *Gaussian Modulated Spherical Fibre Distribution Ogden hyperelastic (GMSFD)*.

The isotropic and ground matrix responses were all equivalently modelled using the following decoupled first order Ogden hyperelastic formulation:

$$\Psi_{\text{iso}}(\tilde{\mathbf{C}}, J) = \Psi_{\text{dev\_iso}}(\tilde{\mathbf{C}}) + \Psi_{\text{vol\_iso}}(J) \quad 8-13$$

Here  $\Psi_{\text{dev\_iso}}$  and  $\Psi_{\text{vol\_iso}}$  represent the deviatoric and volumetric isotropic response respectively ( $\tilde{\mathbf{C}} = \tilde{\mathbf{F}}^T \tilde{\mathbf{F}}$  the deviatoric right Cauchy Green Tensor, such that  $\det(\tilde{\mathbf{C}}) = 1$  and  $\mathbf{F} = J^{\frac{1}{3}} \tilde{\mathbf{F}}$  the deformation gradient tensor, see section 2.2.10.3 ). Due to the near incompressibility of muscle tissue (reported for instance in <sup>21, 22</sup>) the volume ratio or the Jacobian  $J = \det(\mathbf{F}) \approx 1$ . The isotropic and ground matrix deviatoric contribution is defined by:

$$\begin{aligned} \Psi_{\text{dev\_iso}}(\tilde{\mathbf{C}}) &= \Psi_{\text{dev\_iso}}(\tilde{\lambda}_1, \tilde{\lambda}_2, \tilde{\lambda}_3) = \frac{\mu}{\alpha} (\tilde{\lambda}_1^\alpha + \tilde{\lambda}_2^\alpha + \tilde{\lambda}_3^\alpha - 3) \\ \Psi_{\text{vol\_iso}}(J) &= \frac{1}{2} \kappa (\ln(J))^2 \end{aligned} \quad 8-14$$

with  $\mu$  and  $\alpha$  the Ogden model material parameters,  $\kappa$  the bulk modulus and  $\tilde{\lambda}_i = J^{-\frac{1}{3}} \lambda_i$  the deviatoric principal stretches. A non-linear ground matrix formulation was implemented (rather than the more linear Mooney-Rivlin type formulations often implemented) since for compression in the fibre direction (for which theoretically fibres are buckling and thus the response is solely due to the ground matrix) the behaviour is significantly non-linear. Obviously this isotropic formulation may only capture the average response and large deviations may occur depending on the degree of anisotropy. These were also quantified for this model.

For the anisotropic formulations implemented the following strain energy function form is used:

$$\Psi(\mathbf{a}, \tilde{\mathbf{C}}, J) = \Psi_{\text{iso}}(\tilde{\mathbf{C}}, J) + \Psi_f(\mathbf{a}, \tilde{\mathbf{C}}) \quad 8-15$$

where  $\Psi_{\text{iso}}(\tilde{\mathbf{C}}, J)$  defines the isotropic ground matrix response (equation 8-14) and anisotropy is introduced through the addition of a fibre strain energy term  $\Psi_f(\mathbf{a}, \tilde{\mathbf{C}})$ . The latter is a function of the global (muscle) fibre direction specified by the vector  $\mathbf{a}$  and  $\tilde{\mathbf{C}}$ . The fibre direction vector  $\mathbf{a}$  is analogous to  $\mathbf{a}_3$  in Figure 8.18.

A common method for modelling transverse isotropy is to superimpose a single reinforcing fibre family onto the ground matrix response. For the current study such a model was evaluated in the form of a single fibre family reinforced transversely isotropic

Ogden hyperelastic (TISO). The following fibre strain energy term  $\Psi_f(\mathbf{a}, \tilde{\mathbf{C}}) = \Psi_f(\tilde{\lambda}_f)$  was implemented:

$$\Psi_f(\tilde{\lambda}_f) = \begin{cases} c_1 (e^{c_2(\tilde{\lambda}_f^{-1})} - 1) & \tilde{\lambda}_f > 1 \\ 0 & \tilde{\lambda}_f \leq 1 \end{cases} \quad 8-16$$

where  $c_1$  and  $c_2$  are material parameters and  $\tilde{\lambda}_f = \sqrt{\mathbf{a} \cdot \tilde{\mathbf{C}} \mathbf{a}}$  is the deviatoric fibre stretch. Since for this type of model fibres only contribute for tensile fibre stretch this formulation thus introduces a degree of tension compression non-linearity. Geometrically the single fibre family used in this modelling approach describes a single periodic function with load angle. Since the fibre family can only add to the response of the ground matrix and is minimal for along fibre compression (i.e. zero) it cannot capture the intermediate angle softening observed by Van Looke *et al.* 2006<sup>21</sup>. Instead it will predict a gradually increasing contribution for rotation from perpendicular to parallel tensile loading. In addition the fact that the fibre family reinforces the material along the axis of transverse isotropy rather than orthogonal to it, this modelling approach cannot be used to model the tensile data by Takaza *et al.* (unpublished)<sup>22</sup>. Therefore the model is only presented for modelling in compression.

A more complex model featuring 3 initially mutually orthogonal fibre families is the tension compression non-linear orthotropic which Ateshian *et al.* 2007<sup>65</sup> introduced in combination with a Mooney-Rivlin ground matrix. However here, as discussed an Ogden ground matrix is implemented. The fibre strain energy  $\Psi_f(\mathbf{a}_1, \mathbf{a}_2, \mathbf{a}_3, \tilde{\mathbf{C}})$  which is a function of three orthonormal texture directions  $\mathbf{a}_i$ , takes the form:

$$\Psi_f(\mathbf{a}_1, \mathbf{a}_2, \mathbf{a}_3, \tilde{\mathbf{C}}) = \sum_{i=1}^3 \Psi_{fs}(\mathbf{a}_i, \tilde{\mathbf{C}}) \quad 8-17$$

where

$$\Psi_{fs}(\tilde{\lambda}_{f_i}) = \begin{cases} \xi_i (\tilde{\lambda}_{f_i}^2 - 1)^{\beta_i} & \tilde{\lambda}_{f_i} > 1 \\ 0 & \tilde{\lambda}_{f_i} \leq 1 \end{cases} \quad 8-18$$

$$\xi_i \geq 0, \beta_i \geq 2$$

with  $\xi_i$  and  $\beta_i$  triplets of material parameters and  $\tilde{\lambda}_{f_i} = \sqrt{\mathbf{a}_i \cdot \tilde{\mathbf{C}} \mathbf{a}_i}$ . For the current study the parameters are constrained as:

$$\xi_1 = \xi_2 = \xi_T, \xi_3 = \xi_L \text{ and } \beta_1 = \beta_2 = \beta_3 = \beta \quad 8-19$$

Since the fibre triplet only acts in tension it is clear that this model may enable modelling of more complex anisotropy. For instance, recalling Figure 8.18, for uni-axial compressive loading in the fibre direction  $\mathbf{a}_3$  the fibres along  $\mathbf{a}_3$  buckle and do not contribute while the fibres along  $\mathbf{a}_1$  and  $\mathbf{a}_2$  are both loaded in tension due to the Poisson's effect induced expansion. However at  $45^\circ$  to the fibre direction both  $\mathbf{a}_2$  and  $\mathbf{a}_3$  initially buckle (while  $\mathbf{a}_1$  is still loaded in tension) hence this geometric and tension-compression non-linear effect allows one to model softening for intermediate angles. However this effect also highlights that since the model only contains three orthotropic tension compression non-linear fibres it does not reduce to a transversely isotropic model even under the constraints 8-19 (e.g. the transverse loading response should be invariant to rotation around the axis of transverse isotropy, however for this model in transverse compression initially the largest response is obtained when loading is orthogonal to either  $\mathbf{a}_1$  or  $\mathbf{a}_2$  and lowest when loading is  $45^\circ$  to both  $\mathbf{a}_1$  and  $\mathbf{a}_2$ ). Hence the model is only used here to illustrate that more complex anisotropic behaviour can be introduced through the implementation of multiple tension compression non-linear fibre families and that geometrically the buckling leads to softening.

A multiple fibre direction modelling approach which does reduce to transverse isotropy under the appropriate constraints are the models based on spherical fibre distributions. For instance Atheshian *et al.* 2009<sup>64</sup> proposed a model termed the ellipsoidal fibre distribution (EFD) Mooney-Rivlin. For the implementation used here the Mooney-Rivlin ground-matrix was again replaced by the Ogden form. The model contains spherically distributed fibres whose contributions follow an ellipsoidal form, whereby the constitutive parameters for each fibre are driven by an ellipsoidal function defined by its three axes. A spherically distributed set of fibres  $\mathbf{n}_i$  is introduced which are formulated in the local orthonormal basis  $\mathcal{A} = \{\mathbf{a}_1, \mathbf{a}_2, \mathbf{a}_3\}$  defined by the local texture directions relative to the global orthonormal basis  $\mathcal{E} = \{\mathbf{e}_1, \mathbf{e}_2, \mathbf{e}_3\}$ . In an associated spherical coordinate system with angles  $(\Theta, \Phi)$  the fibre vectors  $\mathbf{n}_i$  can be represented as:

$$\mathbf{n}_i = \cos(\Theta_i) \sin(\Phi_i) \mathbf{a}_1 + \sin(\Theta_i) \sin(\Phi_i) \mathbf{a}_2 + \cos(\Phi_i) \mathbf{a}_3 \quad 8-20$$

The strain energy for a single fibre  $\Psi_{f_i}$  is defined as:

$$\Psi_{f_i}(\mathbf{n}_i, \tilde{\mathbf{C}}) = \begin{cases} \xi(\mathbf{n}_i) (\tilde{\lambda}_{f_i}^2 - 1)^{\beta(\mathbf{n}_i)} & \tilde{\lambda}_{f_i} > 1 \\ 0 & \tilde{\lambda}_{f_i} \leq 1 \end{cases} \quad 8-21$$

$$\beta \geq 2$$

here  $\tilde{\lambda}_{f_i} = \sqrt{\mathbf{n}_i \cdot \tilde{\mathbf{C}}\mathbf{n}_i}$  is the stretch along the fibre direction  $\mathbf{n}_i$ . The parameter  $\xi(\mathbf{n}_i)$  and  $\beta(\mathbf{n}_i)$  vary with fibre orientation according to the ellipsoidal function:

$$\begin{aligned}\xi(\mathbf{n}_i) &= \left( \frac{\cos(\Theta_i)^2 \sin(\Phi_i)^2}{\xi_1^2} + \frac{\sin(\Theta_i)^2 \sin(\Phi_i)^2}{\xi_2^2} + \frac{\cos(\Phi_i)^2}{\xi_3^2} \right)^{-\frac{1}{2}} \\ \beta(\mathbf{n}_i) &= \left( \frac{\cos(\Theta_i)^2 \sin(\Phi_i)^2}{\beta_1^2} + \frac{\sin(\Theta_i)^2 \sin(\Phi_i)^2}{\beta_2^2} + \frac{\cos(\Phi_i)^2}{\beta_3^2} \right)^{-\frac{1}{2}}\end{aligned}\tag{8-22}$$

This model was implemented using the transversely isotropic constraints:

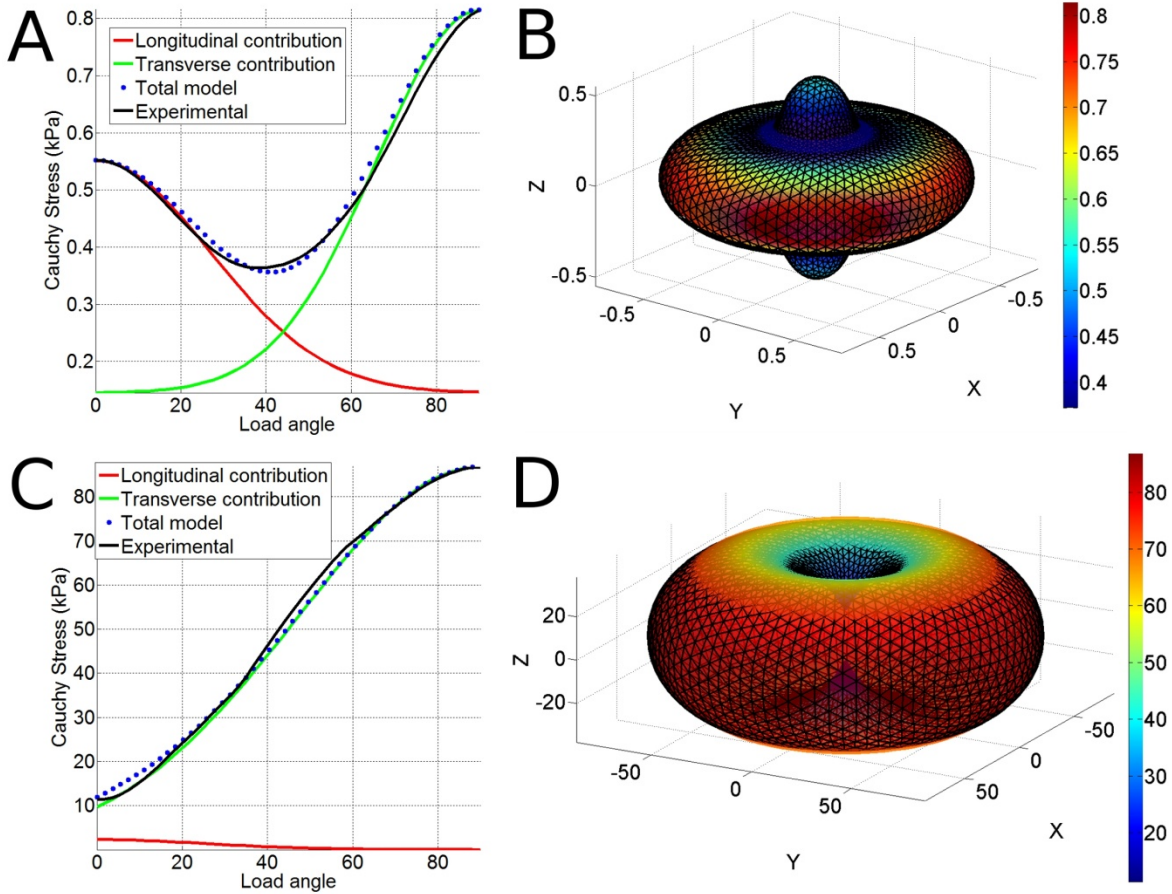
$$\xi_1 = \xi_2 = \xi_T, \xi_3 = \xi_L \text{ and } \beta_1 = \beta_2 = \beta_T, \beta_3 = \beta_L\tag{8-23}$$

Due to the spherical fibre distribution despite the fact that fibres only contribute in fibre-tension (conversely to single fibre family reinforced transversely isotropic models) no compressive loading directions exists in which none of fibres contribute. In addition due to the presence of fibres at intermediate angles to the transverse and longitudinal directions (whose mechanical parameters are mapped in an ellipsoidal fashion and are thus intermediate rather than lower) this model is unlikely to be able to capture the intermediate softening found by Van Loocke *et al.* 2006<sup>21</sup>.

The above existing constitutive modelling approaches all inherently lack the ability to model the complex anisotropic behaviour of skeletal muscle tissue appropriately. Therefore a new model is proposed based on spherical fibre distributions but rather than an ellipsoidal mapping as described by Atheshian *et al.* 2009<sup>64</sup>, the constitutive parameters are a function of the summed Gaussian modulated behaviour for longitudinal and transverse fibrous contributions.

Since muscle tissue presents with a complex connective tissue arrangement with fibrous structures orientated not only along but also orthogonal to the muscle fibre direction (see also section 3.2). Under the assumption of transverse isotropy (with respect to the main muscle fibre direction) any reinforcing structure, whether parallel or oblique to the fibre axis, presents with a periodic reinforcing behaviour under rotation of load angle (with respect to the main muscle fibre direction). For instance longitudinal fibrous structures capable of resisting tension act most in longitudinal extension and least in cross-fibre extension where the structures buckle due to the Poisson's effect induced compression. Conversely transverse fibrous structures which are capable of resisting tension act most in transverse extension and least in longitudinal extension. Hence it was postulated that the complex transversely isotropic behaviour is

decomposable into the sum of periodic fibre reinforcing functions. It was assumed that such behaviour can be modelled by appropriate adjustment or modulation of the contribution of a spherically distributed set of tensile reinforcing fibres. Further it was assumed that for each fibre direction within this set the response can be modelled as the summed Gaussian weighted effect of a longitudinal and transverse contribution. These assumptions are motivated by the fibrous architecture of muscle tissue which is composed of multitude of orientations (see section 3.2.2 ) and the experimental stress-stretch data. Figure 8.21A-C shows the final stresses (for tension up to a stretch of 1.12 since this is where all curves exist) as a function of angle for both tension and compression experimental data. Recall that  $0^\circ$  represents the muscle fibre direction and  $90^\circ$  the transverse direction. As Figure 8.21A shows, the final stresses (black curve) are highest for transverse compression and the minima around  $45^\circ$  is clearly visible. In addition shown as red and green curves are two Gaussian functions one centred at  $0^\circ$ , the other at  $90^\circ$  which represent longitudinal and transverse contributions respectively. As the blue dotted curve in Figure 8.21A shows, which represents the sum of the two contributions, the experimental final stress relationship with angle can be approximately represented by the sum of two Gaussian functions. Figure 8.21B shows the same data except for now transverse isotropy is assumed around the z-axis, the load angle is the positive angle with the Z-axis and the radius of the shape is the final stress. The same is shown for tension in Figure 8.21C-D. For both tension and compression the transverse direction loading produces the most dominant response and it is clear from Figure 8.21B-D that in both cases the final stresses do not describe an ellipsoidal shape under the assumption of transverse isotropy. For compression the shape appears more like the sum of two approximate ellipsoidal functions which supports the summed contributions approach proposed here. For tension the shape is more like a torus due to the predominant nature of the transverse contribution. For both shapes the wireframe overlain in Figure 8.21B-D represents the double Gaussian modulated fit (equivalent to blue dots). This supports the hypothesis that a model implementing summed Gaussian weighted contributions of the transverse and longitudinal direction can be used to model the complex anisotropic behaviour observed. This constitutive modelling approach is purely phenomenological. However a physical interpretation of the Gaussian decay functions with angle may be possible following histological investigation. For instance it may represent density or stiffness changes of the fibres with angle.



The novel modelling approach, termed Gaussian Modulated Spherical Fibre Distribution Ogden hyperelastic (GMSFD) is based on the FEBio implementation of the ellipsoidal fibre distribution models. The strain energy for a single fibre  $\Psi_{f_i}$  was defined as:

$$\Psi_{f_i}(\mathbf{n}_i, \tilde{\mathbf{C}}) = \begin{cases} \xi(\mathbf{n}_i) (\tilde{\lambda}_{f_i}^2 - 1)^\beta & \tilde{\lambda}_{f_i} > 1 \\ 0 & \tilde{\lambda}_{f_i} \leq 1 \end{cases} \quad 8-24$$

$$\beta \geq 2$$

here  $\beta$  is a (homogeneous) material parameter and  $\tilde{\lambda}_{f_i} = \sqrt{\mathbf{n}_i \cdot \tilde{\mathbf{C}} \mathbf{n}_i}$  is the stretch along the fibre direction  $\mathbf{n}_i$ . The parameter  $\xi(\mathbf{n}_i)$  varies with fibre orientation and, rather than an ellipsoidal mapping as described by Atheshian *et al.* 2009<sup>64</sup>, is a function of the summed Gaussian modulated behaviour for longitudinal and transverse fibrous contributions:



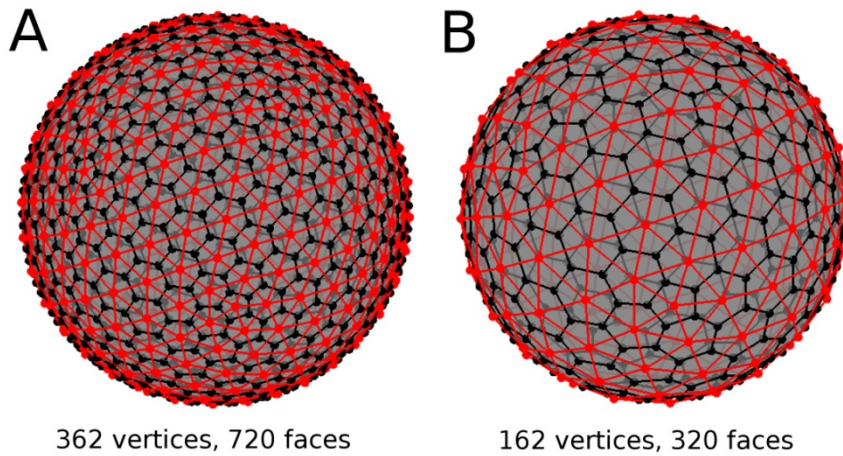
$$\xi(\mathbf{n}_i) = \xi_L e^{\left(\frac{-\gamma(\mathbf{n}_i)^2}{2\zeta_L^2}\right)} + \xi_T e^{\left(\frac{-(\gamma(\mathbf{n}_i)-\pi/2)^2}{2\zeta_T^2}\right)} \quad 8-25$$

where  $\xi_L$  and  $\xi_T$  are material parameters representing the longitudinal and transverse direction respectively. The variable  $\gamma(\mathbf{n}_i)$  is the angle (in the range  $(0, \frac{\pi}{2})$ ) of the fibre  $\mathbf{n}_i$  with respect to the longitudinal direction (e.g. if  $\mathbf{a}_3$  represents the global muscle fibre direction then  $\gamma(\mathbf{n}_i) = \text{acos}(|n_{i3}|)$ ). The amplitude of the Gaussian functions are  $\xi_L$  and  $\xi_T$ . The extent of the contribution of the longitudinal and transverse fibrous structures with respect to angle is dictated by  $\zeta_L$  and  $\zeta_T$  which define longitudinal and transverse standard deviations respectively (the limit  $\zeta_L = \zeta_T = \infty$  results in isotropic symmetry with  $\xi(\mathbf{n}_i) = \xi = \xi_L + \xi_T$ ).

The following implementation was used for both the EFD and GMSFD models. For a continuous distribution of spherically oriented fibres the total contribution can be derived through integration across the sphere. For computational efficiency this integration is performed numerically (see also <sup>64</sup>) for a discrete set of fibres. An approximate geodesic tessellation of the unit sphere was created by sub-triangulating the icosahedron 5 times (subdividing triangles into 4 sub-triangles and introducing 3 new vertices with each iteration) leading to 720 triangles and 362 vertices (see Figure 8.22A). A total of  $m = 362$  fibres are defined running from the centre of the sphere to each of the vertices of the triangulation (red vertices/edges in Figure 8.22A). Each fibre ‘‘acts’’ on the faces (hexagons and pentagons) of the triangulations dual polyhedron, a Buckminster Fuller dome (black vertices/edges in Figure 8.22A). The total fibre strain energy contribution  $\Psi_f$  can be derived through numerical integration using<sup>64</sup>:

$$\Psi_f \approx \sum_{i=1}^m \Psi_{f_i}(\mathbf{n}_i, \tilde{\mathbf{C}}) \Delta A_i \quad 8-26$$

where  $\Delta A_i$  represents the surface area of the dual polyhedron area element at fibre  $i$ .



This implemented tessellation differs from the standard FEBio implementation (open source version 1.3.0.1540) for ellipsoidal fibre distribution models (Figure 8.22B). For such models (e.g. <sup>64</sup>) implemented in FEBio the numerical integration occurs using fibres defined on the vertices of the Buckminster Fuller dome acting on the triangular faces (rather than the other way around as used here). Although this leads to more homogeneous surface area elements for the tessellation of the sphere (all triangles rather than pentagons and hexagons) it has a less homogeneous fibre distribution (i.e. the black vertices in Figure 8.22 are less evenly spaced than the red vertices). The standard implementation in FEBio is a Buckminster Fuller dome with 320 vertices (black points in Figure 8.22B) with fibres acting on the faces of its dual polyhedron, a 3<sup>rd</sup> order sub-triangulation of the icosahedron containing 320 triangles and 162 vertices (a higher resolution triangulation is also an option in FEBio, however integration across its 1280 triangles computationally intensive). Since for a polyhedron with  $m$  faces and  $n$  vertices its dual polyhedron has  $n$  faces and  $m$  vertices, a denser tessellation (720 triangles as opposed to 320) could be used while the number of fibres implemented (defined on triangle vertices rather than triangle centres) remained similar (362 compared to 320) thus resulting in comparable computational efficiency. In addition the icosahedron used for the sub-triangulation based construction of the geodesic triangulations was oriented such that the resulting fibre family always includes fibres aligned with the local orthonormal basis  $\mathcal{A}$ .

### 8.7.3 *Modelling of volumetric tension compression non-linearity*

For a true incompressible material the Jacobian  $J = \det(\mathbf{F}) = 1$ . However in the current study the FEA implementations require uncoupled constitutive equations whereby the stresses are split into deviatoric (volume preserving deformation) and volumetric deformation (recall equation 8-13). In FEA incompressibility is enforced by an appropriate choice of the bulk modulus  $\kappa$ . However in FEA implementations of uncoupled material laws incompressibility is never fully enforced leading to  $J = \det(\mathbf{F}) \approx 1$  and  $J > 1$  for tension and  $J < 1$  for compression. Therefore  $J$  in this case provides information on whether loading is predominantly in compression or tension and can be used as a switch for material behavior. For instance for a particular constitutive parameter  $P$  one can switch it to have a quantity for tension,  $P_{tension}$  or compression  $P_{compression}$  using

$$P = \begin{cases} P_{tension} & J > 1 \\ P_{compression} & J \leq 1 \end{cases} \quad 8-27$$

This approach was implemented in FEBio to test the joint modelling of both the tensile and compressive behaviour.

### 8.7.4 *Inverse FEA based constitutive model evaluation*

The above constitutive formulations were implemented in the FEA software FEBio (open source version 1.3.0.1540, Musculoskeletal Research Laboratories, The University of Utah, USA). Based on the experimental work by Van Looke *et al.* 2006<sup>21</sup> and Takaza *et al.* (unpublished)<sup>22</sup> a compression (Figure 8.22A) and tension (Figure 8.22B) model were created respectively.

For the compression model a 10x10x10 mm muscle volume was uniformly meshed using 6x6x6=216 solid 8-node tri-linear hexahedral elements. Unconfined compression loading was applied through prescribed displacement (-3.2mm, where 0.2mm is the initial surface offset to allow for contact establishment, corresponding to a compressive stretch of 0.7) of a rigid body compressor surface (24x24 mm, 15x15=225 0.01 mm thick rigid quadrilateral shell elements). The top and bottom faces of the muscle cube were allowed to slide with respect to the “floor” and the compressor surface (modelled using frictionless sliding contact).

For the tension model a 10x10x30 mm muscle volume was meshed using 5x5x25=625 solid 8-node tri-linear hexahedral elements. The element size was biased in the load direction such that element height was smallest at the model top and bottom. The bottom face was fully constrained while the top face was rigidly connected to a rigid body surface (12x12 mm, 12x12=144 0.01 mm thick rigid quadrilateral shell elements). Tensile load was applied by prescribing the displacement of the rigid body (9mm corresponding to a tensile stretch of 1.3).

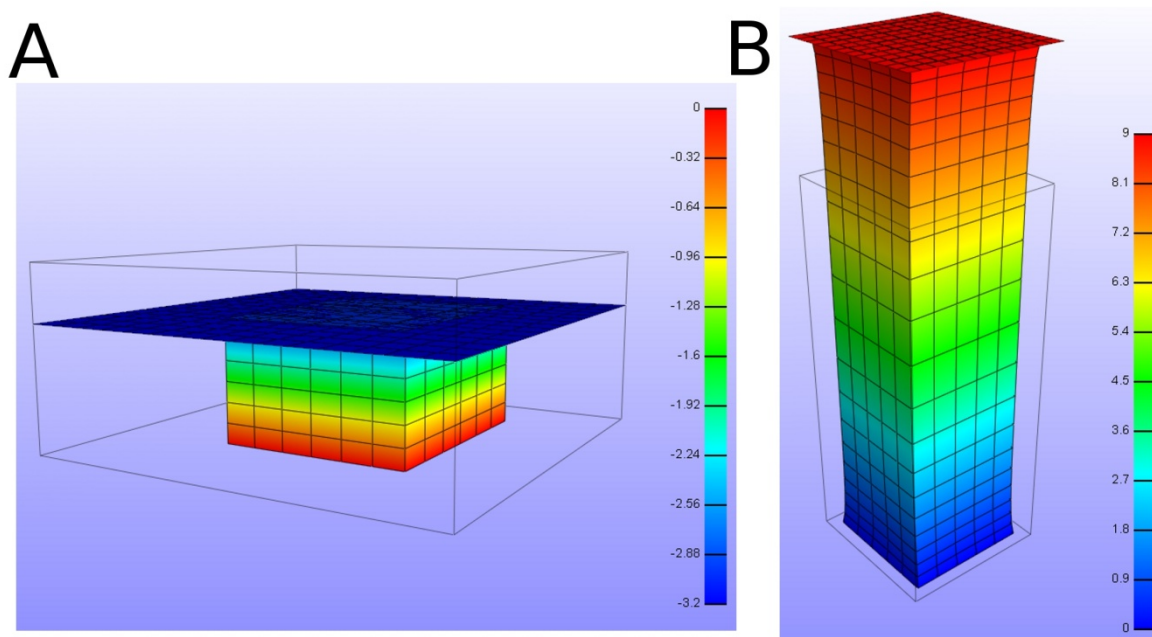
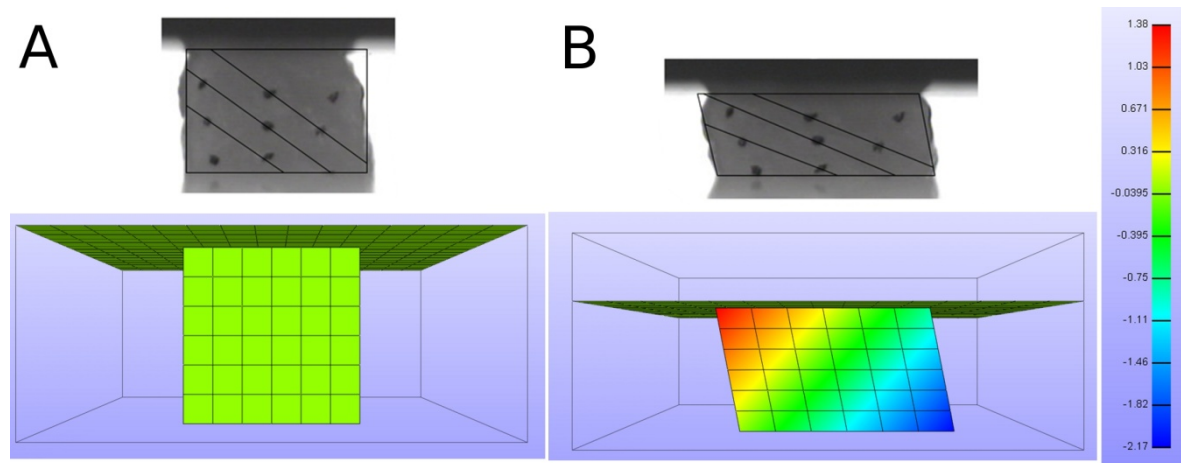


Figure 8.23: Example inverse FEA results showing the deformed models for the compression (A) and tension (B) experiments. Element shading represents displacement along the loading direction (mm).

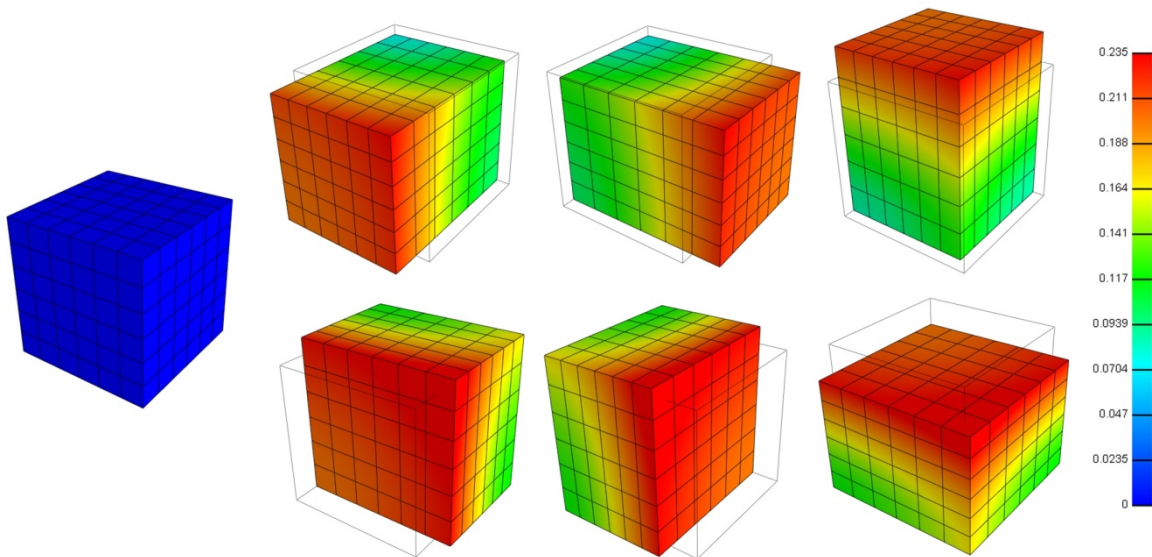
For the experimental work described by Van Looke *et al.* 2006<sup>21</sup> and Takaza *et al.* (unpublished)<sup>22</sup> the experimental measures include applied stretch and a measure of Cauchy stress. In the latter uni-axial loading is assumed and thus shearing effects (which occur for non-parallel or non-orthogonal loading with respect to the fibre direction) are not included. Hence rather than outputting the along load-direction Cauchy stress an equivalent simulated measure of the experimental Cauchy stress was derived. The applied uni-axial stretch was defined as the original sample height over the deformed sample height. In order to derive a measure of the experimental Cauchy stress the sum of the load-direction reaction forces on the rigid bodies were recorded and divided by the original surface area divided by the applied stretch. Dividing the original surface area by the stretch thus simulates the surface area used for Cauchy stress derivation under the assumption of pure uni-axial loading.

Figure 8.24 shows how under the boundary conditions implemented (sliding allowed) shearing behaviour observed by Van Looke et al. 2006 is allowed to occur in the models.



A MATLAB (7.8 R2009a The Mathworks Inc., Natick, MA) based control code was generated whereby FEBio input files were generated containing appropriate analysis and constitutive parameters. The MATLAB algorithm controls an iterative process whereby FEBio computations are initiated, results are uploaded following completion and simulated stretch-Cauchy stress curves are compared to experimental data allowing for optimisation based formulation of a novel set of constitutive parameters for the next iteration. Constitutive parameters were determined using Levenberg-Marquardt (MATLAB *lsqnonlin* function) based optimisation. Initial parameters were manually determined and optimisation was limited to 100 iterations. For all constitutive models the following summary statistics will be computed with respect to the experimental data: 1)  $R^2$ , 2) root mean square (RMS) of the differences, 3) sum of squared differences (SSQD) and 4) the maximum difference (Max.Diff.).

In addition to the individual constitutive model evaluations separately for tension and compression a joint modelling approach was tested through the implementation of the Jacobian based switching discussed in the previous section. A cubic model (Figure 8.25) composed of  $6 \times 6 \times 6 = 216$  solid 8-node tri-linear hexahedral elements was subjected to tension followed by compression for each of the three axis directions.



## 8.8 Results

### 8.8.1 *Isotropic Ogden hyperelastic (ISO)*

Figure 8.26 shows the isotropic experimental and ISO constitutive model response. For both loading cases the first order Ogden model provided an appropriate fit. Table 8-3 illustrates the material parameters used and Table 8-4 shows summary statistics for the fits. Although good agreement with the isotropic response was seen (both curves present with  $R^2 = 1$ ) the isotropic response deviates from the anisotropic response by a maximum of 0.327kPa and 31.231kPa for compression and tension respectively

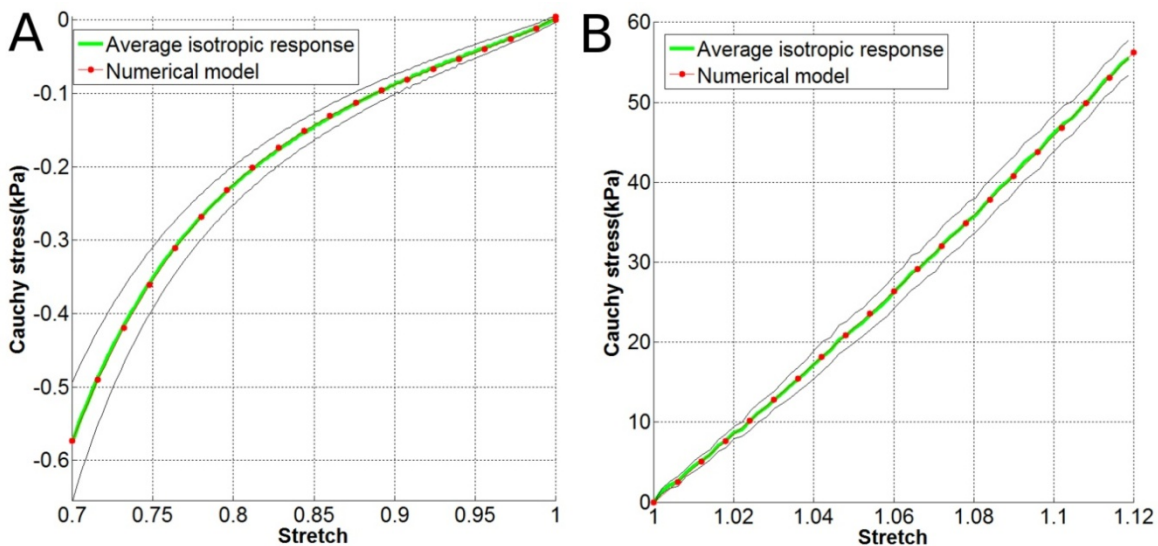


Figure 8.26 The isotropic stress-stretch response for compression (A) and tension (B). Green curves are the experimental isotropic response, black curves are offset for plus and minus the standard deviation, red dots are the model fit.

Material parameter	Compression	Tension
$\mu$	0.665 kPa	276.360 kPa
$\alpha$	13.989	5.646

Table 8-3: Material parameters for isotropic Ogden model

Difference measure	Compression	Tension
	$R^2$	1.00
RMS (kPa)	0.002	0.153
SSQD (kPa)	9.2876e-005	0.491
Max.diff. isotropic (kPa)	0.0042015	0.386
Max.diff. anisotropic (kPa)	0.327	31.213

Table 8-4: Difference parameters for isotropic Ogden model

### 8.8.2 Fibre reinforced transversely isotropic Ogden hyperelastic (TISO)

Figure 8.27 shows the results for the TISO model compared to the anisotropic experimental data. The material parameters are listed in Table 8-5 and Table 8-6 shows summary statistics. The isotropic ground matrix response for this model was initiated as the isotropic model discussed in the previous section and adjusted such that a best match for the longitudinal direction loading could be obtained (where fibres do not contribute due to buckling). Then the fibre material parameters were adjusted to obtain a best match with the transverse loading case.

As predicted the model allows capturing of both the transverse and longitudinal behaviour ( $R^2 = 1$  in both cases). For intermediate angles the response is also intermediate and therefore no softening is initiated. Hence here the model deviates from the experimental data to a maximum difference of 0.192 kPa for loading at 45°.

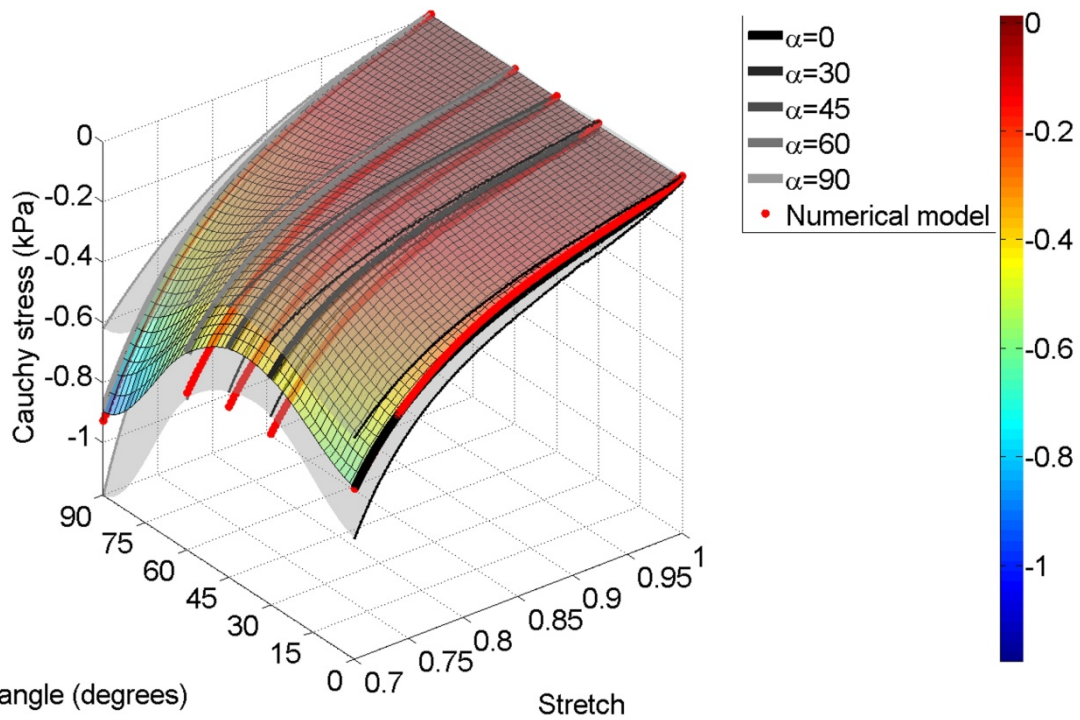


Figure 8.27 The anisotropic non-linear elastic behaviour of skeletal muscle tissue in compression (surface and grey-scale curves) and the TISO numerical model fit (red dots).

Material parameter	Value
$\mu$	0.742 kPa
$\alpha$	13.542
$c_1$	0.215 kPa
$c_2$	7.877
$\kappa$	100 kPa

Table 8-5: Material parameters for the TISO constitutive law for compression

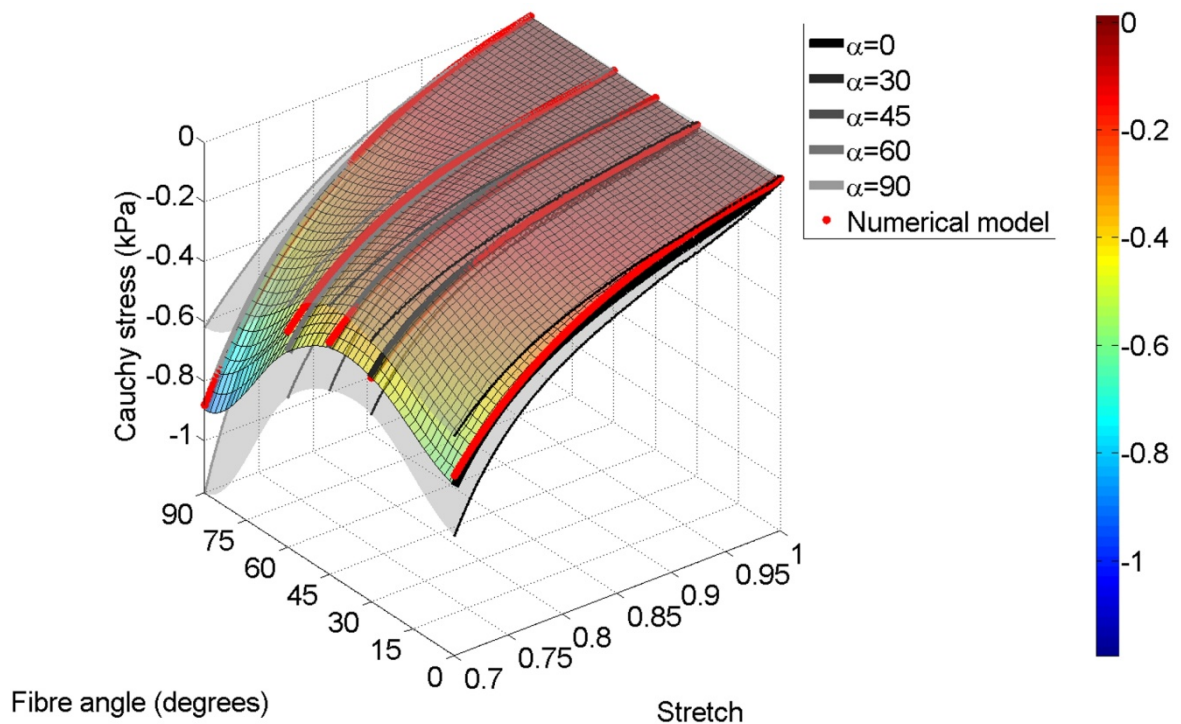
Difference measure	Fibre angle with respect to load direction (degrees)				
	0	30	45	60	90
$R^2$	1.00	0.58	0.47	0.86	1.00
RMS (kPa)	0.013	0.087	0.097	0.063	0.018
SSQD (kPa)	0.002	0.106	0.133	0.055	0.005
Max.diff.(kPa)	0.020	0.184	0.192	0.134	0.034

Table 8-6 Summary statistics for the TISO constitutive law for compression



### 8.8.3 Orthotropic fibre family reinforced Ogden (TCNL) model for compression

Figure 8.28 shows the TCNL constitutive law and the anisotropic experimental data for compression. As was mentioned in section 8.7.2 this model does not reduce to transverse isotropy. However it was used here to illustrate that transverse fibre family addition allows modelling of intermediate angle softening observed by Van Loocke *et al.* 2006. As the curves in Figure 8.28 and the summary statistics in Table 8-8 show the constitutive law (using the parameters in Table 8-7) shows excellent agreement to the anisotropic response of muscle tissue in compression.



Material parameter	Value
$\mu$	0.32 kPa
$\alpha$	13.571
$\xi_L$	4.3 kPa
$\xi_T$	1.2 kPa
$\beta$	2.5
$\kappa$	100 kPa

Table 8-7: Material parameters for the TCNL constitutive law for compression

Difference measure	Fibre angle with respect to load direction (degrees)				
	0	30	45	60	90
$R^2$	0.98	1.00	1.00	0.96	1.00
RMS (kPa)	0.024	0.008	0.006	0.030	0.012
SSQD (kPa)	0.013	0.001	0.001	0.018	0.003
Max.diff.(kPa)	0.037	0.012	0.020	0.018	0.023

Table 8-8 Summary statistics for the for the TCNL constitutive law for compression

### 8.8.4 Ellipsoidal fibre distribution (EFD) models for tension and compression

Figure 8.29 shows the response for the EFD model in compression compared to the experimental data. The material parameters are listed in Table 8-9. Table 8-10 shows summary statistics for the fits. As expected the EFD model performs similar to a single fibre family reinforced transversely isotropic as it is able to capture the transverse and longitudinal behaviour ( $R^2 = 1.00$  and  $R^2 = 0.98$  respectively). However it predicts an intermediate response for intermediate angles resulting in over estimation of up to 0.279 kPa for the final stress at 45 degree loading.

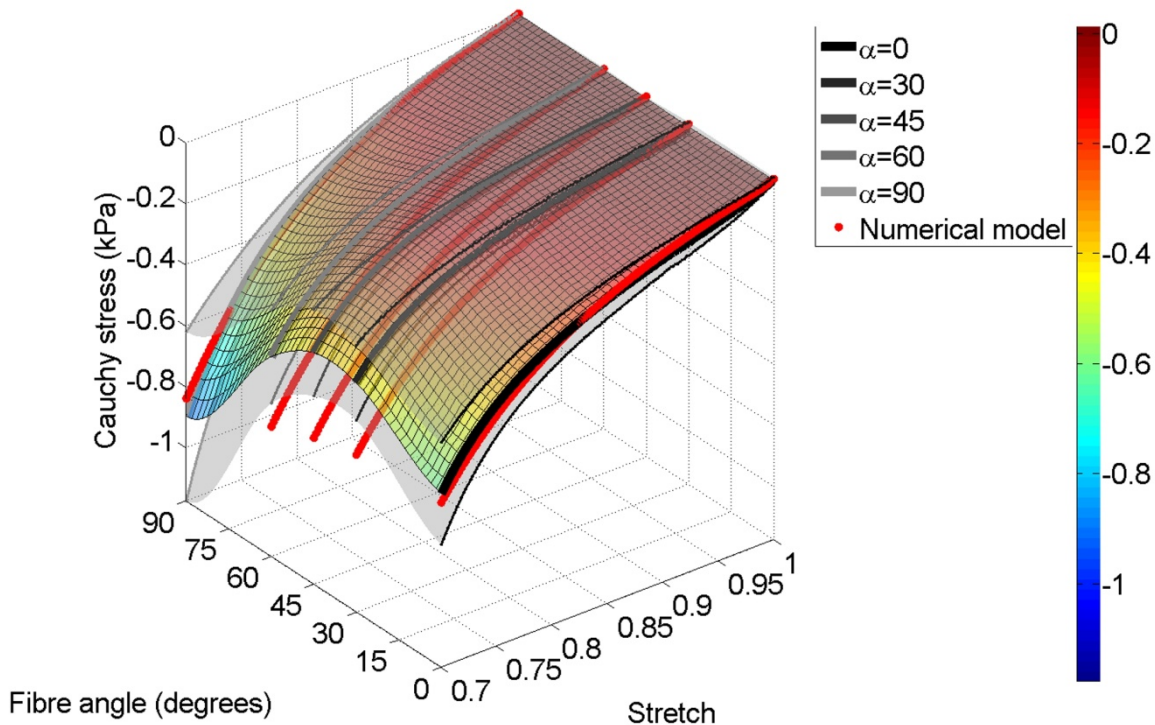


Figure 8.29 The anisotropic non-linear elastic behaviour of skeletal muscle tissue in compression (surface and grey-scale curves) and the EFD numerical model fit (red dots).

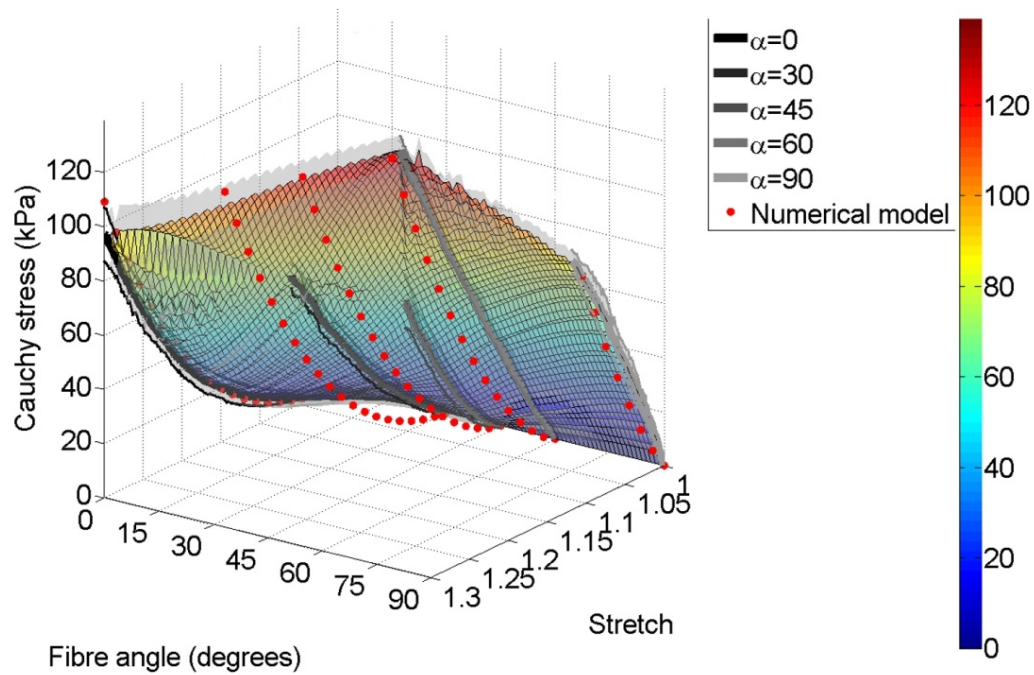
Material parameter	Value
$\mu$	0.32 kPa
$\alpha$	13.571
$\xi_L$	0.3 kPa
$\xi_T$	0.065 kPa
$\beta_T = \beta_L = \beta$	2.1
$\kappa$	100 kPa

Table 8-9: Material parameters for the EFD constitutive law for compression

Difference measure	Fibre angle with respect to load direction (degrees)				
	0	30	45	60	90
$R^2$	0.98	0.07	-0.46	0.42	1.00
RMS (kPa)	0.021	0.115	0.142	0.114	0.016
SSQD (kPa)	0.009	0.276	0.42	0.272	0.006
Max.diff. (kPa)	0.039	0.236	0.279	0.230	0.06

Table 8-10: Difference parameters for the EFD constitutive law for compression

Figure 8.30 shows the response for the EFD model in tension compared to the experimental data. The material parameters are listed in Table 8-11. Table 8-12 shows summary statistics for the fits. For tension the EFD model provides an approximate fit for the response and the differences in the degree of non-linearity for the transverse and longitudinal direction ( $R^2 = 0.90$  and  $R^2 = 0.97$  respectively). However the non-linearity for intermediate orientations is again intermediate and in this case led to underestimation of the stress for a large portion of the intermediate curves. The largest deviation was 30.354 kPa for the 45 degree orientation.



Material parameter	Value
$\mu$	1 kPa
$\alpha$	13.571
$\xi_L$	15 kPa
$\xi_T$	120 kPa
$\beta_L$	2.1
$\beta_T$	3.5
$\kappa$	100 kPa

Table 8-11: Material parameters for the EFD constitutive law for tension

Difference measure	Fibre angle with respect to load direction (degrees)				
	0	30	45	60	90
$R^2$	0.97	0.52	0.31	0.79	0.90
RMS (kPa)	4.656	16.430	16.720	18.446	8.576
SSQD (kPa)	455.329	3779.407	2515.950	4763.730	588.37
Max.diff. (kPa)	12.127	24.165	30.354	24.178	12.400

Table 8-12: Difference parameters for the EFD constitutive law for tension

### 8.8.5 Gaussian Modulated Spherical Fibre Distribution Ogden hyperelastic (GMSFD) model for tension and compression

Figure 8.31 shows the fitting results for the GMSFD model for compression. The material parameters are listed in Table 8-13 and the summary statistics in Table 8-14. For compression the GMSFD model is able to provide an appropriate fit for all orientations tested since  $R^2$  levels are all in the range 0.97-1.00. The maximum difference found was 0.059 kPa for the transverse test direction.

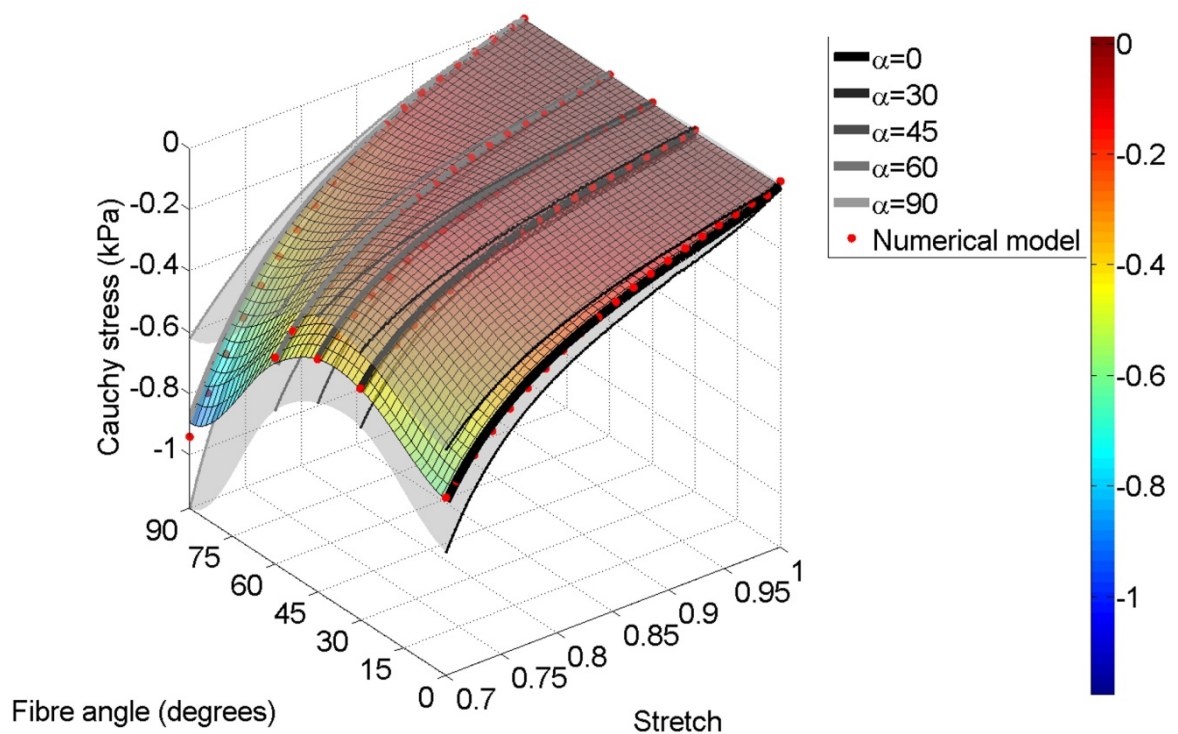


Figure 8.31 The anisotropic non-linear elastic behaviour of skeletal muscle tissue in compression (surface and grey-scale curves) and the GMSFD numerical model fit (red dots).

Material parameter	Value
$\mu$	0.15 kPa
$\alpha$	13.571
$\xi_L$	2.1 kPa
$\xi_T$	0.15 kPa
$\beta$	2.1
$\zeta_L$	0.2 rad

$\zeta_T$	0.2 rad
$\kappa$	100 kPa

Table 8-13: Material parameters for GMSFD constitutive law for compression

Difference measure	Fibre angle with respect to load direction (degrees)				
	0	30	45	60	90
$R^2$	0.99	0.99	0.97	1.00	0.98
RMS (kPa)	0.016	0.010	0.017	0.005	0.032
SSQD (kPa)	0.005	0.002	0.005	0	0.018
Max.diff. (kPa)	0.023	0.017	0.029	0.009	0.059

Table 8-14 Summary statistics for the GMSFD constitutive law for compression

Figure 8.32 shows the fitting results for the GMSFD model for tension. Two views are shown for clarity. The material parameters are listed in Table 8-15 and the summary statistics in Table 8-16. For tension the GMSFD model provides a reasonable fit for all directions. The  $R^2$  levels are in the range 0.96-0.98 for 0-45 degree loading (Table 8-16). For 60 and 90 degree loading the  $R^2$  levels were lower, 0.91 and 0.93 respectively, due to overestimation of stress. The maximum difference found was 30.770 kPa for the 60 degree orientation.

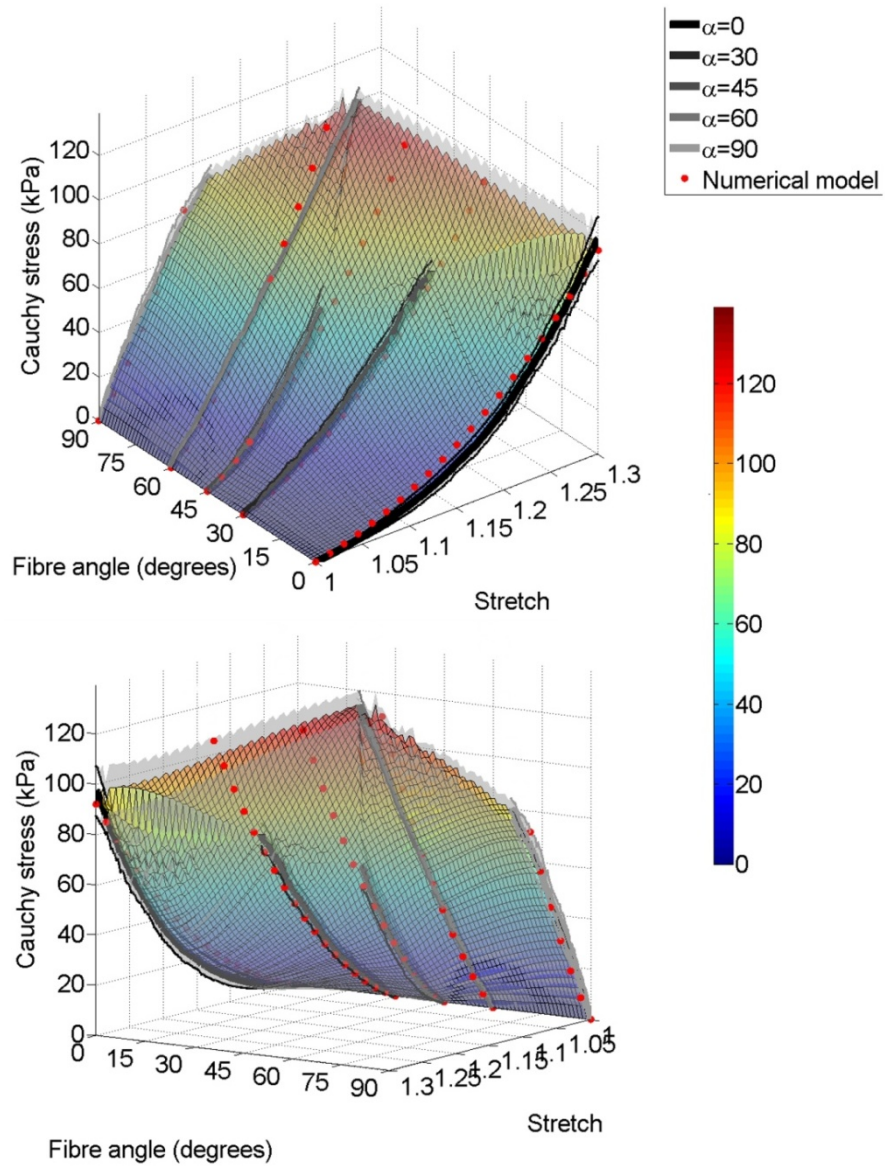


Figure 8.32 The anisotropic non-linear elastic behaviour of skeletal muscle tissue in tension (surface and grey-scale curves) and the GMSFD numerical model fit (red dots).

Material parameter	Value
$\mu$	0.6 kPa
$\alpha$	13.571
$\xi_L$	1 kPa
$\xi_T$	85 kPa
$\beta$	2.1
$\varsigma_L$	0.52 rad
$\varsigma_T$	0.3 rad
$\kappa$	100 kPa

Table 8-15: Material parameters for GMSFD constitutive law for tension

Difference measure	Fibre angle with respect to load direction (degrees)				
	0	30	45	60	90
$R^2$	0.96	0.97	0.98	0.91	0.93
RMS (kPa)	5.921	3.844	3.152	12.373	6.966
SSQD (kPa)	736.302	206.812	89.393	2143.1232	388.214
Max.diff. (kPa)	9.485	6.355	7.274	30.770	14.777

Table 8-16 Summary statistics for the GMSFD constitutive law for tension

### 8.8.6 Modelling of volumetric tension compression non-linearity

The Jacobian based switching between tension and compression parameters was implemented for the ISO and EFD constitutive laws. However for both material models the computations in FEBio were unstable and simulations failed at the point of switching parameters. Hence this approach is not suitable for the combined modelling of the tension compression behaviour.

## 8.9 Discussion

Using inverse FEA this study evaluated the performance of a multitude of common constitutive models for skeletal muscle tissue. Since isotropic models provide only an average fit to the average tissue response they may deviate significantly from the response depending on load angle. First order isotropic hyperelastic Ogden models were presented and demonstrated maximum differences of 0.327 and 31.3kPa respective for tension and compression with respect to the anisotropic response. Expansion of such an isotropic model with single longitudinal fibre family reinforcement allowed accurate modelling for compression for the transverse and longitudinal directions respectively but not for intermediate orientations since these models can only predict an intermediate response and thus deviate from the more complex anisotropic behaviour (up to 0.192kPa for compression). Using an orthotropic fibre family model (which however does not reduce to transverse isotropy) it was shown that transverse contributions do allow for



modelling of more complex anisotropy seen for intermediate load orientations. Motivated by this an ellipsoidal fibre distribution model was evaluated for tension and compression. Although reasonable overall fits were obtained for this model the ellipsoidal constitutive behaviour mapping provided limited flexibility to model the intermediate responses accurately. In compression the model did not perform better than the single fibre family transversely isotropic model with maximum deviations of 0.279 kPa at 45 degree loading. For tension the changing degree of non-linearity for intermediate load angles was not accounted for appropriately leading to large deviations and poor  $R^2$  values at these orientations (e.g. 0.31 kPa at 45°). Finally a novel constitutive model based on the ellipsoidal fibre distribution approach by Atheshian *et al.* 2009<sup>64</sup> was proposed. The model, termed the Gaussian modulated spherical fibre distribution Ogden hyperelastic proposes that depending on angle with the longitudinal direction all fibrous components contain a Gaussian weighted transverse and longitudinal contribution. This model accurately captured the anisotropic compression (lowest  $R^2 = 0.97$ , maximum deviation 0.029 kPa) and tension (lowest  $R^2 = 0.91$ , maximum deviation 30.77 kPa) response including the 45 degree softening reported for compression by Van Loocke *et al.* 2006<sup>21</sup> and the load orientation dependent non-linearity observed by Takaza *et al.* (unpublished)<sup>22</sup> for tension.

The tension and compression properties of muscle vary greatly and it is hypothesised that muscle tissue presents with a type of volumetric tension compression non-linearity which current modelling approaches do not account for. Attempts to implement Jacobian based tension-compression parameter switching proposed in the current study were unsuccessful due to the fact that the rapid changes in stiffness cause numerical instabilities for FEA.

The constitutive modelling approach has several limitations. Due to the spherical fibre distribution it requires computationally intensive numerical integration making this model more time consuming than modelling approaches which do not require integration. In addition the fibrous structure contributions are weighted according to spherical area elements in this approach (and also for ellipsoidal fibre distribution models). For non-linear mappings like proposed here this distorts the physical interpretation of the material parameters. In addition the discrete geodesic shape may not accurately capture the non-linear mapping accurately for all of the spherical fibre directions. This may be compensated for through an appropriate choice of material

parameters however it further removes some of their physical meaning (i.e. they may have to be exaggerated if the discrete nature of the geodesic tessellation causes under sampling).

Currently initial parameter sets were manually determined followed by iterative Levenberg-Marquardt driven inverse FEA based optimisation (limited to 100 iterations). The uniqueness of the parameters obtained has not been investigated at present but will be the subject of future work.

## 8.10 Conclusions

This study evaluated common constitutive formulations for their ability to model the passive, anisotropic and non-linear elastic behaviour of muscle tissue for not only longitudinal and transverse but also intermediate load orientations. To the authors knowledge this detailed evaluation has not been previously reported in the literature. Current modelling approaches do not appropriately account for the complex anisotropic behaviour observed in tension and compression for passive skeletal muscle tissue. The novel constitutive model proposed based on Gaussian modulated transverse and longitudinal contributions is promising. However the physical interpretation of the parameters is unclear and the model requires computationally intensive numerical integration. Future modelling approaches should further explore the role of the connective tissue structures which are oriented both longitudinal and transverse to the fibre direction and shed light on the tension-compression non-linearity.

## 9 STUDY VII

# MRI Based Derivation of Detailed Finite Element Models Incorporating Fibre Architecture

## 9.1 Introduction

As mentioned in section 3.8 in the current thesis inverse FEA of the mechanical properties of muscle tissue is of interest based on indentation of volunteer soft tissue sites while MRI is used as a non-invasive modality to record soft tissue boundary conditions, such as 3D deformation (see chapters 7 and 8), tissue geometry derivable from anatomical MRI and muscle fibre architecture derivable from Diffusion Tensor MRI (see section 2.3.10.2 and Froeling *et al.* 2010<sup>33</sup>).

This study presents custom methods for the accurate derivation of FEA geometries and indentation boundary conditions from anatomical MRI. In addition the incorporation of fibre architecture as an element wise material axis mapping is discussed. For the FEA model the distinction is made between skin, adipose (fat) and muscle tissue.

## 9.2 Methods

All data processing and visualisations presented here were performed using custom made algorithms in MATLAB (7.8 R2009a The Mathworks Inc., Natick, MA). Generation of 2D mother meshes was done using CUBIT (version 13.0, Sandia Corporation, USA). Models were implemented for FEA with the freely available software FEBio (open source version 1.3.0.1540, Musculoskeletal Research Laboratories, The University of Utah, USA).

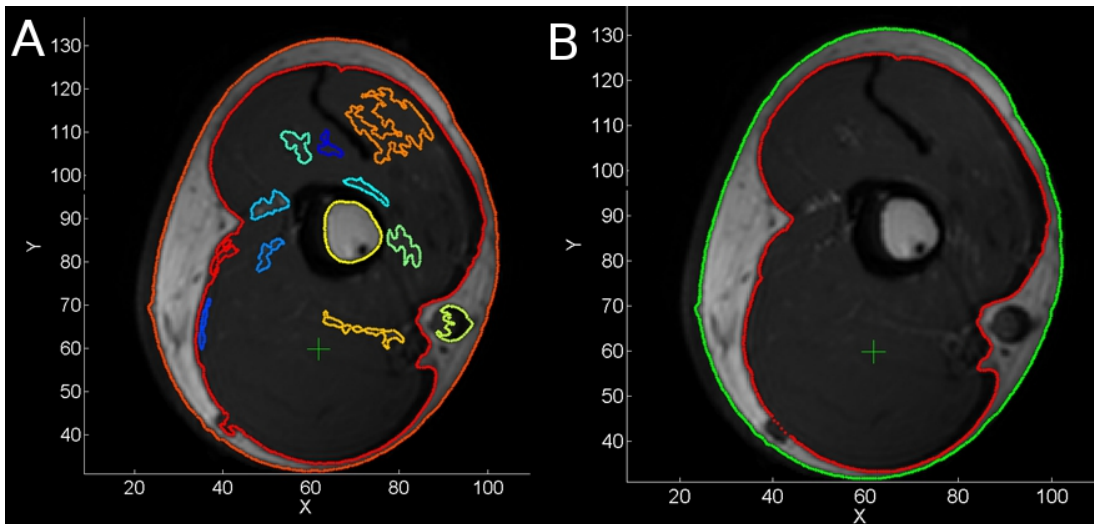
### 9.2.1 *MRI based indentation experiments*

This study focusses on the indentation experiments presented for a human volunteer in chapter 8. A healthy male volunteer (ethical approval obtained at the Academic Medical Centre Amsterdam, ethical committee) was subjected to transverse indentation using the indenter system described in chapter 4. During indentation deformation was recorded using SPAMM tagged MRI (chapter 8) and force was recorded using an optical Fibre Bragg Grating based Force sensor (chapter 4). Prior to indentation and after indentation static anatomical T1 weighted MRI was recorded (voxel size 0.5x0.5x4, field of view 160x160x160mm) and also diffusion tensor MRI of the same field of view (voxel size 2x2x4 mm, see Froeling *et al.* 2010<sup>33</sup> for method description). The latter yielded a vector for each voxel describing the main direction of diffusion and thus most likely the muscle fibre direction.

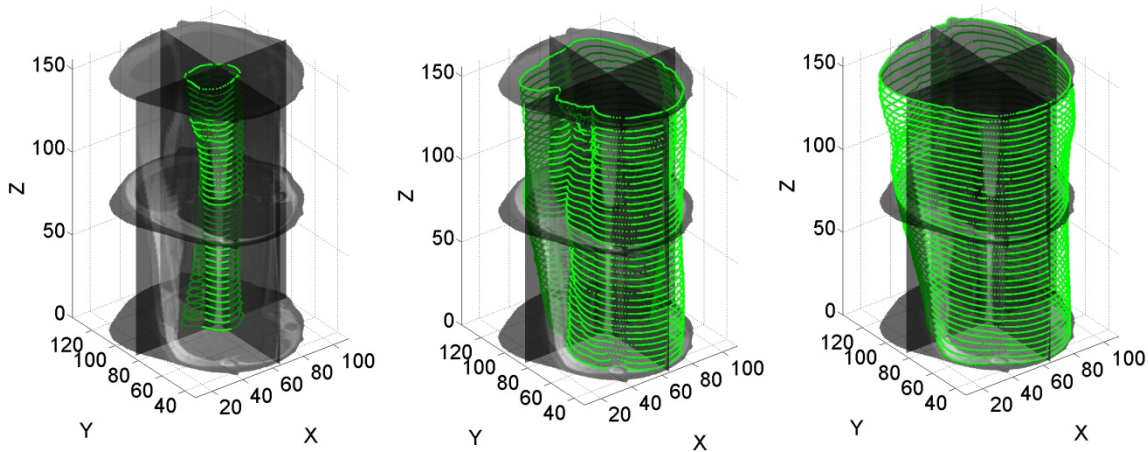
## 9.2.2 *FE model construction*

### 9.2.2.1 **Semi-automatic tissue boundary segmentation**

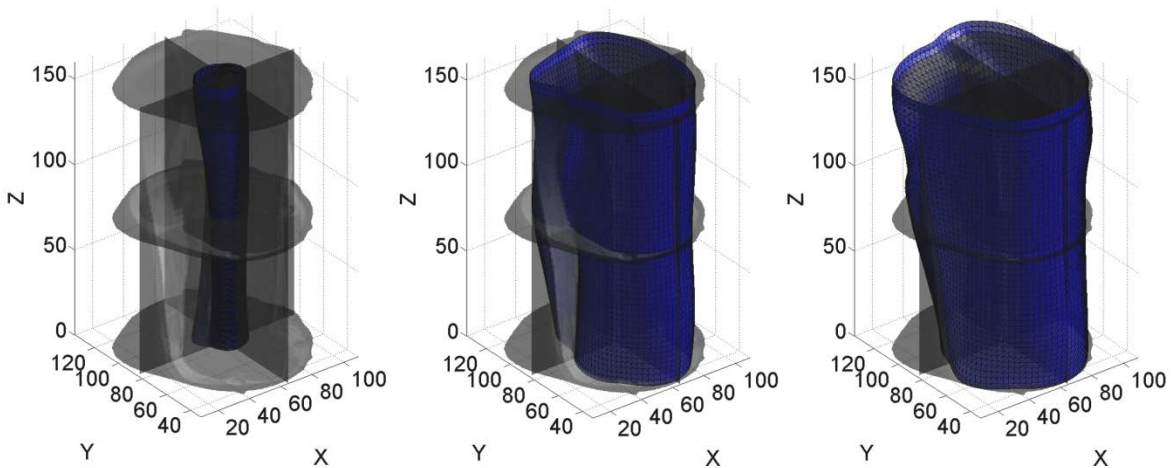
Figure 9.1A shows how standard iso-contour levels highlight a multitude of features for the upper arm due to the presence of anatomical features which present with similar signal intensities. In addition no single iso-contour level can separate all features of interest (skin, fat bone). This is also due to signal intensity variations depending on proximity to the imaging coils. Standard iso-contours also contain irregularities such as the blood vessels and nerve structures which interrupt the boundaries and would result in sudden sharp feature transitions. Therefore semi-automatic segmentation software was developed. The algorithm is based on iso-contour levels such as in Figure 9.1A. However for each slice the user is able to scroll through difference iso-contour levels and select the best (Figure 9.1B). A single contour boundary may be decomposed by segments selected from multiple iso-contour levels. In addition irregularities can be cropped out and manually drawn in contour portions can also be added. Note how in the bottom left in Figure 9.1A a sharp feature exists due to an anatomical feature at the muscle (gray) and fat (white) boundary. This feature was manually removed and the gap manually drawn in in Figure 9.1B.



Through this slice by slice semi-automatic segmentation the boundaries for the bone, muscle-fat and skin could be segmented (Figure 9.2).



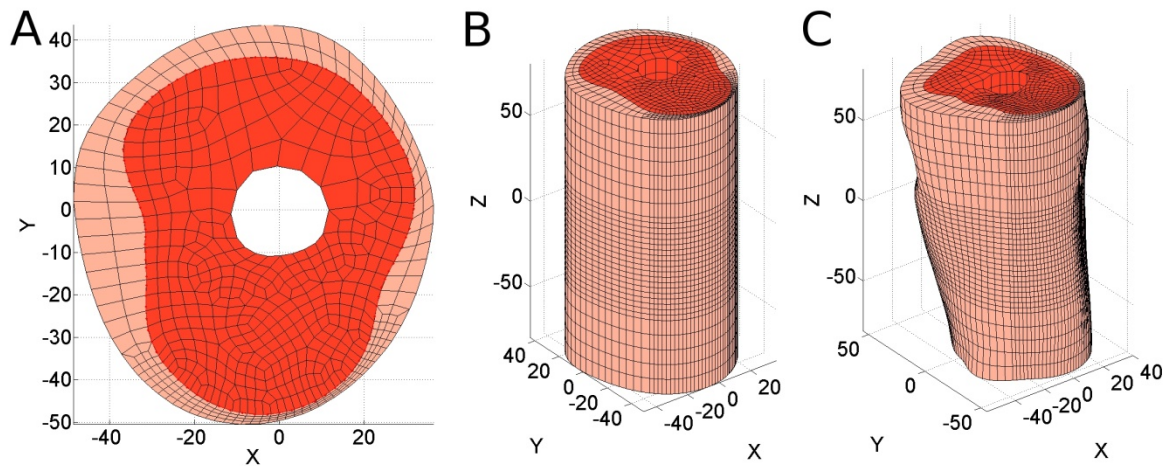
Using the bone central axis a densely triangulated cylinder was warped to each tissue boundary (Figure 9.3). These were then mildly smoothed using HC-Laplacian smoothing which is a technique (see <sup>274</sup>) which allows smoothing of triangulated structures while ensuring shape shrinkage is limited. The removal of sharp features and irregularities aids in meshing while the main anatomical detail is preserved.



### 9.2.2.2 Meshing and FEA geometry warping

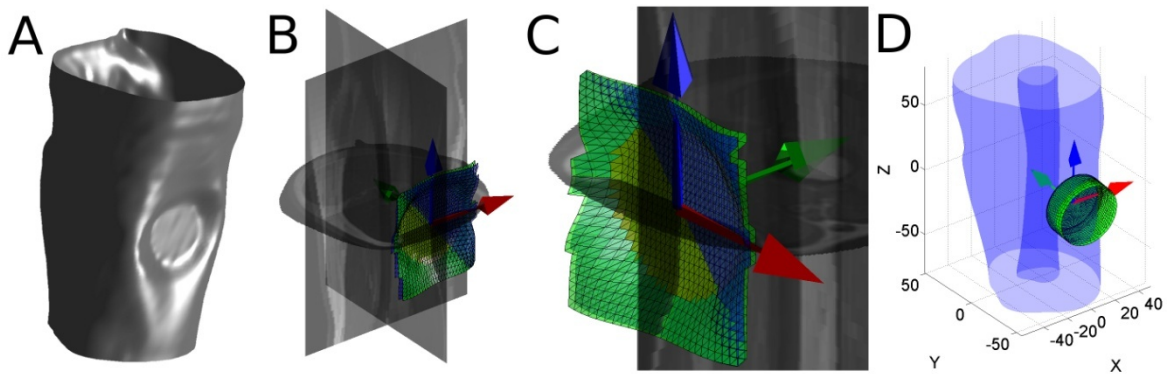
Based on the 3D triangulated surface models an average 2D contour set was derived and imported into CUBIT for 2D quadrilateral meshing (Figure 9.4A). The mesh was refined close to the indentation site and near complex features. This mesh was then imported into MATLAB and extruded to form an offset 3D hexahedral mesh (Figure 9.4B). The mesh was biased along the Z-axis such that mesh density is highest near the indentation site. The regular 3D mesh was then warped (Figure 9.4B) (deformed using angular and

radial mapping with respect to central bone axis whereby elements maintain tissue type) according to the 3D triangulated surface boundary models (Figure 9.3). MATLAB was then used to write ABAQUS and FEBio input files. The former can be imported into CUBIT (and other FEA packages) for mesh quality checking and possible adjustment and or refinement. A quadrilateral shell element layer is later added on top of the fat layer in FEBio to model skin. Bone is modelled as a cavity in which the surface nodes will be rigidly supported.



### 9.2.2.3 Derivation of indentation boundary conditions

Figure 9.5A shows the segmented indented skin surface. This was used for segmentation of the indentation site based on its flat nature in contrast to the curved nature of the rest of the surface. Figure 9.5B-C show the surface region for the indentation and the segmented circular flat indentation imprint left by the indenter. This surface and its centre provided a means to reorient all models in a coordinate system whereby the indenter path is aligned with the Y-axis. The indenter path was defined as the distance the indenter needs to be offset along the Y-axis (starting with its indenter face aligned with the imprint surface) until it no longer touches the FEA model geometry. The indenter geometry was derived from its computer aided design model (see chapter 4) modelled as a rigid body and meshed using CUBIT with quadrilateral shell elements. After appropriate alignment of the indenter the meshed models (arm geometry and indenter) were exported as FEBio input files with their appropriate relative positions.



#### 9.2.2.4 Incorporation of diffusion tensor MRI derived muscle fibre architecture

Figure 9.6 shows a visualisation of the diffusion tensor MRI derived muscle fibre trajectory estimates. The technique (Froeling *et al.* 2010<sup>33</sup>) provides per voxel fibre direction vectors. These can be incorporated in FEBio input files by simply appending text such as:

```
<element id="137">
    <fiber>0,1,0</fiber>
</element>
```

to the FEBio input file ElementData section. The example illustrates the fibre direction aligned with the Y-direction for element 127. Since the MRI voxels and the FEA elements do not coincide the fibre direction mapping requires interpolation of the vector components at the element centres.

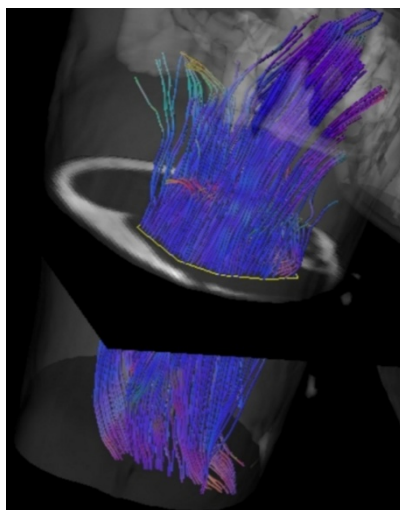


Figure 9.6 Visualisation of the diffusion tensor MRI derived muscle fibre trajectories.

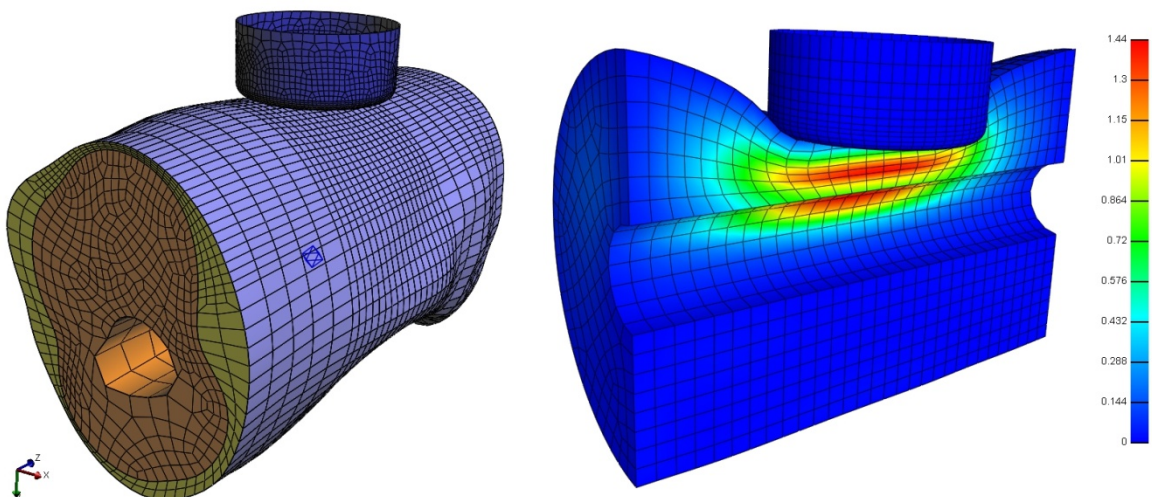


### 9.2.3 Iterative inverse FEA based optimisation

Similar to section 8.7.4 MATLAB based control code was generated whereby FEBio input files were generated containing appropriate FEA geometry, and fibre architecture and analysis and constitutive parameters. The MATLAB algorithm controls an iterative process whereby FEBio computations are initiated and results are uploaded following completion of simulations. For the MRI based indentation experiments the 3D displacement field can be directly compared to the SPAMM tagged MRI displacement. In addition the indenter force can be compared to simulated indenter rigid body reaction force. Constitutive parameters can be determined through inverse optimisation. Two types of optimisation routines are implemented 1) a stochastic differential evolution based algorithm<sup>278</sup>, and 2) a gradient descent based Levenberg-Marquardt algorithm (MATLAB *lsqnonlin* function).

## 9.3 Results

The left side of Figure 9.7 shows an example model for the human volunteer as derived from the MRI data. The model contains skin, fat and muscle tissue while bone is represented by a rigidly supported central cavity. The indenter was modelled using rigid shell elements. The image on the right in Figure 9.7 shows example indentation results for a similarly obtained phantom geometry model.



## 9.4 Discussion

This study presents a flexible and simple framework for the generation of detailed MRI data derived 3D FEA models incorporating skin, fat and muscle tissue as deformable elements. For muscle tissue diffusion tensor MRI derived muscle fibre directions are prescribed for each element thus allowing for the evaluation of anisotropic constitutive laws. Incorporating diffusion tensor MRI into 3D FE models has been implemented by Blemker *et al.* 2007<sup>80</sup>. However most studies use a simplified geometrical mapping estimations of fibre directions (e.g. <sup>23</sup>) rather than direct measurement presented here.

In addition a Matlab controlled inverse analysis framework is presented.

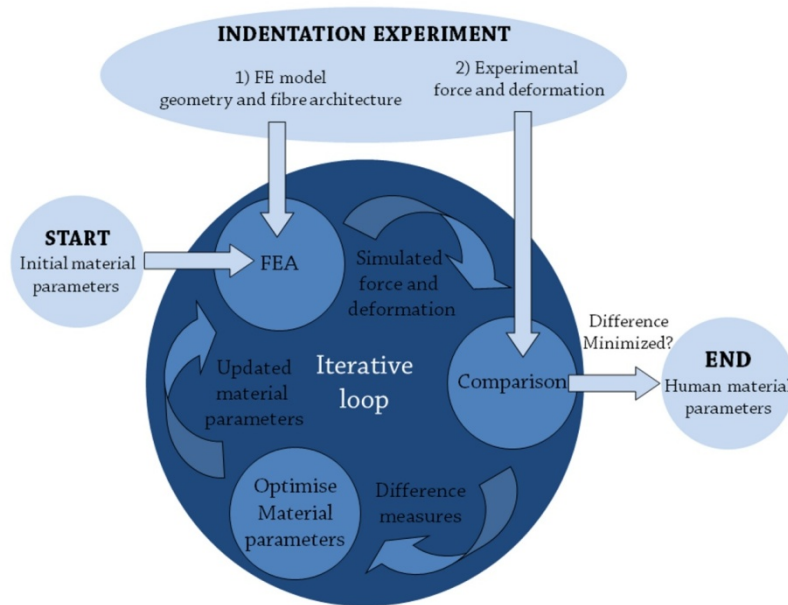
Future work will focus on further refinement of the mesh quality and on application of these models to inverse FEA based determination of the mechanical properties of skeletal muscle tissue.

## 9.5 Conclusions

Anatomical and diffusion tensor MRI data was recorded prior to and after indentation to the upper arm of a volunteer. The anatomical MRI data could be used to derive anatomically accurate FE model geometries where skin, fat and muscle are separately represented. In addition muscle fibre directions could be mapped for each muscle element. The incorporation of tissue anisotropy allows for the inverse FEA based evaluation of anisotropic constitutive laws which is the focus of future work.

# 10 Discussion, conclusions and future work

This thesis focusses on the development of an experimental and computational framework for the non-invasive analysis of the passive (non-linear and viscoelastic) mechanical properties of skeletal muscle tissue. Figure 10.1 shows a diagram for the proposed approach framework. An appropriate constitutive model and initial parameters are formulated based on data from the literature and are implemented in FEA. Then an indentation experiment is performed on healthy volunteers during which experimental boundary conditions are measured such as: 1) the geometry and fibre architecture, and 2) the indentation force and tissue deformation. The former is used for the construction of the FE model and for mapping of the per element fibre directions. The indentation is then simulated using FEA yielding simulated measures of indentation force and soft tissue deformation. These are then compared to the true experimental force and deformation to derive difference measures for the optimisation based derivation of a new material parameter set. An iterative optimisation process composed of the following is then repeated until the difference measures are minimised: 1) *FEA simulation*, 2) *comparison of FEA and experimental boundary conditions* and 3) *material parameter optimisation*. This thesis related to setting up and validating all the experimental and computational methods required in the diagram of Figure 10.1.



In study I (chapter 4) a novel MRI compatible soft tissue indenter system and optical FBG based force sensor have been presented. The computer controlled indenter motion is highly repeatable since MRI acquisitions during repeated indenter motions did not induce significant additional variation on top of what is expected due to noise. In addition the indenter device and force sensor are fully MRI compatible as they are manufactured from non-ferromagnetic materials. The MRI compatibility was also evident following evaluation inside an MRI scanner and no negative effects such as SNR increase and or image artefacts were observed. The force sensor allowed sampling at 100Hz and measurement of viscoelastic force curves. The force sensor was calibrated for forces up to 15 N and demonstrated a maximum force difference percentage of 3.1% (corresponding to a 0.031 N difference from 1 N) and a maximum force error magnitude of 0.043 N (corresponding to 0.7% difference with respect to 6 N).

Due to the way that compressive forces are converted to tensile forces in the FBG sensor within the current design, measurement of forces in the range 0~0.94 N are not possible at present since the weight of the indenter head (0.94 N) assembly needs to be overcome (only the case for downward indentation). The force measurement range 0.94~15 N is however sufficient for many purposes including large strain biomechanical soft tissue investigation. The FBG signal was stored at 100Hz. However this is currently a control software speed limitation. The optical interrogator system allows up to 1 kHz force measurement.

In study II (chapter 5) an alternative imaging modality DIC was evaluated as an alternative to MRI for the inverse FEA based analysis of bulk soft tissue properties. Results showed that DIC could be combined with inverse FEA to determine the bulk Neo-Hookean material parameters of a silicone gel soft tissue phantom subjected to indentation. However DIC is limited to surfaces deformation measurements and hence it is not suitable for sub-dermal *in-vivo* anisotropic constitutive parameter identification.

Study III (chapter 6) treated validation methods for MRI based deformation measurement. A novel marker tracking method was presented and validated using simulated image data. The marker tracking method is robust and the maximum geometric bias was  $5.560 \times 10^{-3}$  voxels while the error due to noise remains below 0.1127 voxels for Rician noise distributions with signal to noise ratios of 5 up to 35. This appears to be the only marker tracking algorithm suitable for the validation of MRI based deformation measurement which itself has been validated against a 'gold standard'.

In study IV (chapter 7) a novel MRI sequence based on SPAMM for the measurement of 3D soft tissue deformation following just three deformation cycles was presented. The techniques were evaluated in a phantom and *in-vivo* for the upper arm of a volunteer. Following comparison to marker tracking in the phantom, the SPAMM tagged MRI derived displacement demonstrated sub-voxel accuracy and precision with a mean displacement difference of  $72\mu\text{m}$  and a standard deviation of  $289\mu\text{m}$ . Displacement magnitude precision was evaluated also for both data sets. The standard deviations of displacement magnitude with respect to the average displacement magnitude were  $75\mu\text{m}$  and  $169\mu\text{m}$  for the phantom and volunteer data respectively. The sub-voxel accuracy and precision demonstrated in the phantom in combination with the precision comparison between the phantom and volunteer data provide confidence in the methods presented for measurement of soft tissue deformation *in-vivo*. Since only three motion cycles are required the presented methodology is, to our knowledge, the fastest currently available for the non-invasive measurement of static 3D soft tissue deformation. However the methods presented are only suitable for static deformation measurements and post-processing is semi-automatic.

In study V (chapter 8) the static and semi-automatic SPAMM based deformation measurements were expanded to fully automatic dynamic deformation measurement. Novel SPAMM tagged MRI based methods are presented for high speed measurement of complex dynamic 3D soft tissue deformation following just 3 motion cycles. Deformation

is derived using a novel and fully automatic Gabor filtering based post-processing framework. The techniques were validated using marker tracking in a silicone gel soft tissue phantom for indentation induced dynamic deformation measurement. In addition *in-vivo* evaluation for the measurement of indentation induced deformation of the biceps region of the upper arm was performed. The techniques do not require *a priori* assumptions on the nature of the deformation or the mechanical properties and demonstrate dynamic measurement of complex 3D soft tissue deformation at sub-voxel accuracy and precision and were validated for 3.3-3.6Hz sampling of deformation speeds up to 12mm/s. For the phantom and volunteer tag point location precision was 44  $\mu\text{m}$  and 92  $\mu\text{m}$  respectively resulting in individual displacements precisions of 61  $\mu\text{m}$  and 91  $\mu\text{m}$  respectively. For both the phantom and volunteer data cumulative displacement measurement accuracy could be evaluated and the difference between initial and final locations showed a mean and standard deviation of 0.44 mm and 0.59 mm for the phantom and 0.40 mm and 0.73 mm for the human data. Finally accuracy of (cumulative) displacement was evaluated using marker tracking in the silicone gel phantom. Differences between true and predicted marker locations showed a mean of 0.35 mm and a standard deviation of 0.63 mm. Since only 3 deformation cycles are required the techniques presented are to the authors' knowledge the fastest currently available for the derivation of 3D dynamic deformation. This allows for the expansion of the SPAMM tagged MRI based measurement of dynamic deformation to cases where motion is less repeatable or where large numbers of repetitions are not clinically feasible. For the current thesis the limited number of repetitions required ensured volunteer comfort and reduced repeatability constraints.

In Study VI (chapter 0) a multitude of constitutive models such as isotropic Ogden hyper elastic, single fibre family reinforced transversely isotropic Ogden and ellipsoidal fibre distribution models were evaluated for inverse FEA based fitting to compression<sup>21</sup> and tension<sup>22</sup> data for excised tissue samples subjected to uni-axial loading for various fibre orientations. A novel constitutive model was proposed employing a spherical fibre distribution<sup>64</sup>. The model, termed the Gaussian modulated spherical fibre distribution Ogden hyperelastic proposes that depending on angle with the longitudinal direction all fibrous components contain a Gaussian weighted transverse and longitudinal contribution. This model accurately captured the anisotropic compression (lowest  $R^2 = 0.97$ , maximum deviation 0.029 kPa) and tension (lowest  $R^2 = 0.91$ , maximum

deviation 30.77 kPa) response including the 45 degree softening reported for compression by Van Loocke *et al.* 2006 <sup>21</sup> and the load orientation dependent non-linearity observed by Takaza *et al.* (unpublished)<sup>22</sup> for tension. This is the first constitutive model for passive skeletal muscle tissue that has been evaluated for both tension and compression and for multiple load angles.

Due to the extreme difference in tension and compression response observed for muscle tissue currently two parameter sets were required for all models. An approach implemented whereby parameter switching was implemented in FEA based on the magnitude of the Jacobian were unsuccessful as sudden stiffness changes results in unstable computations.

Due to the spherical fibre distribution it requires computationally intensive numerical integration making this model more time consuming than modelling approaches which do not require integration. In addition the fibrous structure contributions are weighted according to spherical area elements in this approach (and also for ellipsoidal fibre distribution models). For non-linear mappings like proposed here this distorts the physical interpretation of the material parameters.

Currently initial parameter sets were manually determined followed by iterative Levenberg-Marquardt driven inverse FEA based optimisation (limited to 100 iterations). The uniqueness of the parameters obtained has not been investigated at present but will be the subject of future work.

Future work will also focus on exploring the constitutive modelling approach recently proposed by Ehret *et al.* 2011<sup>190</sup>. This modelling may be promising for passive muscle tissue behaviour as it is also defined using the sum of a transverse and longitudinal contribution. In addition the modelling approach does not require numerical integration and hence is more computationally efficient than the model proposed here.

Finally in study VII (chapter 9) a FE model construction framework was created. Anatomical and diffusion tensor MRI data were recorded prior to and after indentation to the upper arm of a volunteer. The anatomical MRI data could be used to derive anatomically accurate FE model geometries where skin, fat and muscle are separately represented. In addition muscle fibre directions could be mapped for each muscle element. The incorporation of tissue anisotropy allows for the inverse FEA based evaluation of anisotropic constitutive laws which is the focus of future work.

This thesis describes a large array of methods required for the non-invasive analysis of the large strain, non-linear, anisotropic and viscoelastic mechanical properties of passive living muscle tissue. In addition a rich set experimental data bank was created consisting of: 1) *anatomical MRI data for FE model construction*, 2) *Diffusion Tensor MRI data for fibre architecture mapping in FEA*, 3) *SPAMM tagged MRI derived 3D dynamic soft tissue displacement data* and 4) *viscoelastic force relaxation curves*. This data will be made available for other researchers for biomechanical analysis.

Future work will focus on the application of the framework of techniques presented to analyse the mechanical properties of muscle tissue including viscoelastic analysis.



# 11 REFERENCES

1. Forbes, P.A., Cronin, D.S., Deng, Y.C. and Boismenu, M., "Numerical Human Model to Predict Side Impact Thoracic Trauma", in *IUTAM Symposium on Impact Biomechanics: From Fundamental Insights to Applications, Vol. 124*, edited by M. D. Gilchrist (Springer Netherlands, Berlin, 2005), pp. 441-450.
2. Muggenthaler, H., von Merten, K., Peldschus, S., Holley, S., Adamec, J., Praxl, N. and Graw, M., "Experimental tests for the validation of active numerical human models", *Forensic Science International* 177, 184-191 (2008).
3. Ivancic, P.C., Ito, S. and Panjabi, M.M., "Dynamic sagittal flexibility coefficients of the human cervical spine", *Accident Analysis & Prevention* 39, 688-695 (2007).
4. Portnoy, S., Shabshin, N., Siev-Ner, I., Kristal, A. and Gefen, A., "MRI Integrated with Computational Methods for Determining Internal Soft Tissue Loads as Related to Chronic Wounds", in *Bioengineering Research of Chronic Wounds, Vol. 1*, (Springer Berlin Heidelberg, 2009), pp. 169-180.
5. Portnoy, S., Yizhar, Z., Shabshin, N., Itzchak, Y., Kristal, A., Dotan-Marom, Y., Siev-Ner, I. and Gefen, A., "Internal mechanical conditions in the soft tissues of a residual limb of a trans-tibial amputee", *Journal of Biomechanics* 41, 1897-1909 (2008).
6. Linder-Ganz, E., Shabshin, N., Itzchak, Y. and Gefen, A., "Assessment of mechanical conditions in sub-dermal tissues during sitting: A combined experimental-MRI and finite element approach", *Journal of Biomechanics* 40, 1443-1454 (2007).
7. Linder-Ganz, E., Shabshin, N., Itzchak, Y., Yizhar, Z., Siev-Ner, I. and Gefen, A., "Strains and stresses in sub-dermal tissues of the buttocks are greater in paraplegics than in healthy during sitting", *Journal of Biomechanics* 41, 567-580 (2008).
8. Neu, C.P., Arastu, H.F., Curtiss, S. and Reddi, A.H., "Characterization of engineered tissue construct mechanical function by magnetic resonance imaging", *Journal of Tissue Engineering and Regenerative Medicine* 3, 477-485 (2009).
9. Hinds, S., Bian, W., Dennis, R.G. and Bursac, N., "The role of extracellular matrix composition in structure and function of bioengineered skeletal muscle", *Biomaterials* 32, 3575-3583 (2011).
10. Mathur, R., Tewari, R.P. and Saxena, V., "Mechanical Behaviour of Human Leg Skeletal Muscles for Gait Studies", in *6th World Congress of Biomechanics (WCB 2010). August 1-6, 2010 Singapore, Vol. 31*, edited by C. T. Lim and J. C. H. Goh (Springer Berlin Heidelberg, 2010), pp. 973-976.
11. Lim, Y.-J. and De, S., "Real time simulation of nonlinear tissue response in virtual surgery using the point collocation-based method of finite spheres", *Computer Methods in Applied Mechanics and Engineering* 196, 3011-3024 (2007).
12. Audette, M.A., Hayward, V., Astley, O., Doyon, M., McCallister, G.A. and Chinzei, K., "A PC-based system architecture for real-time finite element-based tool-specific surgical simulation", *International Congress Series* 1268, 378-383 (2004).
13. Guccione, J.M., Moonly, S.M., Wallace, A.W. and Ratcliffe, M.B., "Residual stress produced by ventricular volume reduction surgery has little effect on ventricular function and mechanics: A finite element model study", *Journal of Thoracic and Cardiovascular Surgery* 122, 592-599 (2001).
14. Famaey, N. and Sloten, J.V., "Soft tissue modelling for applications in virtual surgery and surgical robotics", *Computer Methods in Biomechanics and Biomedical Engineering* 11, 351 - 366 (2008).
15. Wu, P.I.K. and Edelman, E.R., "Structural biomechanics modulate intramuscular distribution of locally delivered drugs", *Journal of Biomechanics* 41, 2884-2891 (2008).
16. Wu, P.I.K., Minisini, S. and Edelman, E.R., "Intramuscular drug transport under mechanical loading: Resonance between tissue function and uptake", *Journal of Controlled Release* 136, 99-109 (2009).
17. Wei, Q., Sueda, S. and Pai, D.K., "Physically-based modeling and simulation of extraocular muscles", *Progress in Biophysics and Molecular Biology* 103, 273-283 (2010).
18. Nazari, M.A., Perrier, P., Chabanas, M. and Payan, Y., "Simulation of dynamic orofacial movements using a constitutive law varying with muscle activation", *Computer Methods in Biomechanics and Biomedical Engineering* 13, 469-482 (2010).
19. Dorfmann, A., Trimmer, B.A. and Woods, W.A., "A constitutive model for muscle properties in a soft-bodied arthropod", *Journal of The Royal Society Interface* 4, 257-269 (2007).
20. Tang, C.Y., Zhang, G. and Tsui, C.P., "A 3D skeletal muscle model coupled with active contraction of muscle fibres and hyperelastic behaviour", *Journal of Biomechanics* 42, 865-872 (2009).
21. Loocke Van, M., Lyons, C.G. and Simms, C.K., "A validated model of passive muscle in compression", *Journal of Biomechanics* 39, 2999-3009 (2006).

22. Takaza, M., Moerman, K.M., Gindre, J., Lyons, C.G. and Simms, C.K., "The anisotropic mechanical behaviour of passive skeletal muscle tissue subjected to large tensile strain", *Journal of the Mechanical Behavior of Biomedical Materials* (in review).
23. Blemker, S.S., Pinsky, P.M. and Delp, S.L., "A 3D model of muscle reveals the causes of nonuniform strains in the biceps brachii", *Journal of Biomechanics* 38, 657-665 (2005).
24. Calvo, B., Ramirez, A., Alonso, A., Grasa, J., Soteras, F., Osta, R. and Muñoz, M.J., "Passive nonlinear elastic behaviour of skeletal muscle: Experimental results and model formulation", *Journal of Biomechanics* 43, 318-325 (2010).
25. Sinkus, R., Siegmann, K., Xydeas, T., Tanter, M., Claussen, C.D. and Fink, M., "MR elastography of breast lesions: Understanding the solid/liquid duality can improve the specificity of contrast-enhanced MR mammography", *Magnetic Resonance in Medicine* 58, 1135-1144 (2007).
26. Loerakker, S., Stekelenburg, A., Strijkers, G., Rijpkema, J., Baaijens, F., Bader, D., Nicolay, K. and Oomens, C., "Temporal Effects of Mechanical Loading on Deformation-Induced Damage in Skeletal Muscle Tissue", *Annals of Biomedical Engineering* 38, 2577-2587 (2010).
27. Deprez, J., "On the potential of ultrasound elastography for pressure ulcer early detection", *Med. Phys.* 38, 1943 (2011).
28. Ringleb, S.I., Bensamoun, S.F., Chen, Q., Manduca, A., An, K.-N. and Ehman, R.L., "Applications of magnetic resonance elastography to healthy and pathologic skeletal muscle", *Journal of Magnetic Resonance Imaging* 25, 301-309 (2007).
29. Muraki, T., Domire, Z.J., McCullough, M.B., Chen, Q. and An, K.-N., "Measurement of stiffness changes in immobilized muscle using magnetic resonance elastography", *Clinical Biomechanics* 25, 499-503 (2010).
30. Gefen, A., Gefen, N., Linder-Ganz, E. and Margulies, S.S., "In Vivo Muscle Stiffening Under Bone Compression Promotes Deep Pressure Sores", *Journal of Biomechanical Engineering* 127, 512-524 (2005).
31. Palevski, A., Glaich, I., Portnoy, S., Linder-Ganz, E. and Gefen, A., "Stress Relaxation of Porcine Gluteus Muscle Subjected to Sudden Transverse Deformation as Related to Pressure Sore Modeling", *Journal of Biomechanical Engineering* 128, 782-787 (2006).
32. Manduca, A., Oliphant, T.E., Dresner, M.A., Mahowald, J.L., Kruse, S.A., Amromin, E., Felmlee, J.P., Greenleaf, J.F. and Ehman, R.L., "Magnetic resonance elastography: Non-invasive mapping of tissue elasticity", *Medical Image Analysis* 5, 237-254 (2001).
33. Froeling, M., Oudeman, J., van den Berg, S., Nicolay, K., Maas, M., Strijkers, G.J., Drost, M.R. and Nederveen, A.J., "Reproducibility of diffusion tensor imaging in human forearm muscles at 3.0 T in a clinical setting", *Magnetic Resonance in Medicine* 64, 1182-1190 (2010).
34. Ozturk, C., Derbyshire, J.A. and McVeigh, E.R., "Estimating Motion from MRI Data", *Proceedings of the IEEE* 91, 1627-1648 (2003).
35. Elhawary, H., Tse, Z.T.H., Hamed, A., Rea, M., Davies, B.L. and Lamperth, M.U., "The case for MR-compatible robotics: a review of the state of the art", *The International Journal of Medical Robotics and Computer Assisted Surgery* 4, 105-113 (2008).
36. Yu, N. and Riener, R., "Review on MR-Compatible Robotic Systems", presented at the Biomedical Robotics and Biomechatronics, 2006. BioRob 2006. The First IEEE/RAS-EMBS International Conference on, Pisa, Italy, 2006.
37. Hamed, A., Tse, Z., Young, I. and Lamperth, M., "MR Compatible Tactile Sensing and Noise Analysis in a 1.5 Tesla MR System", in *Medical Imaging and Augmented Reality*, (2008), pp. 220-230.
38. Park, Y.-L., Elayaperumal, S., Daniel, B., Seok Chang, R., Mihye, S., Savall, J., Black, R.J., Moslehi, B. and Cutkosky, M.R., "Real-Time Estimation of 3-D Needle Shape and Deflection for MRI-Guided Interventions", *Mechatronics, IEEE/ASME Transactions on* 15, 906-915 (2010).
39. Song, H., Kim, K. and Lee, J., "Development of optical fiber Bragg grating force-reflection sensor system of medical application for safe minimally invasive robotic surgery", *Rev. Sci. Instrum.* 82, 074301 (2011).
40. Polygerinos, P., Zbyszewski, D., Schaeffter, T., Razavi, R., Seneviratne, L.D. and Althoefer, K., "MRI-Compatible Fiber-Optic Force Sensors for Catheterization Procedures", *Sensors Journal, IEEE* 10, 1598-1608 (2010).
41. Rogers, B., Zhang, W., Narayana, S., Lancaster, J.L., Robin, D.A. and Fox, P.T., "Force sensing system for automated assessment of motor performance during fMRI", *Journal of Neuroscience Methods* 190, 92-94 (2010).
42. Briggs, R.W., Dy-Liacco, I., Malcolm, M.P., Lee, H., Peck, K.K., Gopinath, K.S., Himes, N.C., Soltysik, D.A., Browne, P. and Tran-Son-Tay, R., "A pneumatic vibrotactile stimulation device for fMRI", *Magnetic Resonance in Medicine* 51, 640-643 (2004).
43. Stekelenburg, A., Oomens, C.W.J., Strijkers, G.J., de Graaf, L., Bader, D.L. and Nicolay, K., "A new MR-compatible loading device to study in vivo muscle damage development in rats due to compressive loading", *Medical Engineering & Physics* 28, 331-338 (2006).

44. Frøkjær, J.B., Drewes, A.M. and Gregersen, H., "Imaging of the gastrointestinal tract-novel technologies", World Journal of Gastroenterology 15, 160-168 (2009).
45. Kovacs, A., Hadjiev, J., Lakosi, F., Antal, G., Vandulek, C., Somogyine Ezer, E., Bogner, P., Horvath, A. and Repa, I., "Dynamic MR Based Analysis of Tumor Movement in Upper and Mid Lobe Localized Lung Cancer", Pathology & Oncology Research 15, 269-277 (2009).
46. Herzka, D. and McVeigh, E., "MRI of myocardial infarction with tissue tagging", Current Cardiovascular Imaging Reports 2, 73-82 (2009).
47. Yoshioka, I., Saiki, Y., Ichinose, A., Takase, K., Takahashi, S., Ohashi, T., Sato, M. and Tabayashi, K., "Tagged cine magnetic resonance imaging with a finite element model can predict the severity of retrosternal adhesions prior to redo cardiac surgery", J Thorac Cardiovasc Surg 137, 957-962 (2009).
48. Shehata, M., Cheng, S., Osman, N., Bluemke, D. and Lima, J., "Myocardial tissue tagging with cardiovascular magnetic resonance", Journal of Cardiovascular Magnetic Resonance 11, 55 (2009).
49. Axel, L., Montillo, A. and Kim, D., "Tagged Magnetic Resonance Imaging of the Heart: A Survey", Medical Image Analysis 9, 376-393 (2005).
50. Parthasarathy, V., Prince, J.L., Stone, M., Murano, E.Z. and NessAiver, M., "Measuring tongue motion from tagged cine-MRI using harmonic phase (HARP) processing", The Journal of the Acoustical Society of America 121, 491-504 (2007).
51. Sabet, A.A., Christoforou, E., Zatlín, B., Genin, G.M. and Bayly, P.V., "Deformation of the human brain induced by mild angular head acceleration", Journal of Biomechanics 41, 307-315 (2008).
52. Piccirelli, M., Luechinger, R., Sturm, V., Boesiger, P., Landau, K. and Bergamin, O., "Local Deformation of Extraocular Muscles during Eye Movement", Invest. Ophthalmol. Vis. Sci. 50, 5189-5196 (2009).
53. Itskov, M., *Tensor Algebra and Tensor Analysis for Engineers*, 2 ed. (Springer, 2009).
54. Spencer, A.J.M., *Continuum Mechanics*. (Dover Publications Inc., 2004).
55. Chandrasekharaiah, D.S. and Debnath, L., *Continuum Mechanics*. (Academic Press Inc., San Diego, 1994).
56. Holzapfel, G.A., *Nonlinear Solid Mechanics, A continuum approach for engineering*. (John Wiley & Sons Ltd., 2004).
57. Ogden, R.W., *Non-linear Elastic Deformations*. (Dover Publications Inc., Mineola, New York, 1997).
58. McDonald, P.H., *Continuum mechanics*. (International Thomson Publishing, PWS Publishing Company, Boston, MA, USA, 1996).
59. Dill, E.H., *Continuum Mechanics. Elasticity, Plasticity, Viscoelasticity*. (CRC Press, Taylor & Francis Group, Boca Raton, 2007).
60. Rivlin, R.S. and Saunders, D.W., "Large Elastic Deformations of Isotropic Materials. VII. Experiments on the Deformation of Rubber", Philosophical Transactions of the Royal Society of London. Series A, Mathematical and Physical Sciences 243, 251-288 (1951).
61. Ogden, R.W., Saccomandi, G. and Sgura, I., "Fitting hyperelastic models to experimental data", Computational Mechanics 34, 484-502 (2004).
62. Ogden, R.W., "Large Deformation Isotropic Elasticity - On the Correlation of Theory and Experiment for Incompressible Rubberlike Solids", Proceedings of the Royal Society of London. Series A, Mathematical and Physical Sciences 326, 565-584 (1972).
63. Ehret, A. and Itskov, M., "A polyconvex hyperelastic model for fiber-reinforced materials in application to soft tissues", Journal of Materials Science 42, 8853-8863 (2007).
64. Ateshian, G.A., Rajan, V., Chahine, N.O., Canal, C.E. and Hung, C.T., "Modeling the Matrix of Articular Cartilage Using a Continuous Fiber Angular Distribution Predicts Many Observed Phenomena", Journal of Biomechanical Engineering 131, 061003-061010 (2009).
65. Ateshian, G.A., Ellis, B.J. and Weiss, J.A., "Equivalence Between Short-Time Biphasic and Incompressible Elastic Material Responses", Journal of Biomechanical Engineering 129, 405-412 (2007).
66. Criscione, J.C., Douglas, A.S. and Hunter, W.C., "Physically based strain invariant set for materials exhibiting transversely isotropic behavior", Journal of the Mechanics and Physics of Solids 49, 871-897 (2001).
67. Fung, Y.C., *Biomechanics, Mechanical Properties of Living Tissues*. (Springer-Verlag New York Inc., New York, 1993).
68. Drapaca, C.S., Sivaloganathan, S. and Tenti, G., "Nonlinear Constitutive Laws in Viscoelasticity", Mathematics and Mechanics of Solids 12, 475-501 (2007).
69. Fung, Y.C., *Stress-Strain-History Relations of Soft Tissues in Simple Elongation*. In: Y.C. Fung, N. Perrone and M. Anliker, Editors, *Biomechanics: Its Foundations and Objectives*. (Prentice-Hall, Englewood Cliffs, NJ., 1972).
70. Puso, M.A. and Weiss, J.A., "Finite Element Implementation of Anisotropic Quasi-Linear Viscoelasticity Using a Discrete Spectrum Approximation", Journal of Biomechanical Engineering 120, 62-70 (1998).
71. Haacke, E.M., Brown, R.W., Thompson, M.R. and Venkatesan, R., *Magnetic Resonance Imaging: Physical Principles and Sequence Design*. (John Wiley & Sons, Inc., 1999).

72. Cowan, B.P., *Nuclear Magnetic Resonance and Relaxation*, Paperback 2005 ed. (Cambridge University Press, 1997).
73. Suetens, P., Man De, B., D'hooge, J., Maes, F., Michiels, J., Nuyts, J., Cleynenbreugel Van, J. and Velde Vande, K., *Fundamentals of Medical Imaging*, Reprinted 2005 ed. (Cambridge University Press, 2002).
74. Gold, G.E., Han, E., Stainsby, J., Wright, G., Brittain, J. and Beaulieu, C., "Musculoskeletal MRI at 3.0 T: Relaxation Times and Image Contrast", *Am. J. Roentgenol.* 183, 343-351 (2004).
75. de Bazelaire, C.M.J., Duhamel, G.D., Rofsky, N.M. and Alsop, D.C., "MR Imaging Relaxation Times of Abdominal and Pelvic Tissues Measured in Vivo at 3.0 T: Preliminary Results", *Radiology* 230, 652-659 (2004).
76. Stanisz, G.J., Odobina, E.E., Pun, J., Escaravage, M., Graham, S.J., Bronskill, M.J. and Henkelman, R.M., "T1, T2 relaxation and magnetization transfer in tissue at 3T", *Magnetic Resonance in Medicine* 54, 507-512 (2005).
77. Smith, H.E., Mosher, T.J., Dardzinski, B.J., Collins, B.G., Collins, C.M., Yang, Q.X., Schmithorst, V.J. and Smith, M.B., "Spatial variation in cartilage T2 of the knee", *Journal of Magnetic Resonance Imaging* 14, 50-55 (2001).
78. Mori, S. and Zhang, J., "Principles of Diffusion Tensor Imaging and Its Applications to Basic Neuroscience Research", *Neuron* 51, 527-539 (2006).
79. Berquist, T.H., *MRI of the musculoskeletal system*, Fifth edition ed. (Lippincott Williams & Wilkins, Philadelphia, PA, USA, 2006).
80. Blemker, S.S., Asakawa, D.S., Gold, G.E. and Delp, S.L., "Image-based musculoskeletal modeling: Applications, advances, and future opportunities", *Journal of Magnetic Resonance Imaging* 25, 441-451 (2007).
81. Manning, W.J. and Pennell, D.J., *Cardiovascular Magnetic Resonance*. (Churchill Livingstone, 2002).
82. Axel, L., "Biomechanical Dynamics of the Heart with MRI", *Annual Review of Biomedical Engineering* 4, 321-347 (2002).
83. Sundgren, P.C., "Diffusion Tensor Imaging of the Brain: Background and Review of Clinical Applications", *Imaging Decisions MRI* 9, 2-15 (2005).
84. Augenstein, K., Cowan, B., LeGrice, I. and Young, A., "Estimation of Cardiac Hyperelastic Material Properties from MRI Tissue Tagging and Diffusion Tensor Imaging", in *Medical Image Computing and Computer-Assisted Intervention – MICCAI 2006*, Vol. 4190, edited by R. Larsen, M. Nielsen and J. Sporring (Springer Berlin / Heidelberg, 2006), pp. 628-635.
85. Zhukov, L. and Barr, A.H., "Heart-muscle fiber reconstruction from diffusion tensor MRI", in *Proceedings of the 14th IEEE Visualization 2003*, (IEEE Computer Society Washington, DC, USA, Seattle, Washinton, USA, 2003), pp. 597-602.
86. Dou, J., Reese, T.G., Tseng, W.-Y.I. and Wedeen Van, J., "Cardiac diffusion MRI without motion effects", *Magnetic Resonance in Medicine* 48, 105-114 (2002).
87. Lansdown, D.A., Ding, Z., Wadington, M., Hornberger, J.L. and Damon, B.M., "Quantitative diffusion tensor MRI-based fiber tracking of human skeletal muscle", *J Appl Physiol* 103, 673-681 (2007).
88. Gilbert, R.J., Magnusson, L.H., Napadow, V.J., Benner, T., Wang, R. and Wedeen, V.J., "Mapping Complex Myoarchitecture in the Bovine Tongue with Diffusion-Spectrum Magnetic Resonance Imaging", *Biophysical Journal* 91, 1014-1022 (2006).
89. Zarskaya, T., Kumbhare, D. and Noseworthy, M.D., "Diffusion tensor imaging in evaluation of human skeletal muscle injury", *Journal of Magnetic Resonance Imaging* 24, 402-408 (2006).
90. Heemskerk, A.M., Strijkers, G.J., Vilanova, A., Drost, M.R. and Nicolay, K., "Determination of mouse skeletal muscle architecture using three-dimensional diffusion tensor imaging", *Magnetic Resonance in Medicine* 53, 1333-1340 (2005).
91. Galbán, C.J., Maderwald, S., Uffmann, K., Greiff de, A. and Ladd, M.E., "Diffusive sensitivity to muscle architecture: a magnetic resonance diffusion tensor imaging study of the human calf", *European Journal of Applied Physiology* V93, 253-262 (2004).
92. Damon, B.M., Ding, Z., Anderson, A.W., Freyer, A.S. and Gore, J.C., "Validation of diffusion tensor MRI-based muscle fiber tracking", *Magnetic Resonance in Medicine* 48, 97-104 (2002).
93. Sinha, U. and Yao, L., "In vivo diffusion tensor imaging of human calf muscle", *Journal of Magnetic Resonance Imaging* 15, 87-95 (2002).
94. Wedeen Van, J., Reese, T.G., Napadow, V.J. and Gilbert, R.J., "Demonstration of Primary and Secondary Muscle Fiber Architecture of the Bovine Tongue by Diffusion Tensor Magnetic Resonance Imaging", *Biophysical Journal* 80, 1024-1028 (2001).
95. Napadow, V.J., Chen, Q., Mai, V., So, P.T.C. and Gilbert, R.J., "Quantitative Analysis of Three-Dimensional-Resolved Fiber Architecture in Heterogeneous Skeletal Muscle Tissue Using NMR and Optical Imaging Methods", *Biophysical Journal* 80, 2968-2975 (2001).
96. Donkelaar van, C.C., Kretzers, L.J.G., Bovendeerd, P.H.M., Lataster, L.M.A., Nicolay, K., Janssen, J.D. and Drost, M.R., "Diffusion tensor imaging in biomechanical studies of skeletal muscle function", *Journal of Anatomy* 194, 79-88 (1999).

- 97.** Visser De, S.K., Crawford, R.W. and Pope, J.M., "*Structural adaptations in compressed articular cartilage measured by diffusion tensor imaging*", *Osteoarthritis and Cartilage* 16, 83-89 (2008).
- 98.** Mori, S. and Zijl Van, P.C.M., "*Fiber tracking: principles and strategies - a technical review*", *NMR in Biomedicine* 15, 468-480 (2002).
- 99.** Masutani, Y., Aoki, S., Abe, O., Hayashi, N. and Otomo, K., "*MR diffusion tensor imaging: recent advance and new techniques for diffusion tensor visualization*", *European Journal of Radiology* 46, 53-66 (2003).
- 100.** Basser, P.J. and Jones, D.K., "*Diffusion-tensor MRI: Theory, Experimental Design and data analysis - a technical review*", *NMR in Biomedicine, Diffusion tensor imaging and axonal mapping - state of the art* 15, 456-467 (2002).
- 101.** Gatehouse, P.D., Keegan, J., Crowe, L.A., Masood, S., Mohiaddin, R.H., Kreitner, K.-F. and Firmin, D.N., "*Applications of phase-contrast flow and velocity imaging in cardiovascular MRI*", *European Radiology* V15, 2172-2184 (2005).
- 102.** Jung, B., Markl, M., Foll, D. and Hennig, J., "*Investigating myocardial motion by MRI using tissue phase mapping*", *Eur J Cardiothorac Surg* 29, S150-157 (2006).
- 103.** Jung, B.A., Kreher, B.W., Markl, M. and Hennig, J., "*Visualization of tissue velocity data from cardiac wall motion measurements with myocardial fiber tracking: principles and implications for cardiac fiber structures*", *Eur J Cardiothorac Surg* 29, S158-164 (2006).
- 104.** Petersen, S.E., Jung, B.A., Wiesmann, F., Selvanayagam, J.B., Francis, J.M., Hennig, J., Neubauer, S. and Robson, M.D., "*Myocardial Tissue Phase Mapping with Cine Phase-Contrast MR Imaging: Regional Wall Motion Analysis in Healthy Volunteers*", *Radiology* 238, 816-826 (2006).
- 105.** Selskog, P., Heiberg, E., Ebbers, T., Wigstrom, L. and Karlsson, M., "*Kinematics of the heart: strain-rate imaging from time-resolved three-dimensional phase contrast MRI*", *Medical Imaging, IEEE Transactions on* 21, 1105-1109 (2002).
- 106.** Markl, M., Schneider, B. and Hennig, J., "*Fast phase contrast cardiac magnetic resonance imaging: Improved assessment and analysis of left ventricular wall motion*", *Journal of Magnetic Resonance Imaging* 15, 642-653 (2002).
- 107.** Wedding, K.L., Draney, M.T., Herfkens, R.J., Zarins, C.K., Taylor, C.A. and Pelc, N.J., "*Measurement of vessel wall strain using cine phase contrast MRI*", *Journal of Magnetic Resonance Imaging* 15, 418-428 (2002).
- 108.** Jung, B., Föll, D., Böttler, P., Petersen, S., Hennig, J. and Markl, M., "*Detailed analysis of myocardial motion in volunteers and patients using high-temporal-resolution MR tissue phase mapping*", *Journal of Magnetic Resonance Imaging* 24, 1033-1039 (2006).
- 109.** Markl, M., Bammer, R., Alley, M.T., Elkins, C.J., Draney, M.T., Barnett, A., Moseley, M.E., Glover, G.H. and Pelc, N.J., "*Generalized reconstruction of phase contrast MRI: Analysis and correction of the effect of gradient field distortions*", *Magnetic Resonance in Medicine* 50, 791-801 (2003).
- 110.** Markl, M., Chan, F.P., Alley, M.T., Wedding, K.L., Draney, M.T., Elkins, C.J., Parker, D.W., Wicker, R., Taylor, C.A., Herfkens, R.J. and Pelc, N.J., "*Time-resolved three-dimensional phase-contrast MRI*", *Journal of Magnetic Resonance Imaging* 17, 499-506 (2003).
- 111.** Sinha, S., Hodgson, J.A., Finni, T., Lai, A.M., Grinstead, J. and Edgerton, V.R., "*Muscle kinematics during isometric contraction: Development of phase contrast and spin tag techniques to study healthy and atrophied muscles*", *Journal of Magnetic Resonance Imaging* 20, 1008-1019 (2004).
- 112.** Zhou, H. and Novotny, J.E., "*Cine phase contrast MRI to measure continuum Lagrangian finite strain fields in contracting skeletal muscle*", *Journal of Magnetic Resonance Imaging* 25, 175-184 (2007).
- 113.** Asakawa, D.S., Papas, P., Blemker, S.S., Drace, J.E. and Delp, S.L., "*Cine Phase-Contrast Magnetic Resonance Imaging As a Tool for Quantification of Skeletal Muscle Motion*", *Seminars in musculoskeletal radiology* 7, 287-295 (2003).
- 114.** Asakawa, D.S., Nayak, K.S., Blemker, S.S., Delp, S.L., Nishimura, D.G. and Gold, G.E., "*Real-Time Imaging of Skeletal Muscle Velocity*", *Journal of Magnetic Resonance Imaging* 18, 734-739 (2003).
- 115.** Drace, J.E. and Pelc, N.J., "*Skeletal muscle contraction: analysis with use of velocity distributions from phase-contrast MR imaging*", *Radiology* 193, 423-429 (1994).
- 116.** Bensamoun, S.F., Ringleb, S.I., Littrell, L., Chen, Q., Brennan, M., Ehman, R.L. and An, K.-N., "*Determination of Thigh Muscle Stiffness Using Magnetic Resonance Elastography*", *Journal of Magnetic Resonance Imaging* 23, 242-247 (2006).
- 117.** Papazoglou, S., Rump, J., Braun, J. and Sack, I., "*Shear wave group velocity inversion in MR elastography of human skeletal muscle*", *Magnetic Resonance in Medicine* 56, 489-497 (2006).
- 118.** Bensamoun, S., Glaser, K., Chen, Q., Ringleb, S., Ehman, R. and An, K.N., "*Rapid magnetic resonance elastography of skeletal muscle using one dimensional projection*", *Journal of Biomechanics* 39, S37-S37 (2006).
- 119.** Uffmann, K., Maderwald, S., Ajaj, W., Galban, C.G., Mateiescu, S., Quick, H.H. and Ladd, M.E., "*In vivo elasticity measurements of extremity skeletal muscle with MR elastography*", *NMR in Biomedicine* 17, 181-190 (2004).

- 120.** Catheline, S., Gennisson, J.L., Delon, G., Fink, M., Sinkus, R., Abouelkaram, S. and Culioli, J., "Measurement of viscoelastic properties of homogeneous soft solid using transient elastography: An inverse problem approach", *The Journal of the Acoustical Society of America* 116, 3734-3741 (2004).
- 121.** Basford, J.R., Jenkyn, T.R., An, K.-N., Ehman, R.L., Heers, G. and Kaufman, K.R., "Evaluation of Healthy and Diseased Muscle With Magnetic Resonance Elastography", *Archives of Physical Medicine and Rehabilitation* 83, 1530-1536 (2002).
- 122.** Sinkus, R., Tanter, M., Catheline, S., Lorenzen, J., Kuhl, C., Sondermann, E. and Fink, M., "Imaging anisotropic and viscous properties of breast tissue by magnetic resonance-elastography", *Magnetic Resonance in Medicine* 53, 372-387 (2005).
- 123.** Morse, O.C. and Singer, J.R., "Blood Velocity Measurements in Intact Subjects", *Science* 170, 440-441 (1970).
- 124.** Zerhouni, E.A., Parish, D.M., Rogers, W.J., Yang, A. and Shapiro, E.P., "Human heart: tagging with MR imaging--a method for noninvasive assessment of myocardial motion", *Radiology* 169, 59-63 (1988).
- 125.** Axel, L. and Dougherty, L., "MR Imaging of Motion with Spatial Modulation of Magnetization", *Radiology* 171, 841-845 (1989).
- 126.** Axel, L. and Dougherty, L., "Heart wall motion: improved method of spatial modulation of magnetization for MR imaging", *Radiology* 172, 349-350 (1989).
- 127.** Fischer, S.E. and McKinnon, S.E., "Improved myocardial tagging contrast", *Magnetic Resonance Medicine* 30, 191-200 (1993).
- 128.** Mosher, T.J. and Smith, M.B., "A DANTE tagging sequence for the evaluation of translational sample motion", *Magnetic Resonance in Medicine* 15, 334-339 (1990).
- 129.** Aletras, A.H., Ding, S., Balaban, R.S. and Wen, H., "DENSE: Displacement Encoding with Stimulated Echoes in Cardiac Functional MRI", *Journal of Magnetic Resonance* 137, 247-252 (1999).
- 130.** Osman, N.F., Kerwin, W.S., McVeigh, E.R. and Prince, J.L., "Cardiac Motion Tracking Using CINE Harmonic Phase (HARP) Magnetic Resonance Imaging", *Magnetic Resonance Imaging in Medicine* 42, 1048-1060 (1999).
- 131.** Atalar, E. and McVeigh, E.R., "Optimization of tag thickness for measuring position with magnetic resonance imaging", *Medical Imaging, IEEE Transactions on* 13, 152-160 (1994).
- 132.** Gonzalez, R.C., Woods, R.E. and Eddins, S.L., *Digital Image Processing using Matlab*, 3 ed. (Pearson, Prentice Hall, 2004).
- 133.** Gonzalez, R.C. and Woods, R.E., *Digital Image Processing*, 3 ed. (Pearson, Prentice Hall, New Jersey, 2008).
- 134.** Holden, M., "A Review of Geometric Transformations for Nonrigid Body Registration", *Medical Imaging, IEEE Transactions on* 27, 111-128 (2008).
- 135.** Helm, J., "Three-dimensional image correlation for surface-displacement measurement", *Proc. SPIE* 2350, 32 (1994).
- 136.** Crum, W.R., Hartkens, T. and Hill, D.L.G., "Non-rigid image registration: theory and practice", *Br J Radiol* 77, S140-153 (2004).
- 137.** Vignos, P.J. and Lefkowitz, M., "A Biochemical Study of Certain Skeletal Muscle Constituents in Human Progressive Muscular Dystrophy", *The Journal of Clinical Investigation* 38, 873-881 (1959).
- 138.** Bendall, J.R., "The elastin content of various muscles of beef animals", *Journal of the Science of Food and Agriculture* 18, 553-558 (1967).
- 139.** Martini, F.H., *Fundamentals of Anatomy & Physiology*, 7 ed. (Pearson Education Inc., Benjamin Cummings, San Francisco, USA, 2006).
- 140.** Clark, K.A., McElhinny, A.S., Beckerle, M.C. and Gregorio, C.C., "Striated Muscle Cytoarchitecture: An Intricate Web of Form and Function", *Annual Review of Cell and Developmental Biology* 18, 637-706 (2002).
- 141.** Drake, R.L., Wayne, V. and Mitchell, A.W.M., *Gray's Anatomy for Students*. (Elsevier Inc., Churchill Livingstone, Philadelphia, USA, 2005).
- 142.** "InterActive Physiology CD-Rom, version 1.1.", in *Fundamentals of Anatomy & Physiology*, (Pearson Education Inc., Benjamin Cummings, 2006).
- 143.** Purslow, P.P., "The extracellular matrix of skeletal and cardiac muscle", in *Collagen: Structure and Mechanics Vertebrates*, edited by P. Fratzl (Springer New York, 2008), pp. 325-358.
- 144.** Passerieux, E., Rossignol, R., Chopard, A., Carnino, A., Marini, J.F., Letellier, T. and Delage, J.P., "Structural organization of the perimysium in bovine skeletal muscle: Junctional plates and associated intracellular subdomains", *Journal of Structural Biology* 154, 206-216 (2006).
- 145.** Purslow, P.P. and Trotter, J.A., "The morphology and mechanical properties of endomysium in series-fibred muscles: variations with muscle length", *Journal of Muscle Research and Cell Motility* 15, 299-308 (1994).
- 146.** Gao, Y., Waas, A.M., Faulkner, J.A., Kostrominova, T.Y. and Wineman, A.S., "Micromechanical modeling of the epimysium of the skeletal muscles", *Journal of Biomechanics* 41, 1-10 (2008).

- 147.** Wang, K., McCarter, R., Wright, J., Beverly, J. and Ramirez-Mitchell, R., "Viscoelasticity of the sarcomere matrix of skeletal muscles. The titin-myosin composite filament is a dual-stage molecular spring", *Biophys. J.* 64, 1161-1177 (1993).
- 148.** Labeit, D., Watanabe, K., Witt, C., Fujita, H., Wu, Y., Lahmers, S., Funck, T., Labeit, S. and Granzier, H., "Calcium-dependent molecular spring elements in the giant protein titin", *Proceedings of the National Academy of Sciences* 100, 13716-13721 (2003).
- 149.** Minajeva, A., Kulke, M., Fernandez, J.M. and Linke, W.A., "Unfolding of Titin Domains Explains the Viscoelastic Behavior of Skeletal Myofibrils", *Biophys. J.* 80, 1442-1451 (2001).
- 150.** Ranatunga, K.W., "Sarcomeric visco-elasticity of chemically skinned skeletal muscle fibres of the rabbit at rest", *Journal of Muscle Research and Cell Motility* 22, 399-414 (2001).
- 151.** Kobayashi, M., Takemori, S. and Yamaguchi, M., "Differential rigor development in red and white muscle revealed by simultaneous measurement of tension and stiffness", *Forensic Science International* 140, 79-84 (2004).
- 152.** Bear, M.F., Connors, B.W. and Paradiso, M.A., *Neuroscience, Exploring the brain*, 3 ed. (Lippincott Williams & Wilkins, Baltimore, MD, USA, 2007).
- 153.** Waterhouse, J. and Campbell, I., "Reflexes: principles and properties", *Anaesthesia & Intensive Care Medicine* 9, 210-215 (2008).
- 154.** Windhorst, U., "Muscle proprioceptive feedback and spinal networks", *Brain Research Bulletin* 73, 155-202 (2007).
- 155.** Christensen, M., Kok, C. and Ertbjerg, P., "Mechanical properties of type I and type IIB single porcine muscle fibres", *Meat Science* 73, 422-425 (2006).
- 156.** Mutungi, G. and Ranatunga, K.W., "Temperature-dependent changes in the viscoelasticity of intact resting mammalian (rat) fast- and slow-twitch muscle fibres", *J Physiol* 508, 253-265 (1998).
- 157.** Mutungi, G. and Ranatunga, K.W., "The viscous, viscoelastic and elastic characteristics of resting fast and slow mammalian (rat) muscle fibres", *J Physiol* 496, 827-836 (1996).
- 158.** Looke Van, M., Lyons, C.G. and Simms, C.K., "Viscoelastic properties of passive skeletal muscle in compression: Stress-relaxation behaviour and constitutive modelling", *Journal of Biomechanics* 41, 1555-1566 (2008).
- 159.** Looke Van, M., Simms, C.K. and Lyons, C.G., "Viscoelastic properties of passive skeletal muscle in compression--Cyclic behaviour", *Journal of Biomechanics* 42, 1038-1048 (2009).
- 160.** Grieve, A.P. and Armstrong, C.G., *Compressive properties of soft tissues*. (Free University Press, Amsterdam, 1988).
- 161.** Aïmeidieu, P., Mitton, D., Faure, J.P., Denninger, L. and Lavaste, F., "Dynamic Stiffness and Damping of Porcine Muscle Specimens", *Medical Engineering & Physics* 25, 795-799 (2003).
- 162.** Sligtenhorst Van, C., Cronin, D.S. and Wayne Brodland, G., "High strain rate compressive properties of bovine muscle tissue determined using a split Hopkinson bar apparatus", *Journal of Biomechanics* 39, 1852-1858 (2006).
- 163.** Song, B., Chen, W., Ge, Y. and Weerasooriya, T., "Dynamic and quasi-static compressive response of porcine muscle", *Journal of Biomechanics* 40, 2999-3005 (2007).
- 164.** Bosboom, E.M.H., Hesselink, M.K.C., Oomens, C.W.J., Bouten, C.V.C., Drost, M.R. and Baaijens, F.P.T., "Passive transverse mechanical properties of skeletal muscle under in vivo compression", *Journal of Biomechanics* 34, 1365-1368 (2001).
- 165.** Davis, J., Kaufman, K.R. and Lieber, R.L., "Correlation between active and passive isometric force and intramuscular pressure in the isolated rabbit tibialis anterior muscle", *Journal of Biomechanics* 36, 505-512 (2003).
- 166.** Nie, X., Cheng, J.-I., Chen, W.W. and Weerasooriya, T., "Dynamic Tensile Response of Porcine Muscle", *Journal of Applied Mechanics* 78, 021009-021005 (2011).
- 167.** Morrow, D.A., Haut Donahue, T.L., Odegard, G.M. and Kaufman, K.R., "Transversely isotropic tensile material properties of skeletal muscle tissue", *Journal of the Mechanical Behavior of Biomedical Materials* 3, 124-129 (2010).
- 168.** Grasa, J., Ramírez, A., Osta, R., Muñoz, M., Soteras, F. and Calvo, B., "A 3D active-passive numerical skeletal muscle model incorporating initial tissue strains. Validation with experimental results on rat tibialis anterior muscle", *Biomechanics and Modeling in Mechanobiology* 10, 779-787 (2011).
- 169.** Zheng, Y.-p. and Mak, A.F., "Effective elastic properties for lower limb soft tissues from manual indentation experiment", *IEEE Transactions on Rehabilitation Engineering* 7, 257-267 (1999).
- 170.** Vannah, W.M. and Childress, D.S., "Indentor tests and finite element modeling of bulk muscular tissue in vivo", *Journal of Rehabilitation Research and Development Service* 33, 239-252 (1996).
- 171.** Tonuk, E. and Silver-Thorn, M.B., "Nonlinear Viscoelastic Material Property Estimation of Lower Extremity Residual Limb Tissues", *Journal of Biomechanical Engineering* 126, 289-300 (2004).
- 172.** Dubuis, L., Avril, S., Debayle, J. and Badel, P., "Identification of the material parameters of soft tissues in the compressed leg", *Computer Methods in Biomechanics and Biomedical Engineering*, 1-9 (2011).

- 173.** Tran, H.V., Charleux, F., Rachik, M., Ehrlacher, A. and Ho Ba Tho, M.C., "In vivo characterization of the mechanical properties of human skin derived from MRI and indentation techniques", *Computer Methods in Biomechanics and Biomedical Engineering* 10, 401-407 (2007).
- 174.** Ceelen, K.K., Stekelenburg, A., Mulders, J.L.J., Strijkers, G.J., Baaijens, F.P.T., Nicolay, K. and Oomens, C.W.J., "Validation of a Numerical Model of Skeletal Muscle Compression With MR Tagging: A Contribution to Pressure Ulcer Research", *Journal of Biomechanical Engineering* 130, 061015-061018 (2008).
- 175.** Pappas, G.P., Asakawa, D.S., Delp, S.L., Zajac, F.E. and Drace, J.E., "Nonuniform shortening in the biceps brachii during elbow flexion", *Journal of Applied Physiology* 92, 2381-2389 (2002).
- 176.** Parker, K.J. and et al., "Imaging the elastic properties of tissue: the 20 year perspective", *Physics in Medicine and Biology* 56, R1 (2011).
- 177.** Dresner, M.A., Rose, G.H., Rossman, P.J., Muthupillai, R., Manduca, A. and Ehman, R.L., "Magnetic resonance elastography of skeletal muscle", *Journal of Magnetic Resonance Imaging* 13, 269-276 (2001).
- 178.** Debernard, L., Robert, L., Charleux, F. and Bensamoun, S.F., "Analysis of thigh muscle stiffness from childhood to adulthood using magnetic resonance elastography (MRE) technique", *Clinical Biomechanics* 26, 836-840 (2011).
- 179.** Jenkyn, T.R., Ehman, R.L. and An, K.-N., "Noninvasive muscle tension measurement using the novel technique of magnetic resonance elastography (MRE)", *Journal of Biomechanics* 36, 1917-1921 (2003).
- 180.** Klatt, D., Papazoglou, S., Braun, J. and Sack, I., "Viscoelasticity-based MR elastography of skeletal muscle", *Physics in Medicine and Biology* 55, 6445 (2010).
- 181.** Levinson, S.F., Shinagawa, M. and Sato, T., "Sonoelastic determination of human skeletal muscle elasticity", *Journal of Biomechanics* 28, 1145-1154 (1995).
- 182.** Gennisson, J.L., Cornu, C., Catheline, S., Fink, M. and Portero, P., "Human muscle hardness assessment during incremental isometric contraction using transient elastography", *Journal of Biomechanics* 38, 1543-1550 (2005).
- 183.** Perrinez, P.R., Kennedy, F.E., Van Houten, E.E.W., Weaver, J.B. and Paulsen, K.D., "Modeling of Soft Poroelastic Tissue in Time-Harmonic MR Elastography", *Biomedical Engineering, IEEE Transactions on* 56, 598-608 (2009).
- 184.** Doyley, M.M., "The performance of steady-state harmonic magnetic resonance elastography when applied to viscoelastic materials", *Med. Phys.* 37, 3970 (2010).
- 185.** Baghani, A., Salcudean, S. and Rohling, R., "Theoretical limitations of the elastic wave equation inversion for tissue elastography", *The Journal of the Acoustical Society of America* 126, 1541-1551 (2009).
- 186.** Gennisson, J.-L., Deffieux, T., Macé, E., Montaldo, G., Fink, M. and Tanter, M., "Viscoelastic and Anisotropic Mechanical Properties of in vivo Muscle Tissue Assessed by Supersonic Shear Imaging", *Ultrasound in Medicine & Biology* 36, 789-801 (2010).
- 187.** Rouviere, O., Yin, M., Dresner, M.A., Rossman, P.J., Burgart, L.J., Fidler, J.L. and Ehman, R.L., "MR Elastography of the Liver: Preliminary Results", *Radiology* 240, 440-448 (2006).
- 188.** Schröder, J. and Neff, P., "Invariant formulation of hyperelastic transverse isotropy based on polyconvex free energy functions", *International Journal of Solids and Structures* 40, 401-445 (2003).
- 189.** Odegard, G.M., Donahue, T.L.H., Morrow, D.A. and Kaufman, K.R., "Constitutive Modeling of Skeletal Muscle Tissue With an Explicit Strain-Energy Function", *Journal of Biomechanical Engineering* 130, 061017-061019 (2008).
- 190.** Ehret, A.E., Böl, M. and Itskov, M., "A continuum constitutive model for the active behaviour of skeletal muscle", *Journal of the Mechanics and Physics of Solids* 59, 625-636 (2011).
- 191.** Hawkins, D. and Bey, M., "Muscle and tendon force-length properties and their interactions in vivo", *Journal of Biomechanics* 30, 63-70 (1997).
- 192.** Böl, M., Sturmat, M., Weichert, C. and Kober, C., "A new approach for the validation of skeletal muscle modelling using MRI data", *Computational Mechanics* 47, 591-601 (2011).
- 193.** Böl, M., "Micromechanical modelling of skeletal muscles: from the single fibre to the whole muscle", *Archive of Applied Mechanics* 80, 557-567 (2010).
- 194.** Sharafi, B. and Blemker, S.S., "A micromechanical model of skeletal muscle to explore the effects of fiber and fascicle geometry", *Journal of Biomechanics* 43, 3207-3213 (2010).
- 195.** Bischoff, J., "Reduced Parameter Formulation for Incorporating Fiber Level Viscoelasticity into Tissue Level Biomechanical Models", *Annals of Biomedical Engineering* 34, 1164-1172 (2006).
- 196.** DeFrate, L. and Li, G., "The prediction of stress-relaxation of ligaments and tendons using the quasi-linear viscoelastic model", *Biomechanics and Modeling in Mechanobiology* 6, 245-251 (2007).
- 197.** Ledoux, W.R. and Blevins, J.J., "The compressive material properties of the plantar soft tissue", *Journal of Biomechanics* 40, 2975-2981 (2007).
- 198.** Zhang, W., Liu, Y. and Kassab, G.S., "Viscoelasticity reduces the dynamic stresses and strains in the vessel wall: implications for vessel fatigue", *Am J Physiol Heart Circ Physiol* 293, H2355-2360 (2007).



- 199.** Snedeker, J.G., Niederer, P., Schmidlin, F.R., Farshad, M., Demetropoulos, C.K., Lee, J.B. and Yang, K.H., "Strain-rate dependent material properties of the porcine and human kidney capsule", *Journal of Biomechanics* 38, 1011-1021 (2005).
- 200.** Brands, D.W.A., Peters, G.W.M. and Bovendeerd, P.H.M., "Design and numerical implementation of a 3-D non-linear viscoelastic constitutive model for brain tissue during impact", *Journal of biomechanics* 37, 127-134 (2004).
- 201.** Mariappan, Y.K., Glaser, K.J. and Ehman, R.L., "Magnetic resonance elastography: A review", *Clinical Anatomy* 23, 497-511 (2010).
- 202.** Shellock, F.G., *Reference manual for magnetic resonance safety, implants, and devices: 2010 edition.* (Biomedical Research Publishing group, Los Angeles, 2010).
- 203.** Gassert, R., Yamamoto, A., Chapuis, D., Dovat, L., Bleuler, H. and Burdet, E., "Actuation methods for applications in MR environments", *Concepts in Magnetic Resonance Part B: Magnetic Resonance Engineering* 29B, 191-209 (2006).
- 204.** Gassert, R., Chapuis, D., Bleuler, H. and Burdet, E., "Sensors for Applications in Magnetic Resonance Environments", *Mechatronics, IEEE/ASME Transactions on* 13, 335-344 (2008).
- 205.** Ceelen, K.K., Stekelenburg, A., Loerakker, S., Strijkers, G.J., Bader, D.L., Nicolay, K., Baaijens, F.P.T. and Oomens, C.W.J., "Compression-induced damage and internal tissue strains are related", *Journal of Biomechanics* 41, 3399-3404 (2008).
- 206.** Tada, M., Nagai, N. and Maeno, T., "Material properties estimation of layered soft tissue based on MR observation and iterative FE simulation", *Med Image Comput Comput Assist Interv Int Conf Med Image Comput Comput Assist Interv* 8, 633-640 (2005).
- 207.** Tada, M., Nagai, N., Yoshida, H. and Maeno, T., "Iterative FE analysis for non-invasive material modeling of a fingertip with layered structure", presented at the EuroHaptics 2006, Paris, France, 2006.
- 208.** Then, C., Menger, J., Vogl, T.J., Hubner, F. and Silber, G., "Mechanical gluteal soft tissue material parameter validation under complex tissue loading", *Technol. Health Care* 17, 393-401 (2009).
- 209.** Fu, Y., Chui, C., Teo, C. and Kobayashi, E., "Motion Tracking and Strain Map Computation for Quasi-Static Magnetic Resonance Elastography", in *Medical Image Computing and Computer-Assisted Intervention – MICCAI 2011, Vol. 6891*, edited by G. Fichtinger, A. Martel and T. Peters (Springer Berlin / Heidelberg, 2011), pp. 428-435.
- 210.** Polygerinos, P., Puangmali, P., Schaeffter, T., Razavi, R., Seneviratne, L.D. and Althoefer, K., "Novel miniature MRI-compatible fiber-optic force sensor for cardiac catheterization procedures", in *Robotics and Automation (ICRA), 2010 IEEE International Conference on*, (IEEE, Anchorage, AK, USA, 2010), pp. 2598-2603.
- 211.** Tada, M. and Kanade, T., "Design of an MR-compatible three-axis force sensor", in *Intelligent Robots and Systems, 2005. (IROS 2005). 2005 IEEE/RSJ International Conference on*, (IEEE, 2005), pp. 3505-3510.
- 212.** O'Connell, G.D.B.S., Johannessen, W.P., Vresilovic, E.J.M.D.P. and Elliott, D.M.P., "Human Internal Disc Strains in Axial Compression Measured Noninvasively Using Magnetic Resonance Imaging", *Spine* 32, 2860-2868 (2007).
- 213.** Gilchrist, C.L., Xia, J.Q., Setton, L.A. and Hsu, E.W., "High-resolution determination of soft tissue deformations using MRI and first-order texture correlation", *Medical Imaging, IEEE Transactions on* 23, 546-553 (2004).
- 214.** Phatak, N., Sun, Q., Kim, S.-E., Parker, D., Sanders, R.K., Veress, A., Ellis, B. and Weiss, J., "Noninvasive Determination of Ligament Strain with Deformable Image Registration", *Annals of Biomedical Engineering* 35, 1175-1187 (2007).
- 215.** Nichol, A.M., Brock, K.K., Lockwood, G.A., Moseley, D.J., Rosewall, T., Warde, P.R., Catton, C.N. and Jaffray, D.A., "A magnetic resonance imaging study of prostate deformation relative to implanted gold fiducial markers", *International Journal of Radiation Oncology\*Biophysics* 67, 48-56 (2007).
- 216.** Moran, P.R., "A flow velocity zeugmatographic interlace for NMR imaging in humans", *Magnetic Resonance Imaging* 1, 197-203 (1982).
- 217.** McVeigh, E.R., "MRI of myocardial function: motion tracking techniques", *Magnetic Resonance Imaging* 14, 137-150 (1996).
- 218.** Cai, J., Sheng, K., Benedict, S.H., Read, P.W., Larner, J.M., Mugler III, J.P., de Lange, E.E., Cates Jr, G.D. and Miller, G.W., "Dynamic MRI of Grid-Tagged Hyperpolarized Helium-3 for the Assessment of Lung Motion During Breathing", *International Journal of Radiation Oncology\*Biophysics* 75, 276-284 (2009).
- 219.** Chen, T., Wang, X., Chung, S., Metaxas, D. and Axel, L., "Automated 3D Motion Tracking Using Gabor Filter Bank, Robust Point Matching, and Deformable Models", *Medical Imaging, IEEE Transactions on* 29, 1-11 (2010).
- 220.** Frangi, A.F., Niessen, W.J. and Viergever, M.A., "Three-dimensional modeling for functional analysis of cardiac images, a review", *IEEE Transactions on Medical Imaging* 20, 2-5 (2001).
- 221.** Amini, A.A., Chen, Y., Elayyadi, M. and Radeva, P., "Tag Surface Reconstruction and Tracking of Myocardial Beads from SPAMM-MRI with Parametric B-Spline Surfaces", *IEEE Transactions on Medical Imaging* 20, 94-103 (2001).

- 222.** Deng, X. and Denney, T.S., Jr., "Three-dimensional myocardial strain reconstruction from tagged MRI using a cylindrical B-spline model", *Medical Imaging*, IEEE Transactions on 23, 861-867 (2004).
- 223.** Chandrashekara, R., Mohiaddin, R.H. and Rueckert, D., "Cardiac Motion Tracking in Tagged MR Images Using a 4D B-Spline Motion Model and Nonrigid Image Registration", *IEEE International Symposium on Biomedical Imaging: Macro to Nano*, 2004. 1, 468-471 (2004).
- 224.** Chandrashekara, R., Mohiaddin, R.H. and Rueckert, D., "Analysis of 3-D myocardial motion in tagged MR images using nonrigid image registration", *IEEE Transactions on Medical Imaging* 23, 1245-1250 (2004).
- 225.** Ledesma-Carbayo, M.J., Derbyshire, J.A., Sampath, S., Santos, A., Desco, M. and McVeigh, E.R., "Unsupervised estimation of myocardial displacement from tagged MR sequences using nonrigid registration", *Magnetic Resonance in Medicine* 59, 181-189 (2008).
- 226.** Xu, C., Pilla, J., Isaac, G., Gorman, J., Blom, A., Gorman, R., Ling, Z. and Dougherty, L., "Deformation analysis of 3D tagged cardiac images using an optical flow method", *Journal of Cardiovascular Magnetic Resonance* 12, 19 (2010).
- 227.** Kerwin, W.S. and Prince, J.L., "Tracking MR Tag Surfaces Using a Spatiotemporal Filter and Interpolator", *International Journal of Imaging Systems and Technology* 10, 128 - 142 (1999).
- 228.** Venkatesh, B.A., Gupta, H., Lloyd, S., G., Dell'Italia, L. and Denney, T.S., "3D left ventricular strain from unwrapped harmonic phase measurements", *Journal of Magnetic Resonance Imaging* 31, 854-862 (2010).
- 229.** Young, A.A., Axel, L., Dougherty, L., Bogen, D.K. and Parenteau, C.S., "Validation of tagging with MR imaging to estimate material deformation", *Radiology* 188, 101-108 (1993).
- 230.** Moore, C.C., Reeder, S.B. and McVeigh, E.R., "Tagged MR imaging in a deforming phantom: photographic validation", *Radiology* 190, 765-769 (1994).
- 231.** Yeon, S.B., Reichek, N., Tallant, B.A., Lima, J.A.C., Calhoun, L.P., Clark, N.R., Hoffman, E.A., Ho, K.K.L. and Axel, L., "Validation of in vivo myocardial strain measurement by magnetic resonance tagging with sonomicrometry", *J Am Coll Cardiol* 38, 555-561 (2001).
- 232.** Neu, C.P., Hull, M.L. and Walton, J.H., "Error optimization of a three-dimensional magnetic resonance imaging tagging-based cartilage deformation technique", *Magnetic Resonance in Medicine* 54, 1290-1294 (2005).
- 233.** Neu, C.P., Hull, M.L., Walton, J.H. and Buonocore, M.H., "Toward An MRI-Based Method To Determine Three-Dimensional Deformations In Articular Cartilage", in *Summer Bioengineering Conference*, (Sonesta Beach Resort in Key Biscayne, Florida, 2003), pp. Starting page 855.
- 234.** Hill, K.O. and Meltz, G., "Fiber Bragg grating technology fundamentals and overview", *Lightwave Technology, Journal of* 15, 1263-1276 (1997).
- 235.** Kersey, A.D., Davis, M.A., Patrick, H.J., M., L., P., K.K., Askins, C.G., Putnam, M.A. and J., F.E., "Fiber grating sensors", *Lightwave Technology, Journal of* 15, 1442-1463 (1997).
- 236.** Lee, B., "Review of the present status of optical fiber sensors", *Optical Fiber Technology* 9, 57-79 (2003).
- 237.** Roosbroeck, J.V., Vlekken, J., Voet, E. and Voet, M., "A New Methodology for Fiber Optic Strain Gage Measurements and its Characterization", in *Proceedings of the SENSOR+TEST Conference Opto*, (Nürnberg, Germany, 2009), pp. 59 - 64.
- 238.** Moerman, K.M., Sprengers, A.M., Simms, C.K., Lamerichs, R.M., Stoker, J. and Nederveen, A.J., "Validation of SPAMM tagged MRI based measurement of 3D soft tissue deformation", *Medical Physics* 38, 13 (2011).
- 239.** Moerman, K.M., Sprengers, A.M., Simms, C.K., Lamerichs, R., Stoker, J. and Nederveen, A.J., "Validation of Fast Dynamic SPAMM Tagged MRI Based Measurement of Non-linear 3D Soft Tissue Deformation", in *ISMRM ESMRMB Joint Annual Meeting*, (Montreal, 2011).
- 240.** ASTM, "F2503: Standard Practice for Marking Medical Devices and Other Items for Safety in the Magnetic Resonance Environment", (American Society for Testing and Materials International, West Conshohocken, PA, USA).
- 241.** Tse, Z.T.H., Elhawary, H., Montesinos, C.A.F., Rea, M., Young, I. and Lamperth, M., "Testing MR image artifacts generated by engineering materials", *Concepts in Magnetic Resonance Part B: Magnetic Resonance Engineering* 39B, 109-117 (2011).
- 242.** Moerman, K.M., Sprengers, A.M., Simms, C.K., Bohte, A.E., Lamerichs, R., Sinkus, R. and Nederveen, A.J., "Combined MRE and SPAMM tagged MRI for the analysis of large strain soft tissue mechanical properties", in *ISMRM ESMRMB Joint Annual Meeting*, (Montreal, 2011).
- 243.** Moerman, K.M., Holt, C.A., Evans, S.L. and Simms, C.K., "Digital image correlation and finite element modelling as a method to determine mechanical properties of human soft tissue in vivo", *Journal of Biomechanics* 42, 1150-1153 (2009).
- 244.** Tokuno, T., Tada, M. and Umeda, K., "High-precision MRI-compatible force sensor with parallel plate structure", in *Biomedical Robotics and Biomechatronics, 2008. BioRob 2008. 2nd IEEE RAS & EMBS International Conference on*, (IEEE, 2008), pp. 33-38.
- 245.** Tan, U.X., Yang, B., Gullapalli, R. and Desai, J.P., "Triaxial MRI-Compatible Fiber-optic Force Sensor", *Robotics, IEEE Transactions on* 27, 65-74 (2011).

- 246.** Cheng, T., Dai, C. and Gan, R., "Viscoelastic Properties of Human Tympanic Membrane", *Annals of Biomedical Engineering* 35, 305-314 (2007).
- 247.** Thompson, M.S., Schell, H., Lienau, J. and Duda, G.N., "Digital image correlation: A technique for determining local mechanical conditions within early bone callus", *Medical Engineering & Physics* 29, 820-823 (2007).
- 248.** Myers, K.M., Paskaleva, A.P., House, M. and Socrate, S., "Mechanical and biochemical properties of human cervical tissue", *Acta Biomaterialia* 4, 104-116 (2008).
- 249.** Boyce, B.L., Grazier, J.M., Jones, R.E. and Nguyen, T.D., "Full-field deformation of bovine cornea under constrained inflation conditions", *Biomaterials* 29, 3896-3904 (2008).
- 250.** Sutton, M.A., Ke, X., Lessner, S.M., Goldbach, M., Yost, M., Zhao, F. and Schreier, H.W., "Strain field measurements on mouse carotid arteries using microscopic three-dimensional digital image correlation", *Journal of Biomedical Materials Research Part A* 84A, 178-190 (2008).
- 251.** Spencer, M., Siegmund, T. and Mongeau, L., "Determination of superior surface strains and stresses, and vocal fold contact pressure in a synthetic larynx model using digital image correlation", *The Journal of the Acoustical Society of America* 123, pp. 1089-1103 (2008).
- 252.** Goldstein, D.C., Kundel, H.L., Daube-Witherspoon, M.E., Thibault, L.E. and Goldstein, E.J., "A silicone gel phantom suitable for multimodality imaging", *Invest Radiol* 22, 153-157 (1987).
- 253.** Augenstein, K.F., Cowan, B.R., LeGrice, I.J., Nielsen, P.M.F. and Young, A.A., "Method and Apparatus for Soft Tissue Material Parameter Estimation Using Tissue Tagged Magnetic Resonance Imaging", *Journal of Biomechanical Engineering* 127, 148-157 (2005).
- 254.** Denney, T.S., Jr., Prince, J.L., Lopez, M.J. and McVeigh, E.R., "Optimal tag pattern validation using magnetic resonance imaging", in *Image Processing, 1994. Proceedings. ICIP-94., IEEE International Conference, Vol. 1*, (IEEE, Austin, TX, USA, 1994), pp. 881-885.
- 255.** Fahmy, A.S., Krieger, A. and Osman, N.F., "An integrated system for real-time detection of stiff masses with a single compression", *Biomedical Engineering, IEEE Transactions on* 53, 1286-1293 (2006).
- 256.** Kraitchman, D.L., Young, A.A., Cheng-Ning, C. and Axel, L., "Semi-automatic tracking of myocardial motion in MR tagged images", *Medical Imaging, IEEE Transactions on* 14, 422-433 (1995).
- 257.** Osman, N.F., "Detecting stiff masses using strain-encoded (SENC) imaging", *Magnetic Resonance in Medicine* 49, 605-608 (2003).
- 258.** Sampath, S., Parthasarathy, V. and Prince, J.L., "A phantom validation of the FastHARP pulse sequence", in *Biomedical Imaging, 2002. Proceedings. 2002 IEEE International Symposium on* (IEEE, 2002), pp. 117-120.
- 259.** Wyman, B.T., Ph.D dissertation, The Johns Hopkins University, The Department of Biomedical Engineering, 1999.
- 260.** Young, A.A., Kraitchman, D.L., Dougherty, L. and Axel, L., "Tracking and finite element analysis of stripe deformation in magnetic resonance tagging", *Medical Imaging, IEEE Transactions on* 14, 413-421 (1995).
- 261.** Henkelman, R.M., "Measurement of signal intensities in the presence of noise in MR images", *Medical Physics* 12, 232-233 (1985).
- 262.** Gudbjartsson, H. and Patz, S., "The rician distribution of noisy mri data", *Magnetic Resonance in Medicine* 34, 910-914 (1995).
- 263.** Cárdenas-Blanco, A., Tejos, C., Irarrazaval, P. and Cameron, I., "Noise in magnitude magnetic resonance images", *Concepts in Magnetic Resonance Part A* 32A, 409-416 (2008).
- 264.** Aja-Fernandez, S., Alberola-Lopez, C. and Westin, C.F., "Noise and Signal Estimation in Magnitude MRI and Rician Distributed Images: A LMMSE Approach", *Image Processing, IEEE Transactions on* 17, 1383-1398 (2008).
- 265.** Rice, S.O., "Mathematical Analysis of Random Noise", *Bell Systems Technical Journal* 23, 282-332 (1944).
- 266.** Rice, S.O., "Mathematical Analysis of Random Noise", *Bell Systems Technical Journal* 24, 46-156 (1945).
- 267.** Sprengers, A.M.J., Nederveen, A.J., Lamerichs, R. and Stoker, J., "Validation of automated motion assessment in the abdomen", presented at the Proceedings of the International Society for Magnetic Resonance in Medicine 18, Stockholm, Sweden, 2010.
- 268.** Reinsch, C., "Smoothing by spline functions", *Numerische Mathematik* 10, 177-183 (1967).
- 269.** McLachlan, G. and Peel, D., *Finite Mixture Models*. (John Wiley & Sons, New York, 2000).
- 270.** Gabor, D., "Theory of communication. Part 1: The analysis of information", *Electrical Engineers - Part III: Radio and Communication Engineering, Journal of the Institution of* 93, 429-441 (1946).
- 271.** Qian, Z., Metaxas, D.N. and Axel, L., "Extraction and Tracking of MRI Tagging Sheets Using a 3D Gabor Filter Bank", in *Engineering in Medicine and Biology Society, 2006. EMBS '06. 28th Annual International Conference of the IEEE*, (New York, New York, USA, 2006), pp. 711-714.
- 272.** Axel, L., Sohae, C. and Ting, C., "TAGGED MRI ANALYSIS USING GABOR FILTERS", in *Biomedical Imaging: From Nano to Macro, 2007. ISBI 2007. 4th IEEE International Symposium on*, (IEEE, Arlington, Virginia, USA, 2007), pp. 684-687.

- 273.** Shimizu, Y., Amano, A. and Matsuda, T., "*Oblique 3D MRI tags for the estimation of true 3D cardiac motion parameters*", The International Journal of Cardiovascular Imaging (formerly Cardiac Imaging) 26, 905-921 (2010).
- 274.** Vollmer, J., Mencl, R. and Müller, H., "*Improved Laplacian Smoothing of Noisy Surface Meshes*", Computer Graphics Forum 18, 131-138 (1999).
- 275.** Chui, H. and Rangarajan, A., "*A new point matching algorithm for non-rigid registration*", Computer Vision and Image Understanding 89, 114-141 (2003).
- 276.** Moerman, K.M., Kerskens, C.M., Lally, C., Flamini, V. and Simms, C.K., "*Evaluation of a Validation Method for MR Imaging-Based Motion Tracking Using Image Simulation*", EURASIP Journal on Advances in Signal Processing 2010, 11 pages (2010).
- 277.** Phatak, N.S., Maas, S.A., Veress, A.I., Pack, N.A., Di Bella, E.V.R. and Weiss, J.A., "*Strain measurement in the left ventricle during systole with deformable image registration*", Medical Image Analysis 13, 354-361 (2009).
- 278.** Storn, R. and Price, K., "*Differential Evolution – A Simple and Efficient Heuristic for global Optimization over Continuous Spaces*", Journal of Global Optimization 11, 341-359 (1997).